Emplacement and flow dynamics of dykes and lava flows using magnetic techniques: Implications for creating a sense of intangible science via geoheritage

Thesis submitted in partial fulfilment of the requirements for the degree

Doctor of Philosophy in the

Department of Earth Sciences

UNIVERSITÀ DI TORINO

UNIVERSITÀ DEGLI STUDI DI TORINO

XXXVI Cycle

PhD Student: **Rasia Shajahan**

Supervisor   : Dr Elena Zanella

Co-supervisors: Dr Andrew Harris

Dr Benjamin van Wyk de Vries

Dr Sara Mana

Ph.D. Programme Co-ordinator: Francesco Dela Pierre

Academic year: 2020 – 2023

Code of scientific discipline: GEO/10 – SOLID EARTH GEOPHYSICS

ABSTRACT

Comprehending the intricate volcanic processes involves tracing the journey of magma from the magma chamber through the intrusive networks to the extrusive emplacement of lava in the surrounding environment. Effectively conveying these scientific insights to non-scientific individuals is vital for engaging the general public in science and ensuring the practical applicability of the obtained results for them. To address this, I studied the emplacement dynamics of dykes and lava flow through an interdisciplinary approach and finally presented a way to effectively communicate my scientific findings to a wider audience using geoheritage.

Starting with dykes, the emplacement mechanism and flow dynamics of small dyke swarms associated with monogenetic eruptive centres are less studied than those of large swarms associated with shield volcanoes and flood basalts. This is due to their limited exposure and ease of reworking by later events. However, the study of small dykes helps to better constrain the forces controlling dyke propagation and thus reconstruct the emplacement history of the volcanic system. This case study presents a multidisciplinary analysis of Mount Calanna (Mount Etna, Italy) where we study two groups of dykes: 1) sub-vertical dykes from the upper part of the system, and 2) sub-horizontal dykes from the lower part. To infer the magma flow direction, we used Anisotropy of Magnetic Susceptibility (AMS) and compared the results to the Shape Preferred Orientation (SPO) of the plagioclase crystal fabric. To quantify the relative timing of dyke emplacement, and to characterise the magma plumbing system, we also used the palaeomagnetic and geochemical signature of the sampled dykes. The fabric analysis highlights a NE-SW flow direction in the sub-vertical dykes, and a NE-SW and NW-SE direction in the sub-horizontal dykes. Dykes emplaced at the lowest levels in the swarm show sub-vertical to inclined magma flow, whereas those towards the top of Mount Calanna show inclined to sub-horizontal flow. The combined structural and geochemical analyses suggest the Mount Calanna swarm is a coherent intrusive complex associated with a phase of activity of the Ancient Alkaline Centre (AAC), with Mount Calanna representing an example of the uppermost portion of a shallow plumbing system in which intrusion orientations are controlled by regional tectonics.

The second case study addresses the flow dynamics of a lava entry into a water body. When a lava flow enters a body of water, either a lake, sea, river, or ocean, explosive interaction may arise. However, when it is an 'a'ā lava flow entering water, a more complex interaction occurs, that is very poorly described and

documented in literature. In this paper, we analyse the 2-4 ka San Bartolo lava flow field emplaced on the north flank of Stromboli volcano, Italy. The lava flow field extends from ~ 650 m elevation where the eruptive fissure emplaced following the main structural trend of the island to the NE coast through two prominent lava channels at middle elevations. Along the coast, the lava flow field expands to form a lava delta ~ 1 km wide characterized by 16 lava flow units. We use a field survey to characterize the features of lava entering the sea and the associated formation of different components and collected oriented hand-samples and drilled cores in order to obtain magnetic measurements to infer the flow fabrics and emplacement process of the lava flow system. We measured the density, porosity, and connectivity of several specimens to analyse the effect of lava-water interaction on the content in vesicles and their connectivity, and conducted a clast count at selected sites to infer the character of the eroded offshore segment of the lava flow field and its component flow units. The collected data allowed us to define the main components of a lava delta fed by 'a'ā lava flows, with its channels, littoral units, ramps, lava tubes, and inflated pāhoehoe flows fed by the arterial 'a'ā flow fronts. The spatial organization of these components allowed us to build a model for 'a'ā entering a water body which is characterized by three main phases. The initial stage corresponds to the entry of channel-fed 'a'ā lava flow into the sea which fragments to form metric blocks of 'a'ā lava. Continued lava supply to the foreshore causes flow units to stall while spreading over this substrate. Subsequent 'a'ā lava flow units ramp up behind the stalled flow front barrier. Lava tubes extending through the stalled flow barrier feed the seaward extension of a bench made of several pāhoehoe flow units.

Finally, as an application of my research, I endeavoured to introduce a method to introduce the obtained scientific results to the non-scientific community. This initiative stems from the recognition that scientific studies, their methods, and results are often difficult to understand for non-specialists due to their esoteric nature. Lack of understanding means that such work is removed from our normal life experience, and thus, the applicability, interest, and use of such work can be minimal. In natural sites, visitors often have their most direct access to science, and this is an opportunity for scientists to make things clear. The challenge is to make science and scientific techniques accessible to all so their usefulness can be broadened. AMS (anisotropy of magnetic susceptibility) is a good example of such an inaccessible technique far removed from everyday experience. Even the full name is hard to understand, and even to say. However, it is an extremely useful geoscience technique with many applications, including finding strain and flow sense in rocks. We explore here how to make 'AMS' understandable, using three different volcanic sites where the flow of molten rock is an important aspect situated in different types of

geoheritage visitation contexts (e.g., wild trekkers, beach visitors, and walkers). The method we develop and test follows the production of simple, adapted explanations, coupled with geoheritage inventorying and communication. We use all the tangible geological features of outcrops, coupled with intangible elements (i.e., rock magnetic data), and a geoheritage inventory (using the M-GAM method) and we build narratives for popular comprehension. This method could be useful for scientific studies to allow them to reach out to a wider public, using their input in the simple explanation stage to con-construct a narrative. This can then be consolidated with the geoheritage inventory to identify the best target sites for communication and to integrate the 'arcane' science. Once done, further scientific work can only benefit from the solid grounding it would have in simple communication. This would provide a way for science to be more widely appreciated, useful, and applicable.

ACKNOWLEDGMENT

LIST OF FIGURES

LIST OF TABLES

CONTENTS

x

Chapter 1

INTRODUCTION

1.1 Rationale

Flow dynamics and emplacement mechanisms are two principal domains associated with the intrusive (e.g., dykes, batholiths, sills) as well as extrusive units (e.g., lava, pyroclastic flows) of a volcanic system. They provide insights into the internal structure of intrusive (e.g., Tibaldi, 2015; Burchardt and Galland, 2016; Cruden and Weinberg 2018) and extrusive systems (e.g., Calvari and Pinkerton, 1999; Passey and Bell, 2007; El Hachimi et al., 2011; Dietterich et al., 2012; Cardona et al., 2021), and help us to better describe the various mechanisms that define volcanic activity.

The study of the propagation and emplacement dynamics of the intrusive system is of primary importance for understanding the structure and evolution of the magma plumbing system. Within the magma plumbing system, magma moves between storage zones, and into the volcanic construct, via connecting structures (i.e., dykes and sills); which sometimes feed eruptive activity and sometimes remain intrusive (Francis et al., 1993). The location, orientation, size, and shape of the resulting dyke or sill depends on the regional extensional stresses acting on the volcanic system (e.g., Acocella and Neri, 2009; Woo and Kilburn, 2010; Daniels and Menand, 2015). Thus, studying the emplacement of and magma flow in dykes and sills is essential in understanding how feeder systems develop, as well as flow dynamics within that system (e.g., Wiegand et al., 2017; Minakov et al., 2018; Das and Mallik, 2020; Datta et al., 2023). Thus far most of the studies on dykes have focused on giant dyke swarms, such as those of the Mackenzie (Ernst and Baragar, 1992) and Deccan (Ray et al., 2007) flood basalts, as well as in Iceland (Eriksson et al., 2015) and Rio Cearfi-Mirim (Archanjo and Launeau, 2004). In contrast, small dyke swarms at single eruptive centres (stratovolcanoes), are poorly studied. Nevertheless, the study of small dykes enables us to better characterize the forces that control dyke propagation and therefore reconstruct a more reliable emplacement history of the volcanic system.

Molten rock issuing from the feeder system might reach the surface creating extrusive products that flow and migrate laterally across the ground surface, forming a "flow system". Deciphering the dynamics of lava and pyroclastic flow is more challenging because the flow is less constrained, compared to the "feeder system", as the flow occurs in an open environment. Local environmental conditions i.e.,

subareal, submarine, or even subglacial emplacement, have a significant impact on the propagation of a lava flow from its source region (Kilburn, 2000). Apart from the two most common situations of subaerial and submarine emplacement of lava, the "entry of lava into water system" is also a common occurrence, as observed at volcanic islands (e.g., Mattox and Mangan, 1997; Poland and Orr, 2014; Bosman et al., 2014), effusive centres adjacent to lakes (e.g., Jenks and Bonnichsen, 1989; Obata and Umino, 1999; Tucker and Scott, 2009), or volcanoes near coastlines (Mueller et al., 2000; Mulas et al., 2016). Studying the lava entry of water enhances our understanding of the factors that control the style and intensity of hydrovolcanic explosions, as well as the morphology of different volcanic features. Extensive research has been conducted to comprehend the water entry of lava flows; however, most studies have focused on the interaction between water and pāhoehoe flows (e.g., Mattox and Mangan, 1997; Obata and Umino, 1999; Skilling 2002; Bosman et al., 2014; Poland and Orr, 2014). Limited knowledge exists about the 'a'a entry into lakes, seas, or oceans (Maeno and Taniguchi, 2006; Maeno et al., 2016; Alonso et al., 2023).

The process as well as the techniques used to describe the emplacement dynamics are often challenging for non-specialists and even academics to understand. This is not an exclusive feature of our study but applies to all scientific works due to its complex and esoteric nature, making it less accessible to the general population. Luckily, the communication of geoscience finds a natural conduit through geoheritage to reach the non-scientific community. In most cases, the scientific techniques and their basic concepts make it difficult for people to understand. Anisotropy of magnetic susceptibility (AMS) is a good example of such an inaccessible technique, far removed from everyday experience. At the same time, it is an extremely useful geoscience technique with many applications, including finding strain and flow sense in rocks. In this regard, it is becoming increasingly obvious that simple, adapted explanations, coupled with their applications, will help to bring these scientific works and their applicability to the public.

1.2 Objective

The primary aim of this thesis is to gain a wider understanding of the flow dynamics and emplacement mechanism of volcanic feeders and flow systems through a multidisciplinary approach. Further, this thesis tries to make the main technique used in my thesis, i.e., AMS, accessible to all using geoheritage, so its usefulness can be broadened. The objectives of this thesis are divided into three different parts.

The first part focuses on the emplacement process of a small intrusive system (Figure 1.1). To this purpose, I studied a small but significant dyke swarm, Mount Calanna (Mount Etna, Italy). Mount Calanna dyke swarm is an isolated hill located on the south-west of Mount Etna. Here, I am trying to understand the flow dynamics of two groups of dykes, sub-vertically and sub-horizontally emplaced ones, to better constrain the emplacement model of Mount Calanna dyke swarms. The study of small dykes may help better constrain all the forces controlling dyke propagation and thus reconstruct a more robust emplacement history of the volcanic system. Further, I try to propose a new approach to interpret magma flow direction in dykes by combining the AMS technique with previously accepted methods. The data and results of this chapter have been submitted to the Journal of Volcanology and Geothermal Research with the title '**Emplacement of, and flow dynamics in, a small volcanic dyke swarm: the example of Mount Calanna (Etna, Italy)**'.

The second part of this thesis focuses on the sea entry of a flow system (Figure 1.1). The San Bartolo lava flow of Stromboli (Italy) is a fine laboratory for studying the sea entry of lava where the formation of various flow components along the coast are well preserved. My focus here is on the flow dynamics of channel-fed 'a'a lava entering the sea, to reconstruct the emplacement process by correlating the magnetic fabrics with the field observations (Manuscript ready to submit under the title '**When the lava meets the sea: emplacement of the 2-4 ka San Bartolo lava flow field, Stromboli volcano (Italy)**'.).

Finally, intending to make the work described above intelligible to all, I try to make the AMS technique (the most used technique in this thesis) understandable to all via geoheritage (Figure 1.1). This can be achieved using the case study from three different volcanic sites; 1) the dyke swarms of Mount Calanna (Etna, Italy); 2) the lava flow of the San Bartolo (Stromboli, Italy), and; 3) the lava flow of Thones le Vieux and Thones le Jeune of Massif Central (France). The method I am testing is the use of simple, adapted explanations, coupled with a geoheritage inventory (Manuscript submitted to the International Journal of Geoheritage and Parks entitled '**Creating a sense of intangible science: making it understandable to a broad public via Geoheritage**').
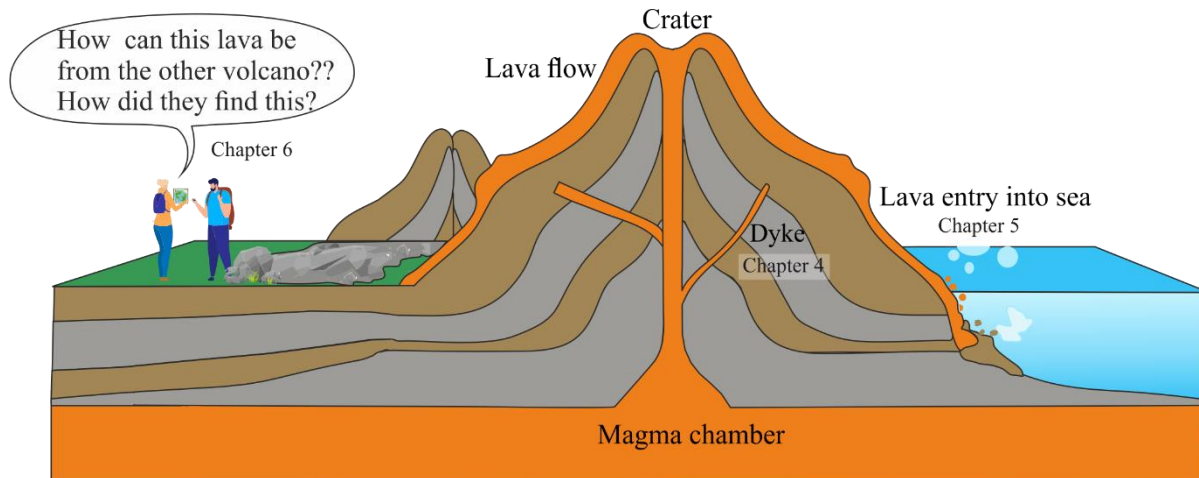
Figure 1. 1. Schematic illustration of a volcanic setting showing the volcanic plumbing system and the respective thesis chapters.

1.3 Thesis scheme

This thesis is structured into seven chapters with the following organization:

Chapter 1: This chapter provides a basic introduction to this thesis, highlighting the main motivation, challenges, and questions that the thesis seeks to address.

Chapter 2: This chapter gives a general description of the available knowledge of AMS application in volcanic settings, especially in dykes and lava flows. The chapter begins with an overview of the importance of magnetic fabrics in volcanology, followed by a review of the evolution of the use of the AMS technique to decipher the direction of magma or lava flow.

Chapter 3: This chapter provides a general description of the applied methodologies. It comprises mainly rock magnetic, textural, and geochemical analysis.

Chapter 4: This chapter reports my findings and discussion from the first case study of the Mount Calanna dyke swarm. The chapter begins with a summary of the geological setting of Mount Calanna, followed by the main results and discussions. Here, I also present a new approach to deciphering the magma flow direction in dykes using the AMS technique. I further present the models for the emplacement of sub-vertical and sub-horizontal dykes in a small dyke swarm.

Chapter 5: This chapter reports the results from the second case study of the San Bartolo lava flow of Stromboli. It explores the emplacement mechanism of the ocean entry of the channel-fed 'a'a flow and the associated formation of different flow components. A comprehensive component description and its

emplacement models are documented. Finally, I illustrate the spatial distribution of the different components and the ocean entry model of the San Bartolo lava flow along the coast.

Chapter 6: In this chapter, I explore how to make 'AMS' understandable, using three different volcanic sites where flow is an important aspect. It deals with making simple adapted explanations for AMS coupled with geoheritage inventorying. I use all the tangible geological features of outcrops, coupled with intangible elements (e.g., rock magnetic data), in the inventory, and we build narratives for popular comprehension. The chapter concluded by pointing out the necessity of making sense of any esoteric scientific data/research depending on the context. The inventory of three volcanic sites is added in the appendix section.

Chapter 7: This chapter summarises the main findings of my thesis.

Chapter 2

A BRIEF OVERVIEW OF THE APPLICATION OF AMS IN DYKES AND LAVA FLOWS

2.1 Introduction to AMS in volcanic domains

According to Hirt and Almqvist (2011), the rock fabric forms due to the distribution of minerals in a uniform direction under anisotropic stress. In volcanic settings, rock fabrics can be formed during magma intrusion (in dykes, sills, batholiths, or even large plutons), emplacement of feeders and flow systems, and its post-emplacement processes. Studying the rock fabrics can thus unravel the internal dynamics and evolutionary history of the volcanoes. Examining macroscale and microscale petrofabrics using conventional methods such as mineral lineation, gas bubbles, crystal alignment and vesicle orientations (e.g., Coward, 1980; Pan et al., 2014; Ohashi et al., 2018) is time-demanding and often the fabrics are not well developed. With the pioneering proposal of the directional property of magnetic minerals by Graham (1954), low-field anisotropy of magnetic susceptibility (AMS) has been widely used as a petrofabric tool in the field of volcanology for more than six decades. The magnetic property of minerals to align in a common direction results in their magnetic anisotropy, which is determined by the shape and crystallography of each mineral. Following the use of AMS, the domain of volcanology has experienced significant progress in comprehending the flow dynamics and internal structure of magma plumbing systems.

The key, well-established application of AMS in the domain of volcanology is the study of emplacement dynamics and its associated processes related to intrusive and extrusive activity. The preferred alignment of magnetic minerals in volcanic rocks can provide insight into the formation history of rocks and information concerning the flow dynamics of magma and/or lava. AMS technique along with other rock magnetic techniques can provide valuable information to the field of volcanology including the flow path (e.g., Knight and Walker, 1988; Cagnoli and Tarling, 1997; Giordano et al., 2008; Guimarães et al., 2017), emplacement mechanism (e.g., Schneider and Fisher, 1998; Stevenson et al., 2008; Wei et al., 2014a; Wiegand et al., 2017; Lyra et al., 2018), relative timing of emplacement (e.g., Duermeijer et al., 1998;

Mertanen and Karell, 2011; Lubnina et al., 2016; Bhatt et al., 2017), and the tectonic rotation of rocks (e.g., Aubry et al., 1996; Duermeijer et al., 1998; Lefort et al., 2001; Yu et al., 2014).

In basaltic rocks, the AMS is primarily controlled by ferromagnetic minerals (mainly magnetite and titanomagnetite) as the susceptibility value is $> 10^{-3}$ SI (Rochette, 1987; Rochette et al., 1991; Hroudra, 1993). In ferromagnetic minerals magnetic fabric is driven by a) magnetocrystalline anisotropy: primarily for minerals with low crystal lattice symmetry such as hematite or pyrrhotite (Moskowitz, 1981); b) distribution anisotropy: which is due to the interaction of magnetic grains (Hargraves et al., 1991); c) shape anisotropy: shape-controlled anisotropy primarily for multidomain magnetite (Cañón-Tapia and Coe, 2002).

2.1.1 Magma flow in dykes and its AMS application

The propagation and emplacement of dykes is a major area of focus in volcanology as they offer the most efficient path for magma movement within the Earth's crust. Dykes propagate both vertically as well as laterally to feed the eruption (feeder dykes) or to arrest at various depths (non-feeder dykes) (Gudmundsson, 1990). Knowing the nature of the dyke intrusion mode and the internal structure of the magma plumbing system helps to predict the lateral extent of the eruption from the source region, as well as later eruptive behaviour. Moreover, studying the dyke emplacement mode, whether lateral or vertical helps to understand the magma chamber position as well as the relative time of activity of feeder dykes. The processes of magma dynamics cannot be observed directly but require either the exposed plumbing system due to erosion (e.g., Németh and Martin, 2007; Keating et al., 2008; Kiyosugi et al., 2012) or data from geophysical measurements (e.g., Cañón-Tapia, 2004; Peltier et al., 2005; Taisne et al., 2011; Bakker et al., 2016; Nagaraju and Parashuramulu, 2019). Low-field anisotropy of magnetic susceptibility (AMS) is one such geophysical technique that facilitates the study of magma flow, dyke propagation, and magma source location. This enables the development of emplacement models and understanding of post-emplacement processes (e.g., Khan, 1962; Chadima et al., 2009; Delcamp et al., 2015; Wiegand et al., 2017; Otmane et al., 2018; Das et al., 2019a; Das and Mallik, 2020; Trippanera et al., 2020).

2.1.1.1 Unravelling magma flow: the evolution of the AMS technique

The AMS interpretation of magma flow in dykes has evolved since Graham (1954) proposed the possibility of using it as a proxy for flow fabrics, and it is still a topic of discussion (Cañón-Tapia, 2004; Delcamp et al., 2014; Hrouda et al., 2019). Khan (1962) was the first to explore the potential use of AMS for the study of magma flow direction in dykes. According to Khan (1962) and Ellwood (1978), the

direction of magma flow is determined by the intermediate axis (K_2 or K_{int}) of the susceptibility ellipsoid, which is oriented within the dyke plane (Figure 2.1a). They rely solely on the theoretical model of susceptibility ellipsoid motion, without sufficient consideration of field observations.

Later, Knight and Walker (1988) were able to propose a more widely accepted interpretation of the AMS results from the Hawaiian dykes, where they supported their findings with macroscopic field observations. They proposed that the maximum susceptibility axis/ lineation (K_1 or K_{max}) is aligned with the magma flow direction, with the K_1-K_2 plane remaining mostly within the dyke plane. Fabrics of this type, where the K_1 axis is parallel to the dyke wall, are considered 'normal' fabrics. They also noted a bimodal clustering of the K_1 axes, consistent with the macroscopic surface lineation on the dyke wall. The authors interpret this clustering of the K_1 axes on both sides of the dyke wall as an imbrication of the susceptibility ellipsoid during laminar flow (Figure 2.1b). They also interpreted the proximity of the clustering of K_1 axes to the dyke width and linked it to the velocity gradient of magma within the dyke. Later, many studies used magnetic lineation imbrication at the dyke boundary to determine the direction of magma flow as well as the sense of flow (Moreira et al., 1999; Varga et al., 1998).
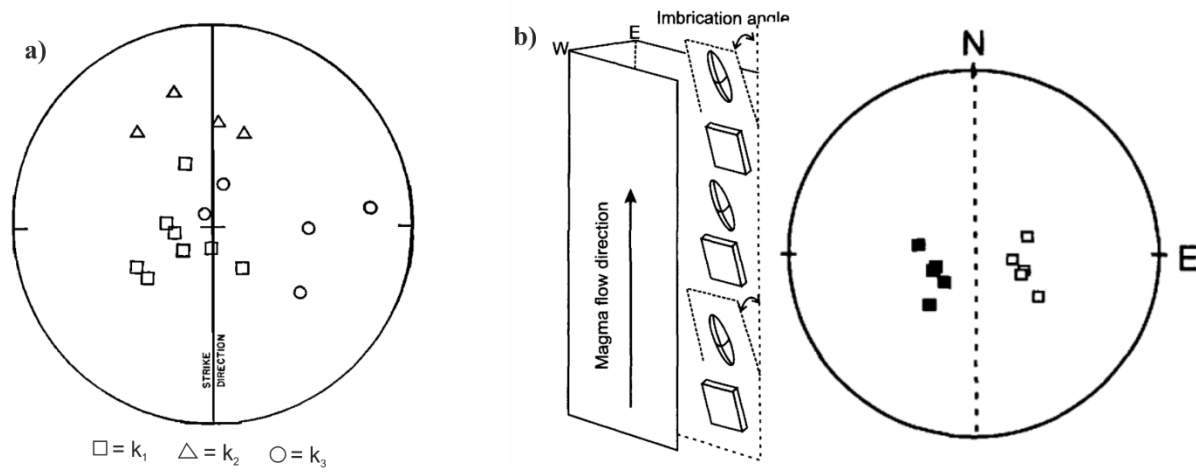
Figure 2. 1. a) Distribution of intermediate (K_2) susceptibility axes along dyke plane with the maximum and minimum axes incline to the dyke wall (Khan, 1962). **b)** Schematic representation of the magma flow in dyke with the imbrication of prolate and platy minerals (left), and the stereographic projection showing the imbrication of K_1 axes (after Cañón-Tapia, 2004).

At the same time, Potter and Stephenson (1988) demonstrated the effect of particle size on AMS interpretation using laboratory-prepared samples. They explained that for multi-domain magnetite (>20 nm), the K_1 axes of the susceptibility ellipsoid show parallelism with the easy axis of magnetization, and for single-domain (SD) particles (<20nm) the K_1 axis is perpendicular to the easy axes of magnetization. Subsequent studies have interpreted this exchange of K_1 and K_3 axes, where K_3 is parallel to the magma

flow direction, in the light of the single-domain effect (Rochette, 1988). Rochette et al. (1992) termed these fabrics, where the K_1 and K_3 axes are interchanged, as 'inverse' fabrics.

In addition to the normal and inverse magnetic fabrics, Rochette et al. (1992) and Rochette et al. (1991) presented the 'intermediate' (i.e., the K_2 axes perpendicular to the flow direction) and 'oblique' fabrics (where the three axes show a completely random orientation). Intermediate fabrics are formed either by the presence of both normal and inverse fabrics (Rochette et al., 1999). All fabrics other than normal are referred to in most studies as 'anomalous' fabrics. Knight and Walker (1988) attributed the random orientation of the susceptibility axes (here, oblique fabrics) to the turbulent magma flow and post-emplacement process. Park et al. (1988) correlated the formation of anomalous fabrics with changes in the domain structure of magnetite grains due to post-emplacement tectonic reworking. The interaction of adjacent magnetic grains (Cañón-Tapia, 1996; Fanjat et al., 2012) or hydrothermal processes leading to the reorientation of magnetic grains along the fluid direction (Rochette et al., 1991) or cyclic movement of ellipsoid particles (Canon-Tapia and Alvarez, 2004) and the formation of magnetite dendrites due to rapid quenching of magma (Shaar and Feinberg, 2013) can also results in the formation of anomalous fabrics. Subsequently, many other studies also tried to explain the reason for the formation of 'anomalous' fabrics (i.e., Dragoni et al., 1997; Archanjo and Launeau, 2004; DeFrates et al., 2006; Philpotts and Philpotts, 2007; Chadima et al., 2009). Thus, the reason for the formation of anomalous fabrics is not simply the SD effect and it is not straightforward to interpret (Cañón-Tapia, 2004 and references therein).

Correa-Gomes et al. (2001) studied the flow fabrics of a vertically emplaced dyke, considering all coaxial stresses using a conceptual model and compared the results with field data. They suggested that for the interpretation of the magma flow direction, it is necessary to consider the geometric relationship between the dyke symmetry plane and the fabric symmetry plane, all external shears, and the flow plane lateral obliquities (Figure 2.2). Thus, taking into account buoyancy-related magma stress (internal) in conjunction with tectonic stress (external) helps to better understand and model dyke emplacement dynamics.

TECTONIC SETTING

EXPECTED LATERAL FABRIC ELLIPSES

DYKE SYMMETRY PLAN (DSP) X FABRIC SYMMETRY PLAN (FSP)

SINISTRAL PURE TRANSCURRENT FAULT

(a)

CASE 1
Magma Flow Velocity (MFV)
>>
Wall Displacement Velocity (WDV)/2

MFV (1.0 m/s) >>WDV/2 (0.0 m/s)

lateral resultant velocity 1.0 m/s

lateral resultant velocity 1.0 m/s

1.0 m/s

DSP = FSP

(b)

CASE 2
MFV**>**WDV/2

MFV (1.0 m/s) > WDV/2 (0.5 m/s)

1.5 m/s

0.5 m/s

1.0 m/s

DSP ≠ FSP

FSP with the sense of external shear rotation

(c)

CASE 3
MFV=WDV/2

MFV (1.0 m/s) = WDV/2 (1.0 m/s)

2.0 m/s

0.0 m/s

1.0 m/s

NO FSP

(d)

CASE 4
MFV<WDV/2

MFV (1.0 m/s) < WDV/2 (1.5 m/s)

2.5 m/s

-0.5 m/s

1.0 m/s

DSP ≠ FSP

FSP counter sense of external shear rotation

(e)

CASE 5
MFV<<WDV/2

MFV (1.0 m/s) << WDV/2 (10.0 m/s)

11.0 m/s

-9.0 m/s

1.0 m/s

NO FSP

⇕ Shearing due to magma buoyancy-related stress

⇗ Shearing due to external, tectonic-related stress

—— Fabric symmetry plan (FSP)

- - - - Dyke symmetry plan (DSP)

10

Figure 2. 2. a-e. Different scenarios for the development of petrofabrics when both magma buoyancy-related stress and tectonic-related stress act at the same time (Correa-Gomes et al., 2001).

A later study by Geoffroy et al. (2002) using image analysis showed that the flow direction obtained using the K_1 axes differed from the field observations, whereas the K_3 axes coincided with the magma flow direction. They proposed a geometric method where the imbrication of the foliation plane yielded a more realistic flow direction in the oblate ellipsoid rather than the lineation which was mostly found perpendicular to the dyke wall (i.e., K_1 is along the intersection axis of the subfabrics). Subsequent studies have also shown that the K_1 axis doesn't always follow the direction of dyke propagation, and imbrication of the AMS ellipsoid on the opposite side of the dyke can give a more reliable sense of the magma flow (Cañón-Tapia, 2004; Geoffroy et al., 2007; Philpotts and Philpotts, 2007; Aubourg et al., 2008; Delcamp et al., 2014). However, this way of interpreting the flow fabrics from the imbrication (foliation or lineation) of the AMS ellipsoid from the opposite side of the dyke gives mostly local fabrics (not for large dyke swarms). Therefore, a better approach is to consider the bulk fabrics where the flow direction or emplacement mechanism of a large dyke swarm is of interest (Archanjo and Launeau, 2004; Philpotts and Philpotts, 2007; Hastie et al., 2014).

Several studies have attempted to complement AMS data with shape preferred orientation (SPO) or crystallographic preferred orientation (CPO) of minerals (Geoffroy et al., 2002; Archanjo and Launeau, 2004; Hastie et al., 2011a; Hastie et al., 2011b; Roni et al., 2014; Silva et al., 2014; Das and Mallik, 2020). For example, the AMS study of the Rio Ceará-Mirim mafic dyke by Archanjo and Launeau (2004), found different magnetic and silicate fabrics because of the different cooling time and fabric acquisition processes (Figure 2.3). Moreover, the low-temperature oxidation may produce SD grains that can potentially influence the overall magnetic anisotropy. This may lead to the development of intermediate magnetic fabrics and/or the occurrence of normal magnetic fabrics within an unconventional silicate fabric context. Accordingly, they advised adding other data, to complement the magnetic fabrics from AMS analysis. This helps to ensure that the AMS fabrics are directly related to the initial magma flow, rather than formed by the late-stage secondary process, such as the backflow of magma in vertical dykes due to gravitational forces, or recrystallisation caused by alteration or deformation due to post-tectonic processes.
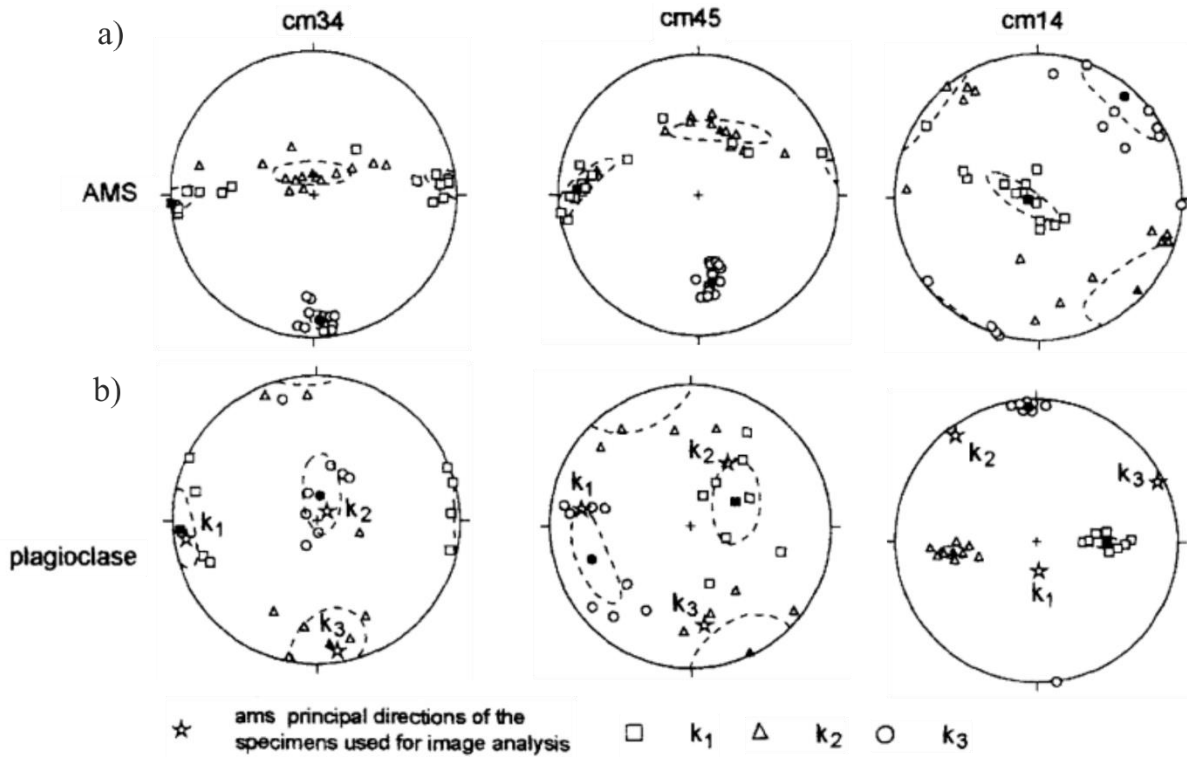
Figure 2. 3. Comparison of magnetic fabrics from **a)** AMS analysis and **b)** SPO of plagioclase from three representative sites (Archanjo and Launeau, 2004).

Philpotts and Philpotts (2007), on the study of a wide cretaceous camptonite dyke suggest that it is important to consider the sampling location within dyke, i.e., whether at dyke wall or near to the dyke wall. Through the field observations and AMS analysis, they stated that the central part of the thick dykes has a high tenancy of late-stage back flow, which results in unrelated flow fabrics. Therefore, they advised future works to consider the samples close to the dyke wall, where the primary flow fabric is preserved. A recent study by Das and Mallik (2020) addressed the concerns raised by McHone et al. (2005) and Ray et al. (2007) regarding the credibility of AMS data. They studied the magma flow fabrics using SPO of plagioclase grains and AMS fabrics and explained the variation of flow fabrics in dyke centre and boundary with respect to flow velocity and friction. Results showed that samples from the centre of thicker dykes (>10 m) displayed unrealistic magnetic fabrics due to backflow, whereas thinner dykes gave consistent flow fabrics (Figure 2.4). In the case of thinner dykes, both dyke boundary and dyke centre samples exhibited coherent silicate and magnetic fabrics.
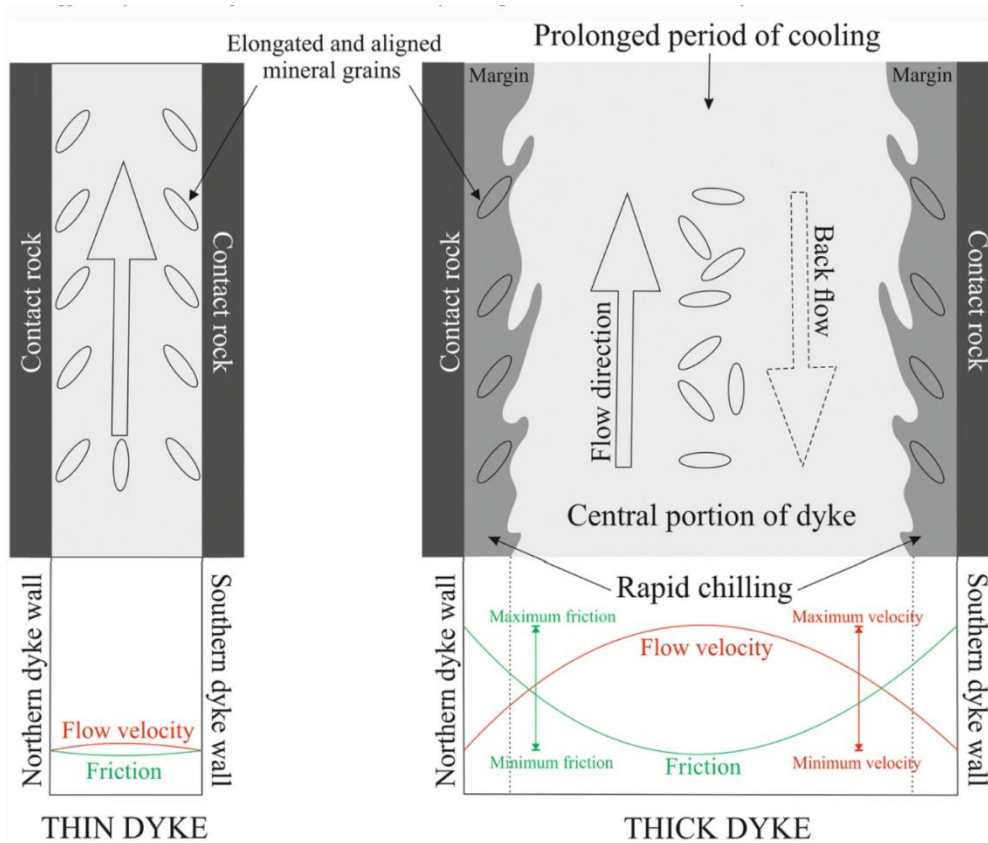
Figure 2. 4. Schematic representation of magma flow inside thin and thick dykes based on the flow velocity and friction (Das and Mallik, 2020).

Delcamp et al. (2014) studied the flow sense of shallow basaltic dykes in the NE Tenerife rift zone and observed a more complex dyke propagation rather than the normal uniform magma flow in the rift zones. They used the imbrication of the foliation plane (K_1-K_2) with respect to the wall in the case of oblate fabrics and the orientation of the lineation (K_1) in the case of prolate fabrics to obtain the direction and sense of flow. Hence, this way of interpreting magma flow direction based on the shape of the AMS fabrics is becoming more accepted as an established practice (Geoffroy et al., 2002).

2.1.2 AMS application in lava flows

Unlike dykes, the interpretation of AMS fabrics in lava flows is not straightforward, as the flow is less constrained and has no wall or margin on both sides for imbrication (Canon-Tapia et al., 1995; Herrero-Bervera et al., 2002; Zananiri et al., 2004; Köpping et al., 2023). In addition, lava emplacements in a sub-area environment are less stable due to possible syn- or post-displacement at the top of the lava.

The seminal study of Tertiary lava flow from the Island of Skye and Deception by Khan (1962) found a correlation between the K_2 axis of AMS fabrics and the local flow direction. In order to check the

reliability/applicability of the AMS technique for inferring flow direction in lava, he studied the AMS of a lava flow where the flow direction was already known. Although he found some scattering of the susceptibility axes, the K_2 axes were mostly aligned with the flow direction. Then, Symons (1975) studied Aiyansh lava flow and associated the flow direction with the K_1 axis without providing additional details and reasoning. A later study by Kolofikova (1976) showed how the magnetic fabrics vary with local flow conditions and found a good correlation of the K_1 axis with the direction of lava flow. He found that near the vent, where magma flows slowly, the AMS fabrics are less defined, possibly due to slow cooling and high viscosity (Figure 2.5a). On the other hand, far from the vent, at the lava toe, where the lava flows relatively faster, the AMS fabric is well clustered and defined (Figure 2.5a). After Symons (1975) raised concerns regarding the reliability of AMS fabrics in interpreting flow direction in lava flow, the use of AMS in lava flow remained dormant for over a decade.

Cañón-Tapia et al. (1995) studied the magnetic fabric and flow direction in basaltic pāhoehoe lava of Xitle volcano (Mexico) and suggested that the degree of anisotropy can be related to the viscosity of the lava and the local morphology of the terrain. On steeper slopes, lava flows tend to align their local flow directions with the overall flow direction of the field, following the slope consistently downhill (Figure 2.5b). When lava encounters a less sloped terrain, it experiences both thickening, leading to a vertical component, and widening, resulting in a lateral component (Figure 2.5b). This can yield AMS fabrics in two distinct directions. Henry et al. (2003) also showed similar results where they observed good clustering of the K_1 axis as the lava passes through the steep slope and scattering of the K_1 axes as it encounters the less sloping terrain.
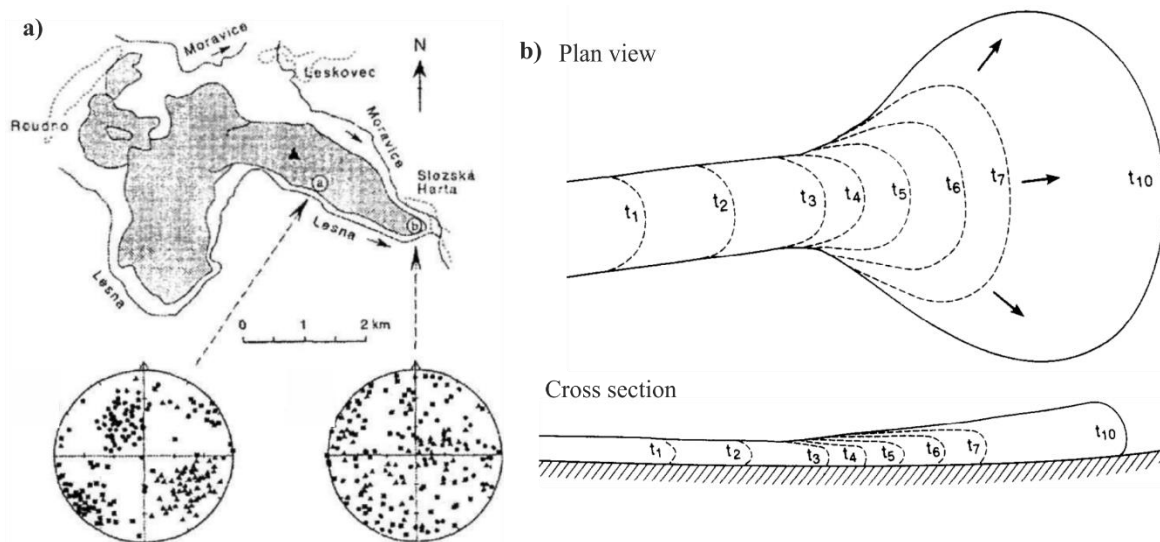
Figure 2. 5. a) Areal view of the Chribsky Les lava flow, showing the distribution of magnetic susceptibility axes at the lava toe and nose of the flow (Kolofikova, 1976). **b)** Plan and cross section of a lava flow from the dormant slope to the less sloped terrain. 'tn' shows the position of the lava flow front at the same time interval (Cañón-Tapia et al., 1995).

Later, using an experimental approach (where a recent lava flow from Kilauea was melted and subjected to multiple strain rates and cooling), Canon-Tapia and Pinkerton (2000) studied the magnetic fabrics of lava flows. They found a strong relationship between the degree of anisotropy and the shearing and thermal history of the lava. Lava that quenches rapidly is found to have a high degree of anisotropy, whereas lava that undergoes the same shear stress but cools slowly has a low degree of anisotropy. Thus, the nature of the shear stress, together with its solidification time, is important in the development of the degree of anisotropy in a basaltic rock. They also addressed the different degrees of anisotropy obtained for the Hawaiian 'a'ā and pāhoehoe lava flows by Cañón-Tapia et al. (1997). The high value of the degree of anisotropy for the 'a'ā lava flow can be related to the viscosity and different strain rates associated with its emplacement.

In lava flows, magnetic lineations are generally oriented along the flow direction when the flow is along a slope, whereas the pole of the magnetic foliation plane is oriented perpendicular to the flow plane (Cañón-Tapia, 2004 and references therein). As with magma flow in dykes, the magnetic foliation plane in lava flow shows small imbrications with the flow plane, with the plane tilting up or down. However, in lava flows, where the magnetic phase is dominated by ferromagnetic minerals, the interpretation of the magnetic flow fabrics is controlled by other factors than in dykes, and the fabrics can be classified into different groups (normal, inverse, intermediate, and oblique fabrics) based on the orientation of the susceptibility axis with respect to the flow plane (see section 2.1.1).

Apart from finding the direction of flow, AMS fabrics have also been used to find the vent position. Zhu et al. (2003) studied the AMS fabrics of Hannuoba basalt (northern China) to find the vent position of the lava sequence and obtained an intersection of the magnetic lineation trend from different locations where they perfectly aligned with the already known vent position.

Bascou et al. (2005) studied the magnetic and crystallographic fabrics in a 13 m thick basaltic lava flow in the open quarry. They found good agreement with the magnetic and crystallographic foliation in the lower part of the flow, suggesting that the initially solidified silicate fabrics control the development of the magnetic fabrics. In contrast, in the middle and upper parts of the flow, late-stage cooling or unstable movement of lava blocks could influence the AMS fabrics. A later study by Boiron et al. (2013) on the basaltic lava flow of La Palisse volcano (French Massif Central) also showed that the imbrication of the foliation plane for samples collected from the base of the lava flow provides a more reliable flow direction. However, a recent study by Atarita et al. (2019), which used the preferred pore orientation in lava flows to support the flow direction obtained from AMS analysis, found good agreement with the flow direction obtained using both methods, and no disturbance was found in the lava flow direction at the base and top of the lava flow.

Several works have correlated the degree of anisotropy with the viscosity of lavas, Hrouda et al. (2005) explored this relationship by studying lavas of different alkaline compositions from the same volcanic region, to rule out the possible influence of local factors. Before comparing the viscosity of different rock types, they ensured that all rock types had the same intrinsic magnetic susceptibility (i.e., similar Curie temperature) and magnetic fabrics acquired during their formation (i.e., primary fabrics). This ensured that the different degrees of anisotropy analyzed were solely due to the different preferred orientations of the magnetic minerals. They found a positive relationship between the degree of anisotropy and viscosity, where in a highly viscous lava the increased friction between the magnetic grains and the matrix leads to better orientation of the magnetic grains. The AMS study by Loock et al. (2008) on a well-exposed lava flow in France uses the K_1 axis and the variation in the degree of anisotropy along with field evidence to demonstrate possible variations in the rheological regime and flow direction, thus defining distinct units within a flow.

The AMS study by Fanjat et al. (2012), of the Kerguelen flood basalt lava flow, yielded two fabric patterns: a) the usual expected normal fabric, which is parallel to the flow direction, and b) an abnormal fabric, which is completely unrelated to the flow direction. They attributed the abnormal fabrics to the

increased interaction of single-domain magnetic minerals due to their tight clustering which results in a higher susceptibility value.

A later study by Sangode et al. (2017) on different lava types of Deccan volcanism found that magnetic fabrics are mainly controlled by cooling style and flow mechanism. In normal pāhoehoe type lava, they found the predominance of the oblate ellipsoid with no preferred alignment of the susceptibility ellipsoid, showing crystal settling of magnetic grains as the primary process for the formation of magnetic fabrics. Whereas in rubble pāhoehoe, the predominance of the prolate ellipsoid along a shallow plane with clustered K_1 axes shows the influence of both viscosity shear and gravitational settling of magnetic grains. A recent study by Sangode et al. (2022) presented an updated model of magnetic fabric development under different conditions, showing the influence of various parameters such as lava temperature gradient, flow turbulence, and accommodation spaces, together with gravitational setting and viscous shear (Figure 2.6a). They studied the flow dynamics of a lava channel, where they observed imbrication of the K_1 axis along the flow direction in the steep part of the lava channel (Figure 2.6b). Another pattern of K_1 imbrication was found perpendicular to the flow direction, probably due to the orientation of K_1 along the easy direction as a result of viscous shear (Figure 2.6b).
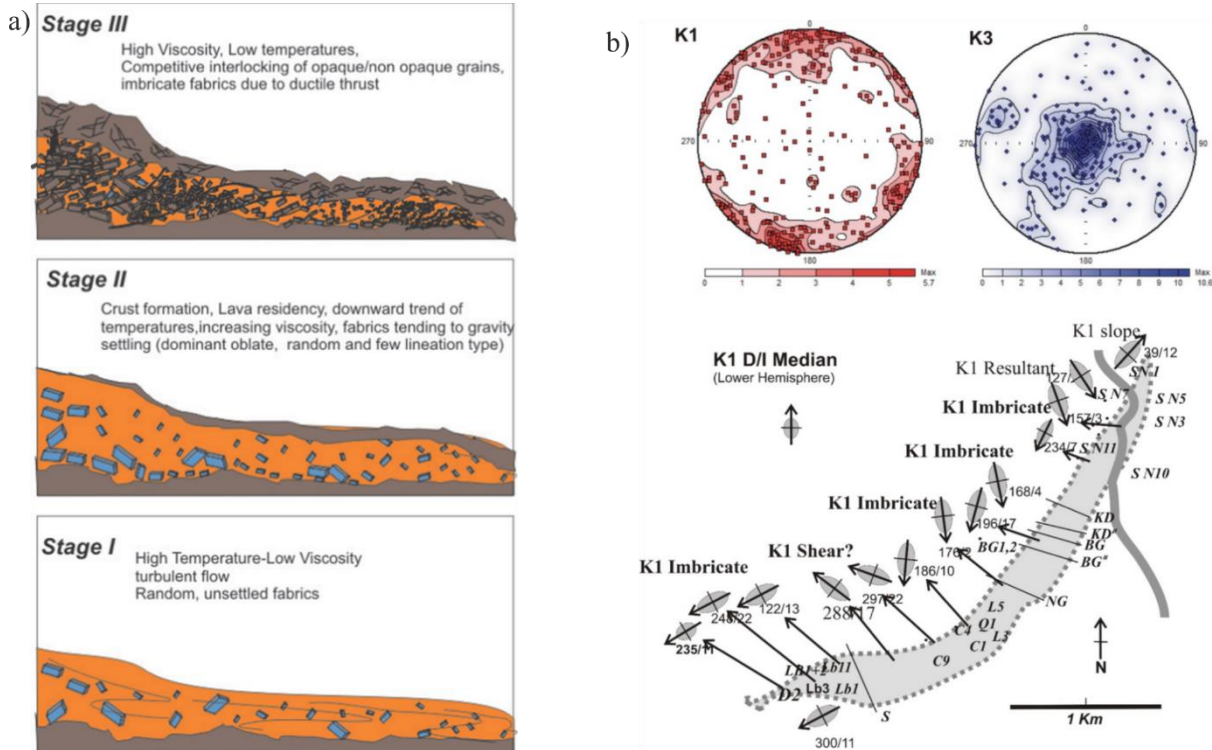
Figure 2. 6. a) Schematic representation of the arrangement and orientation of magnetic minerals under different conditions. **b)** The mean distribution of K_1 and K_3 axes on the stereonet along with the orientation and imbrication of the susceptibility ellipsoid for each local site (Sangode et al., 2022).

Chapter 3

METHODOLOGY

3.1 Rock magnetism

3.1.1 Sampling and sample preparation

The strategy for paleomagnetic sampling primarily depends on the condition of the outcrop and the overall objectives of the study. The two principal sampling methods involve collecting oriented hand-samples and using portable petrol-powered drills to drill cores. In our study, we used both methods following the outcropping conditions. In both scenarios, the samples were carefully oriented using magnetic and solar compasses given the strong magnetic properties of the volcanic rocks.

In the case of the Mount Calanna dykes, which are highly weathered and poorly consolidated, we collected hand-samples. The sampled dykes were continuous, more than 0.5m thick, and samples were collected from both the marginal and central parts of each dyke. From each dyke, we made sure to collect 3 – 5 hand-samples. For the San Bartolo lava flow, we sampled both drilled cores and hand-samples according to standard practice for magnetic measurements (Tarling and Hrouda, 1993). We also made sure that we sampled both the base and the top of each lava flow unit. Importantly, the samples drilled near the beach were returned and glued after the measurements.

The collected samples were subsequently cored and cut into standard cylindrical specimens (diameter = 25 mm, height = 22 mm), mini-cores (diameter = 10 mm, height = 20 mm), and equidimensional chips (size ~1 × 1 cm). At each site, we ensured that at least 8 to 12 samples were available to yield statistically significant data. All magnetic measurements were performed at the Alpine Laboratory of Paleomagnetism (Italy).

3.1.2 Anisotropy of magnetic susceptibility (AMS)

The AMS is measured by applying a low-intensity field to the specimen and measuring the susceptibility along 15 different directions (Jelinek, 1977). The resultant measurements give a second order ellipsoid tensor defined by three principal susceptibility axes which usually represent as $K_1 > K_2 > K_3$.

AMS measurements were performed on all specimens (standard cores, mini-cores, and chips) using a KLY-3 Kappabridge (AGICO). To ensure that the specimens were statistically anisotropic with 95% confidence, only samples with F-tests for anisotropy of > 5 were selected for further analyses (Hext, 1963). The selected data were analysed using the ANISOFT 4.2 software (Chadima and Jelínek, 2008) which computes the susceptibility tensor in the form of an ellipsoid. The principal susceptibility axes of AMS ellipsoid can be represented on equal-area projection with their confidence angle and tensor mean (Jelinek, 1978) Each specimen was weighed to calculate the mass magnetic susceptibility (χ_m express in $\times 10^{-3}$ m^3 kg^{-1}) for data comparison. The AMS ellipsoid is defined by scalar parameters including:

1. Mean susceptibility, $K_m = (K_1 + K_2 + K_3)/3$ (Nagata, 1961), which is characterized by the presence of all major rock-forming minerals.

2. Degree of magnetic anisotropy, $P' = \exp\{2[(\ln K_1 - \ln K_m)^2 + (\ln K_2 - \ln K_m)^2 + (\ln K_3 - \ln K_m)^2]\}^{1/2}$ (Jelinek, 1981), which defined the stretching and the preferred orientation of the AMS ellipsoid

3. Shape parameter, $T = [\{2\ln(K_2/K_3)\}/\ln(K_1/K_3)]^{-1}$, where the value of T varies from +1 for Oblate to -1 for prolate fabric (Jelínek, 1981);

4. Magnetic lineation, $L = K_1/K_2$ (Balsley and Buddington, 1960);

5. Magnetic foliation, $F = K_2/K_3$ (Stacey et al., 1960).

Other than the shape parameter, both magnetic lineation and foliation define the shape of the susceptibility ellipsoid in the frame of the magnitude of susceptibility axes. For the interpretation of magnetic fabrics, the shape of the AMS ellipsoid is important (see Chapter 2). In the case of lava flow (Chapter 5), I use a consistent approach to infer flow direction based on the magnetic fabric type of the shape of the AMS ellipsoid (Delcamp et al. 2014; Callot and Guichet 2003). For the oblate ellipsoid, the imbrication of the foliation plane is used to infer the flow direction, while for the prolate ellipsoid, the orientation of the magnetic lineation is considered.

3.1.3 Palaeomagnetism

Volcanic rocks contain mostly ferromagnetic and ferrimagnetic minerals, which record the strength and direction of past geomagnetic fields. The total record of natural remanent magnetization (NRM) includes that acquired during its formation, as well as any magnetisation acquired subsequently. The remanent magnetisation which acquired during the formation of a rock is called the characteristic remanent

magnetization (ChRM). By removing all secondary component(s) using demagnetisation techniques, we can isolate the ChRM.

For our study, initially, the natural remanent magnetization (NRM) of all the specimens was measured using the AGICO-JR6 spinner magnetometer. Four pilot samples were demagnetised from each site, two using alternating field (AF) and two by thermal demagnetisation, to select the most appropriate demagnetisation method.

Stepwise demagnetisation of the AF was carried out with a field varying from 5 mT to 120 mT. Here the specimen is subjected to an alternating field in the form of a sinusoidal wave where the intensity of current decreases with time. Thermal demagnetisation was carried out with a stepwise increase in temperature from 20 °C to a peak value of 600 °C. After each step of demagnetisation, the magnetic intensity was measured using a spinner magneto meter. In the case of thermal demagnetisation, due to the multiple steps of heating and cooling, there is a potential for the magnetic phase to be changed. Therefore, after each step of thermal cleaning, we measured the susceptibility to check the stability of the magnetic carriers.

Paleomagnetic results are mainly expressed in three different graphical forms: a) the equal area projection in a lower hemisphere stereonet, which gives the directional change during demagnetisation, b) the Zijderveld diagram, or orthogonal diagram, which gives both information on direction and intensity (Zijderveld, 1967), c) and the intensity decay curve, which shows the decay curve of the sample.

Results were processed using the Remasoft 3.0 software (Chadima and Hrouda, 2006). The remanent magnetization components were identified by best fit direction using principal component analysis (Kirschvink, 1980), and mean directions were assessed with Fisher (1953) statistics.

3.2 Methodologies for case study 1 (Chapter 4)

3.2.1 Magnetic mineralogy

The rock magnetic measurements were carried out on representative cores for dyke samples to characterize the different magnetic phases, and to better understand their contribution to both remanence and magnetic fabric. In this study, magnetic mineralogy analysis was mainly focused on investigating changes in magnetic properties resulting from the application of an external magnetic field.

Two samples from each dyke, taken from the dyke centre and dyke boundary, were subjected to isothermal remanent magnetization (IRM) acquisition by systematically increasing the applied field up

to 1.2 T. After each stepwise application of an external magnetic field using an AGICO LDA5 - PUM1 pulse magnetiser, the remanent magnetisation was measured using an AGICO JR-6 spinner magnetometer. Once the specimen reached the saturation of magnetisation, its coercivity of remanence (Bcr) was extrapolated by measuring the back-field curves. The mean remanence coercivity (Bh), and the dispersion parameter (DP) were obtained using the online software MAX UnMix (Maxbauer et al., 2016). The different magnetic components that regulate the magnetic properties (magnetic fabrics and remanent magnetization) of the dykes were later identified based on the Bh and DP values.

Moreover, we performed the thermal demagnetization on the three IRM components (Lowrie, 1990) on one representative specimen from each sample to find the unblocking temperature of each component (soft, medium, and hard coercivity magnetic components). To do this, we applied a field of 1.0, 0.6, and 0.1 T, along the x-, y-, and z-axis of the samples, respectively. Finally, specimens were subjected to progressive thermal demagnetization up to $550 – 600$ °C, where the susceptibility values were recorded after every phase to identify thermally modified mineralogical alterations.

3.2.2 Petrofabric and image analysis

In igneous rocks, the flow fabrics can be attributed to the alignment of rigid particles suspended within a viscous fluid. Petrofabric studies enable the examination of the mineral composition of these rigid particles, while image analysis aids in quantitatively assessing the orientation of silicate fabrics (Shelley, 1985; Geoffroy et al., 2002). Given that ferromagnetic crystals are associated with late-stage crystallization, it is recommended to make a comparison between the silicate fabrics created by plagioclase laths and AMS fabrics before making inferences about the flow direction (e.g., Geoffroy et al., 2002; Ray et al., 2007; Das et al., 2019).

Thin sections were prepared to obtain the mineral assemblage, texture, and shape preferred orientation (SPO) of the silicate fabrics. Two oriented specimens from each dyke were selected: one from dyke centre and one from the dyke boundary, and standard thin sections were prepared along the K_1-K_2, K_2-K_3, and K_1-K_3 planes for specimens having normal, inverse, and intermediate fabrics, respectively (see Section 4.3 for the definition of each fabric type; Figure 3.1a). High spatial resolution images from each thin section were captured using an Olympus B×4 optical microscope (Figure 3.1b). Oriented micrographs were transformed into grayscale, and the plagioclase lath distribution was assessed using ImageJ (Rasband, 2012) (Figure 3.1c). The orientation of plagioclase laths was plotted on a rose diagram (Figure 3.1d) and the direction of flow obtained was compared with the direction obtained from the AMS

analysis. This allows substantiating the reliability of the flow direction acquired from AMS fabrics of the ferromagnetic minerals which crystallize during the later stages of the cooling process, post-magma flow cessation.

| Oriented Core | Captured photograph | Gray scale image | Rose diagram with plagioclase orientation |
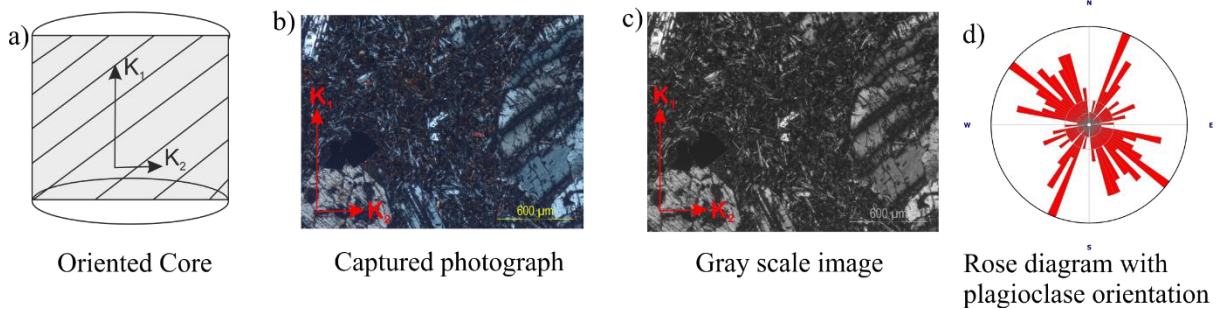
Figure 3. 1. Illustration of the shape preferred orientation (SPO) analysis procedure. **a)** Thin sections were prepared from an oriented core along the K_1-K_2 plane for normal fabrics. **b)** A photograph of the plane was captured**. c)** The acquired image was converted to grayscale and **d)** Plagioclase orientations were determined using ImageJ software and plotted on a rose diagram.

3.2.3 Whole rock geochemistry

Whole rock geochemistry analysis was completed for all nine unaltered samples. Fresh hand-samples were crushed into chips using a hydraulic press fitted with high purity steel plates. Sieved rock chips were rinsed and sonicated in DI water and dried in a low-temperature oven prior to microscopic examination where only chips with minimal surface alteration and free of vesicles were selected for further analyses. Geochemical analyses were carried out on rock powder pulverized using a Spex® ball mill fitted with an alumina vessel. Major element analysis was conducted at the Hamilton Analytical Laboratory, NY, using the 'Thermo ARL Perform'X Spectrometer'. Loss on ignition was measured by heating the samples overnight in silica crucibles at 900°C. REE, HFSE, LFSE and transition metals were analysed on the same samples in Agilent 8900 ICP-MS QQQ housed at the Department of Geology and Geological Engineering, Colorado School of Mines (Colorado). BHVO-2 and an unknown were run to check the precession of data. Filtering of results affected by alteration was made based on Loss on Ignition (LOI) values, where only whole rock analyses having LOI < 3 wt% were considered. This reduced the number of dykes that could be considered fresh to six.

3.3 Methodologies for case study 2 (Chapter 5)

3.3.1 Flow component analysis

Initially, we conducted a thorough survey along the coast of the SB flow field to study the ocean entry of lava and the associated formation of different flow components. For each of the components, we described and quantified, where possible, its geometry (thickness, width, length, slope, orientation); lithology (colour, degree of alteration, nature of minerals), texture (content, size, number, shape and distribution of vesicle, crystal, and void); structures (uniform or brecciated, massive or bedded/layered, with shearing, column, scratch, cooling/quenching structures) and presence of entrained materials like enclaves, anthropic material and clinkers. Moreover, we have conducted a boat survey near the coast to get a broad perspective of the lava entrainment into the sea.

3.3.2 Analysis of porosity and connectivity

We measured the density/porosity and connectivity of a total of 51 specimens, two specimens per sample, to comprehend the effect of lava-water interaction on the content in vesicles and their connectivity. Porosity can be categorized into two main types: connected porosity (Φ'), which represents the fraction of the bulk volume that consists of pore spaces interconnected to the sample's outer surface, and total porosity (Φ), which represents the portion of the bulk volume occupied by all pore spaces, including both connected and isolated pores. The ratio between the connected porosity and the bulk porosity gives, connectivity (C),

$$C = \Phi' / \Phi$$

Density was measured using the Geopyc 1360 Envelope Density Analyzer, while connectivity was measured with a helium displacement AccuPyc II 1350 housed at Laboratoire Magmas et Volcans (LMV), France, following the standard procedures (Thivet et al., 2020). The dense rock equivalent (DRE) of five powdered samples was measured using the Accupyc 1340 Helium Pycnometer. The average DRE from the five measurements of 2.92 kg/m^3 was used to calculate vesicularity following Houghton and Wilson (1989), while the connectivity was derived following Colombier et al. (2017a).

3.3.3 Clast count method

We conducted a clast count within the pebble-to-cobble range (2 – 256 mm) at selected sites to infer the character of the eroded offshore segment of the lava flow field and its component flow units. Clast count was performed at four coastal beaches, two at the flow field left lateral margins (Flows 12 and 7; see Figure 5.1c) and two at the centres (Flows 1 and 4; see Figure 5.1c). At each site, we meticulously counted between 160 and 220 clasts selected as representative and classified according to phenocryst type and vesicularity. At flow 7, we also extended the survey offshore through the dive-based survey to extrapolate the eroded lava bench.

Chapter 4

FIRST CASE STUDY**: DYKE EMPLACEMENT**

The contents of this chapter have been submitted for publication under the title *'Flow dynamics in, and emplacement of, a small volcanic dyke swarm: an example from Mount Calanna (Etna, Italy)'*.

4.1 Geological Setting

4.1.1 Mount Etna

Mount Etna is a Quaternary stratovolcano located on the eastern coast of Sicily (Southern Italy) and over the front of the Apennine - Maghrebian thrust (Gvirtzmann and Nur, 1999). Volcanic activity began about 600 ka with the submarine emission of tholeiitic products, which now outcrop on Etna's southeastern (Aci Trezza Synthem) and southwestern (Adrano Synthem) flanks (Branca et al., 2008). Around 220 ka volcanism became focused to the west of the present-day eastern coastline, with the formation of the Timpe fissure system (Acireale Synthem) and a shift toward Na-alkaline transitional compositions (Tanguy et al., 1997). Volcanic activity related to central-conduit systems began about 130 ka with the construction of Mount Calanna (St. Alfio Synthem), which had a Na-alkaline affinity and represented the first of a series of volcanic centres that developed on the lower eastern flanks (cf. Branca et al., 2011), this being the Valle del Bove Synthem (120-65 ka). The principal eruptive conduit shifted westward over time, reaching the present-day position around 65 ka with the onset of the Ellittico (Concazze Synthem). Development of the Ellittico lasted until 15 ka and ended with a caldera collapse (cf. Nicotra et al., 2010; Nicotra and Viccaro, 2012). Recent activity (Mongibello volcano, Il Piano Synthem) resumed after a short period of quiescence. Eruptive styles have been quite varied, with alternating cycles of Strombolian to Plinian eruptions followed by long periods of effusive activity (Hughes et al., 1990).

4.1.2 Mount Calanna

Mount Calanna has an area of about 0.7 km^2, a peak at 1314 m.a.s.l., and is located on the southeastern flank of Mount Etna (Figures. 4.1a-c). Mount Calanna or the Calanna Formation (Branca et al., 2008) consists of a succession of highly altered faulted lava flows and breccia cut by tens of dykes (Romano

and Sturiale, 1975; Romano, 1982; Ferlito and Nicotra, 2010; Nicotra et al., 2011). Mount Calanna is surrounded by historic lava flows, including those of 1950-51 and 1991-93 (Figures. 4.1c), and its easternmost tip is covered by a small porphyritic hawaiitic lava flow emitted from a 210°N oriented dyke related to a recent (but undated) lateral eruption of Mongibello (Ferlito and Nicotra, 2010).

Initially, Mount Calanna was interpreted as the remains of the Ancient Alkaline Centre (corresponding to the Timpe and Valle del Bove Supersynthem; Klerkx, 1970; Romano, 1982). Later, McGuire (1982) proposed that Mount Calanna represented a volcanic neck that was later dissected by dykes. Instead, Ferrari et al. (1989) defined Mount Calanna as a succession of stacked-up thrust faults, formed by gravitational spreading of the volcanic edifice. However, Ferlito and Nicotra (2010) found no presence of compressional structures at Mount Calanna but confirmed the presence of tens of dykes and several normal faults. Based on structural and geochemical analyses, Ferlito and Nicotra (2010) interpreted Mount Calanna as an intrusive complex that was part of the uppermost portion of a shallow plumbing system.

Due to the high alteration of Mount Calanna, absolute dating is a challenge (Ferrari et al., 1989; Gillot et al., 1994). However, $^{40}Ar/^{39}Ar$ dating of rocks of Val Calanna, a small valley south of Mount Calanna, yielded an age of 128.7±3.8 ka (Branca et al., 2008; De Beni et al., 2005). This locates Mount Calanna at the base of the St. Alfio Synthem, places the intrusive system at the base of the edifice and, thus, during the open phases of activity. The transitional affinity of its products likewise makes Mount Calanna a structure related to the transition of volcanic products of Mount Etna from tholeiitic to alkaline during the beginning of Etna's growth (Ferlito and Nicotra, 2010).

Mount Calanna comprises about 200 dykes (Figure 4.1c) belonging to the Na-alkaline suite of Etna's succession, while the host rock has a basaltic composition (Tanguy et al., 1997; Ferlito and Nicotra, 2010). The dyke swarm has an intensity of intrusion (i.e., the volume ratio between intruded dykes and host rock) of about 40% (Ferlito and Nicotra, 2010). Ferlito and Nicotra (2010) grouped the dykes into two classes: i) E-W oriented and altered, which comprise 90% of the dykes, and ii) ENE-WSW oriented and unaltered, which were interpreted as the feeder systems for the subsequent eruptive events. Both the host rock and altered dyke-group have been reworked by E-W striking faults, intrusion by unaltered dykes, and dissection by joints (Figures 4.1d-e). The joints follow the same orientation as major volcano-tectonic structures in the area, which strike NNW-SSE, ESE-WNW, WSW-ENE, and NE-SW, and which are controlled by the regional tectonics (Lo Giudice et al., 1982; Monaco et al., 1997, 2005).
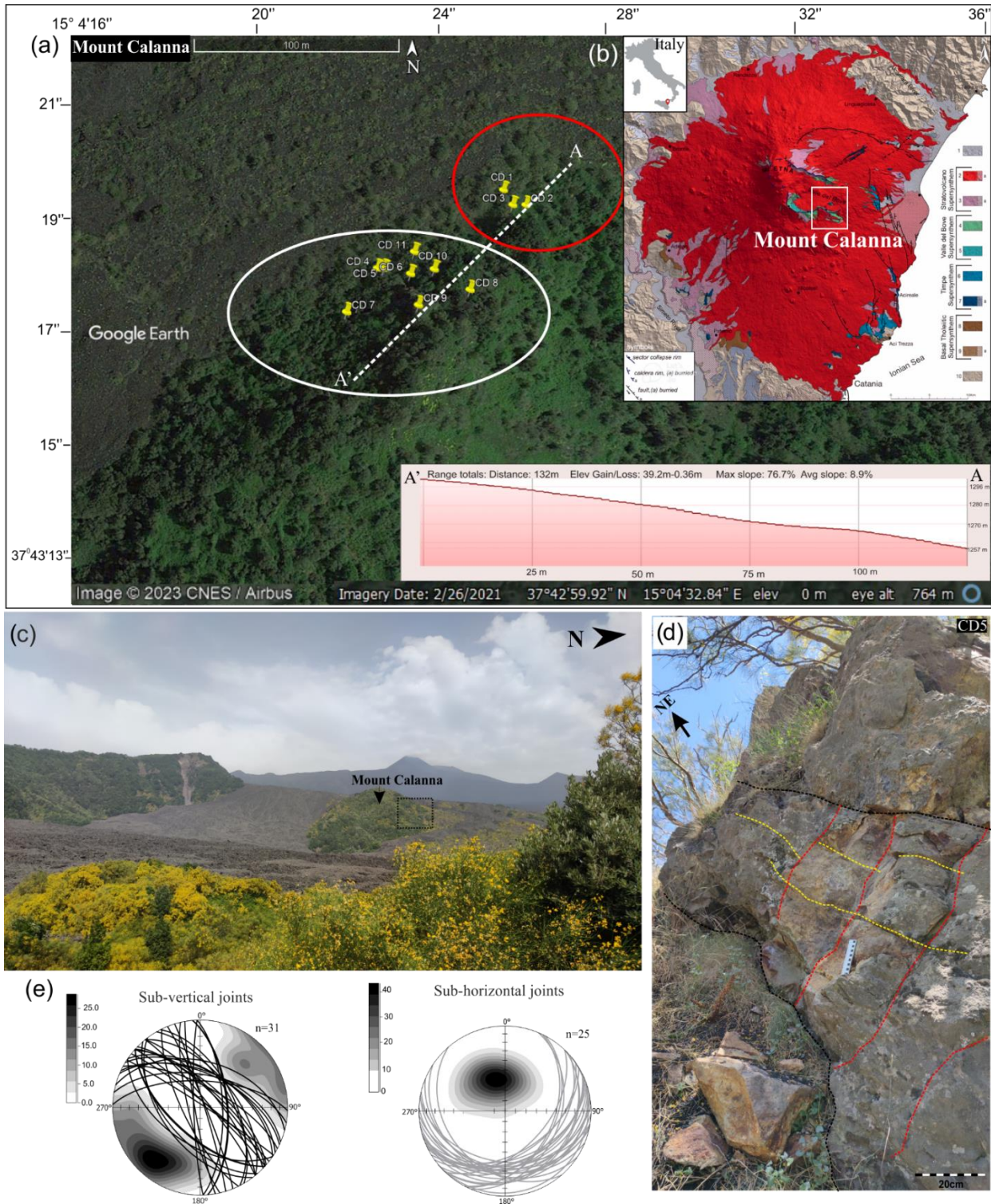
Figure 4. 1. a) Google Earth image showing the spatial distribution of sampled dykes. The two circles outline the sub-vertically (red circle) and sub-horizontally (white circle) emplaced dykes and the left bottom inset shows the elevation profile along A-A' transect. **b)** Digital elevation model (DEM) of Mount Etna along with the position of Mount Calanna (modified after Branca et al., 2011). **c)** Field photo of Mount Calanna surrounded by the recent lava flow of Mount Etna summit eruption (1991-1992). The black dotted square shows the area of sampling. **d)** Field photo of a sub-horizontal dyke (CD 5) showing the contact with country rock and the two sets of joints. **e)** Lower hemisphere equal-area projections of all measured joint orientations with the contour diagrams of their pole.

4.2 Results

The dykes of Mount Calanna are 0.5 – 3 m thick and are dissected by two sets of joints, a NW-SE sub-vertical set and a sub-horizontal NE-SW oriented set (Figure 4.1e). Based on our field observations and structural data, we thus classify the sampled dykes as follows:

1) Those emplaced sub-vertically and located in the lower part of Mount Calanna (CD1, CD2, and CD3);

2) Those emplaced sub-horizontally and located in the upper part of Mount Calanna (CD4 – CD11).

4.2.1   AMS

Among the sampled dykes mass susceptibility (χ_m) does not change significantly between the sub-vertical and sub-horizontal groups. For sub-vertical dykes, χ_m varies between $1.25 – 2.78 \times 10^{-2}$ m^{3}kg^{-1}, with an average of $1.80 \pm 0.49 \times 10^{-2}$ m^{3}kg^{-1} (Figure 4.2a), and for sub-horizontal dykes between 0.99×10^2 and 2.26×10^{-2} with an average of $1.60 \pm 0.31 \times 10^{-2}$ m^{3}kg^{-1}. Dyke CD2 shows a slight positive deviation from the rest of the dykes, and CD11 has lower values (mean χ_m of 1.48×10^{-3} m^{3}kg^{-1}) suggesting different magnetic mineral assemblages for these two cases.

The shape parameter varies from oblate and prolate in both groups (Figure 4.2b). The corrected degree of magnetic anisotropy is relatively low, ranging from 1.013 to 1.070 with an average of 1.040 (Figure 4.2c). No clear correlation was found between the degree of magnetic anisotropy, the shape factor, and dyke type (sub-vertical or sub-horizontal). Within the same dyke, it is common to have both oblate and prolate fabrics (Figure 4.2b). In some dykes this distribution changes systematically across the dyke. For example, in CD5 the shape of the AMS ellipsoid is prolate at the dyke centre, but oblate at the dyke edges (Figure 4.2d). Ten dykes gave well-constrained AMS data, but CD11 gave highly dispersed data due to high degrees of alteration. Low values of χ_m confirm alteration-induced hematite formation in CD11 (Figure 4.S 2). Hence, CD11 was excluded from further magnetic fabric interpretation. The final AMS results are given in Table 4.1.

Table 4. 1. Mean AMS data of Mount Calanna dykes.

Dyke	Samples	n/N	χm (x 10⁻³m³ kg⁻¹)	st. dev.	L	F	P'	T	K₁ D	K₁ I	K₁ E₁₋₂ (°)	K₁ E₁₋₃ (°)	K₂ D	K₂ I	K₂ E₁₋₃ (°)	K₂ E₁₋₂ (°)	K₃ D	K₃ I	K₃ E₃₋₂ (°)	K₃ E₃₋₁ (°)
CD1	CD1-1	7/8	12.89	0.79	1.010	1.023	1.040	0.266	57	24	10.8	6.6	327	4	10.9	5.1	229	66	7.6	4.0
	CD1-4	13/13	12.54	1.92	1.050	1.013	1.070	-0.526	193	24	6.4	4.0	89	28	17.7	5.9	317	52	17.7	4.7
	CD1-2	7/11	14.69	2.30	1.030	1.011	1.040	-0.362	23	4	17.8	3.6	115	26	20.6	14.8	286	64	19.0	4.0
	CD1-3	7/7	18.06	1.35	1.020	1.012	1.070	-0.318	6	4	8.7	5.6	100	43	10.3	7.2	271	47	9.5	6.3
CD2	CD2-2	6/6	27.79	1.77	1.021	1.010	1.033	-0.307	200	45	17.1	9.7	69	33	21.7	12.6	320	27	20.9	6.7
	CD2-3	9/9	20.50	7.74	1.018	1.022	1.041	0.093	196	47	9.3	3.8	81	22	9.3	7.8	335	35	7.9	3.9
	CD2-4	7/9	25.39	1.02	1.027	1.018	1.046	-0.128	118	24	47.7	16.8	224	30	48.5	10.0	356	50	26.0	10.4
	CD3-2	11/13	15.13	1.36	1.013	1.022	1.036	0.294	1	46	11.4	6.6	238	28	13.7	8.8	129	31	11.8	6.7
	CD3-3	11/15	19.41	1.20	1.016	1.018	1.035	0.081	134	53	17.7	5.8	236	9	20.8	12.4	332	35	16.8	5.8
	CD3-4	9/13	13.95	1.90	1.016	1.014	1.031	0.000	269	60	25.8	15.0	97	29	35.7	20.0	5	4	36.3	10.7
	CD3-5	10/13	15.17	1.55	1.016	1.012	1.029	-0.146	222	70	28.5	12.5	117	5	28.9	23.2	25	19	25.3	12.0
CD4	CD4-1	7/9	13.90	0.53	1.011	1.004	1.016	-0.480	53	22	15.3	2.3	271	63	51.6	14.8	149	15	51.5	2.6
	CD4-2	2/2	11.55	0.25	1.026	1.011	1.039	-0.392	102	16	-	-	7	16	-	-	234	68	-	-
	CD4-3	7/7	11.99	0.89	1.010	1.009	1.019	-0.049	230	36	16.8	5.8	106	38	15.6	6.9	346	32	9.7	5.8
	CD4-4	3/3	17.61	0.88	1.006	1.007	1.013	0.178	115	8	-	-	349	77	-	-	206	11	-	-
CD5	CD5-1	4/4	19.24	0.92	1.012	1.028	1.041	0.394	125	1	-	-	215	25	-	-	32	65	-	-
	CD5-2	7/7	12.89	1.22	1.012	1.026	1.039	0.361	116	2	8.0	6.0	208	29	8.0	3.5	23	61	6.3	2.9
	CD5-3	12/12	14.57	1.36	1.016	1.026	1.044	0.233	117	13	6.8	1.5	210	12	7.2	4.8	341	73	5.4	1.4
	CD5-4	18/18	18.00	2.34	1.021	1.024	1.046	0.067	288	12	11.7	7.9	191	29	18.5	6.7	38	59	16.5	8.9
	CD5-5	17/19	17.61	1.54	1.026	1.012	1.039	-0.367	161	26	14.6	4.6	260	19	15.9	11.2	22	57	12.9	4.6
CD6	CD6-1	2/2	17.24	0.62	1.005	1.005	1.010	0.063	59	50	-	-	295	25	-	-	190	29	-	-
	CD6-2	5/6	22.58	0.65	1.013	1.014	1.028	-0.032	6	63	13.8	8.0	179	27	47.2	9.4	270	3	46.8	8.0
	CD6-4	12/15	19.24	5.95	1.012	1.017	1.031	0.064	307	36	31.4	14.0	200	23	32.7	13.1	84	45	18.7	12.0
CD7	CD7-1	6/6	14.00	0.89	1.009	1.021	1.031	0.445	246	61	28.0	8.2	151	3	27.3	7.9	60	29	12.5	5.3
	CD7-2	6/6	13.54	0.79	1.007	1.026	1.035	0.595	208	42	63.0	12.0	319	22	62.4	5.6	68	40	26.3	7.7
	CD7-3	5/6	9.91	6.62	1.010	1.030	1.042	0.514	181	68	12.2	1.7	275	2	17.3	4.1	6	22	13.4	1.8
CD8	CD8-1	10/12	14.39	0.56	1.012	1.020	1.033	0.172	134	42	20.0	7.0	304	48	19.8	2.2	40	5	7.2	2.2
	CD8-2	6/7	17.06	0.75	1.010	1.022	1.032	0.419	147	30	17.6	3.6	256	29	18.0	8.2	20	45	9.4	4.0
CD9	CD9-2	2/2	17.99	0.05	1.029	1.033	1.063	1.073	257	21	-	-	158	23	-	-	26	58	-	-
	CD9-2	19/20	18.65	1.08	1.033	1.033	1.068	0.050	177	26	19.1	2.9	294	43	19.6	12.3	66	36	13.2	2.9
CD10	CD10-1	14/14	13.41	0.34	1.015	1.021	1.037	0.166	314	5	6.8	1.8	221	31	10.7	6.3	52	59	10.7	2.7
	CD10-2	5/6	18.04	0.76	1.008	1.023	1.033	0.448	166	11	26.2	5.7	270	53	27.4	11.2	68	35	14.8	4.9
	CD10-3	5/5	17.62	0.55	1.018	1.021	1.040	0.092	169	34	16.4	7.6	78	2	17.9	8.5	346	56	12.6	5.5

n = Number of specimens considered; N = number of specimens measured; χ_m = mass susceptibility; L = magnetic lineation; F = magnetic foliation; P' = corrected degree of magnetic anisotropy; T = shape parameter; D = declination; I = Inclination; E = confidence limit; K_1 = maximum susceptibility axis; K_2 = intermediate susceptibility axis; K_3 = minimum susceptibility axis
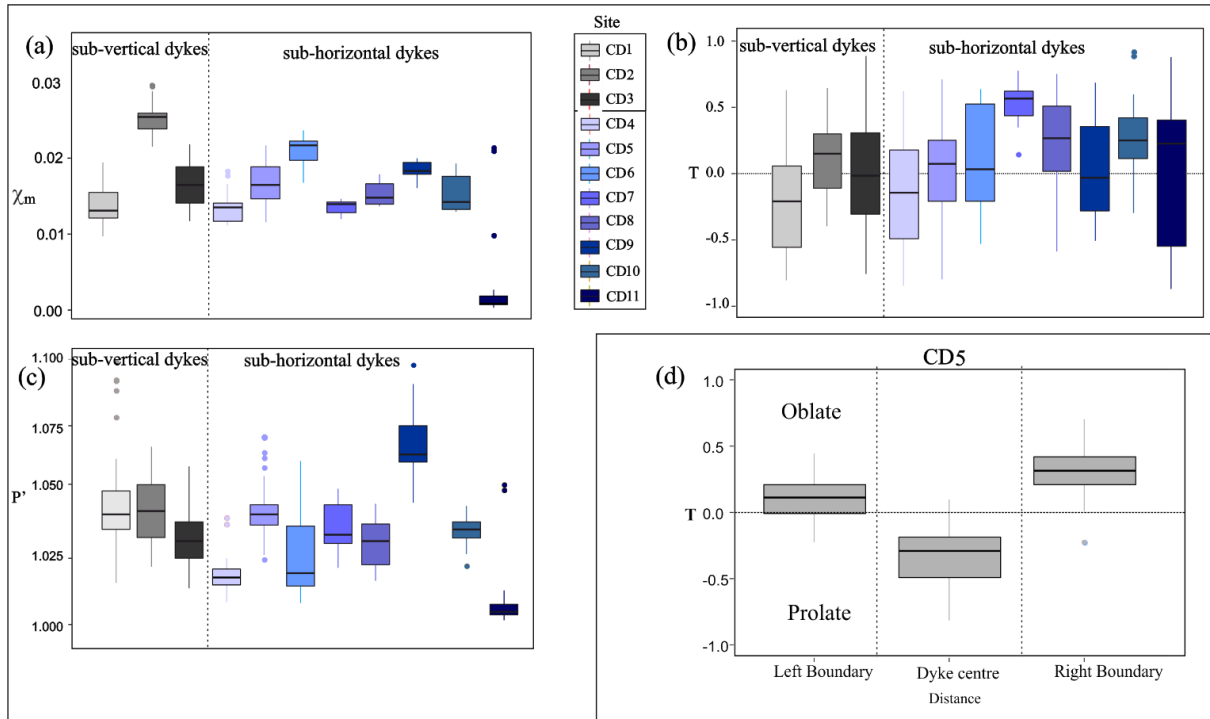
Figure 4. 2. Box plots of **a)** mass susceptibility, **b)** shape parameter, and **c)** corrected degree of anisotropy for the two groups of dykes. **d)** Box plot showing the variation of shape parameter between boundaries and centre for dyke CD5.

The three principal susceptibility axes are generally well-clustered, but their distribution changes with dyke width, changing between dyke centre and edge in each case. Magnetic fabric shows distinct patterns depending on the dyke type (sub-vertical/horizontal). For example:

1. In sub-vertical dyke CD3, at the dyke centre mean K_1 axes are inclined to sub-horizontal and oriented at a high angle with respect to the dyke wall (Figure 4.3b). Instead, near the dyke boundary, the K_1 axis is sub-vertical and aligns with the orientation of the dyke wall (Figure 4.3a).

2. CD2 shows well-clustered AMS axis distributions at the dyke centre (Figure 4.3d), whereas it is less constrained at the dyke boundary (Figure 4.3c). Moreover, the foliation plane of CD2 is parallel/subparallel to the dyke wall at both the dyke centre and boundary.

3. For sub-horizontal dyke CD10, at the dyke boundary the K_1 axes plunge towards the NW (Figure 4.3e), while at the dyke centre K_1 plunges towards the South (Figure 4.3f).

4. Dyke CD8 has a distinct vertical foliation plane near the dyke boundary (Figure 4.3g) and an inclined foliation plane at dyke centre (Figure 4.3h).

In both groups of dykes, the intermediate susceptibility axis has a larger confidence ellipsoid with a high value of confidence angles in comparison to the K_1 and K_3 axis.
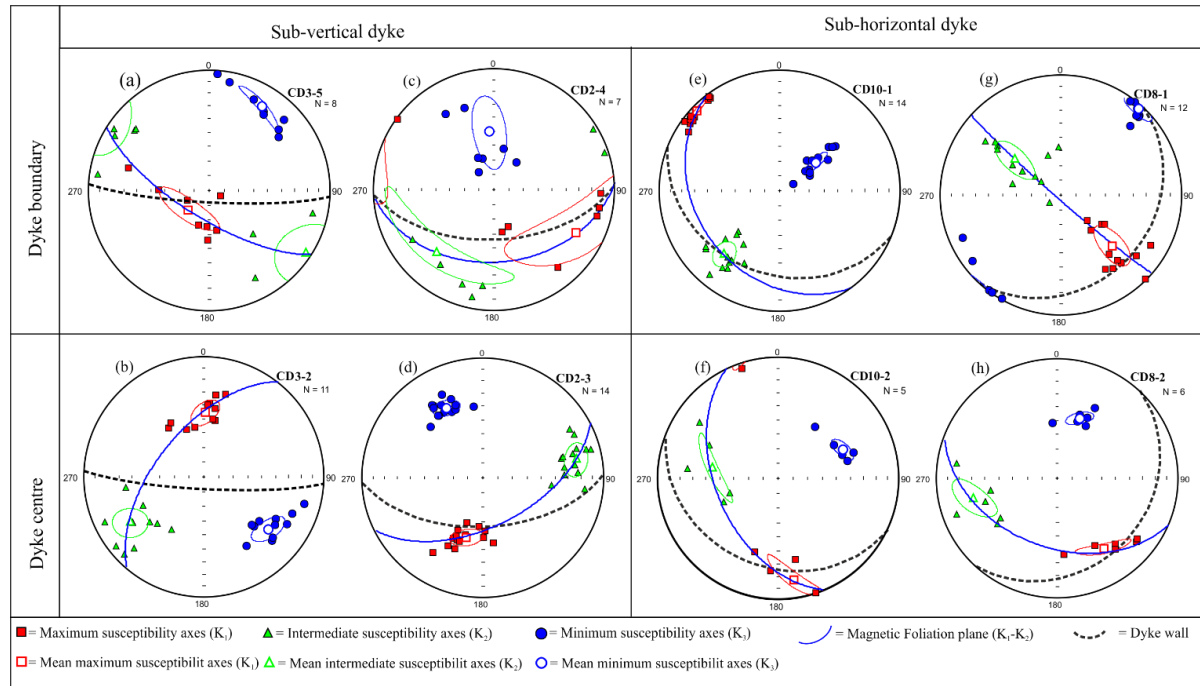
Figure 4. 3. Equal-area projection of the three susceptibility axes, their mean values with associated confidence limits, and magnetic foliation plane (blue line), for sub-vertical (on the left) and sub-horizontal (on the right) dykes. The dotted black line represents the orientation of the dyke wall.

4.2.2 Palaeomagnetism

The NRM value is in the range of 0.9 - 30 Am^{-1}. Because the thermal processing did not give stable results, we used only AF data for interpretation (Figure 4.4). Most of the samples were completely demagnetized within 60-100 mT, and the Median Destructive Field (MDF) ranges from 10 to 20 mT. Zijderveld diagrams confirm the presence of two magnetization components, with a well-defined ChRM that trends towards the origin and a secondary low-coercivity component of possible viscous origin. This behaviour of the magnetization vector is the most common, but for some dykes, the remanent magnetization clearly shows a decrease in inclination during demagnetization (e.g., sample CD5-4AD in Figure 4.4a).
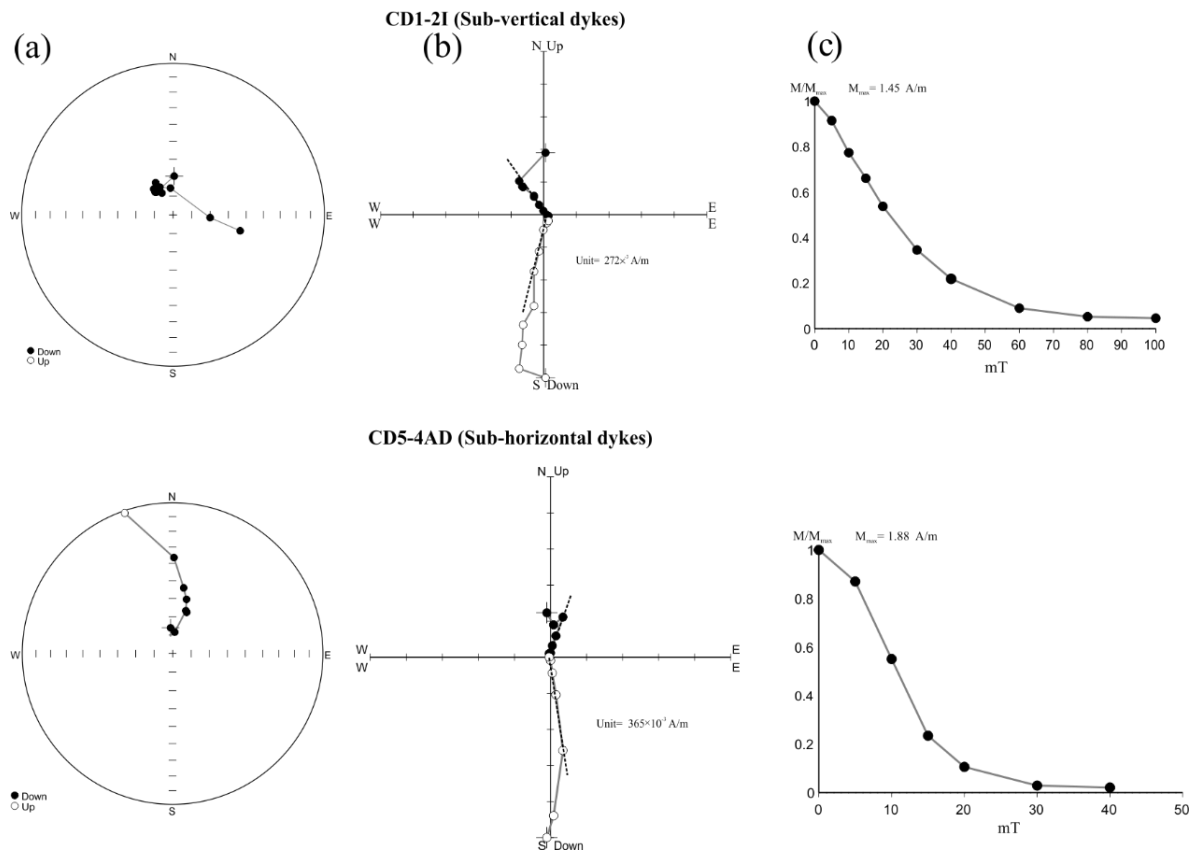
Figure 4. 4. Examples of alternating field (AF) demagnetization behaviour of a sub-vertical dyke (top) and a sub-horizontal dyke (bottom). **a)** Stereographic projection of magnetic direction; **b)** Zijderveld diagrams with solid and open data showing declination and apparent inclination, respectively. Black straight lines are the best-fitted direction interpreted by PCA; **c)** Intensity decay curve of remanent magnetization as a function of the applied field.

Using principal component analysis, we calculated the ChRM, choosing a maximum angular deviation of less than 6°. We applied Fisher's Statistics to compute the mean ChRM at the site level (Table 4.S 1, Figure 4.S 1). The directional result for each dyke is plotted in Figure 4.5. We obtained two clusters for the ChRM directions, one with declination (D) = 352.0°; inclination (I) = 65.0°; precision parameter (k) = 27; and α_{95} confidence cone = 3.4°, and a second cluster shared by three dykes with D = 27.0°, I = 31.0°, k = 17 and α_{95} = 6.8°. The two clusters are independent of the mode of emplacement (sub-vertical and sub-horizontal).
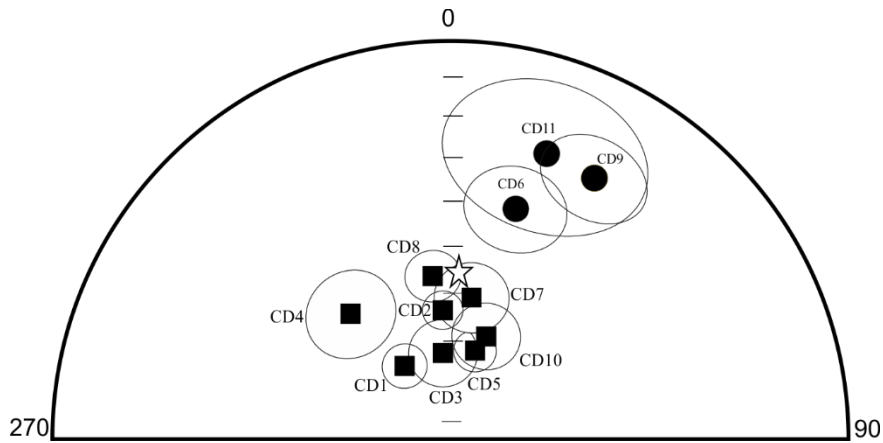
Figure 4. 5. Site mean direction of ChRM of the sampled dykes with their α₉₅ confidence limits. The black square and circle represents the primary and secondary clusters of ChRM respectively. The star is the Geocentric Axial Dipole (GAD) direction at Mount Calanna geographic coordinates.

4.2.3 Rock magnetism

All samples yielded an IRM curve with a saturation of magnetization being attained around 100 – 200 mT, indicating a low coercivity component. The mean remanence coercivity (Bh) and dispersion parameter (DP), after unmixing the IRM curve, do not show any significant change between the two groups (Figure 4.S 2). Irrespective of dyke position and mode of injection, most of the dykes confirm the presence of three components (Figure 4.6a):

1. a low-coercivity component, where the relative contribution varies between 8% and 86%,
2. an intermediate-coercivity component, where the relative contribution varies between 23% and 98%,
3. a high-coercivity component, where the relative contribution ranges between 2% and 14%.

The only exception is shown by CD11 (Figure 4.S 2)., which shows the dominance of a high-coercivity component (49%).

Thermal demagnetization of the three IRM components showed the same behaviour with the dominance of a soft fraction (<0.1T) (Figure 4.6b). The medium component is usually weak, while the hard component is negligible. In most samples, more than 95% of the remanent magnetization was removed at around 350 – 400 °C (Figure 4.S 1). For the rest, unblocking temperatures progressively dropped to a maximum of 550 – 600 °C, suggesting a range of Ti-content. The initial decline of magnetization around 350 °C suggests the presence of soft magnetic carriers such as iron sulphides or Ti-rich titanomagnetite (Weaver et al., 2002). Even

though the three IRM components have the same thermal demagnetization trend in all dykes, the contribution of the intermediate and hard components varies among specimens (Figure 4.6b).
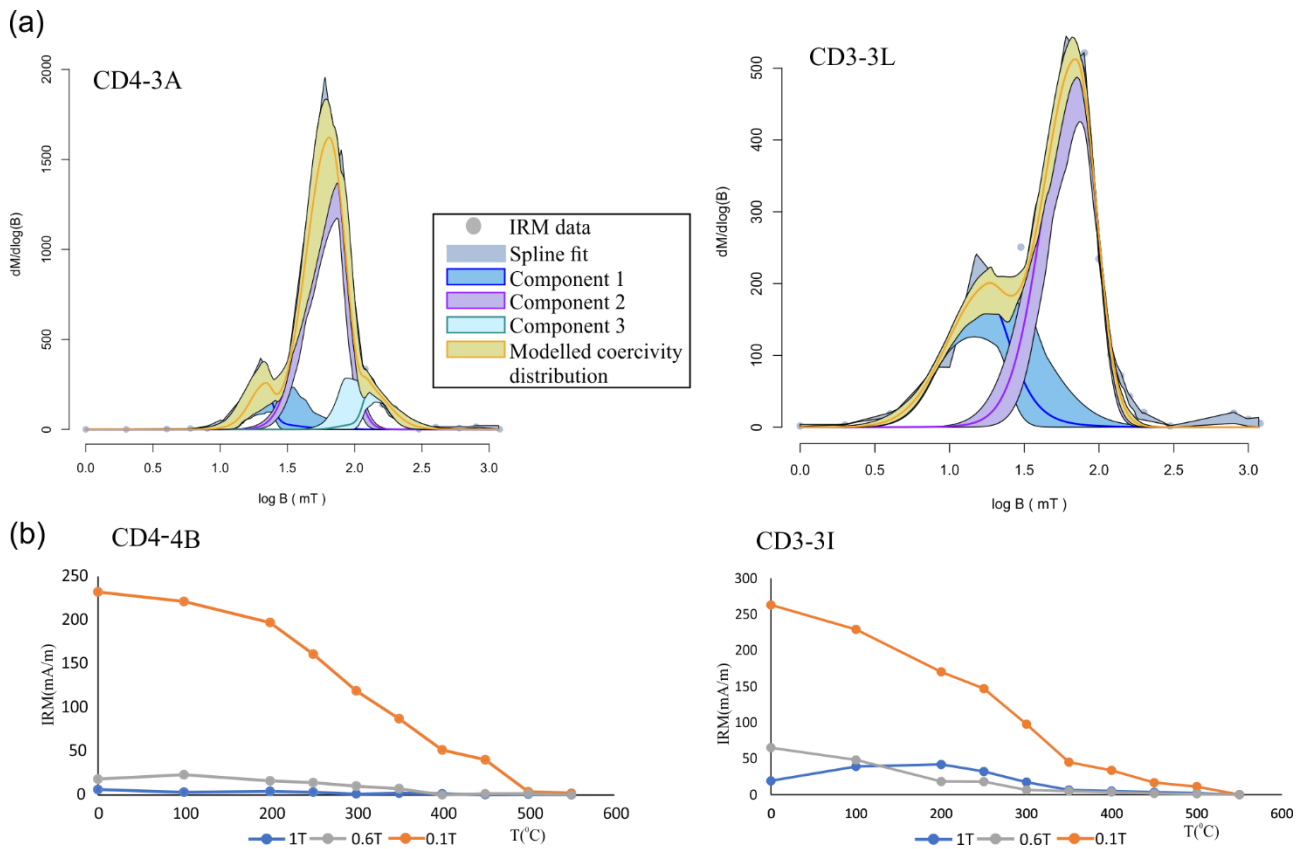
Figure 4. 6. a) Coercivity spectra and unmixing curve of isothermal remanence (IRM) acquisition curves for two representative specimens (Maxbauer et al., 2016) **b)** Thermal demagnetization of three-axial IRM imparted at 0.1T,0.6T and 1T (Lowrie, 1990).

4.2.4   Petro-Fabric and Image Analysis

All dykes exhibit a porphyritic texture with plagioclase and clinopyroxene phenocrysts, with minor olivine and opaque oxides (Figure 4.7). The groundmass has a hyalopilitic texture with plagioclase microlites, along with altered brown glass. Modal analyses yield 1 to 5% of opaque magnetic grains. Phenocrysts are euhedral to subhedral, with sizes varying from 1 to 4 mm. Based on microscopic analyses, CD6 and CD7 are mostly altered, with vesicles filled with reddish-brown secondary minerals (Figure 4.7e). Although the rest of the dykes do not show significant alteration, phenocrysts are highly fractured in most cases, especially in samples collected along the dyke boundaries.

Figure 4.7 shows the comparison of silicate fabric to AMS fabric for three representative dykes, a sub-vertical dyke (CD2), and two sub-horizontal dykes (CD6 and CD8). Seven dykes have

samples collected near the dyke wall that display good consistency between silicate fabrics and magnetic fabrics. Instead, for the dyke centre, in most cases, we obtained more than one direction for silicate fabrics. In CD2, the silicate and AMS fabrics show a consistent orientation, which is that of the NNW-SSE direction for dyke boundary (Figure 4.7a). However, at the dyke centre samples show two flow orientations for silicate fabrics (WNW-ESE and WSW-ENE), but a single ENE-WSW direction for magnetic fabrics. (Figure 4.7b). In CD8, we obtain a small secondary maximum in the NE-SW direction for silicate fabrics for the dyke boundary sample, the primary maximum is oriented in the same direction as that of AMS fabric (Figure 4.7c). However, the dyke centre sample does not show a consistent orientation for plagioclase laths and opaque magnetic minerals inferred from AMS (Figure 4.7d). Similarly, for CD6, the sample from the dyke boundary has plagioclase laths oriented in the same direction as that of opaque minerals (Figure 4.7e), while the sample from dyke centre silicate fabrics and AMS fabrics display different orientations (Figure 4.7f).

(a) CD2-4 (Normal fabrics)

(b) CD2-3 (Normal fabrics)

(c) CD8-1A (Intermediate fabrics)

(d) CD8-2B (Inverse fabrics)

(e) CD6-4 (Inverse fabrics)

(f) CD6-2 (Inverse fabrics)
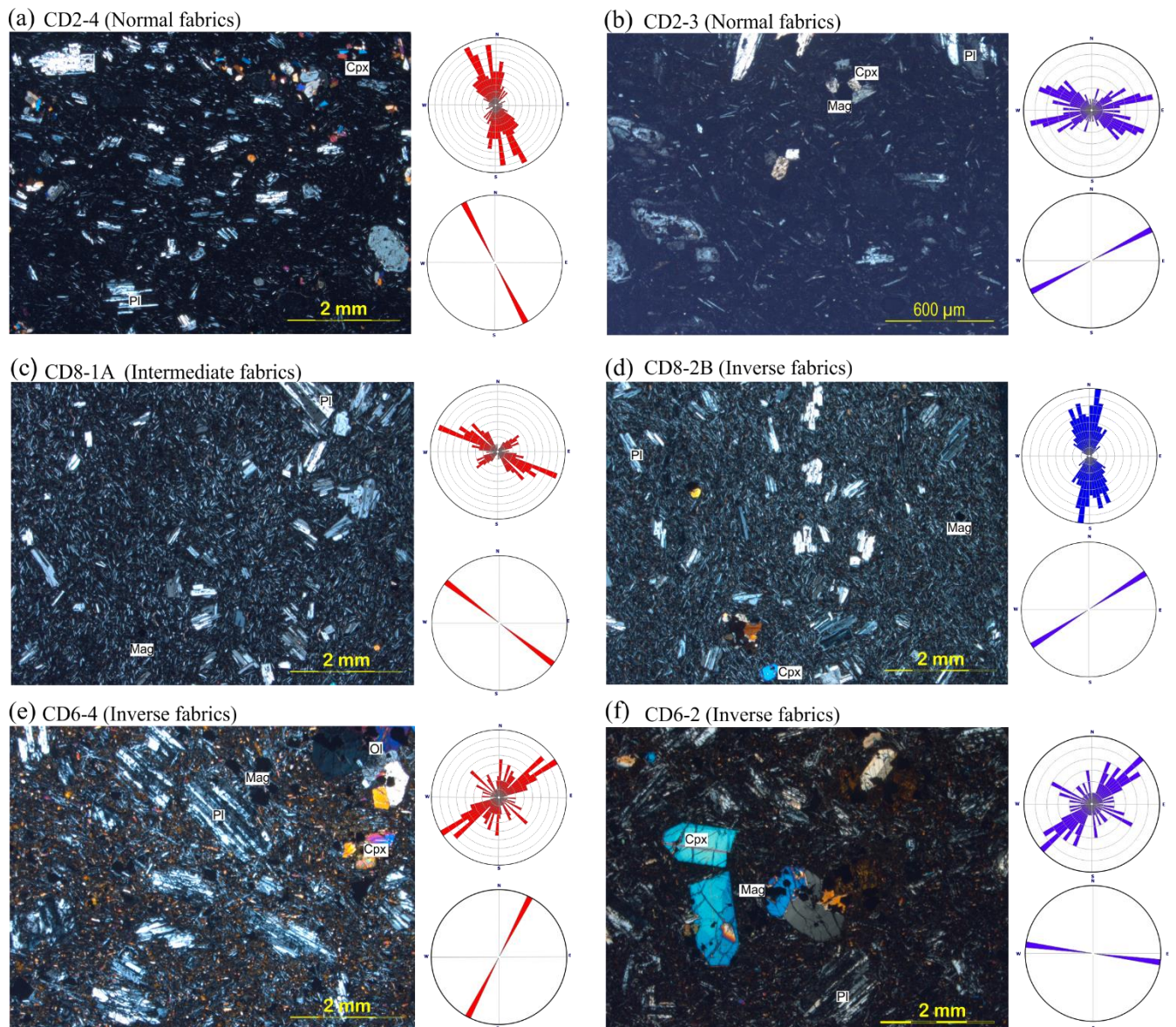
Figure 4. 7. Reflected-light micrograph image of three representative dykes. The top Rose diagram shows the orientation distribution of plagioclase and pyroxene from the dyke walls (red) and dyke centre (blue) obtained with the software program ImageJ (Rasband, 2012). The bottom Rose diagram represents the flow direction obtained from AMS analysis.

4.2.5   *Whole rock geochemistry*

Whole rock major elements mainly plot in the mugearitic field of the Total Alkali Silica (TAS) diagram (Le Maitre et al., 2002; Figure 4.8a). Mount Calanna dykes are typically characterised by SiO_2 of 48.8 – 50.7 wt.%, and high values of TiO_2 (1.590 – 1.966 wt.%) and MgO (8.1–10.6 wt.% MgO) (Table 4.2). This confirms that the dykes of Mount Calanna relate to the Na-alkaline suite of Etnean succession (cf. Cristofolini et al., 1991).

In the TAS diagram, our data mostly plots within the field of Ancient Alkaline centre (AAC), with an overlap on the most basic region of Trifoglietto compositions (Figure 4.8a). When major elements of our dyke samples are plotted together with Ancient Alkaline centre compositions, they fall along an ideal liquid line of descent (Figures 4.8b-c), confirming that they belong to the Ancient Alkaline centre eruptive phase and supporting the findings of Ferlito and Nicotra (2010). In terms of trace element distribution, all dykes, regardless of injection mode, show a similar distribution pattern, confirming all dykes were intruded during the same activity phase (Figure 4.8d).
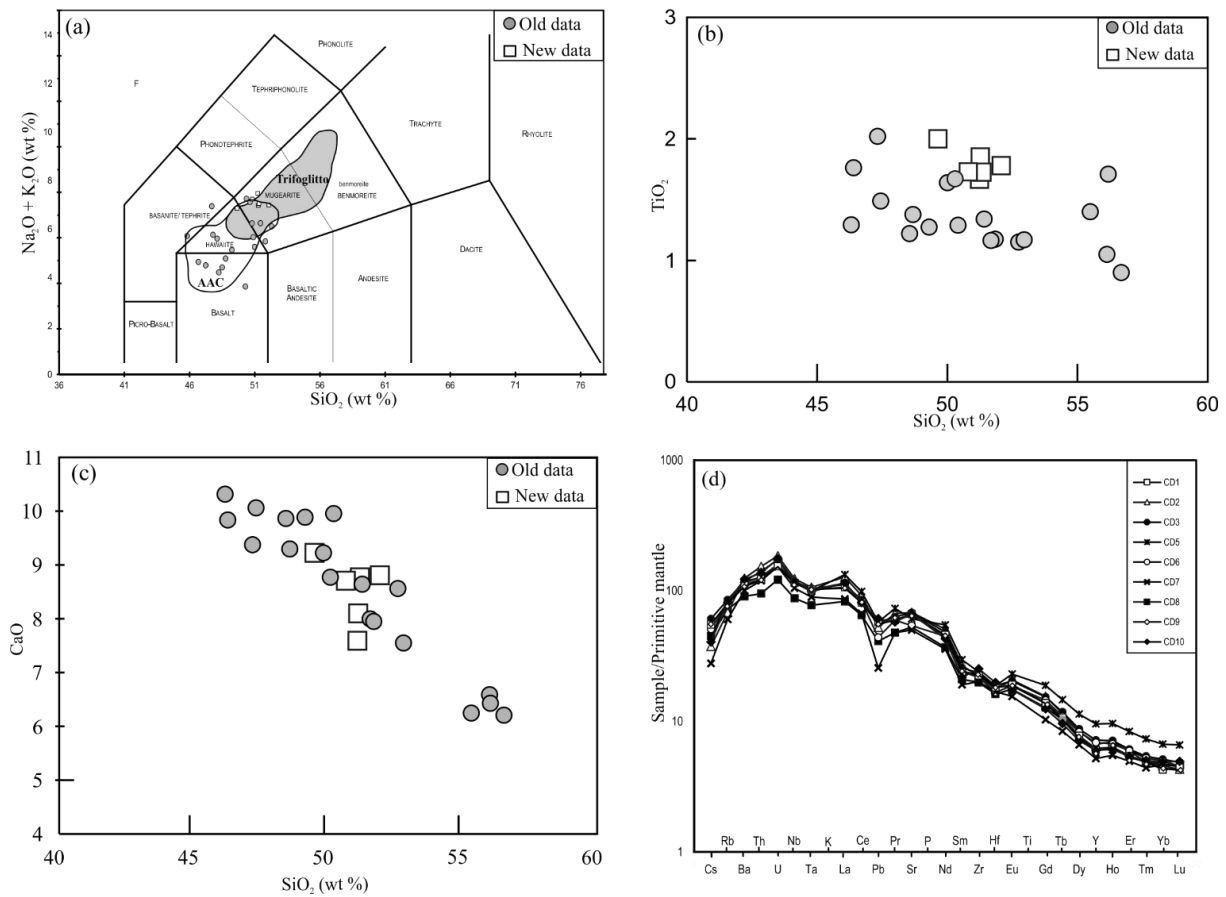
Figure 4. 8. a) Total Alkali Silica diagram for the Mount Calanna dykes and volcanic rock belongs to AAC (old data from Cristofolini et al. (1991), modified after Le Maitre et al., (2002)). **b)** and **c)** Binary diagram with TiO_2 and FeO* plotted against SiO_2 comparing new and old data (Cristofolini et al., 1991). **d)** Trace element spider diagram normalised to the primitive mantle (McDonough and Sun, 1995) for the Mount Calanna dykes

Table 4. 2. Major element on anhydrous basis (wt%) and trace element (ppm) data for the dykes of Mount Calanna.

	CD-1	CD-2	CD-3	CD-5	CD-6	CD-7	CD-8	CD-9	CD-10
SiO2	51.27	49.64	52.07	54.53	51.24	54.70	51.33	50.81	55.12
TiO2	1.85	2.00	1.78	1.53	1.67	2.06	1.73	1.73	1.39
Al2O3	19.57	18.36	19.47	19.66	19.27	20.51	19.27	18.98	19.94
FeO$_{(tot)}$	7.90	9.23	7.57	6.38	8.28	6.46	8.14	8.30	6.44
MnO	0.15	0.18	0.15	0.13	0.16	0.06	0.17	0.17	0.11
MgO	3.26	3.50	2.18	2.66	3.64	4.25	2.61	3.11	2.36
CaO	8.10	9.22	8.81	7.23	7.59	4.63	8.77	8.71	6.86
Na2O	5.04	4.77	4.73	4.82	5.73	4.55	4.87	5.09	4.87
K2O	1.93	2.08	2.25	2.25	1.75	2.01	2.18	2.14	2.32
P2O5	0.93	1.01	0.98	0.80	0.68	0.77	0.93	0.96	0.59
LOI (%)	2.57	0.64	1.38	2.88	3.63	4.69	1.13	0.44	2.25
Ag	0.050	0.055	0.045	0.058	0.058	0.022	0.061	0.050	0.042
As	1.12	2.24	1.50	1.17	1.26	0.88	1.74	1.62	1.61
Ba	598	821	784	780	757	662	733	710	810
Bi	0.034	0.059	0.066	0.052	0.043	0.056	0.062	0.054	0.060
Cd	0.06	0.09	0.12	0.15	0.09	0.07	0.10	0.07	0.10
Cr	7.4	7.6	5.3	8.4	8.0	4.4	4.8	10.7	6.2
Cs	0.9	0.8	1.3	0.9	1.1	0.6	1.2	1.2	0.9
Cu	54.51	58.89	63.12	48.72	42.06	40.13	60.22	59.41	46.13
Ga	22.45	23.80	23.38	23.52	22.18	24.05	23.15	23.17	24.24
Ge	1.59	1.91	1.81	1.97	1.79	2.05	1.89	1.70	1.85
Hf	4.58	4.99	5.30	5.29	4.72	4.78	5.12	5.16	5.61
Mo	2.5	5.2	2.0	2.3	2.4	2.9	3.7	3.6	2.6
Nb	57.58	81.46	77.12	75.61	76.41	68.83	75.62	74.89	77.76
Ni	8.2	10.1	12.5	12.0	10.2	6.7	5.7	8.2	5.5
Pb	6.17	7.86	8.60	8.64	6.58	3.85	8.61	8.30	9.17
Rb	43.20	40.95	51.12	49.80	47.91	36.27	47.99	47.76	48.83
Sb	5.19	5.26	5.31	5.13	5.00	5.37	5.30	5.28	5.30
Sc	12	15	14	9	12	15	13	13	8
Sn	1.77	1.89	1.87	1.80	1.58	1.75	1.80	1.81	1.84
Sr	1046.54	1357.99	1355.14	1215.85	1075.36	996.64	1317.22	1287.62	1324.74
Ta	2.86	3.93	3.86	3.68	3.64	3.31	3.78	3.79	3.78
Th	7.57	12.19	9.98	11.18	10.20	9.49	9.78	9.62	10.87
U	2.47	3.76	3.17	3.50	3.22	3.11	3.13	3.10	3.57
V	141	202	169	127	174	173	159	165	107
Y	26.63	28.54	30.86	41.10	29.60	22.29	25.86	25.49	25.75
Zn	86.19	101.57	98.29	185.47	100.12	129.55	86.98	87.17	103.45
Zr	207.86	232.51	245.03	250.80	229.19	211.04	234.87	238.25	264.73
La	53.65	82.27	72.35	86.01	74.35	55.93	68.98	67.82	74.11
Ce	109.00	154.21	142.69	165.37	138.95	111.91	135.99	135.69	135.86
Pr	12.11	17.01	15.98	18.62	15.12	12.13	15.19	15.12	14.62
Nd	46.16	63.54	60.42	68.33	56.02	44.74	57.42	56.53	53.53
Sm	8.55	10.88	10.47	12.03	9.68	7.74	9.66	9.79	8.80
Eu	2.71	3.20	3.14	3.54	2.89	2.39	2.94	2.89	2.69
Gd	6.95	8.44	8.34	10.25	7.89	5.59	7.51	7.46	6.79
Tb	1.02	1.14	1.17	1.45	1.09	0.83	1.06	1.02	0.95
Dy	5.21	5.66	5.88	7.66	5.58	4.45	5.23	5.03	4.79
Ho	0.94	1.04	1.06	1.43	1.00	0.82	0.95	0.93	0.91
Er	2.390	2.566	2.676	3.659	2.608	2.164	2.380	2.321	2.362
Tm	0.33	0.34	0.37	0.50	0.36	0.30	0.33	0.33	0.34
Yb	2.086	2.014	2.254	2.949	2.192	2.049	1.878	1.923	2.151
Lu	0.311	0.290	0.328	0.445	0.306	0.305	0.299	0.285	0.333

4.3 Discussion

4.3.1 Approach to infer magma flow in dykes

Discussion among rock magnetists has focused on how to interpret magma flow direction in dykes using AMS (e.g., Geoffroy et al., 2002; Callot and Guichet, 2003; Cañón-Tapia, 2004). Khan (1962) was one of the first to use AMS to infer flow fabrics in igneous rocks, using the K_2 axis as a proxy for flow directions in dykes. Later, Wing-Fatt and Stacey (1966) proposed that the maximum susceptibility axis (K_1) is a more precise proxy for flow direction. However, using image analysis of silicate fabrics along with magnetic fabrics in Tertiary basaltic dykes from Greenland, Geoffroy et al. (2002) showed the limitations of using the K_1 axis to represent flow direction. Instead, Geoffroy et al. (2002) proposed that the magnetic foliation plane (K_1-K_2) more precisely defined flow direction in dykes. The most common criteria used to interpret flow direction is the magnetic lineation (K_1) in the case of prolate fabrics, and the magnetic foliation plane for oblate fabrics (Delcamp et al., 2015; Andersson et al., 2016; Schmiedel et al., 2021). Domain structure, along with the orientation of the susceptibility axis with respect to the dyke wall (Hrouda, 1982; Rochette et al., 1992; Das et al., 2021) and the imbrication of the foliation plane at the dyke wall (Knight and Walker, 1988; Das et al., 2021) have also been used to infer flow directions. However, there remains no well-established practise for the study of flow direction in dykes using AMS. We thus use our data to propose a framework for inferring flow direction from AMS data (Figure 4.9).
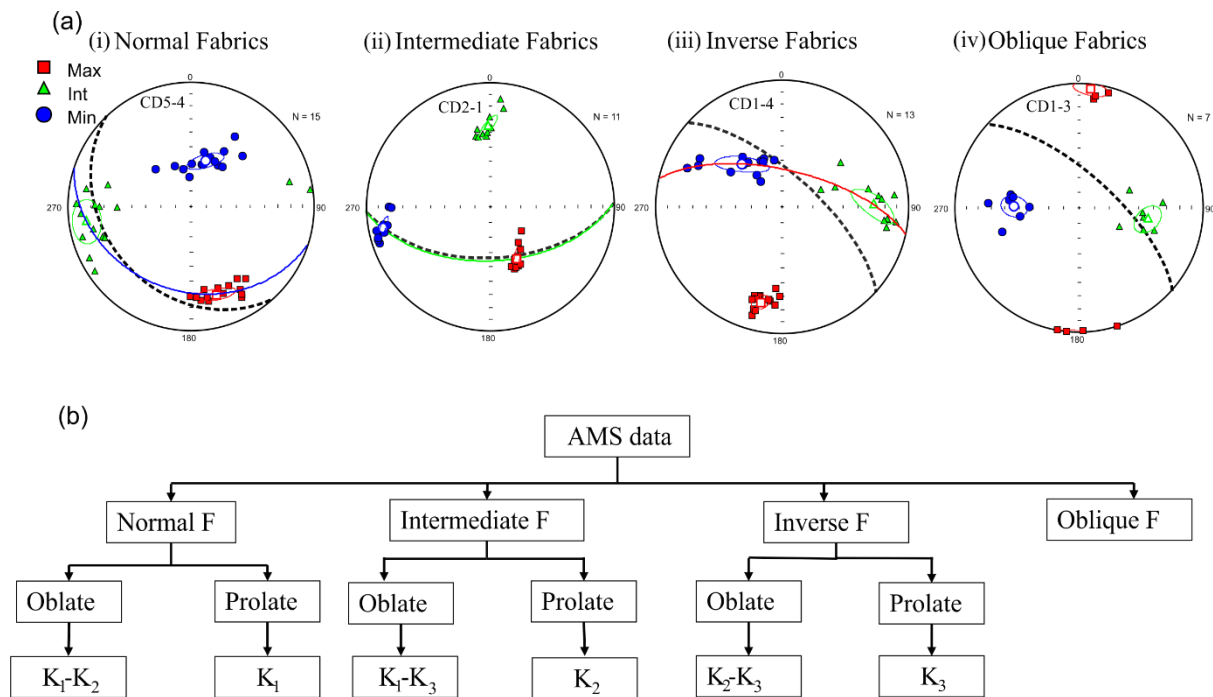
Figure 4. 9. a) Examples of four different types of fabrics namely, Normal, Intermediate, Inverse, and Oblique fabrics respectively; **b)** flow chart showing the proposed approach for AMS flow fabric interpretation.

Based on the orientation of the three susceptibility axes with respect to that of the dyke wall, we grouped the samples into four classes following the classification of Wiegand et al. (2017):

a) *Normal Fabrics*: K_1 and K_2 sub-parallel to the dyke wall, and K_3 is perpendicular to the dyke plane (Figure 4.9a-i);

b) *Intermediate Fabrics*: K_1 and K_3 axes subparallel to the dyke plane, with the K_2 axes perpendicular to the dyke plane (Figure 4.9a-ii);

c) *Inverse Fabrics*: K_1 axis normal to the dyke plane, with the K_2 - K_3 plane parallel to dyke plane (Figure 4.9a-iii);

d) *Oblique Fabrics*: any magnetic fabrics with variable orientations in terms of magnetic foliation and lineation, and with significant discrepancy with respect to the dyke plane and which cannot be accommodated in any of the three classes (Figure 4.9a-iv).

In all cases, a deflection of 35^0 to the dyke plane is accepted (Raposo and Ernesto, 1995; Wiegand et al., 2017). Within these classes we use the shape of the susceptibility ellipsoid, whether prolate or oblate, to infer flow direction (Figure 4.9b).

To validate our approach, we checked the consistency of the magnetic flow fabric with the orientation of the plagioclase laths obtained from thin section analysis. The consistency of flow direction at dyke boundary obtained from both methods, where rapid cooling of magma at the dyke wall freezes in the initial flow direction, confirms the reliability of the approach (Figure

40

4.7). Instead, the random orientation of plagioclase laths at the dyke centre is likely due to the lateral flow, as well as back flow and convection, at dyke centre, as it can remain fluid for days or weeks after emplacement and after the eruptive flow has ceased. We can rule out the possibility of reworking and collapse of the three-dimensional plagioclase network, as pointed out by Philpotts and Dickson (2000), as our dykes are small, where the maximum dyke thickness was 3 m, and cooled relatively quickly.

The flow directions for each dyke, as obtained from the dyke boundary samples are given in Figure 4.10 along with the representative equi-areal projections. The AMS results show more than one flow direction, with sub-horizontal, inclined, and sub-vertical distributions, indicating the complexity of the emplacement process. The structural data of Ferlito and Nicotra, 2010 agree with this classification of the Mount Calanna dykes (Figure 4.S 3) showing, broadly, two classes of dyke in terms of orientation and flow direction.

Flow direction is consistently NE-SW in the case of the sub-vertically emplaced dykes, but NE-SW and NW-SE for sub-horizontal dykes (Figure 4.10). Both directions follow regional tectonic controls (Lo Giudice et al., 1982; McGuire and Pullen, 1989; Monaco et al., 2010; Azzaro et al., 2013; Branca et al., 2014). We also find that dykes towards the top of Mount Calanna have an inclined to sub-horizontal flow direction. The lateral migration of the feeder dyke from the upper part of the central conduit to the surface may be reflected in horizontal magma flow direction toward the top of Mount Calanna. This kind of dyke propagation from the central conduit has already been observed at Mount Etna (Aloisi et al., 2009) and other sites including Stromboli (Acocella et al., 2006a), Hawaii (Decker, 1987) and Vesuvius (Acocella et al., 2006b). In contrast, in the lower part of the Mount Calanna structure, we find sub-vertical to inclined flow directions, where the dykes are fed directly by the deeper magma chamber.
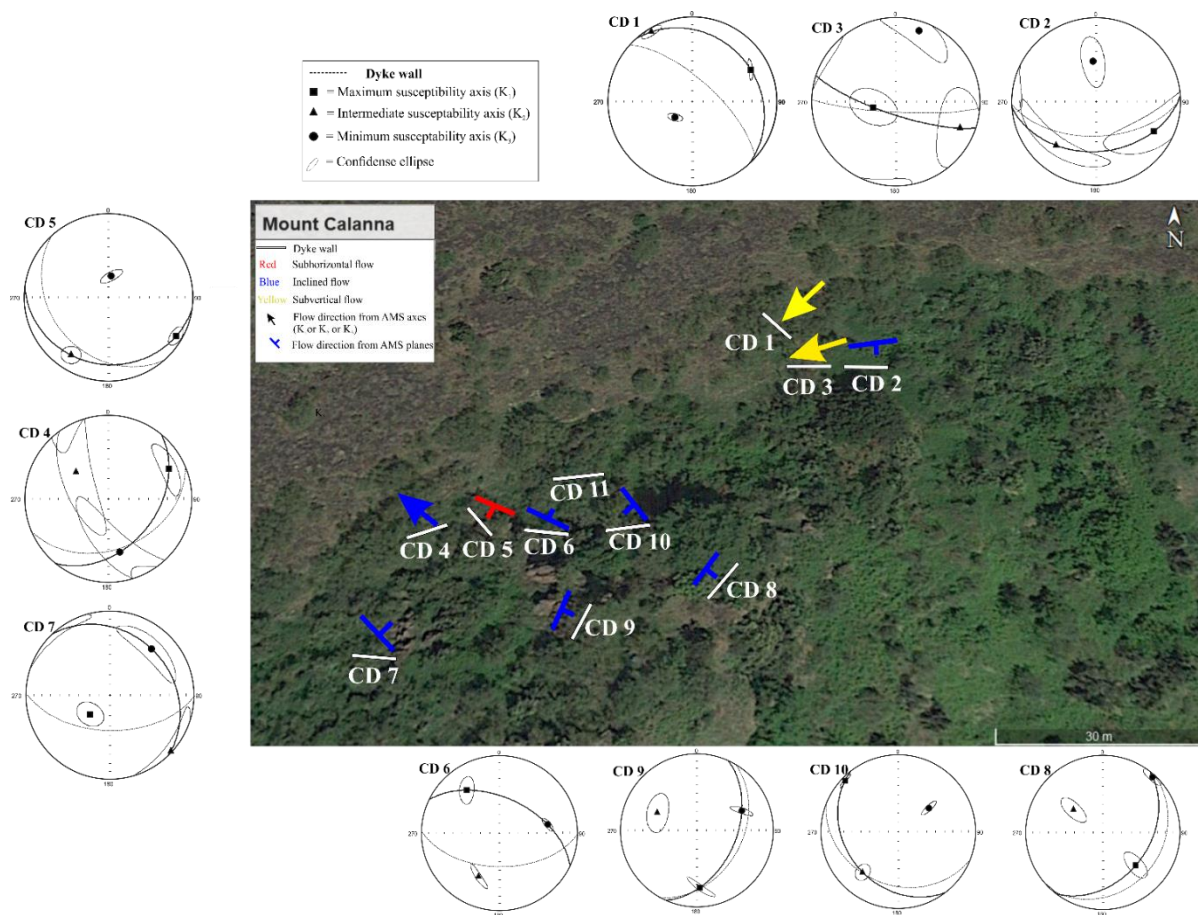
Figure 4. 10. Google Earth image of the northern part of Mount Calanna with the location and orientation of sampled dykes (white line) along with the inferred flow direction by magnetic fabrics. Stereonets depict the orientation of the three susceptibility axes with their relative confidence ellipsoid and the magnetic plane considered to define the flow direction using the proposed practice along with the dyke boundaries.

1.3.2 Magmatic and evolutional setting of Mount Calanna in the framework of Etna's evolution

Previous studies have identified the presence of a few fresh "unaltered dykes" belonging to the Mongibello volcanic phase at Mount Calanna (Ferrari et al., 1989; Ferlito and Nicotra, 2010). Clustering of the ChRM direction, and its conformity with the geocentric axial dipole direction of the primary cluster (Figure 4.5) along with the coherent characteristics of major and trace elements (Figure 4.8), confirms that all dykes considered here erupted in the same epoch. Given that the three dykes that make up the secondary cluster, CD11, CD6, and CD9, lie along a plane with shallow ChRM inclinations and that Mount Calanna is mostly dissected by faults (Ferlito and Nicotra, 2010), the formation of the secondary cluster can be attributed to fault reworking. The Mount Calanna dyke swarm thus resulted from single and/or multiple intrusive events and associated eruptions, that occurred over a short period of time.

The major element composition, especially the high percentages of TiO_2 and P_2O_5, confirm that the Mount Calanna dykes belong to Etna's Ancient Alkaline Centre phase (Table 4.2) (Cristofolini et al., 1991; Ferlito and Nicotra, 2010). Even though the sub-vertical and sub-horizontal dykes were emplaced from the central conduit and magma chamber respectively, major element and trace elements do not show any change in the magma maturity. This is because the magma did not stay in the shallow system for sufficient time to undergo fractional crystallization.

1.3.3   Emplacement mechanism of the Mount Calanna dyke swarm

Despite its small size, the Mount Calanna dyke swarm displays a complex dyke injection process with a high intensity of intrusion (40%) (Ferlito and Nicotra, 2010). Two modes of dyke injection are thus found over a very small area, with a sub-vertical emplacement lower in the intrusive complex and a sub-horizontal emplacement higher up. This highlights the complexity of a shallow intrusive system over small spatial scales. Such complexity of dyke injection over a small area has also been found at other volcanoes, such as at Lemptegy in central France (Petronis et al., 2013) and Komochi in central Japan (Geshi, 2008). The radial dykes of Komochi exhibit similar dyke flow patterns, characterized by lateral flow from the central conduit and vertical flow from the shallow magma chamber, as found at Mount Calanna. To explain the complexity found at Mount Calanna, at-least two dyke emplacement models are thus needed: one for the emplacement of sub-vertical dykes (e.g., CD1), and one for sub-horizontal dykes (e.g., CD5).

4.3.3.1 The case of sub-vertical dyke CD1

Characteristic of sub-vertical dykes, CD1 shows a two-stage emplacement mode controlled by both physical (e.g., bedrock strength, regional stress, and magma pressure) and fluid (e.g., viscosity, thermal) properties of the country rock and magma, respectively (Lister and Kerr, 1991; Anderson, 1937). During the initial stages of magma injection, the fluid is subjected to controls related to magma pressure and thermal stress due to cooling, and physical forces controlled by the nature of the host rock and shear stress. While the thermal stress and physical forces act laterally towards or away from the flowing magma, the magmatic pressure acts vertically (Figure 4.11c). As magma intrudes the host rock, it creates thermal gradients that induce stress in the surrounding rocks. Thermal stress due to cooling, together with the physical forces and simple shear due to the laminar flow of the magma, generates the prolate fabrics (Stage 1 in Figure 4.11c). As flow continues, the increased internal pressure causes bending of

the NNE side of the dyke (Stage 2 in Figure 4.11c) and sagging of the bent side. Sagging, together with the gravity-driven backflow due to its weight, overprints the initial prolate fabrics with oblate fabrics (Figure 4.11b, c) (Andersson et al., 2016; Das et al., 2019).
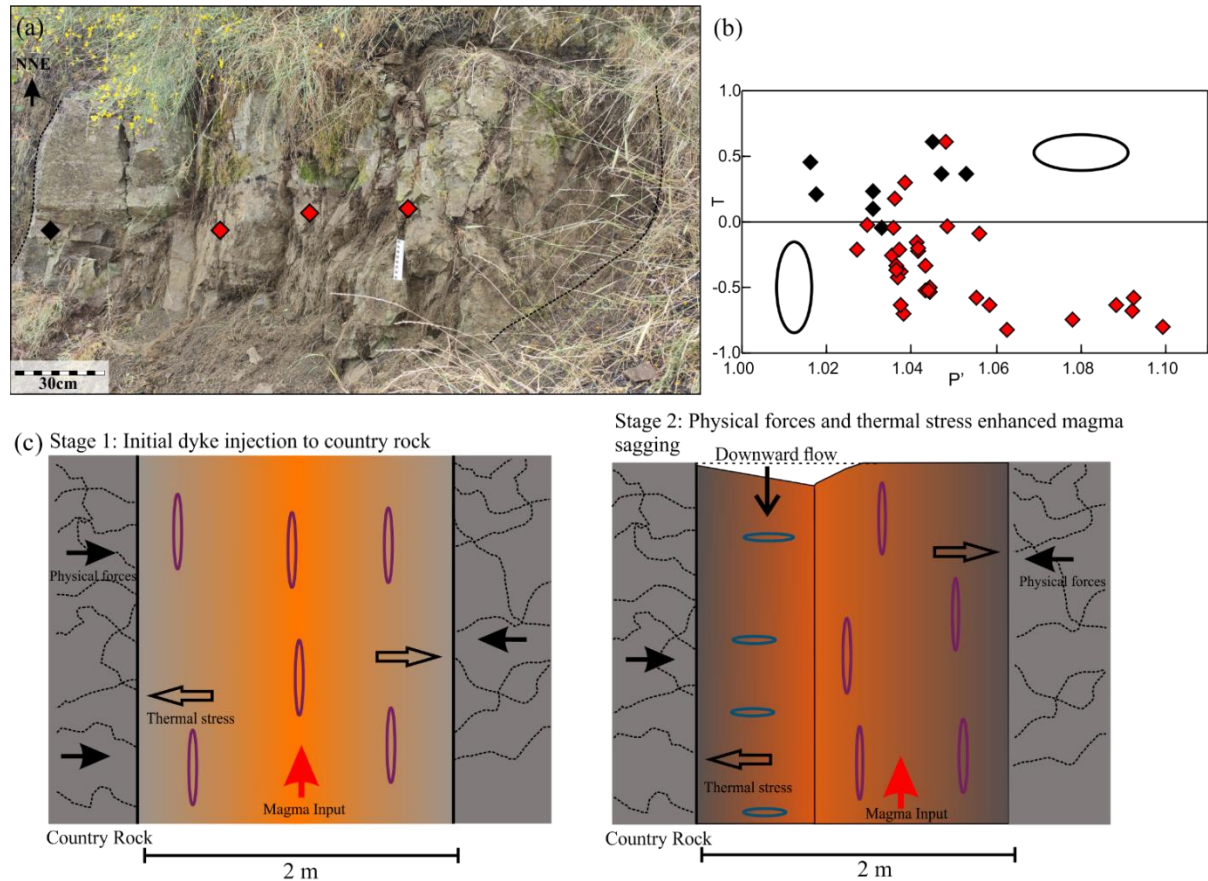
Figure 4. 11. a) Field photo of CD1 (sub-vertically emplaced dyke) with sampling sites. **b)** Distribution of magnetic fabrics ellipsoids along dyke width. The black and red diamonds show oblate and prolate ellipsoids respectively **c)** Model of the syn-and post-emplacement mechanism of dykes. As the magma starts cooling down, the physical forces along with thermal stress increase, resulting in slight bending along a weak plane and sagging of the downward bent part. This sagging and downward flow overprints the primary prolate fabrics along the NNE boundary to Oblate fabrics.

4.3.3.2 The case of sub-horizontal dyke CD5

In the case of CD5, which is typical of sub-horizontally emplaced dykes, we observed a different emplacement model with a symmetrical imbrication of the magnetic fabric ellipsoid at the dyke boundary (Figure 4.12). The systematic variation of the shape of the AMS ellipsoid across the dyke is expressed by oblate fabrics at the dyke boundaries, but prolate ellipsoids at the dyke centre (Figure 4.12b). When magma injects into the country rock, magma at the dyke wall quenches immediately as it comes into contact with the cold country rock. This thus records the initial injection direction. However, near the dyke margin, the cooling direction is inward, and this lateral migration of magma results in an oblate ellipsoid (Figure 4.12b). At the

dyke centre, magma can stay active for days or weeks, even months or years, and the subsequent changes in the flow direction, either in the upward or downward directions, causes prolate ellipsoids (Figure 4.12b).
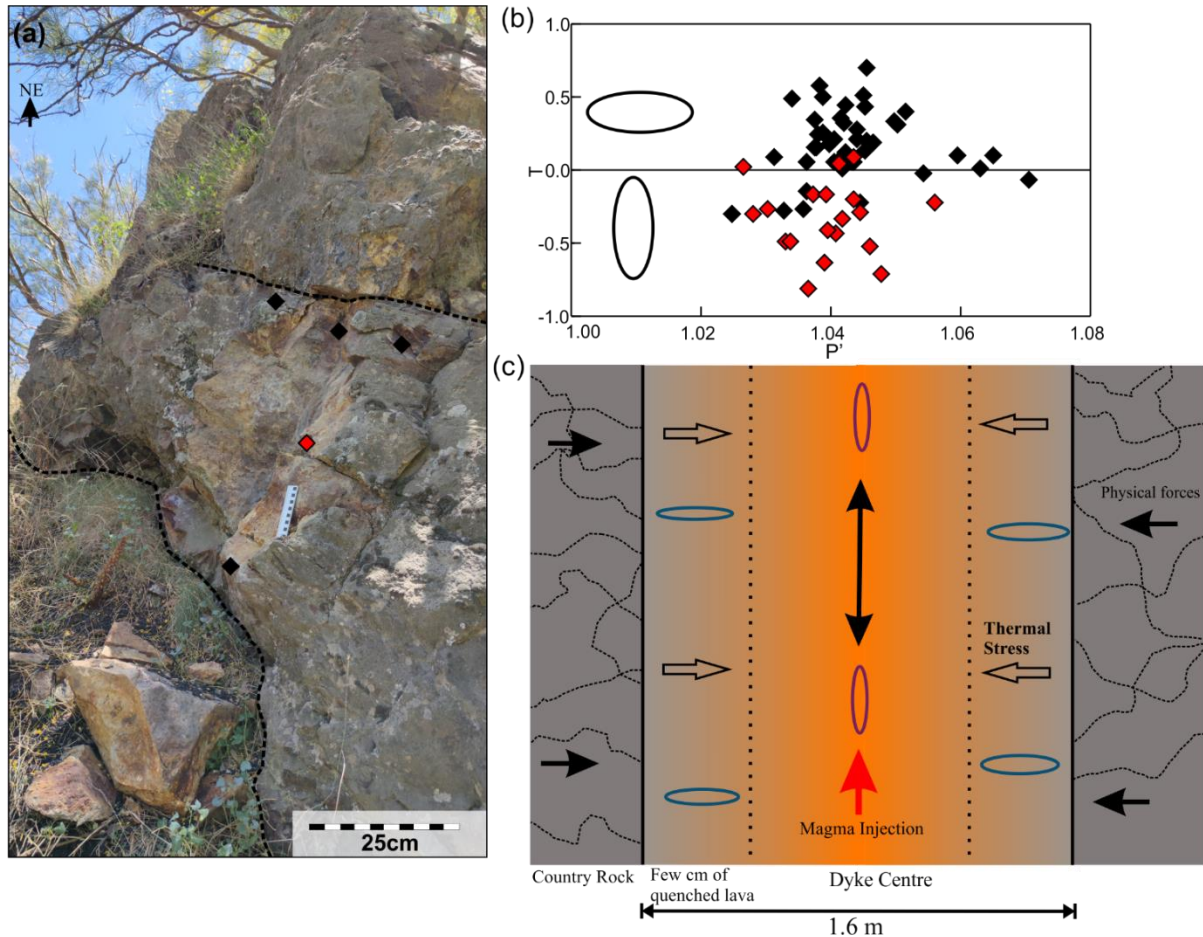
Figure 4. 12. a) Field photo of CD5 (sub-horizontally emplaced dyke) with sampling location. **b)** Distribution of magnetic fabrics ellipsoids along dyke width. **c)** Schematic representation of the magma propagation along the dyke. Near dyke boundary, the few cm of quenched lava had an inward cooling trend and thereby formed oblate. Whereas in the dyke centre, where magma remains active for weeks, even months to years, magma has a lateral flow direction, either in an upward or downward direction

1.4 Conclusion

Interpretation of dyke emplacement is not always straightforward, especially for small dyke swarms which can be easily eroded or covered by subsequent lava flows. However, our work demonstrates how the emplacement dynamics of a small dyke swarm can be unravelled through an interdisciplinary approach involving AMS, fabrics, petrology, and geochemistry, as well as in-field facies analysis.

Our study of the emplacement mechanisms associated with a small intrusive complex provides insights into the flow dynamics and enables us to conclude that:

1. Two distinct groups of dykes are present over a very small area: (a) sub-vertically emplaced dykes which occur in the lower portion of the intrusive complex, and (b) sub-horizontally emplaced dykes in its upper part.

2. We can interpret magma flow directions using the shape of the AMS ellipsoid and imbrication with the dyke wall.

3. There is a dominance of NE-SW flow fabrics for the sub-vertically emplaced dykes, and NE-SW and NW-SE flow directions for the sub-horizontally emplaced dykes; directions which follow the regional stress field.

4. The similarity between the field observations and the AMS results suggests that the sub-horizontal dykes migrated laterally from the central conduit to the surface, whereas the sub-vertical dykes were fed by the deeper magma chamber.

5. The palaeomagnetic results together with the geochemical analysis show coeval emplacement of the dykes that make up the swarm.

These observations further suggest that Mount Calanna is an example of the uppermost part of a shallow plumbing system, where patterns in the magnetic fabrics reveal two modes of dyke emplacement in such a system: one for sub-horizontal dykes and a second for sub-vertical dykes. These models show how magma flow is affected by different forces and how flow varies across the dyke within a small intrusion. The models developed here can be applied to other small intrusions to infer complex emplacement mechanisms and cooling histories of dyke injection.

Chapter 5

SECOND CASE STUDY: **LAVA ENTRY INTO THE SEA**

The contents of this chapter are ready to be submitted for publication under the title *'When the lava meets the sea: emplacement of the 2-4 ka San Bartolo lava flow field, Stromboli volcano (Italy)'*.

5.1 Geological Setting

Stromboli volcano is located on the Aeolian Islands archipelago in the southern Tyrrhenian Sea, off the north coast of Sicily, Italy (Figure 5.1b). The volcano is known for its regular explosive eruptions, often involving the emission of bombs and blocks, scoria, lapilli, and the release of gas and ash clouds (Chouet et al., 1974; Patrick et al., 2007). It is marked by high-K calc-alkaline magmatism, which built up to its present altitude of 924 m over the last 2-5 ka (Francalanci et al., 2013, 2014). The NE flank of Stromboli Island is formed of 11 litho-stratigraphic units from different flank eruptions, with the San Bartolo (SB) lava flow marking the last flank eruption that occurred outside the Sciara del Fuoco depression (Calvari et al., 2011). The SB lava flow field formed by the monogenetic activity of a NE trending fissure at an altitude of 600–650 m.a.s.l. (Figure 5.1a) and has an age of ~ 2-4 ka (Arrighi et al., 2004; Speranza et al., 2008), thus it is emplaced during the Il Pizzo sequence (Francalanci et al., 2014). Considering this age constraint, when the SB lava was emplaced, the sea level was at least 1.35 ± 0.07 m lower than at present, as obtained for the Roman Period on the basis of archaeological constraints (Lambeck et al., 2004). The submerged shelves around the Aeolian Islands are characterized by low-gradient erosive surfaces particularly pronounced along the NE coast of Stromboli, with a steep seaward shelf break commonly located at depths of 100 – 120 m.b.s.l. (Romagnoli, 2013).

The eruptive fissure, which extends NE and downslope, has a depressed feature in its upper part, indicating that an important drainage of the upper eruptive fissure probably occurred during the late stages of the eruption. The lava flow field continues with two master channels in the middle portion, mostly parallel and oriented NE-SW (Figure 5.1a). The NW one is ~ 400 m long and connects the base of the eruptive fissure with the lava apron widening below the village. It has steep levees and is much longer than the SE one which is at most 120 m long and

barely visible in the middle-upper portion of the lava flow field. These two channels apparently connect to the lava tubes at the flow front along the shoreline (Calvari et al., 2023). This recent lava flow field is mostly covered by the settlements of Stromboli village except near the beach (Figure 5.1a). The erupted lava flowed towards the coast along an old drainage line, forming a lava delta ~20 m thick and ~1 km wide (Francalanci et al., 2013; Calvari et al., 2011, 2023). The lava delta is bounded by the Sirenetta wharf to the east and Piscità to the west (Figure 5.1; Calvari et al., 2023). In the SB lava flow field, the well-preserved lava deposition along the coast permitted us to distinguish different morphological features formed by the interaction between lava and seawater.

The notable difference in the eruptive style during the emplacement of the SB lava field from that of recent eruptions can be seen from the significant changes in the geometry of the magma plumbing system and the change in the composition of the erupted materials (Francalanci et al., 1989; Rosi et al., 2000; Laiolo and Cigolini, 2006). The SB lava has high-K calc-alkaline affinity and contains abundant phenocrysts of clinopyroxene, olivine, and plagioclase as well as mafic and ultramafic cumulitic xenoliths, (Laiolo and Cigolini, 2006; Calvari et al., 2011; Francalanci et al., 2014).

The SB flow field splits into 16 ocean entry sites of mostly pāhoehoe lava flow lobes (Calvari et al., 2023) here termed 'Flow' (Figure 5.1c). Each flow can be divided into different portions, based on characteristic components as illustrated in Figure 5.1d.
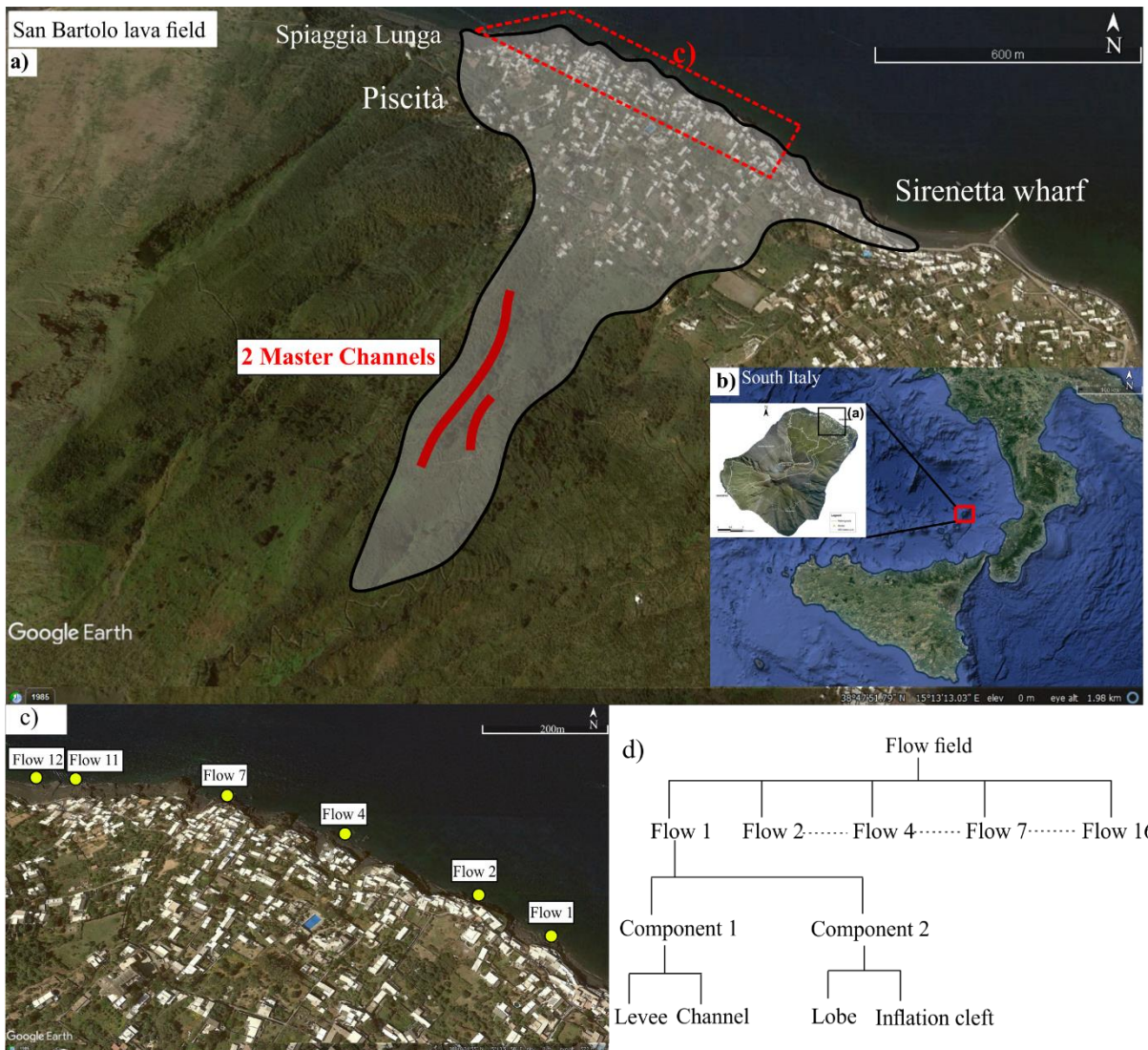
Figure 5. 1. a) Google Earth image of San Bartolo lava flow field of Stromboli volcano (modified after Calvari et al., 2023). **b)** The bottom right inset shows the location of Stromboli volcano in south Italy. **c)** Google Earth image showing different flows with the yellow dots highlighting the studied Flows. **d)** Simplified flowchart of the terminologies used in this study.

5.2 Results

We first define and describe the five main components of the lava flow system, before mapping their distribution along the zone of ocean entry for the SB lava flow field.

5.2.1 Description of components and magnetic fabric

We distinguished five main components, which are: 1. 'A'ā channel-levee; 2. Littoral; 3. Ramp; 4. Lava tube; and 5. Inflated pāhoehoe.

Channels and associated levees can be observed along the coast. The two master channels are well exposed at Flow 2 and 7 (Figure 5.1c) and are orientated to the NW.

a) Channel at Flow 2

At Flow 2, the contact between the dense, massive, vesicle-free lava of the channel and the left bank levee can be observed (Figure 5.2a). The 'a'ā dense channel lava outcrop has a thickness of 14 m and is overlain by a 4 m thick layer of clinker and ramps. The levee has been preferentially eroded by wave action to form a cave of 8 m in height, within which at-least three overflow levees (up to 2 m thick) can be found, with the cave roof being characterized by sheared lava (Figure 5.2b). The cave is overlain by 4 m of 'a'ā flow which runs into two overflow units (up to 2 m thick) that mantle the outer flank of the levee.
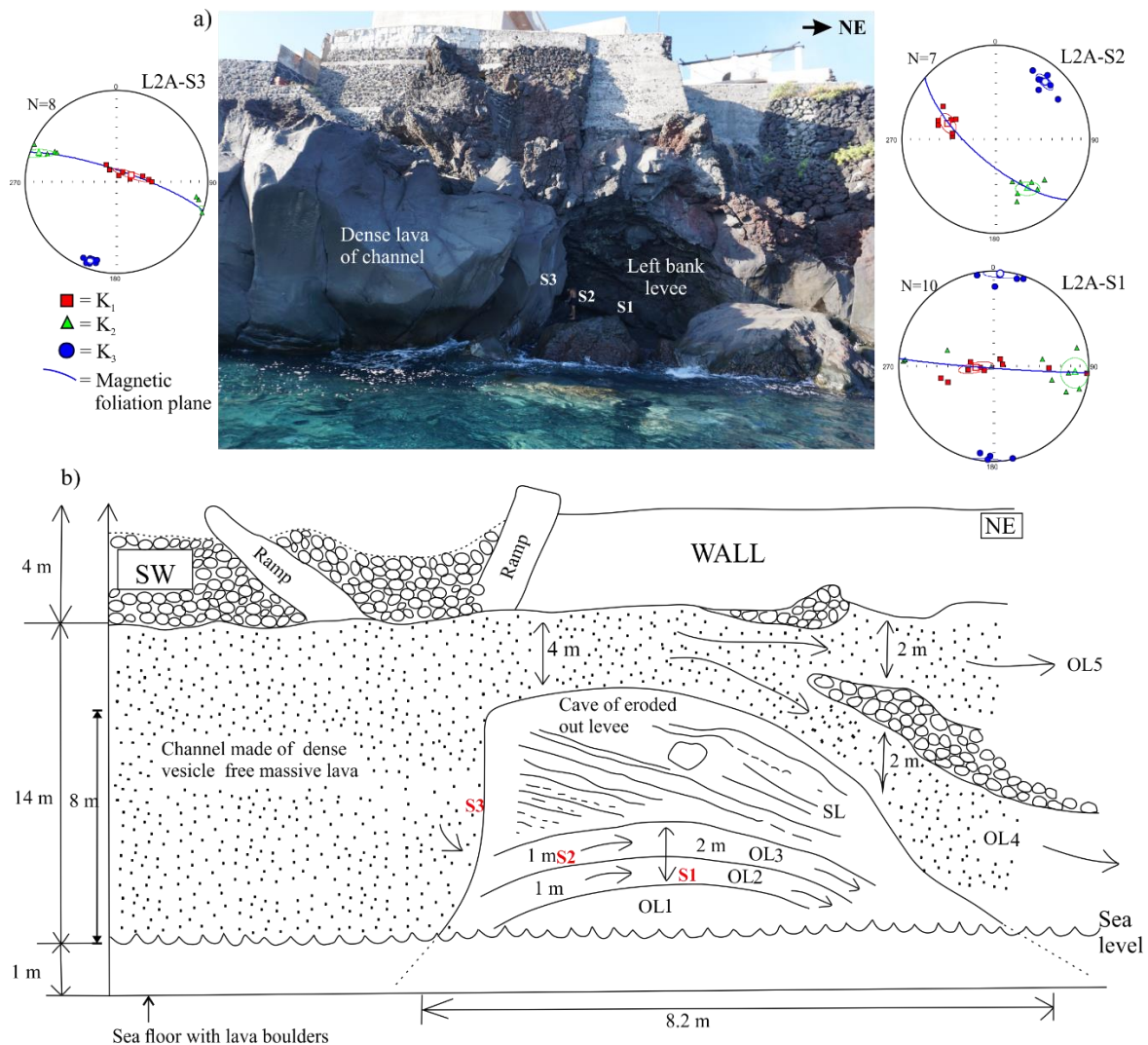
Figure 5. 2. a) Field photo of 'a'ā master channel at Flow 2 showing the location of sampling and AMS result. Lower hemisphere equal-area projection shows magnetic lineation (K_1) and foliation (K_1-K_2). **b)** Diagram of 'a'ā channel and associated levees with measured field parameters. OL = overflow levee; SL = sheared lava. The red labels correspond to the sampling locations.

We collected three hand-samples from Flow 2, one from the dense, massive lava of the master channel (L2A-S3) and two from the overflow levee of the eroded cave (L2A-S1 and L2A-S2). The mass susceptibility ranges from 1.63 - 8.63 (10^{-3} m^3 kg^{-1}), with an average value of 4.25 $\pm$ 3.340 (10^{-3} m^3 kg^{-1}) (Table 5.S 1). More than 90% of the studied specimens show oblate ellipsoid and are characterized by a low corrected degree of anisotropy (Pj = 1.003-1.011) (Table 5.S 1), which is normal for lava flow. Stereographic projection of the susceptibility axis displays a good clustering for sample L2A-S2, whereas the rest of the two (L2A-S1 and L2A-S3) disperse axes along the K_1-K_2 plane (Figure 5.2a). The samples L2A-S1 and L2A-S3 exhibit a similar distribution of susceptibility tensor with a vertical foliation plane striking WNW-ESE, and the K_3 axes forming a cluster along the N-S direction (Figure 5.2a). The stereographic projection of L2A-S2 shows a sub-vertical to inclined foliation plane with the K_3 axes striking NE-SW

b) 'A'ā channel at Flow 7

The right bank rubble levee of the 'a'ā master channel for Flow 7 is exposed at the Grotta di Eolo, another cave system created by erosion of the breccia. The rubble levee is 9 m high and 30 m wide and is capped by a 3.5 m thick overflow levee of massive, vesicle-free lava with shear partings and elongated entrainment bands (length from 0.5 to 1.5m) (Figure 5.3a). Towards the levee base, capping the cave is a unit of identical character to the overflow unit (Figure 5.3), and this may be an intrusion of dense lava into the rubble levee. The rubble is organized into sheared bands of aligned breccia (up to 5 to 10 cm in thickness), with the sense of shear being up and over the levee to the SSE (Figure 5.3). All directional markers are consistent with the same SSE deformation, overflow, and intrusion direction, as detailed in Figure 5.3b.

We drilled cores from the massive lava (L7B) and the sheared plates on the cave roof (L7C). The mass magnetic susceptibility shows a mean value of 6.21 $\pm$ 0.35 (10^{-3} m^3 kg^{-1}) (Table 5.S 1). The mean corrected degree of anisotropy (Pj = 1.016) is the highest among the whole sampled sites. As with the 'a'ā channel described above for Flow 2, the 'a'ā channel observed at Flow 7 also shows mainly oblate ellipsoid. In the stereographic projection, L7B is characterized by a moderate to steeply dipping foliation plane striking NNW-SSE (Figure 5.3b). In the case

of L7C, the foliation plane is gently dipping and strikes along the NNE-SSW direction (Figure 5.3b).
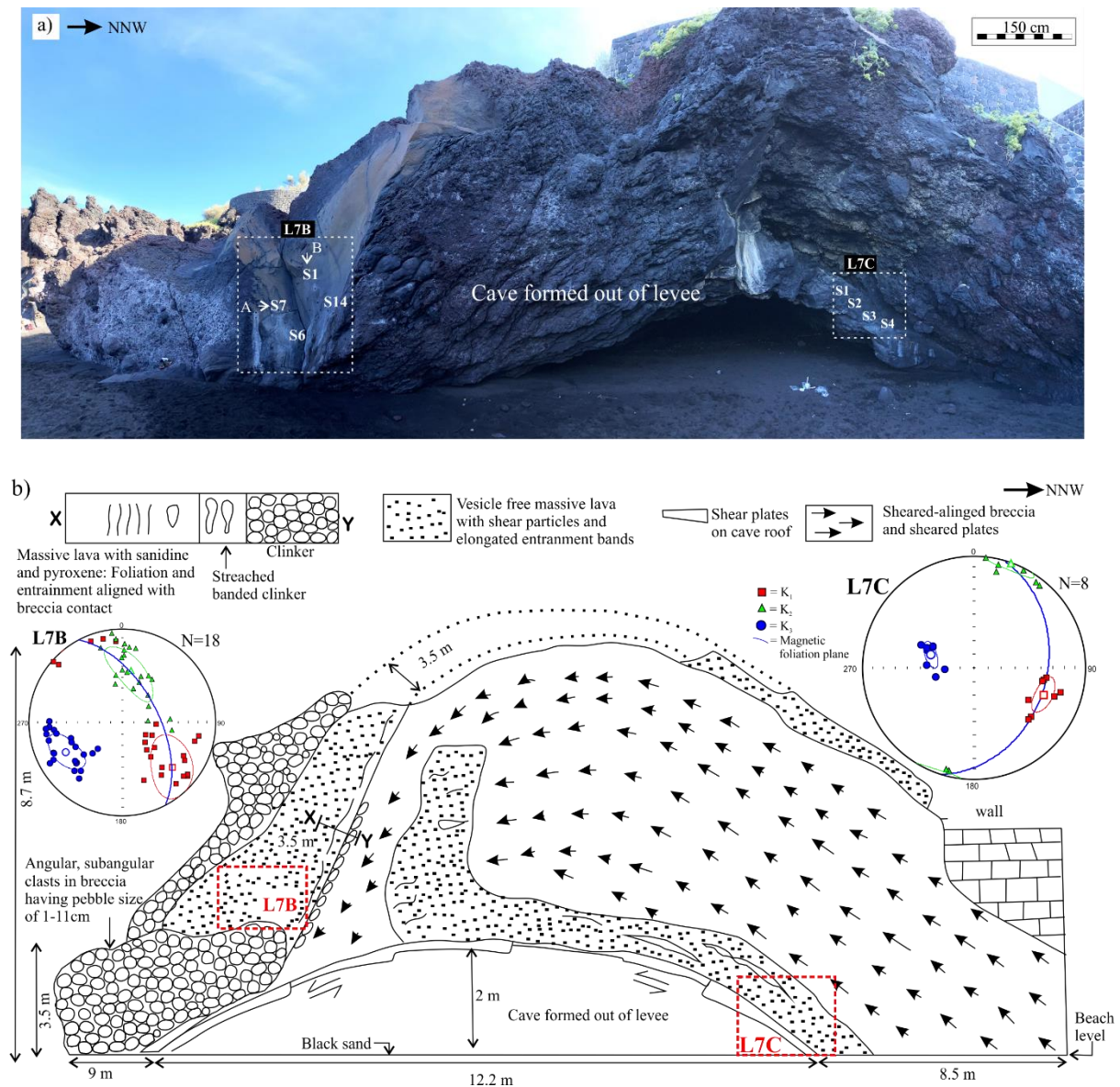
Figure 5. 3. a) Field photo of the channel at Flow 7 above the Grotta di Eolo, showing two sampling location (site L7B and L7C) marked with dotted rectangular lines. **b)** Sketch of the master channel with AMS results. The top flow is partially eroded above the cave, as evidenced by the dotted lines, for a thickness of about 3.5 m. The red labels correspond to the sampling locations, the arrows indicate the flow direction of emplacement.

5.2.1.2 Littoral component

The littoral component is extremely chaotic, and is well-exposed just 20 m to the east (along the shore) of the inflated pāhoehoe Flow 11 (Figure 5.1c). It is oriented N-S, has a total thickness of 3 m and comprises six 'a'ā flow units (Figure 5.4):

A. Inland, the lower portion is 1.6 m thick and contains entrained pockets of 'a'ā clinker up to a meter across, where vesicles (up to 1 cm in diameter) are deformed around the

pockets (Figure 5.4). The base of Unit A is buried by beach cover, but a crust of 'a'ā clinker can be found.

B. Unit A is overlain by a vesicular 'a'ā unit of 40 cm thickness with pyroxene phenocrysts up to 4 mm across (Figure 5.4). The contact with Unit A is marked by a shear zone.

C. Seawards, Units A and B become broken into tilted blocks of 'a'ā (Figure 5.4). Blocks have the same mineralogy as units A and B, and their thickness (1.8 m) is approximately the same thickness as Units A and B.

D. Between Units A and B is a zone of rubble, mixed with slabs of lava having a thickness of 1 m and pockets, up to 35 cm across, of 'a'ā clinker.

E. All units are overlain by a coherent unit of vesicular 'a'ā which drapes over the underlying units. The unit is 80 cm thick, and contains 1–5 mm diameter vesicles and phenocrysts of olivine up to 4 mm. This unit is underlain by a 30–60 cm thick layer of tilted plates (E'). This appears to have been formed by the break-up of the basal shear zone of Unit E (Figure 5.4a).

Because these units broke into blocks (up to 1.3 m), which were then tilted and rotated to varying degrees (Figure 5.4), we did not sample any littoral component for AMS analysis. However, strikes and dips of blocks were taken and are given in Figure 5.4. The highly variable and mixed textural character of this component also meant that we did not sample this unit for vesicularity quantification.
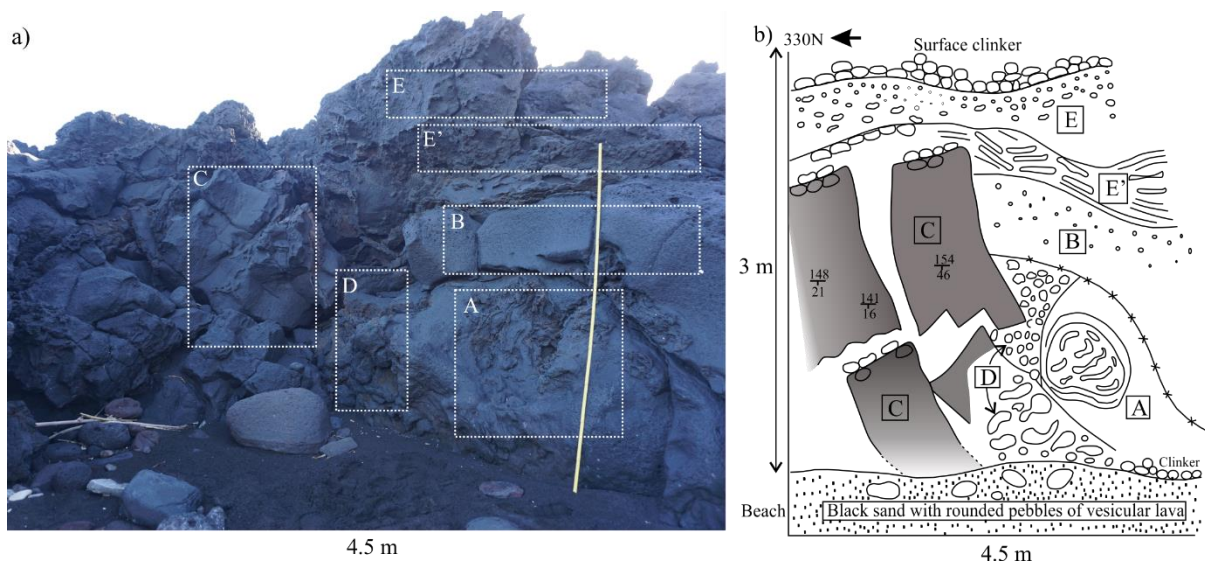
Figure 5. 4. a) Field photo of the extremely chaotic littoral component at Flow 11. **b)** Sketch of the littoral component with five different units. The attitude of tilted blocks of vesicular lava measured from the field is marked in the figure. A = Lower part which contains balls of 'a'ā clinker; B = Less vesicular 'a'ā unit, which shows a sheared contact with A; C = Tilted blocks of vesicular 'a'ā lava; D = Pockets and basal layer of 'a'ā clinker; E = overlying vesicular 'a'ā draped over underlying units; E' = Tilted plated of shear zone of unit E.

<u>5.2.1.3 Ramp</u>

Ramps can be observed along the entire coast from Spiaggia Lunga to the Sirenetta wharf (Figure 5.1a), with the 'a'ā ramp zone extending for 10s of meters inland where it underlies the village (Figure 5.1c).

a) Ramp at Flow 7

Ramping is characterized by upward thrusted slabs of 'a'ā that became stacked in sequence behind the flow front, up to 10 m (Figure 5.5a). Ramps run down into the massive interior, developing an orientation from sub-vertical to vertical towards the flow surface. Entrained clinker pockets (160 cm) and detached bands of deformed clinker can be found between ramps (Figure 5.5b). Below the ramp structures, behind the concrete wharf, lava is massive and dense with horizontal foliation and tension gashes. The best overview of ramping is at Flow 7 where exposure runs 70 m inland. Here, the sense of shear marked by tension gashes of 20-30 mm in length is 4° N, which is the same as the orientation of the ramping.

Samples were collected along two parallel vertical transects to study the variation in flow fabrics along the ramp length. The mean mass susceptibility is 6.84 ± 3.16 (10^{-3} m^3 kg^{-1}). The shape of the AMS ellipsoid includes both oblate and prolate fabrics ($-0.430 < T < 0.590$), with a prevalence of oblate fabrics. Like the other site, this site also has a low mean corrected degree of anisotropy (see Pj values in Table 5.S 1).

The resulting magnetic fabrics show a wider scattering, with K_1 axes forming three different clusters, where the clusters show no relation to the spatial distribution of the specimen. This allowed us to classify them into three sub-fabrics: a) prolate fabrics with gently dipping magnetic foliation and NW-striking magnetic lineation (Figure 5.5c); b) oblate fabrics with gently dipping magnetic lineation and steeply dipping NE-SW striking magnetic foliation (Figure 5.5d); and c) oblate fabrics with NE-striking magnetic lineation and NE-SW striking magnetic foliation plane (Figure 5.5e). The third sub-fabric is characterized by the formation of a fan-like distribution of AMS axes that masks the oblate fabrics of single specimens by a bulk prolate ellipsoid at the site level.
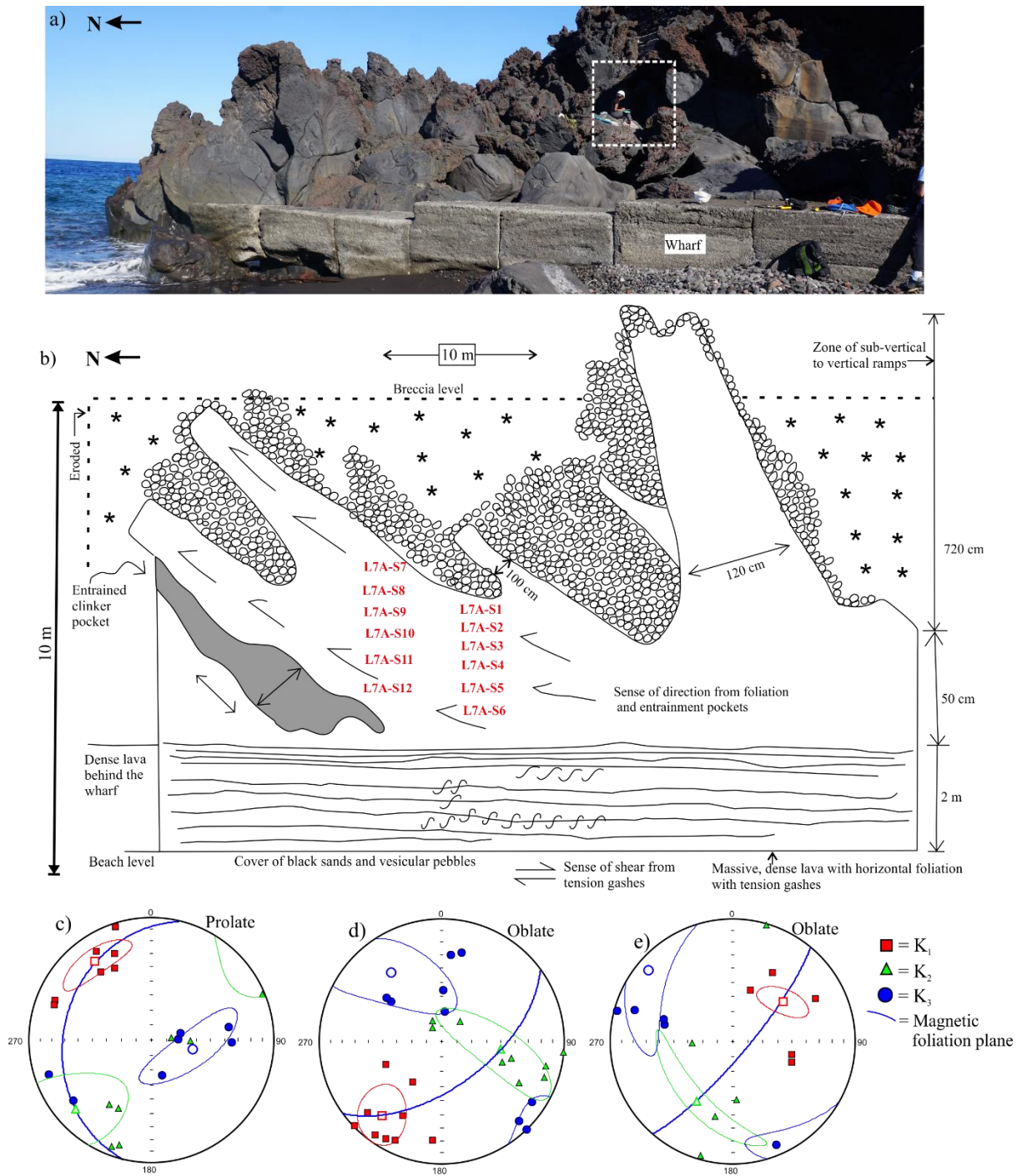
Figure 5. 5. Photo of the ramp observed at Flow 7 where the white dotted box highlights the sampling location shown in b, with samples positions indicated by the red labels. **b)** Sketch of ramps with the sense of flow direction measured in the field. The red labels correspond to the sampling locations. **c), d), e)** Principal susceptibility axes distribution on lower hemisphere equal-area projections.

b) Ramp at Flow 1

The detail of an individual ramp is particularly well exposed at Flow 1 (Figure 5.1c, 5.6). Here we focus on an 'a'ā lava flow unit 7.3 m in height. The whole structure can be grouped into three zones, from bottom to top: (1) a vesicular lava, (2) a massive dense lava, and (3) a ramp.

At the base is a 2 m thick layer of vesicular lava. Vesicle size decreases with depth from 5-15 mm at the top to 1-2 mm at the bottom (Figure 5.6a). Above, there is a 2.8 m thick layer of massive dense lava with entrained clinkers (Figure 5.6a). These clinkers are aligned and orientated 44° NE. The ramp zone comprises the uppermost 2.5 m and has two sub-vertical ramps of 'a'ā (Figure 5.6b). The lava flow is sheared and characterized by deformed vesicles, ~20 mm in length, with entrained 'a'ā clasts up to 10 cm in diameter. Structures and shearing are aligned at 44° NE. While the contact between zones 1 and 2 is gradational, that between zones 2 and 3 is abrupt (Figure 5.6a).
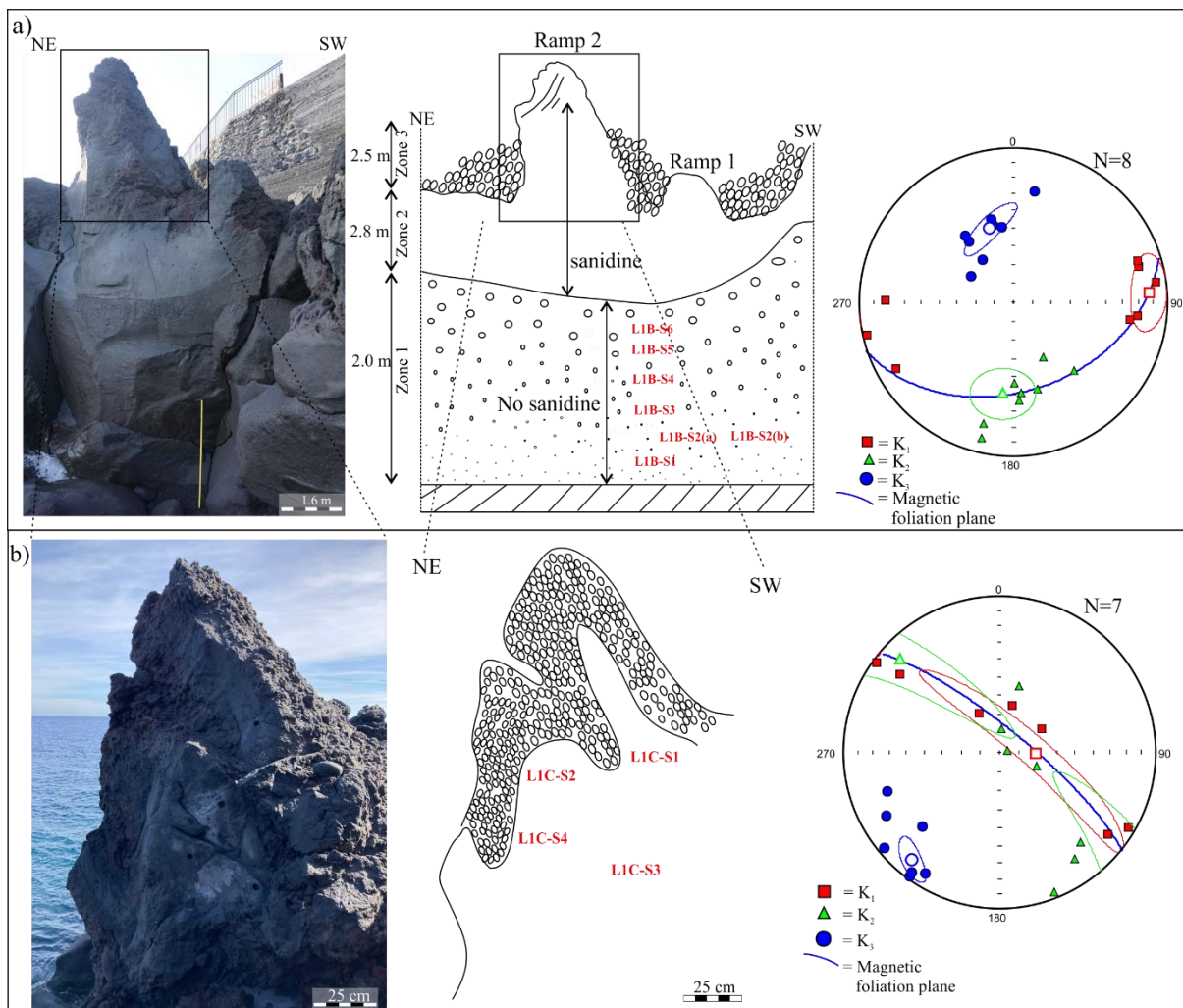
Figure 5. 6. a) Photo and sketch of the lava unit with ramping, massive dense lava, and vesicular lava at Flow 1. For sampling, we considered the lower two zones together and the upper ramp zone separately. **b)** Photo showing a detail of the Flow 1 ramp zone with sampling sites. The red labels correspond to the sampling locations and the equal-area projection shows the AMS fabric.

Cores were drilled from the bottom vesicular lava (Zone 3) and the top ramping structure (Zone 1) to characterise the variation in the flow fabrics along the vertical transect. The bulk χ_m shows no significant variation among the two zones (Table 5.S 1). The mean degree of anisotropy is

similar to the rest of the flow units (Pj = 1.008), and the shape of the AMS ellipsoid is oblate. In the ramp zone, the magnetic foliation plane is steeply dipping and strikes NW-SE (Figure 5.6b). Whereas in the bottom vesicular lava, the three susceptibility axes are well clustered with an inclined foliation plane striking along ENE-WSW (Figure 5.6a).

c) Ramp at Flow 4

At Flow 4 (Figure 5.1c), we find a ramp cut in three dimensions, along and across the axis of ramping (Figure 5.7). As at all flows, ramps are stacked parallel to the shoreline with a long axis oriented 345° N. Five 'a'ā ramps can be identified, stacked in sequence along the flow direction (55° N; Figure 5.7a). Ramp 1 is 1.4 m thick and is characterized by massive, foliated lava with bands of coarse (1-4 mm) vesicles. While the southern part of the outcrop cuts the ramp in the crossflow direction (Figure 5.7b), the northern part cuts it in the downflow direction (Figure 5.7c). The downflow section shows two massive parts to the ramp separated by an entrained clinker band, which is cut in the crossflow direction in the southern part of the outcrop (Figure 5.7). Subsequent ramps also have almost similar characteristic features of thick massive core and clinker top with thickness varying between 1.0 and 1.4 m.

Here, we drilled the cores from the crossflow (L4B) and the downflow section (L4A) of ramp 1 (Figure 5.7a). The χ_m is consistent with the other components observed ($\chi_m = 5.95 \pm 2.55 \times 10^{-3}$ m^3 kg^{-1}), and the corrected degree of anisotropy is low (Pj = 1.008). On the northern half of the ramp, the magnetic foliation is moderately dipping and strikes E-W (Figure 5.7c), whereas, on the southern half, the foliation plane dips gently along E-W (Figure 5.7b). In both cases, the pole of the foliation plane is parallel to the strike of the ramp and the K_1 and K_2 axes distribute along a girdle making a well-defined foliation plane.
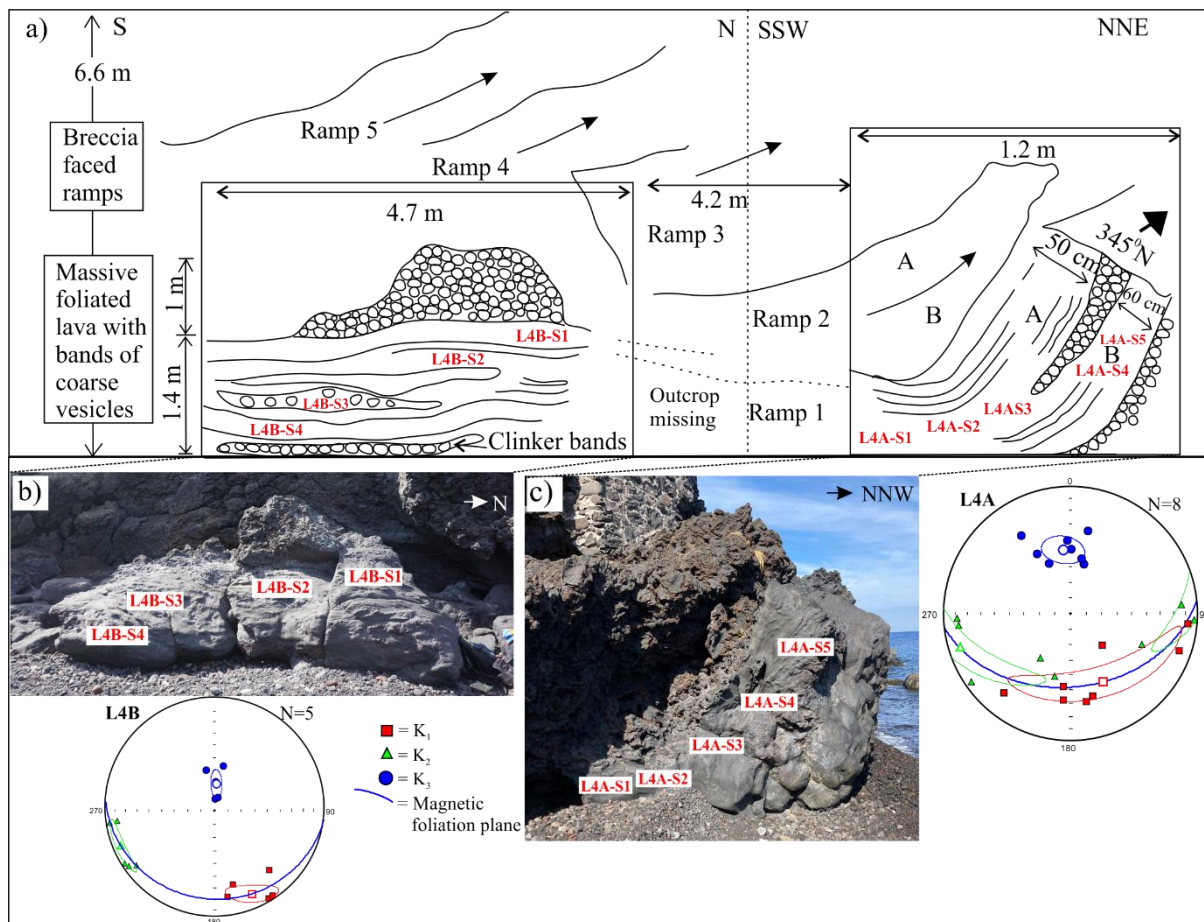
Figure 5. 7. Ramp cut in three dimensions observed at Flow 4. **a)** Sketch of ramping showing the parallelly stacked ramps with foliation direction indicated by sheared lava. **b)** and **c)** showing the southern and northern part of the ramp with the location of sampled cores respectively. Stereographic projection obtained from the AMS study shows the distribution of the three main susceptibility axes.

5.2.1.4 Lava tube

From our field investigation, we identified the presence of tubes across the barrier of the sea surface to feed a seaward bench of pāhoehoe around most 'a'ā flow units. The best exposed example was found in Flow 1 (Figure 5.1c). Here, we found two tubes, extending both NE from a wide vent at the base of a 4 m high 'a'ā flow front. The best developed tube is in the eastern branch, which can be followed for a distance of 15 m. It is 1.6 m high, and 3.6 m wide, trends 34° N before turning 58° N (Figure 5.8a), and has a slope to the NE of 11–12°. The tube walls are characterized by at least five accreted layers with thicknesses of 9-16 cm (Figure 5.8b), characterized by accreted clinkers elongated in the direction of the tube orientation. The roof comprises two arched-over layers with a thickness of 7 and 10 cm. The exposed central stream (Figure 5.8) is 0.9 m wide and has embryonic 'a'ā clasts rooted to the interior lava. The second tube shows the same pattern, but is less well exposed, being eroded by wave action.

However, it shows a similar form to the first tube with a tube cavity that has a height of 1.4 m and three accreted layers.

We collected four hand-samples, one from the central stream (L1A-S2) and three from the accretionary layers (L1A-S1, L1A-S3, and L1A-S4) for magnetic fabric study. Figure 5.8 and Table 5.S 1 show the distribution of the susceptibility axes for each sampling site and the final AMS results, respectively. The bulk χ_m shows an average value of 2.91 ± 0.36 ($\times 10^{-3}$ m^3 kg^{-1}). The Pj value ranges from 1.001 to 1.017, with an average value of 1.006 (Table 5.S 1). Samples collected from the opposite sides of the accretionary layer, NE and SW, show neutral to oblate fabrics, while the central stream shows a mixed fabric. Looking at the distribution of principal susceptibility axes, the magnetic fabrics show well grouped axes, with the exception of L1A-S4 (Figure 5.8b). Samples from the accretionary layers show sub-vertical foliation planes with an E-W orientation, while the central stream shows an inclined foliation plane striking NNW-SSE (Figure 5.8).
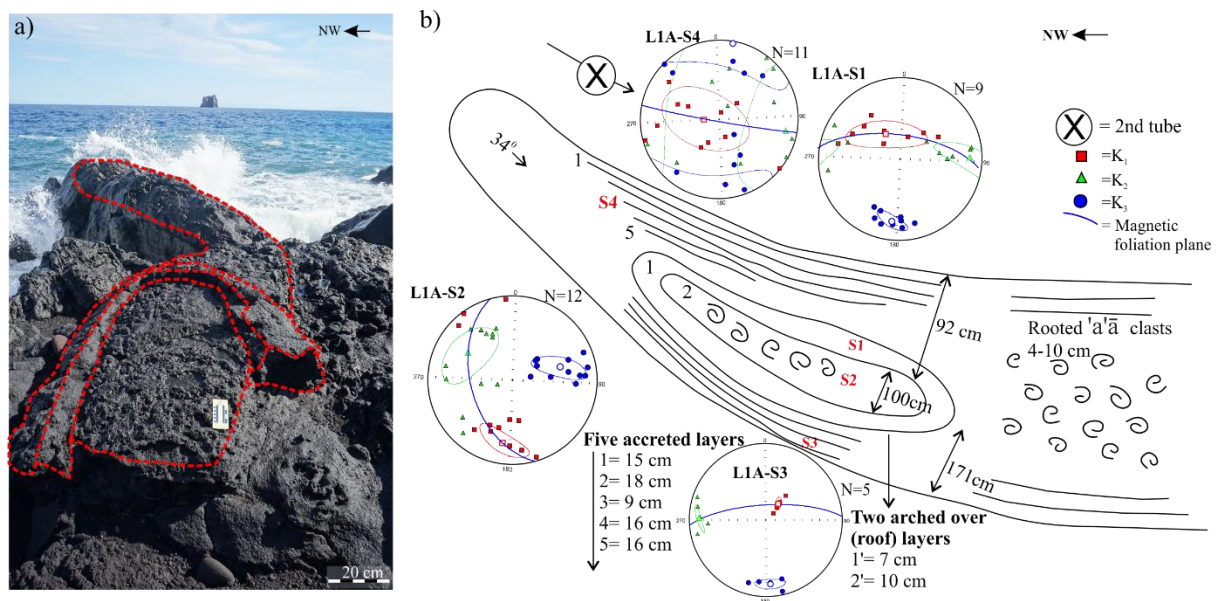
Figure 5. 8. a) Photo of the tube observed at Flow 1 exit (2nd tube is not visible in the photo). **b)** Sketch of the tube along with the sampled location, and view from above. The stereographic projection shows the orientation of three susceptibility axes and foliation planes. Accretionary layers (1 to 5) and arched over roof layers (1' and 2') are highlighted in the sketch and numbered from outer to inner layer.

A second tube can be found exposed high in the cliff at Flow 7 (Figure 5.1c). This tube is 50 cm wide and includes 25 cm of empty space indicating that it is partially drained (Figure 5.9a). The roof displays stalactites and is above a pāhoehoe flow surface (Figure 5.9b). Undrained

lava is vesicular (with vesicles up to 5 mm in diameter) and surrounded by dense lava of the flow front through which the tube cuts.
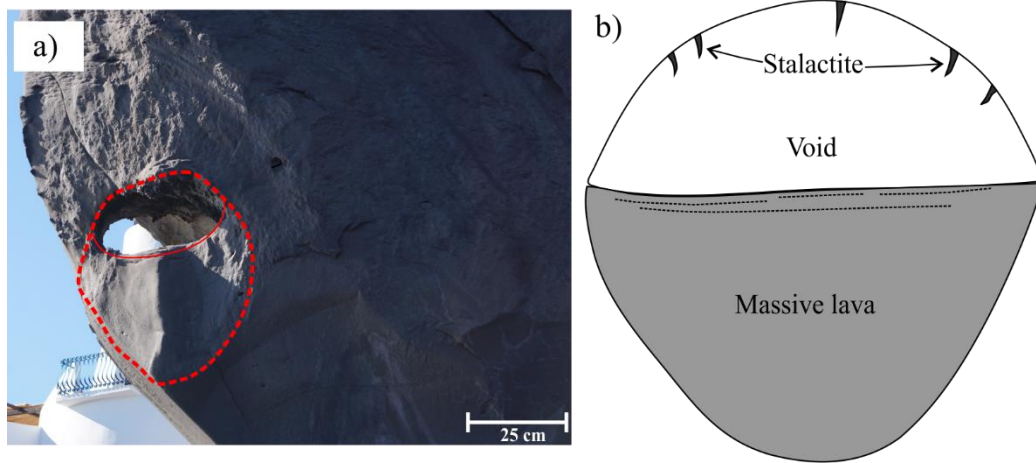
Figure 5. 9. a) Field photo of tube observed at the cliff of Flow 7. The boundary of the tube is marked with red dotted lines. **b)** Section of the observed tube showing the stalactite at the roof of the void space and massive lava with upper foliations.

5.2.1.5 Inflated pāhoehoe

Inflated pāhoehoe can be found all along the coast, especially at the NW and NE margins of the SB lava flow field (Figure 5.1c). The best exposed example is Flow 12 at the NW edge of the lava flow field, where two inflated pāhoehoe flow units can be traced for a distance of 24 and 33 m towards NW and north, respectively with a uniform width of 11 m (Figure 5.10a). The interior is made of dense lava with sheared vesicles (up to 50 mm) and the sense of shear is in the direction 196° N with a slope of 12° downwards to the north (Figure 5.10b). The thickness of the interior increases towards the sea from 1.4 m to 3.2 m. At the same time, a vesicular surface layer can be identified down the entire length of the unit that varies in thickness from 1 to 3 cm. The unit can be divided into four pāhoehoe lobes, which vary in length from 1.3 to 11 m, each being separated by an inflation cleft (Figures 5.10a – 10c). In the transverse section, vesicles are oval, small, and numerous towards the surface, and increase in size from 1 to 5 mm, while decreasing in number towards the lobe centre (Figure 5.S1a). Vesicles also become more sheared towards the lobe centre, with a sense of shear being around a central void (Figure 5.S1b).
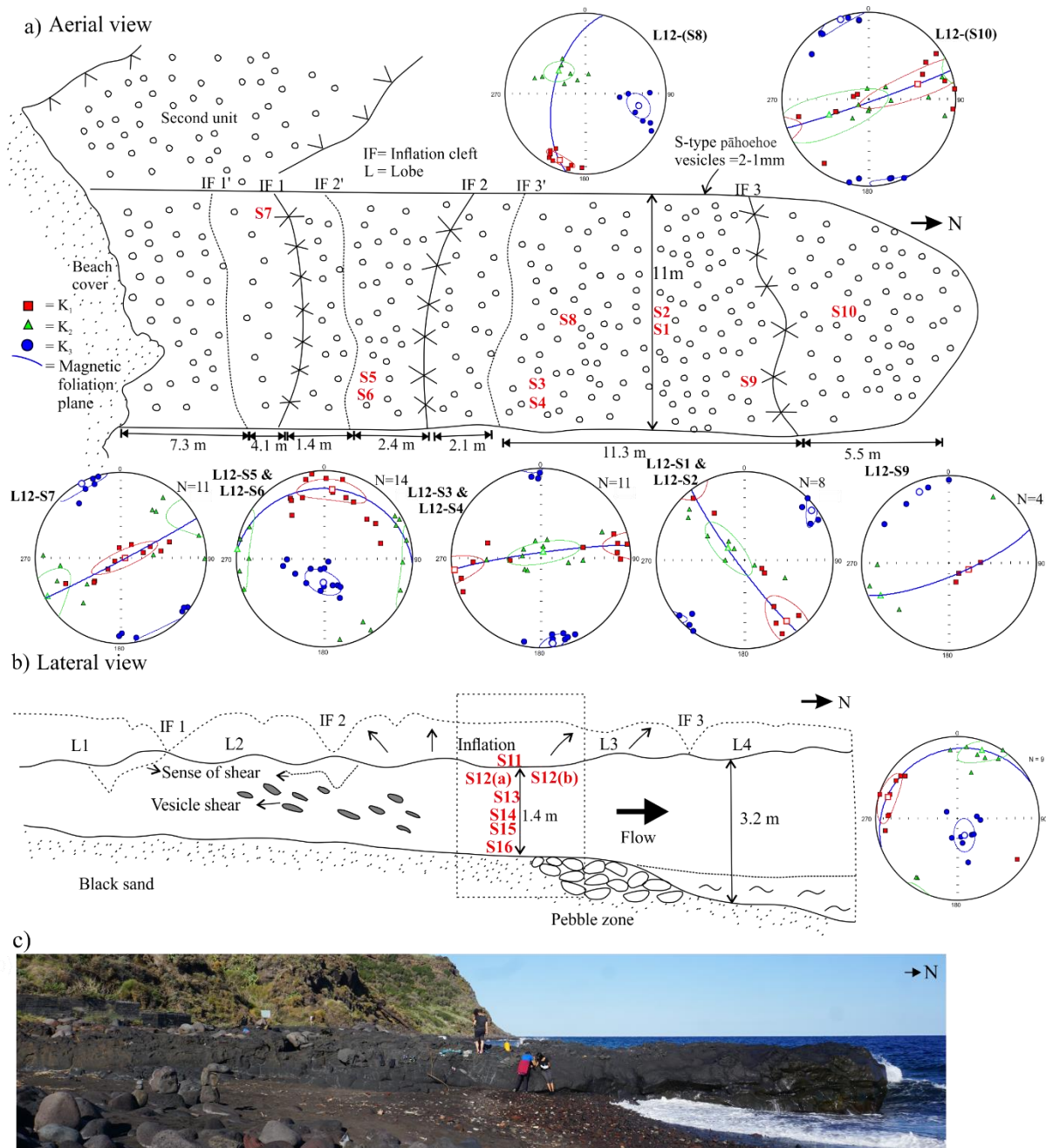
Figure 5. 10. a) Aerial view of the inflated pāhoehoe lobes comprising Flow 12, showing the sampled location and the representative stereonet. **b)** Lateral view showing the sampled sites along with the stereographic projection of the results. The thick black arrow shows the flow direction and the small upper arrows indicates the inflation directions measured in the field. **c)** Field photo showing the lateral view of the Flow 12 inflated pāhoehoe entering the sea.

We collected two hand-samples near the inflation cleft (L12-S5 and L12-S6), eight hand-samples from the top of the vesicular surface layer, and six drilled cores from the lateral side of the dense interior lava (Figure 5.10a-b). The χ_m shows a mean value of 2.14 ± 1.49 (10^{-3} m^3 kg^{-1}) (Table 5.S 1). The corrected degree of anisotropy Pj is relatively low, ranging between 1.001-1.013 (Table 5.S 1). The susceptibility ellipsoids are mostly oblate and are independent

of the degree of anisotropy. For the degree of anisotropy and the shape parameter, no significant differences are observed with respect to the position of the samples (Table 5.S 1).

Samples from the top of the vesicular surface layer show vertical to sub-vertical foliation planes with distinct orientations (Figure 5.10a). For example, samples L12-S7 and L12-S10 provide a vertical foliation oriented ENE-WSW, whereas L12-S1 and L12-S2 show a vertical foliation plane along NW-SE (Figure 5.10a). Here, the K_1 and K_2 axes distribution makes griddles, defining good foliation planes, except for two locations (L12-S8, L12-S9). Samples from the inflation cleft are well clustered, with an E-W oriented sub-horizontal foliation plane and north dipping magnetic lineation (L12-S5 and L12-S6 in Figure 5.10a). Unlike the surface layer, the dense lava of the centre core displays a sub-horizontal foliation plane striking in the NE-SW direction (Figure 5.10b).

5.2.2 Palaeomagnetic results

The paleomagnetic findings are presented using orthogonal vector plots (Zijderveld, 1967), revealing the demagnetization characteristics of each specimen (Figure 5.11a and b). Both AF and thermal demagnetisations show a stable magnetization intensity and a well-defined single magnetization component. The intensity of natural remanent magnetization of the sampled flows shows a wide range, from 3.17–70.64 Am^{-1} (Table 5.S 2). Relatively high NRM intensities (> 30 Am^{-1}) were recorded for tube, inflated pāhoehoe and channel-levee components (Table 5.S 2). Most samples are characterized by univectorial orthogonal plots, as expected for recent lava flow (Figure 5.11). A few samples show the presence of secondary viscous remanent magnetization easily removed within the first few steps of demagnetisation.

The characteristic components were estimated by stepwise demagnetisation, selecting a maximum angular deviation (MAD) threshold of 3°. The ChRM is mostly isolated around 450-540 °C for thermal demagnetisation (Figure 5.11b). Instead for AF demagnetisation, more than 90% of the sample was completely demagnetised around 100-120 mT (Figure 5.11b). For the rest 10% complete demagnetisation required a higher magnetic field, >120 mT. The mean-site ChRM was calculated with Fisher's statistics. The obtained ChRMs show mostly north declinations and positive inclination, consistent with the Geocentric Axial Dipole (GAD) direction at the geographic coordinates. The mean-unit ChRM direction of SB lava flow is inclination (I_{mean}) = 59.8°; declination (D_{mean}) = 1.2° with precision parameter (k) = 37 and α95 confidence cone = 3.4 (Figure 5.11c).

a) L4B-3B (Alternate field demagnetisation)

b) L1A-2A (Thermal demagnetisation)

c)
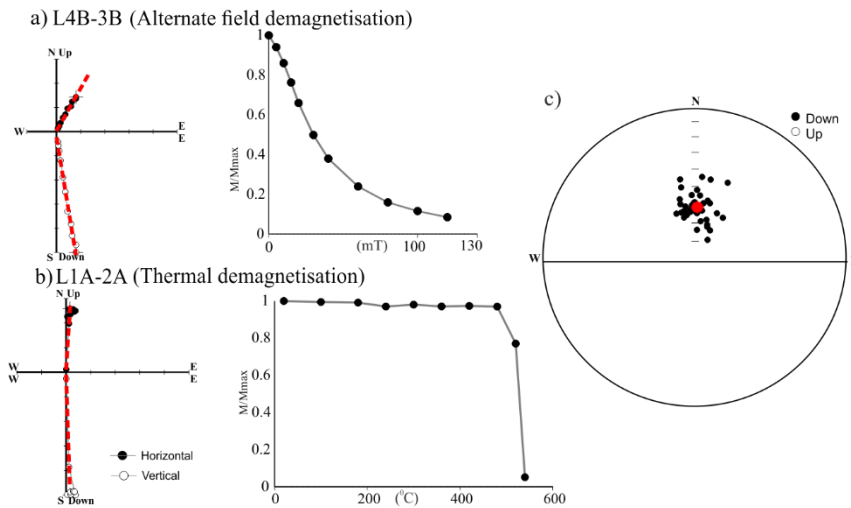
Figure 5. 11. a) Alternate field and **b)** thermal demagnetisation behaviour of two representative specimens showing stereographic projection, normalized intensity curve (M/M$_{max}$) and orthogonal projections. **c)** Site mean ChRM direction with α_{95} confidence limits.

5.2.3 Porosity and connectivity distribution

The distribution of connectivity with respect to the porosity of the SB lava is summarised in Figure 5.12. All the analysed samples displayed a high value of connectivity, which is typical of the rocks formed by an effusive eruption, especially for basaltic lava flows (Colombier et al., 2017). The small dispersion of connectivity, between $0.95 < C < 1.01$ for ramp and channel makes them different from inflated pāhoehoe and tube having $C \approx 1$ (Figure 5.12, Table 5.S 3). This division is even better for the porosity distribution (Figure 5.12). Porosity varies between 0.5-15% for ramp and channel and 20-35% for inflated pāhoehoe and channel-levee system (Figure 5.12). Furthermore, the distribution of connectivity and porosity shows a negative correlation, with the connectivity value becoming more distributed as the porosity of the rock decreases (Figure 5.12).
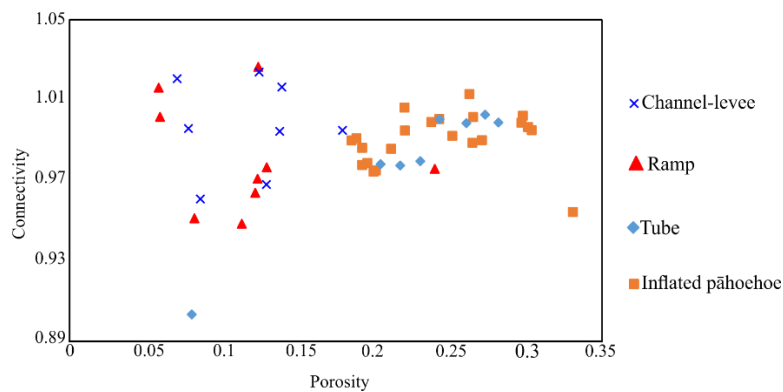
Figure 5. 12. The covariance of connectivity with porosity for ramp (triangle), tube (diamond), inflated pāhoehoe (square), and channel-levee (cross).

63

5.2.4 Clast Counts

Texturally, clasts at all sites could be divided into five groups: 1) clinker; 2) oxidised; 3) finely vesicular (Fv); 4) coarsely vesicular (Cv); and 5) dense. In terms of phenocryst content, they could be divided into sanidine-rich and olivine-bearing. Figure 5.13a shows the spatial distribution of the different clast types along the coast. In general, all clast counts are dominated by coarsely and/or finely vesicular lava, with minor amounts of oxidized and dense lava plus clinkers. While the occurrence of coarsely vesicular lava increases as we move along the coast to the south-east, the incidence of clinker and finely vesicular lava decreases (Figure 5.13a). Also, as we move to the north-west, the quantity and size of olivine phenocrysts decreases, and the number of sanidine-bearing clasts increases. At the dive site, off-shore of Flow 7, we find a shallow platform with a seaward extension of 30 m (Figure 5.13b). Sea-floor clasts are dominated by finely vesicular lava, with concentrations of dense lava and clinker aligning with onshore channels and levees. Clast size also increases seawards, and a zone of oxidized lava can be found aligning with an onshore outcrop of the same character (Figure 5.13b).
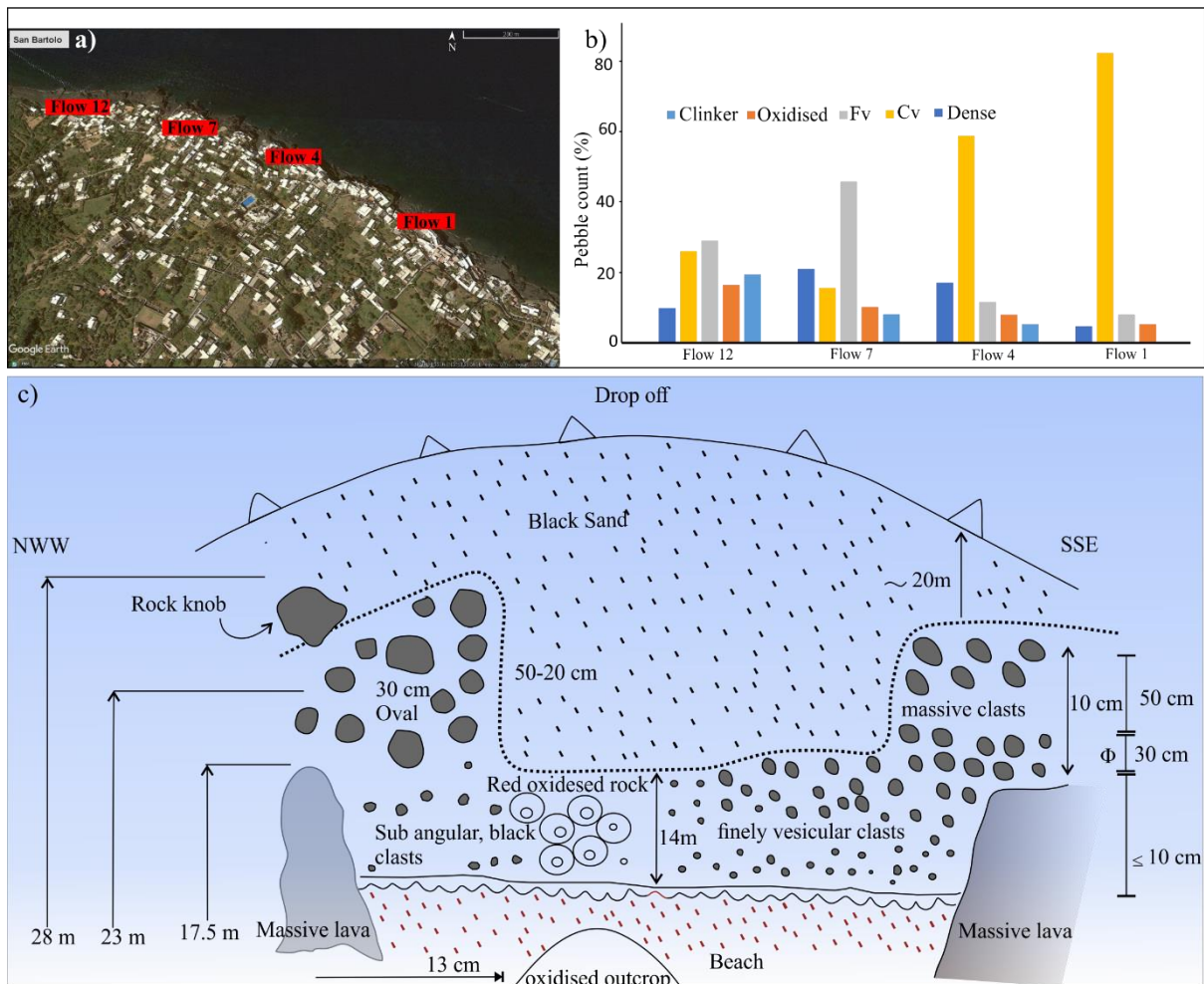
Figure 5. 13. a) Google map of the lava flow units highlighting the flows selected for clast counting. **b)** Histogram showing the distribution of clasts along the coast. Fv = finely vesicular, Cv = coarsely vesicular. **c)** Sketch of an overview of sand and boulder distribution in the shallow region of the sea obtained from the dive survey.

5.3 Discussion

We first describe the magnetic flow fabrics and the emplacement dynamics of each component, before building a model for the formation of a channel-fed 'a'ā lava flow entry into a water system.

5.3.1 Magnetic flow fabrics and emplacement mechanism of lava

The AMS study aids to characterise the flow fabrics of each component and to evaluate the lava flow dynamics and emplacement sequence. Our results highlight the remarkable agreement between the flow direction derived from AMS measurements and the contextual conditions specific to the local environment. In addition, the mean palaeomagnetic direction given by our study is consistent with the proposed age of ~ 2-4 ka (Arrighi et al., 2004; Speranza et al., 2008).

5.3.1.1 'A'ā flow channel-levee

The two master channels formed inland along the middle portion of the SB lava flow field probably connected with Flows 2 and 7, to feed the main ocean entry of lava (Figure 5.1c). The central lava channel is characterized by the flow along the NE-SW direction (Figure 5.14). This lava stream is bounded on both sides by right bank (RB) and left bank (LB) levees, consisting of an overflow, shear, and rubble levee (Figure 5.S2). The initially formed rubble levee is overlayed by the sheared and overflow levee (Hulme, 1974; Sparks et al., 1976; Harris and Rowland, 2015; Lipman and Banks, 1987).

At Flow 2, the upstream flow along the channel to feed the overflow levee is marked by a vertical foliation oriented E-W to NW-SE. The increased flatness of the AMS ellipsoid (T = 0.600) is attributable to the significant shear at the channel boundary (Canon-Tapia and Pinkerton, 2000). Disregarding the samples from the overflow levee to avoid the local variations in the flow direction, the samples collected from the massive lava channel show a SSW flow direction. For the second channel at Flow 7, the well-defined foliation plane and strong oblate ellipsoid provide a flow direction towards WSW (Figure 5.3). For both cases, the obtained flow direction is opposite to the regional flow of the SB lava flow field with the foliation plane dipping towards the known flow direction. The resulting flow direction shows the backward flow of lava in the channel as the lava flow slows down at the shoreline due to the development of pāhoehoe benches.

5.3.1.2 Littoral component

The littoral features formed across the zone of lava-water interaction. The lava-water interaction is a fast and uncontrolled process where the explosive intensity mostly depends on the influx of lava into the sea-water (Mattox and Mangan, 1997; Bosman et al., 2014). The outcrops along the coast observed at SB were formed by the two lava fluxes (Flow 2 and Flow 7), the first of which underwent flow wide break-up and mixing, while the second flowed over the basal unit while remaining intact. The chaotic and reworked character of the littoral component precludes us from studying and interpreting magnetic fabrics.

5.3.1.3 Ramps

Ramping occurs when the lava flow front stalls, and the subsequent lava flow moves upward with the shearing of internal layers due to thrust from the stalled lava flow front (Macdonald, 1972). Here, ramps were formed as the lava backed up in channels behind the ocean entry. The

lava ramps up as fast-flowing lava from the main channel encounters the break in slope and later stalls (Figure 5.14). The vertical to inclined foliation planes observed in all three cases (Flow 1, Flow 2, and Flow 7) of ramping are due to the vertical upward sliding of the lava due to ramping.

In the case of the ramp observed at Flow 1, the distribution of the susceptibility axes shows different patterns for the upper and lower parts of the ramp. The NNW flow direction obtained for the lower part is inconsistent with the known strike direction of the SB flow field. This is probably due to post-emplacement modification by the continuous inflow of lava below the ramp structure to feed the pāhoehoe bench. In fact, the sample collected from the top of the ramp, i.e., away from the subsequent flows, gave a more reliable result with a vertical foliation plane and NE-SW flow direction (Figure 5.6b). Therefore, we avoided considering the lower part of the ramp for flow direction interpretation given the possibility of post-emplacement modification.

The formation of three sub-fabrics for the ramp at Flow 7 further suggests the reworking of the magnetic fabrics by the subsequent lava flow below the ramp (Figure 5.5). Another possible interpretation for the formation of sub-fabric is the presence of detached bands of entrained clinker between the ramps (Figure 5.S3). The hot lava causes the deformation of the clinker and later detaches the deformed clinker to the ramp zone (Figure 5.S3). This can also affect the primary magnetic fabrics of the ramp. For the ramp at Flow 4, the flow direction towards N obtained from AMS is consistent with the known regional flow direction of the SB lava flow field. As there is no subsequent flow underneath the ramp, we can safely eliminate the possibility of post-emplacement modification of the flow fabric (Figure 5.7). The shift of the foliation plane dip from sub-horizontal to inclined at the southern and northern ends of the ramp, respectively, shows the evolution of the ramp formation. Moreover, in the northern ends, the magnetic lineation dispersion on the flow plane might suggest spreading toward the open sea.

5.3.1.4 Tubes

The lava tubes observed along the coast within Flow 7 and Flow 1 are probably the down slope extension of the two 'a'ā lava channels observed in the middle lava flow field (Figure 5.1a), whereas the smaller cavities described within Flow 1 and Flow 7 (Figures 5.8 and 5.9) are incipient lava tubes. They are characterized by a central lava core, multiple accretionary layers, and a roof with stalactite formation (Figure 5.S4). However, close to the coast, the roof has

been often eroded by wave action. Also, lava within the tube at SB undergoes continue thermal erosion and downcutting (Bussey et al., 1997; Allred, 1998; Kerr, 2001; Fagents and Greeley, 2001) which increase both foot space and headspace of the tube respectively (Sawlowicz, 2020). This process has been described at other lava flows, such as in Hawaii (Wood, 1981), Mt St Helens (Kerr, 2009), and California (Greeley and Baer, 1971). The presence of lava tubes and the possibility of thermal erosion evidences a prolonged duration of the flowage within the tube and probably also a turbulent flow within the tube (Hulme, 1973; Kerr, 2001; Kerr, 2009). The thickness of the inner coatings observed at the margins of the tube within Flow 1, being several cm thick, suggests a rather viscous flow (Calvari and Pinkerton, 1999), probably the result of the flowage within the tube during the late stages of the eruption. In fact, the number of inner coatings reveals the life of the tube, with each coating corresponding to a phase of tube filled up, crust breakage and tube draining by ephemeral vent opening at its margins (Calvari and Pinkerton, 1999).

The exposed central stream, due to the erosion of the roof, along with the accretionary layers gives an idea of the internal structure of the tube and its principal mode of formation (Figure 5.8). As Peterson et al. (1994) stated, the initial step in the tube development is channel formation, which involves the solidification of the outer boundary layer and the formation of lateral levees (Hulme, 1974; Sparks et al., 1976). Acknowledging the fact that the quickly chilled magma keeps the initial flow fabrics (Cañón-Tapia and Coe, 2002), we consider the sample from the outer accretionary layer to infer flow sense (L1A-S3). We avoided the intermediate layers to infer flow direction because of the possible modification of magnetic fabrics due to the formation of adjacent layers by the frequent overflow of the central stream (Peterson et al., 1994). Consequently, for the tube at Flow 1, the AMS results indicate a vertical foliation plane with a southward flow direction. Looking at the magnetic fabrics, the vertical to sub-vertical foliation plane reflects an upward magma motion perpendicular to the overall flow direction. This might be due to the overflow of lava due to fluctuating lava input to form the accretionary layer.

5.3.1.5 Inflated pāhoehoe flow

Inflation of a lava flow refers to the swelling or expansion of the preformed surface crustal layer by the continuous input of lava in the middle, resulting in a pressure build-up in the flow unit (Hon et al., 1994). In the SB lava flow field, a marginal and now eroded seaward bench of inflated pāhoehoe developed to form an arcuate bench zone.

The observed inflated flow is characterized by a thin brittle layer at the surface, a viscoelastic layer underneath, a thick central core, and a basal crust, as explained by Hon et al. (1994). The vertical foliation plane strikes in different directions, showing the inflation of the brittle vesicular layer to accommodate the pressure caused by the continuous lava input. The formation of inflation features, such as cleft and lobes, explained by Walker (1991), can be distinguished by the sub-horizontal and sub-vertical magnetic foliation planes, respectively. For the central current, the horizontal flow shows a coherent direction toward the sea, with the flattened ellipsoid highlighting the gravitational settling of crystals (Sangode et al., 2021).

The 'a'ā lava channel marks the initial stage of inflation. Flow stalling, followed by the continuous lava supply from the main vent caused the onset of lava inflation and this stage marked the formation of the thin outer brittle layer. Inflation of the first flow continued, and the brittle outer layer broke to accommodate the inflation of the visco-elastic layer (Figure 5.S5). Later, the visco-elastic and brittle layers broke as the influx of lava flows continued and caused the formation of the second flow (L2). Finally, the continuous pressure made small cracks on the surface crust and caused ooze out of spongy (S-type) flow lobes (Figure 5.S5). The same process of stalling, inflation and breakout is repeated at least four times to extend the length of the system with four pāhoehoe lobes.

5.3.2 *Spatial distribution of different lava components and implications for emplacement sequence*

We use the field observations, in conjunction with physical lava characteristics such as porosity, connectivity and phenocryst type, to generate a comprehensive overview of the spatial distribution of the defined lava components along the coast. Lava entry to sea and/or ocean usually results in the radial distribution of lava like a fan, with the lava tube formed at the flow front to drain the 'a'ā flow and feed the submarine pāhoehoe lava bench (Kauahikaua et al., 1993; Jurado-Chichay et al., 1996; Mattox and Mangan, 1997; Bosman et al., 2014; Di Traglia et al., 2018).
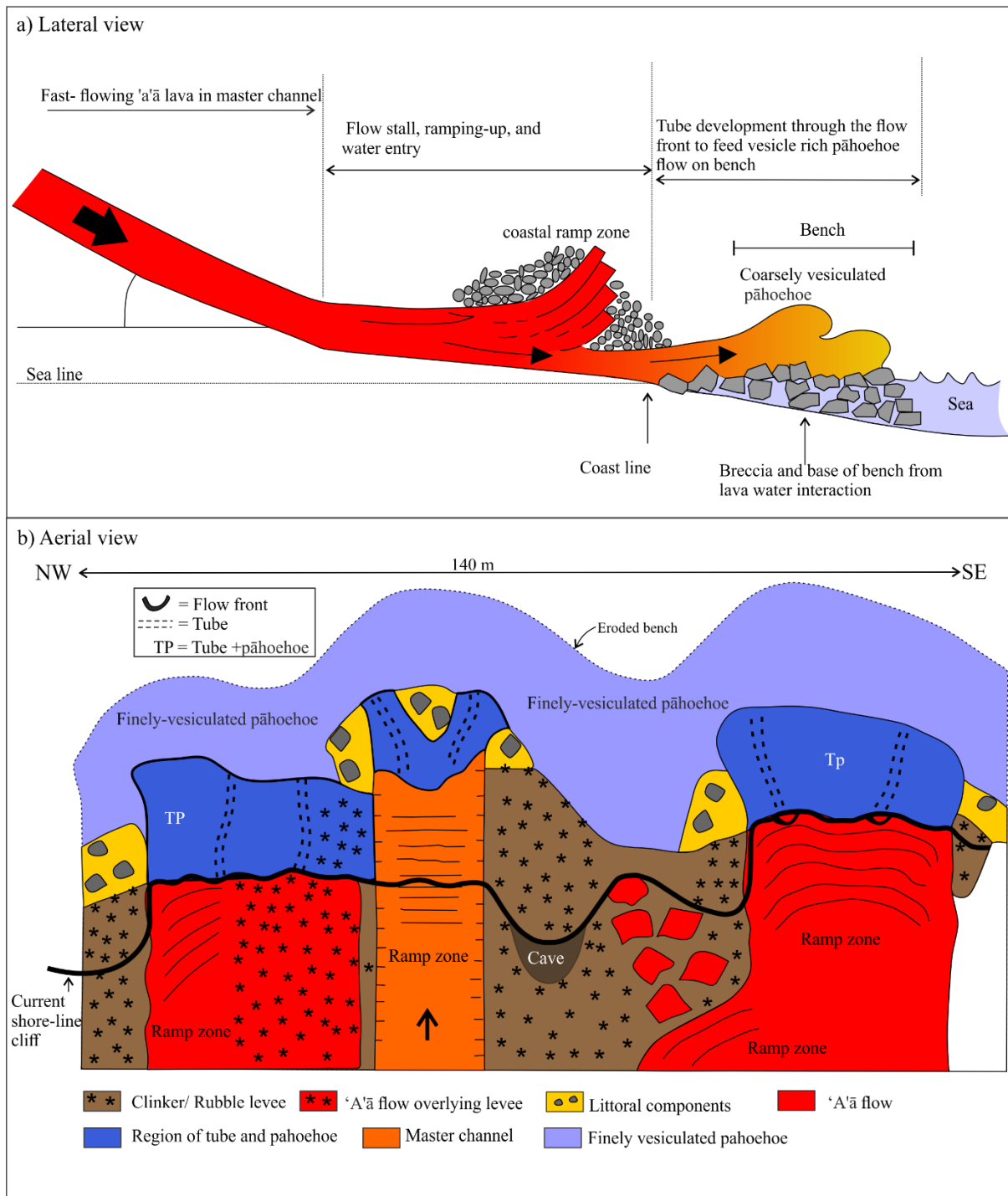
Figure 5. 14. Schematic illustration showing **a)** lateral and **b)** aerial views of lava entry into the ocean and the spatial distribution of associated major lava flow components.

In the direction of the ocean entry, the defined major components of the morphological system are organized in the following sequence: channels, littoral, ramps, tubes and pāhoehoe (Figure 5.14). While the porosity-connectivity distribution allowed us to associate ramps with channels, tubes are associated with the pāhoehoe. In addition, clast count allowed us to infer that the now eroded bench was dominated by vesicular pāhoehoe. The initial lava flow in the

master channel was followed by the ramp formation and later the tube developed at the flow front to feed vesicle–rich pāhoehoe flow (Figure 5.14).

Although the overall vesicularity of the lava depends mainly on the initial vesicle distribution, this can be modified later by various factors, including the cooling conditions (Cashman and Kauahikaua, 1997). The variability in vesicle concentration within the SB lava flow field is also linked to its cooling conditions. The higher proportion of finely vesicular lava observed in the northwest lateral margin of the SB lava flow field (Flow 12) can be attributed to the rapid cooling process due to the absence of adjacent lava flows along the northwest edge of the lava delta. Instead, the presence of coarse vesicles in the central to SE lateral section of the lava is attributed to a pre-existing pāhoehoe lava flow to the right of L1 (L13 - L16). Here, L1 undergoes a more gradual cooling process due to the presence of adjacent pāhoehoe lava to the east (Calvari et al., 2023), allowing sufficient time for vesicle nucleation and growth.

The spatial and temporal organisation of different components can be traced by the porosity distribution. Channels and ramps with low porosity tend to be prevalent further from the zone of lava-water interaction, whereas tubes and inflated pāhoehoe, characterized by higher porosity, occur mainly within the zone of lava-water interaction. Further, the connectivity distribution of the ramp and channel-levee shows a small dispersion compared to the tube and pāhoehoe, where connectivity $\sim$ 1, with no dispersion - suggesting that the vesicles have sufficient time to expand and coalesce to form connected vesicles (Sahagian, 1985). The lava components are thus systematically organized in the flow direction, with ramping and channels being dominant inland, tubes and littoral part at the coastline, and inflated pāhoehoe off-shore (Figure 5.14).

5.3.3 Ocean entry model

The SB lava flow field of Stromboli is a natural laboratory to study the 'a'ā lava flow entry to the sea and the associated formation of different components. Previously, Bosman et al. (2014) documented 'a'ā lava entry from Stromboli volcano during the 2007 eruption, describing the morphological evolution of the lava delta and the dynamics of submarine 'a'ā lava flow emplacement. Unlike pāhoehoe lava, which tends to fragment upon contact with water, 'a'ā lava can intrude water and hold its structure over a considerable distance (Stevenson et al., 2012). Despite this, most studies of lava-water interaction focus on pāhoehoe lava (e.g., Moore et al., 1973; Tribble, 1991; Dundas et al., 2020).

The two possible interpretations of the ocean entry model for the SB lava flow field are shown in Figures 5.15a and b. Model 1 is characterized by a channel-fed 'a'ā lava flow spreading at a low rate, that stops before the coast (Figure 5.15a-i). Here, the initial sanidine-rich flow descends the slope, and upon reaching the break-in slope, the flow slows down, and the flow front stops (Figure 5.15a-i). Continued magma supply to the distal section causes further lava flow inflation and thickening, along with the ramping up of subsequent pulses behind the statically inflated lava flow front. This stage marks the initiation of a ramp (Figure 5.15a-ii). The later lava flow is sanidine poor, and the continuous lava supply causes the flow front to fail and feed the pāhoehoe bench (Figure 5.15a-iii). During this period, the upper crust forms a roof over the flowing lava to facilitate closed channel flow. Later, tubes form at the flow front to feed the lava bench, and the already developed field of blocks breaches the sea level, allowing pāhoehoe to flow without water interaction (Figure 5.15a-iv). The final stage exposes the present shoreline, formed after 2-4 ka of erosion of the lava bench, comprising fine- and coarse-dominated pāhoehoe lava flows with lava tubes, and 'a'ā lava ramps behind (Figure 5.15a-v).
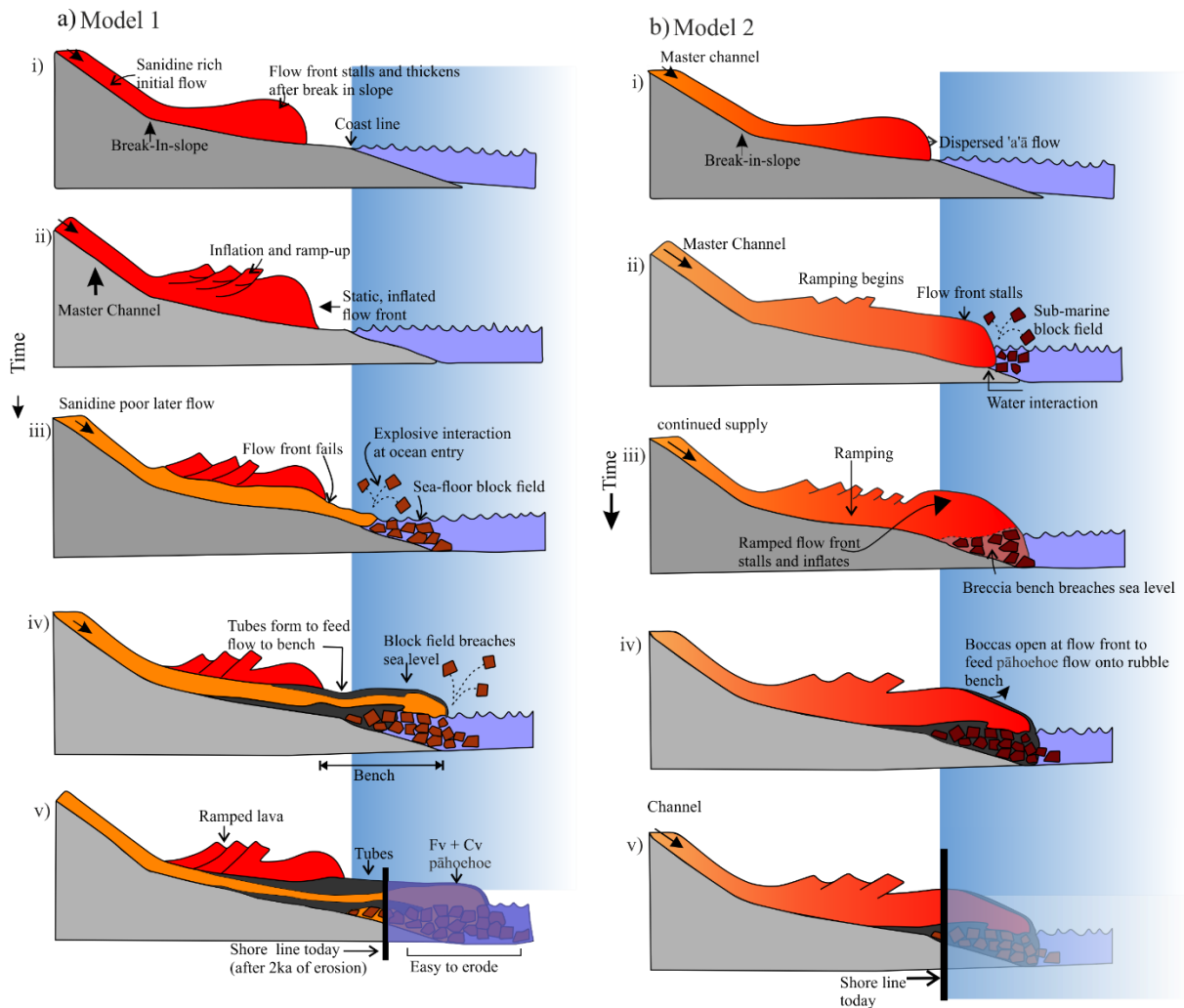
Figure 5. 15. Sea entry models where **a)** the channel fed 'a'ā that stops before the coast and **b)** the channel fed 'a'ā with a high effusion rate that crosses the coastline. Cv and Fv are coarsely and finely vesiculated pāhoehoe respectively. In **a)** the red colour represent sanidine-rich lava, while the orange shades indicate lava with lower sanidine content. In **b),** the color gradient illustrates the temperature gradient resulting from lava solidification.

The second model of 'a'ā lava flow entry (Model 2) is characterized by a channel-fed 'a'ā with high effusion rate crossing the surface zone (Figure 5.15b-i). The fast-moving lava flow on the slope begins to disperse when it encounters the break-in slope, marking the start of ramping. Meanwhile, the interaction of the 'a'ā lava with the sea-water creates a submarine block field (Figures 5.15bi-ii). The high effusion rate causes the formation of left bank (LB) and right bank (RB) rubble levees around the main channel as the ramping continues. The channel cuts through the surface zone, forming a submarine block field due to lava-water interaction. The continuous lava supply creates the breccia bench that accumulates at the sea level. Later, boccas open at the stalled flow front to feed the pāhoehoe flow onto the breccia bench as the lava continues to flow (Figures 5.15biii-iv). Finally, erosion exposes the ramped 'a'ā lava flow with distal pāhoehoe flow lobes.

5.4 Summary

Using the sea-entry lava of Stromboli's SB eruption, we were able to define the main components of a lava delta fed by 'a'ā lava flows. There are a) channels, b) littoral units, c) ramps, d) lava tubes, and e) inflated pāhoehoe lava flows. The spatial organization of these components allowed us to build a model for 'a'ā lava flows entering a water body which is characterized by three main phases. The initial stage corresponds to the entry of channel-fed 'a'ā lava flow into the sea which, as in the case of pāhoehoe, fragments to form metric blocks of 'a'ā. Continued lava supply to the foreshore causes units to stall while spreading over this substrate. Subsequent 'a'ā lava flow units ramp up behind the stalled flow front barrier, creating a degassed ponded volume. Lava tubes extending through the stalled flow barrier feed the seaward extension of a pāhoehoe bench.

As in the case of Hawaii for pāhoehoe-fed benches, at Stromboli, our 'a'ā-fed bench is exceeding unstable and easy to erode, as witnessed by its erosion by wave action in the 2-4 ka since emplacement. Our model is thus one for 'a'ā lava flow arriving at a break-in-slope (from steep to shallow) at a coast, a situation which is common at many island volcanoes. Our model may thus serve as a guide for such 'a'ā lava flow water-entry conditions

Chapter 6

THIRD STUDY: SCIENCE TO SOCIETY

The contents of this chapter have been submitted for publication under the title _'Creating a sense of intangible science: making it understandable to a broad public via Geoheritage'_.

6.1 Introduction

Scientific information is often arcane, clouded in jargon, or marked by complex formulations. These are either built up by esoteric scientific communities or in some cases are, by their nature, difficult and complicated subjects, and techniques. This situation blocks a greater understanding of the science by a wider community, reducing its usefulness and its impact. It can even generate distrust and rejection of ideas and of scientists. It can also inhibit new ideas that might grow from a wider airing of the subject, as the more widely concepts are discussed, the more general inspiration can be generated.

One way to open up science and break down barriers is to use day-to-day features in normal life, which is the object of scientific study. In geosciences, the outcrop is the primary object, and rocks form part of most people's daily life, in one way or another. The description and communication of such outcrops is geoheritage and which provides methods that link geosciences and society. This link, through the use of such geosites, can be used to deal with this esoteric problem. We explore this with a particularly intangible arcane subject, 'AMS'. We develop a simplified way of explaining it, combine this with a geoheritage inventory for three sites, and then explore how to present AMS to the public.

A geosite is a site of geological interest that, in many cases can be part of popular culture, and can be a valuable touristic destination for people both locally and internationally (Dowling and Newsone, 2006; Suzuki and Takagi, 2018;). Examples of such geosites are The Grand Canyon in the USA, The Anashauyco Quarries of Arequipa, Peru, Tana Island in the Pacific state of Vanuatu, and the Afar Depression in Ethiopia. These are all IUGS Global Geosites (IUGS 2022).

Geosites form the basic building blocks for the geological significance of UNESCO Global Geoparks (UNESCO Global Geopark Statutes -

https://www.unesco.org/en/iggp/geoparks/council). Many states now have national geoheritage inventories of geosites, that are strongly based on their scientific importance. Also, geosites are used widely to transmit geoscientific information, usually with interpretation panels, supporting literature, and guides. This is the environment in which arcane science can be included and gain more understandability.

While many geosites are recognised principally for their scientific values, more than half of the tourists who visit them do so for their aesthetic or scenic values (Allan et al., 2015). Science is thus, generally not the most interesting part of such sites to the general public. This could be because science only is part of a site's significance (something not always appreciated by the scientist), but it also is because any scientific communication is more often than not poorly adapted to a broad audience. Even when people try to seek out and understand scientific information concerning the place they are about to visit, the scientific content they might find is often mostly scientific papers, which are difficult for a normal person (non-technical, non-scientific background) to interpret. Scientists also create language barriers by making their own jargon and writing in ways that are not accessible to most other people and then have problems rewording this information into generally intelligible forms.

In order to break out of this esoteric trap, scientists, and any 'expert' for that matter need to find an accessible way to explain their work. This is where it becomes necessary to work out what an 'explanation' really is (Khalifa, 2013). An explanation should fit the receiver, only then further dialogue is possible. You can explain a fact at different levels and using different examples, depending on the receiver's background and their capability to understand the message. It also helps the teller, who is aided by the simplicity of the message. For example, there is always a difference in explaining how Earth formed to a 5-year-old and a 30-year-old, or someone at work or a holidaymaker. In addition, esoteric scientists often have more difficulty than a broader-based communicator in telling their story, as their message can be clouded in complex jargon.

Similarly, the scientific processes and techniques should be explained on a different basis to a person with a science background and without a science background. Even a scientist who does not have a specific background in a specific subject or technique needs to start in a simple manner. In addition, specialised scientists can better understand their work with simple explanations that allow them to see around their subject.

If we bridge the gap between the scientific and non-scientific communities, specialists, and generalists, it would be much easier to bring scientific works to a larger audience and to allow the larger audience to contribute to science.

We are starting with a technique whose very name is difficult even for geoscientists, which is reduced to an acronym partly due to the difficulty of grasping the meaning of the technique, yet the technique is exceptionally useful and powerful in showing important things that could be useful for people to understand. Thus, we look at ways to introduce and explain the results, and techniques of Anisotropy of Magnetic Susceptibility (AMS) and its application in three different geological sites in a simpler and layered way, so that people who visit the geosite and who have no scientific background can understand the scientific explanation for the geosite in addition to its aesthetic beauty.

What is Anisotropy of Magnetic Susceptibility (AMS)?

Anisotropy of Magnetic Susceptibility (AMS) is a rapid and effective scientific method used to find the orientation of magnetic minerals, and this indirectly can be used to infer the past flow of rocks. Simply put, AMS can be defined as a magnetic pointer that shows the direction that magnetic minerals point to. AMS has been used in different fields, including structural geology, tectonics, volcanology, sedimentology, oceanography, and palaeomagnetism (Graham, 1954; Granar, 1958; Fuller, 1963; Khan, 1962; Kent and Lowrie, 1975; Bouchez, 1997; Wassmer et al., 2010; Zhu et al., 2012). In addition to these fields, magnetic susceptibility is used in environmental pollution studies (Bityukova et al., 1999), paleoclimate studies (Franco et al., 2013), and paleoenvironmental studies (Ellwood, 1980; Matasova et al., 2001).

Even though AMS is one of the most widely applied techniques in geoscience, the concept is very difficult for people to grasp, even for those from the scientific community, and AMS researchers have difficulty in communicating their method.

We use three geological sites where we have done AMS work in order to develop and test a communication method. One site is a highly inaccessible part of Mount Etna (Sicily, Italy), another a beach tourist-frequented area of Stromboli Island (Aeolian Islands, Italy), and the third an area near Saint Néctaire, Massif Central, France, where tourism is mainly related to walking and visits to cheese farms. These sites are:

1) Mount Calanna dyke swarm of Mount Etna (Italy): despite being a small dyke swarm, covering an area of about 0.7 km^2 and located southeast of Mount Etna, Mount Calanna is an important geological site to study dyke emplacement mechanisms and the former magma chamber position of Mount Etna (Figure 6.1). At the same time, the volcanic evolution of the Monte Calanna within Mount Etna succession is still a discussion among those experts who have been working on Mount Etna (Romano and Guest, 1979; McGuire, 1982; Romano, 1982; Ferrari et al., 1989; Ferlito and Nicotra, 2010; Nicotra et al., 2011). But owing to the poor accessibility and high alteration of country rock and dykes, which mask the original lithology, it is difficult to explore Monte Calanna. The geotourism potential of Monte Calanna is very low/null due to the difficulty of reaching the site, yet we would like to be able to explain why the site is important to the history of Mount Etna to a broad public. Furthermore, as Mount Calanna is being covered by the recent eruption of Mount Etna, it is high time to conduct a thorough study of the area.
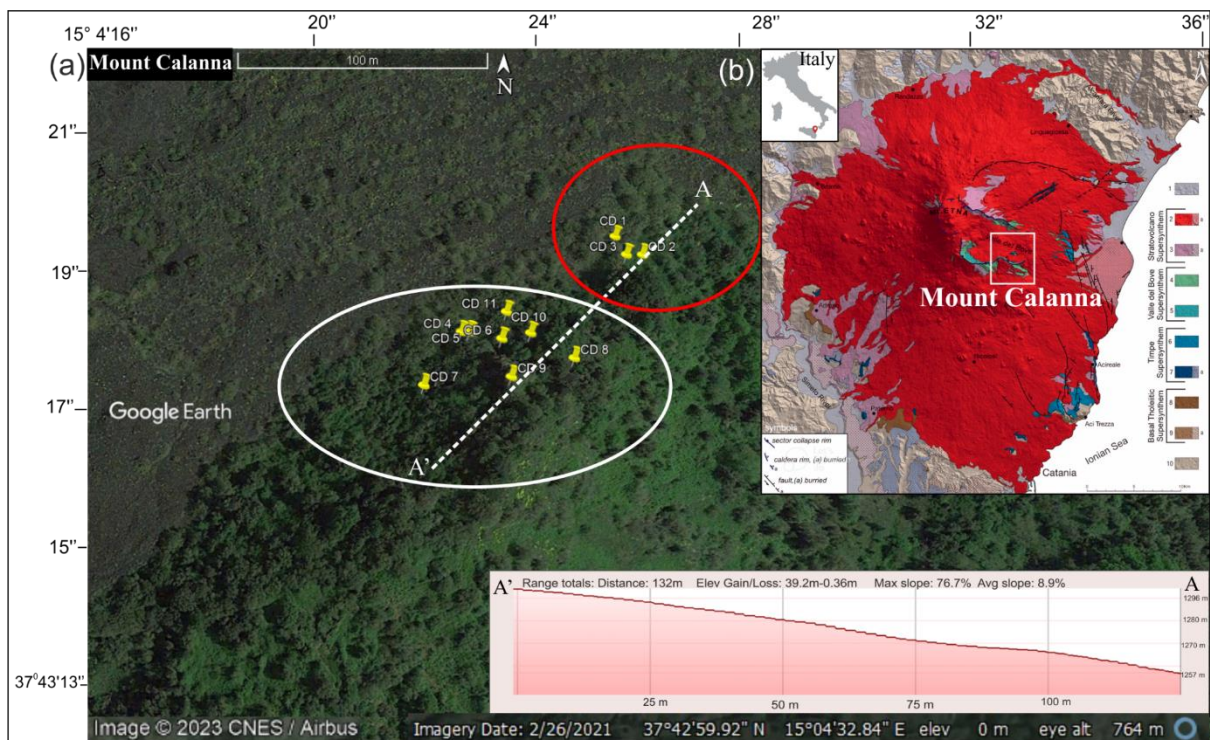
Figure 6. 1. a) Google Earth image depicting the northeastern part of Mount Calanna with geosites marked. **b)** Digital elevation model of Mount Etna with the position of Mount Calanna within the context of Italy (left top inset) (modified after Branca et al., 2011).

2) San Bartolo lava flow of Stromboli (Italy): it is a lava field in the NE part of Stromboli island (Figure 6.2). The entrainment of lava into the sea and the formation of various lava components make San Bartolo an optimal laboratory for geologists, particularly field volcanologists. In

addition, the establishment of one of the island's two townships on the San Bartolo lava field turns it into an important site for locals as well as tourists. More than 70 percent of the island's tourism surrounds this area. So far, tourists might pass by the lavas without a thought, yet some are also attracted to the rocky coast. Our objective here is to render this coast understandable and thus more interesting and potentially more beautiful. We would thus like for the geoheritage to be preserved for not only the esoteric science but for a broader understanding of the place.
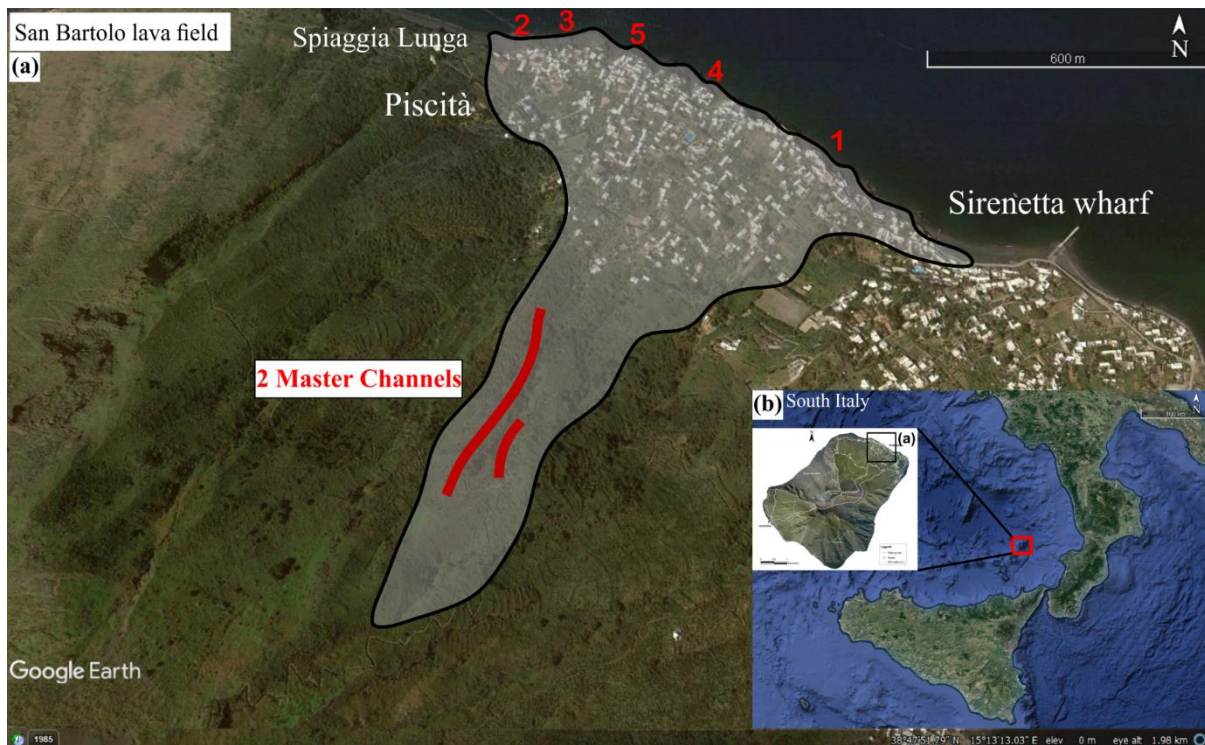
Figure 6. 2. a) Google Earth image illustrating the lateral extent of the San Bartolo lava flow field in the north-eastern part of Stromboli Volcano, with the geosites' locations marked in red (modified after Calvari et al., 2023). **b)** Google Earth image depicting the position of Stromboli volcano within the context of Southern Italy

3) Thones le Vieux and Thones le Farges of Saint-Nectaire, Massif Central of France (Figure 6.3). This is a volcanic setting related, geographically and geologically, to the Massif Central (France). The two different lava successions of Saint-Nectaire are located in the eastern distal sectors of the volcanic complex of Mont Dore, about 20 km east of the Puy de Sancy, between the municipal territories of Saint Nectaire and Grandeyrolles. Saint Nectaire has several geological sites of scientific importance as well as tourist appeal.
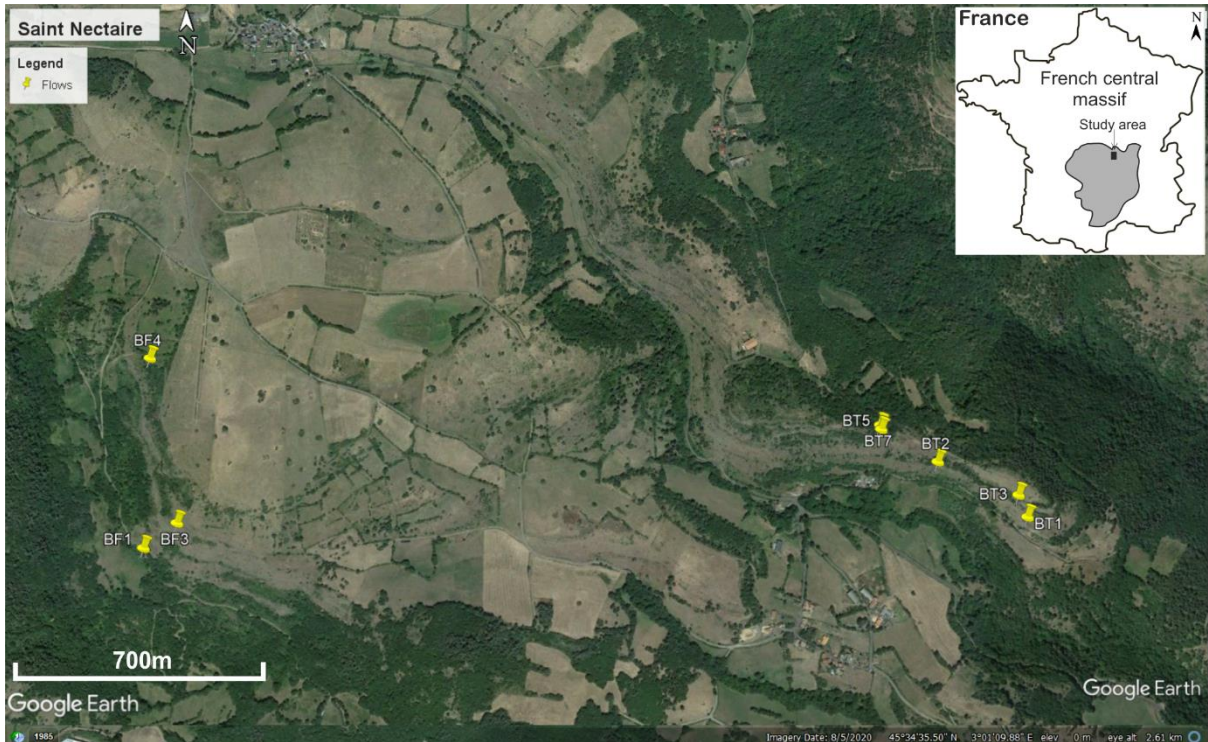
Figure 6. 3. Google Earth image displaying Thones le Vieux (BT) and Thones le Farges (BF) with the designated geosites marked. The top right inset provides the geosite's location within the context of the French Massif Central.

We used AMS on the igneous rocks of all the geological sites described above for various specific geoscience questions. In doing this, we also built a robust geological field and geoheritage inventory as the fieldwork was conducted. The AMS work was added to this, alongside petrological and geochemical information, to make a narrative, to explain the AMS results and technique in a simpler way.

We then explored how this could help local people and tourists understand the local geology and the scientific explanation obtained with AMS. Besides giving a scientific background to tourists and connecting people to their local geology, our study could help normal people get a global awareness of the importance of geosite protection, as the understanding of their scientific significance can lead to the appreciation of an object.

During writing, this process became even more important to us, when on one site, locals complained about the drill holes, which they felt were damaging the beauty of their rocks. Not only did the holes have to be filled back in and hidden, but their importance had to be communicated. This shows that it is good practice to talk to locals and to have a clear explanation of the work for them to appreciate. The scientist should always be sensitive to the needs of the local environment, social, culture and nature, and respect them.

6.2 Methodology

The first step in our process is to find ways to make AMS easy to understand. Then, we wanted to test this on 'naif' people and experts, to see if the message was working. Then, we integrated this into the framework of a geoheritage inventory that was used to choose the best sites for displaying information, and then this allowed us to pick out the salient aspects to use for clear communication.

6.2.1   Making AMS Easy

Making AMS 'easy' is *not* easy. It is not simple to explain one of the most advanced and sensitive techniques in rock magnetism. As pointed out in the introduction, it is always important to understand the background of the target public before giving a definition. Accordingly, to target a wide audience, as well as the more knowledgeable, we developed explanations at three different levels - going from highly simple and general, to highly specific and technical. This is one of the best approaches we have discovered after discussions with teaching staff and communicators with expertise in general public communication. The levels are:

1. The first level has no need for prior knowledge of magnetism and volcanic settings. Here, we have made a simple and easy-to-understand explanation for anyone, school students, locals, and tourists with no scientific background, and it also works for more, so-called 'educated' people to grasp the simplicity of the concept. This can also be done visually, with a simple demonstrative experiment.
2. The second level relates to knowledge of magnetism, particularly magnetism in rocks. These concepts can be introduced after the first message is received and understood.
3. The third level used information and concepts adapted for scientists and any experts who work in different fields or for people who have taken a real interest and developed an understanding through the first steps. Going back to the initial step can always help in understanding the concepts at this detailed level.

The idea of putting simple experimental explanation, and visualization before the theory is following the Confucius quote, 'I hear and I forget. I see and I remember. I do and I understand'. It is reversed, and the doing comes first, then the seeing, then the theory. Even if the latter is

forgotten, the other two form a sound base for understanding, and deliver the important basic message.

6.2.2   Understanding the Audience

The subsequent step was to understand better the background of the target audience. For this purpose, we prepared a questionnaire with different levels of questions. Our primary targets were natives, tourists, and scientific experts. The questions asked to the natives and tourists were not directly addressing the concept of AMS, but rather to check basic knowledge about the geological environment in which they live or visit and to learn whether they know the scientific explanation for its formation. This part was done, as much as possible while doing fieldwork in informal discussions. Explaining the AMS technique in a simpler way would make more sense to them and could easily relate to what they see. We have done this during field visits to the areas. In addition, among scientists and those from a research background, we circulated a questionnaire to check the concept of AMS and its application.

6.2.3   Making a Geoheritage Inventory

An inventory allows information to be ordered and structured in a way that makes it useful. In this case, the mass of observational fieldwork and AMS data is collated and structured, to be able to use it for the communication of AMS. The inventory can also be used for protection, management and other uses. The method we chose for our inventories was the Modified Geoheritage Assessment Method (Tomic and Bozic, 2014; Jonić, 2018), generally called M-GAM, which allows a quick and well-structured data set to be ordered.

The first step was to use the extensive field descriptions for each area to identify and describe the main geosites. That information is used in each case to give values to each geosite for values, such as rarity, representativeness, scientific value (established as in quantity of published information, and AMS value), educational, touristic, aesthetic and cultural aspects. This information forms the core of the inventory, and its use allows geosites with good value to be chosen for the next step of integrating the AMS message.

6.2.4   Integrating explanation and inventory results

This final step matches the inventory and the AMS explanations. A first search is done to find the geosites that most clearly illustrate the AMS processes and features. A second search takes

the best geosites from a didactic point of view, which are also accessible, visible, visited, and safe for the general public. Cross-matching the two allows for a short list of the very best sites to be chosen for communication and provides the background information to be integrated with the explanations. Finally, the explanations should be put in the context of each chosen geosite and the communication prepared (poster, guide explanation, information panels website information, etc.)

6.3 Results

6.3.1 *Construction of the explanations for AMS*

a) First level - doing

For this first level, we have a simple, practical experiment, which can be done with any at-hand everyday materials. Formally, it could be done by a guide, or could be done following a simple set of graphic instructions, in printed format, or as a small video.

Basic concept: Things flow down slopes, and anything in it will point the way it's flowing. We initially made a simple and basic experiment, showing honey (it can be another liquid, but honey flows slowly enough to see the changes) flowing down a slope.

1. In a very basic case, pouring the honey, we ask people to say in which direction the honey is flowing (Figure 6.4a). They can see it move, so this is easy. But then, if you hide all but part of the flow, they can see that it is not so easy now.
2. Then, honey with little sugar 'hundreds and thousands of sprinkles are poured, and these align with the flow (Figure 6.4b). These are analogous to the magnetic minerals in the lava.

So, the concept of flow markers by crystals is introduced. At this point, a magnet can be shown to indicate that in a lava, there are little magnetic crystals. And that even if you don't see them, you can measure their magnetic direction and find the flow direction. A compass can be used as a rudimentary magnetometer, to show how a magnetic mineral can be detected.
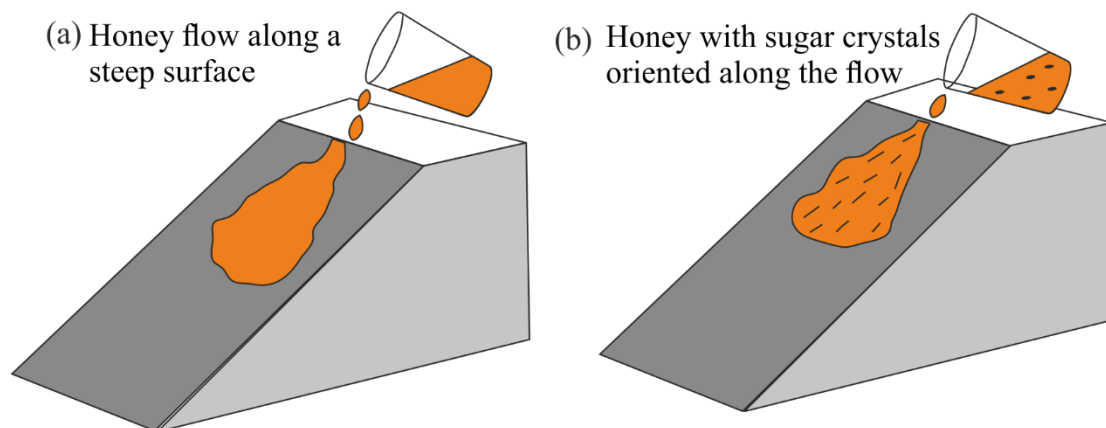
Figure 6. 4. a) Initial stage of the experiment involving the pouring of honey along a sloped surface. **b)** Subsequent introduction of sugar crystals into the honey, resulting in crystal flow and orientation along the honey flow. It could even be done with water on a rock slab, right in the field.

People doing the experiments now have a simple and practical model in their mind's eye, to understand the very basics of AMS. It can help them now to understand simply how the lava flow/dyke they see was flowing, through AMS. In this way, when anybody who has done this experiment hears AMS, they can understand the simple and basic concept behind that. They can think AMS - 'ah! Flow direction detected by measuring magnetic minerals'.

The same experiment and explanation can also be done at the start of level two and level three, as it is always easy to start from a simple 'doing' case, regardless of the target group. In these two cases, however, the concept of explanation becomes more in-depth.

b) Second level - seeing

In the second level, following the introduction with the basic first level experiment, a scientific interpretation of the process is given. This explanation revolves around the principles of magnetic susceptibility and the magnetic properties of rocks. To begin with, the initial honey experiment is reproduced, but with a slight modification.

Instead of pouring the honey onto a sloping surface, it is poured onto a flat surface. In this context, it is not easy to assess the actual direction of flow until the flow itself is observed. However, the honey is then given bubbles (blown in with a straw, or just made by stirring rigorously). Then the honey is poured again (Figure 6.5a). This time not only can they see the way it is flowing, but they also see the progressive stretching and alignment of the bubble in the flow direction - showing the way (Figure 6.5b).

(a) Initial stage of honey with bubbles

(b) Streached bubbles on honey due to the flow

(c) Lava flow with oriented 'bubbles' defined by magnetic susceptability
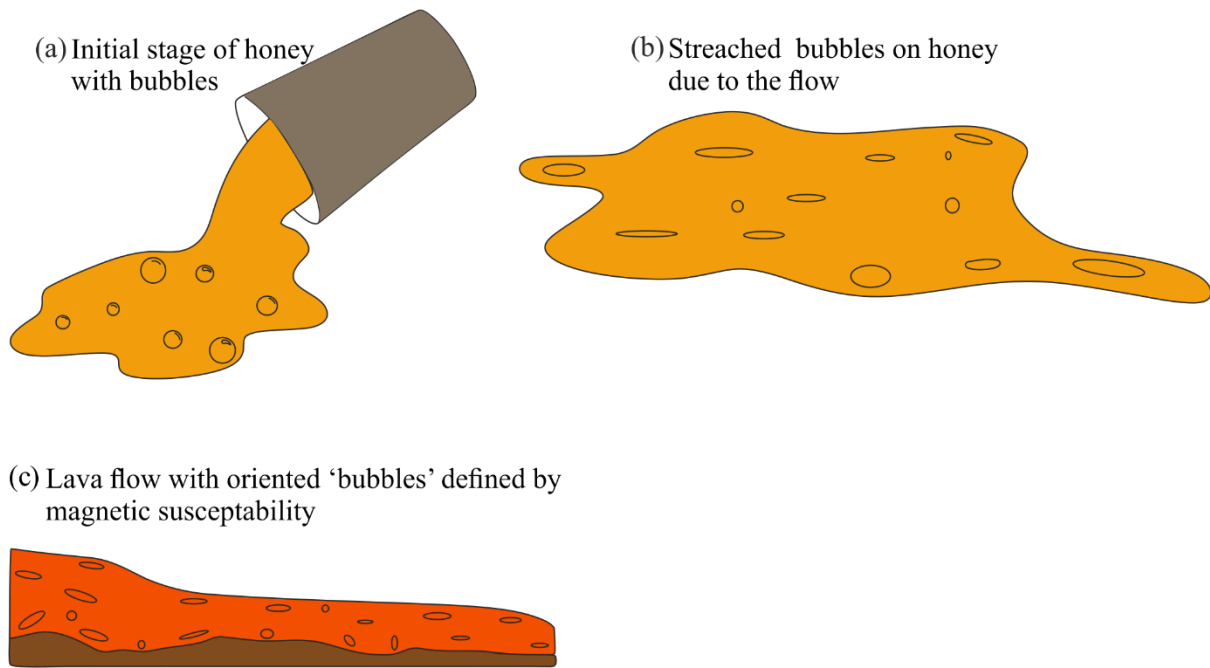
Figure 6. 5. a) Early stage of the experiment showing the honey being poured onto a flat surface with bubbles. You can see the spherical bubbles as the honey hasn't started to move yet. **b)** The bubbles in the honey started to stretch and orient themselves as the honey started to flow. **c)** Schematic diagram showing the distribution of the 'magnetic' 3D bubbles in the lava, which is also the orientation of actual bubbles (vesicles, as geologists call them).

Analogous processes occur within rocks during lava and magma flow. Assuming that each magnetic mineral is an independent bubble, where the 'bubble' is defined by the orientation and magnitude of magnetic property, then the orientation of the bubble can indicate the direction of flow (Figure 6.5c). This magnetic property, which defines the magnitude and direction of the 3D bubble, is called the magnetic susceptibility (K). In other words, it can be explained as a measure of how much (strength) and in which direction (orientation) a magnetic material is magnetised. So, it is the property of the material, i.e., it is specific to each material. Different crystals have different susceptibilities - Iron-rich minerals like magnetite are more susceptible, while those that have little magnetic material, such as feldspar or quartz are not susceptible. Not only does it measure the strength of the response, but also it can have a direction of a particular mineral (not to be confused with the magnetic field shown by the compass).

The length, width, and height of the 'bubble' are indirectly determined by the strength and direction of the magnetic susceptibility. The shape of this 'bubble' is not defined by a single magnet, but rather by the many tiny magnetic minerals in the rock. Now, the combined strength and general direction of the individual magnetic minerals define the shape. If all the magnetic minerals have the same values for length, width, and height, they give a spherical shape (Figure

6.6a). Alternatively, if the height is greater than the width and length, it results in a prolate shape resembling a rugby ball (Figure 6.6b). Conversely, if the height is less than the width and length, the shape becomes flattened, like a disc, forming an oblate shape (Figure 6.6c).
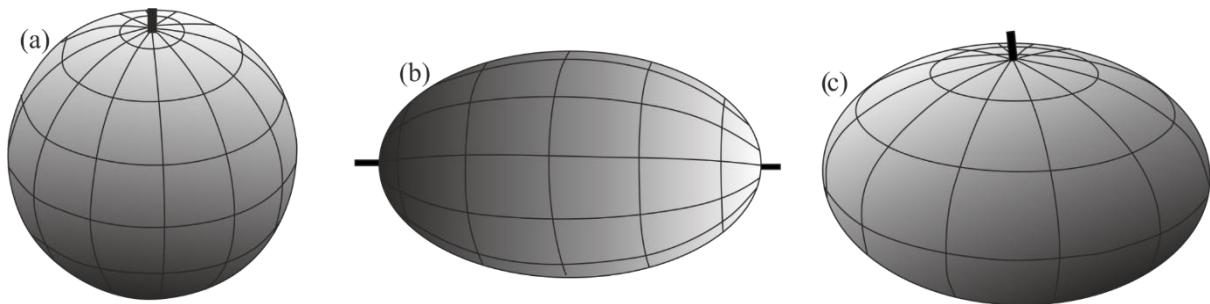
Figure 6. 6. Schematic representation of **a)** sphere, **b)** prolate, and **c)** oblate ellipsoid. These show when lava, or magma is not deformed, or is stretched in one direction, or is flattened.

c)   *Third level - theory*

For the third level, we concentrate on a more in-depth, scientific explanation of AMS with some of its applications. As mentioned before, we start with the basic experiment and theory of the first two levels, always working up to more complex from the simple.

The anisotropy of magnetic susceptibility measurement of a rock gives the results in the form of a triaxial ellipsoid (the virtual 'bubble') with the principal susceptibility axes at right angles to each other, $K_{max} > K_{int} > K_{min}$ (K_{max} = maximum susceptibility; K_{int} = intermediate susceptibility; and K_{min} = minimum susceptibility) (Figure 6.7). K_{max} defines the magnetic lineation and the K_{max}-K_{int} plane defines the magnetic foliation (Figure 6.7).
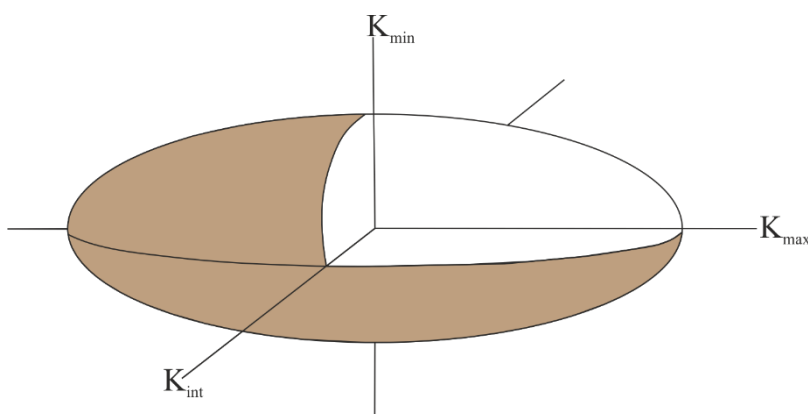
Figure 6. 7. Ellipsoid of magnetic susceptibility with the principal susceptibility axes.

Various quantitative (= scalar = measurable) parameters can be derived from these susceptibility axes to define the AMS ellipsoid, such as the mean susceptibility (K_{mean}), the

corrected degree of anisotropy (Pj), the shape parameter (T) and the magnitude of lineation (L) and foliation (F) (Jelinek, 1981; Borradaile and Jackson, 2004; Cañón-Tapia and Chávez-Álvarez, 2004).

K_{mean} gives the arithmetic mean of the principal susceptibility axes, Pj defines the degree of anisotropy and T gives the shape of the AMS ellipsoid, where T can vary from +1 (oblate) to -1 (prolate). The distribution of the susceptibility axes on an equal-area projection of the lower hemisphere allows the direction of flow to be determined (Figures 6.8b and c). The interpretation of the flow direction is not always straightforward, it requires a thorough study of the type of magnetic phase, magnetic domain, post-emplacement process, and so on.

Coming back to rocks, in volcanic settings, AMS is mostly used to find the flow direction in lava flows and other volcanic processes, such as the emplacement mechanism of dykes. In a lava flow, the ferromagnetic minerals tend to orient themselves parallel to the flow direction (Figure 6.8; Tarling and Hrouda, 1993; Cañón-Tapia, 2004).

A final most advanced complication is that the interpretation can be complicated by several factors, including the prevalence of different magnetic minerals, that hold their magnetism differently. For example, single-domain (SD) magnetic grains that cause inverse magnetic fabric (they are magnetised the wrong way round!), make directional interpretation complex (Potter & Stephenson, 1988; Rochette et al., 1999).
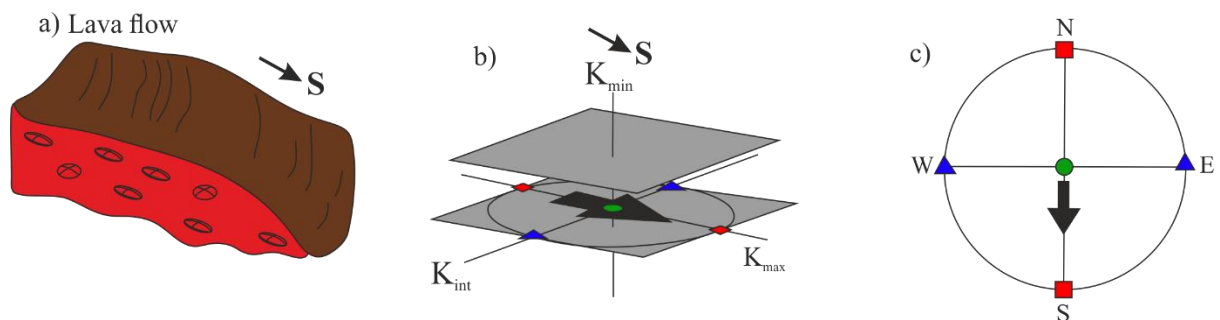
Figure 6. 8. a) Schematic diagram of south-directed lava flow showing the distribution of susceptibility ellipsoid. b) stereographic projection of the 3D ellipsoid on a plane and c) on lower hemisphere equal area projection.

6.3.2   Geoheritage Inventory

Following the methodology outlined above, we have created a robust inventory for each geosite by combining all available data. The M-GAM model allows us to quantitatively assess each geosite and to build a comprehensive framework for each geosite. The proposed inventory of

the Mount Calanna site includes ten geosites, San Bartolo includes five geosites and Saint-Nectaire includes 14 geosites.

6.3.2.1 Mont Calanna: Dykes swarm of Mount Etna, Italy

Mount Calanna dyke swarm is an isolated hill situated in the SE of Mount Etna, spanning an area of ~0.7 km^2 (Figure 6.1). The framework of Mount Calanna is formed by numerous basaltic dykes, altered and unaltered, and lava flows from ancient eruptive centres, which are completely weathered and demolished (Ferlito and Nicotra, 2010). The altered dykes have a uniform E-W orientation and belong to the Mount Calanna unit, while the unaltered dykes have a random orientation and belong to the more recent eruptive age called Mongibello (60 ka to present) (Ferlito and Nicotra, 2010). The altered dykes are mostly dissected by two sets of mutually perpendicular joints and E-W-oriented normal faults.
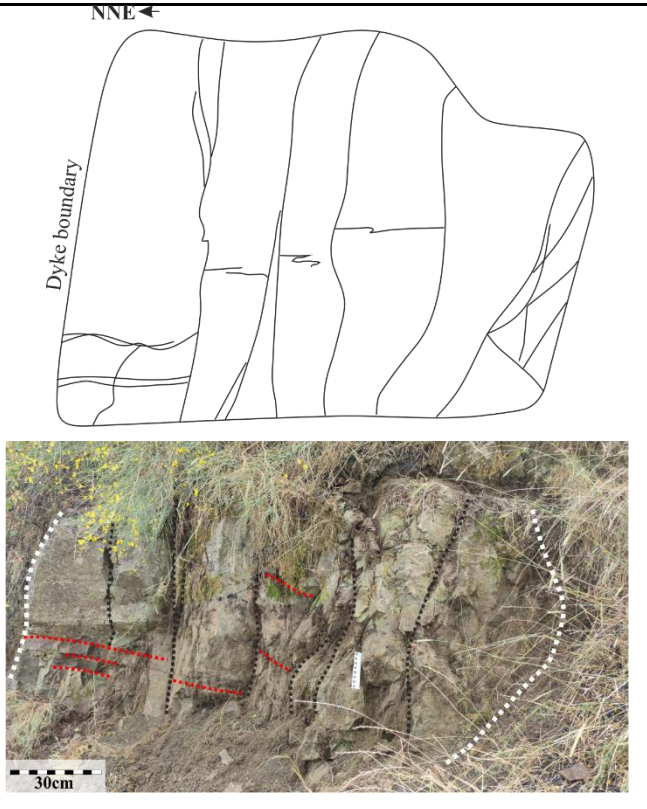
Mount Calanna hill is mostly surrounded by lava flows of different epochs, the north and west being covered by lava flows from the latest eruptions, mainly those of 1991-1993 (Figure 6.9). And the east is covered by the porphyritic lava flow from the recent dykes that erupted across Mount Calanna. Absolute dating of the Mount Calanna dykes is not possible due to their high alteration, but $^{40}Ar/^{39}Ar$ dating of a rock from the valley south of Calanna hill, called Val Calanna, gives an age of 128.7 ± 3.8 ka (Branca et al., 2008).
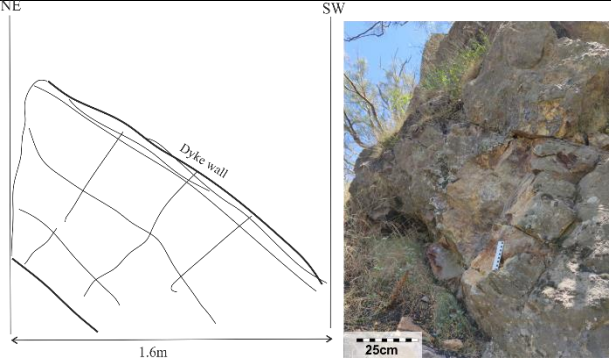
Figure 6. 9. Field Photo of Mount Calanna, which is surrounded by recent lava flow and covered by high vegetation.

This small dyke swarm of Mount Calanna gained considerable interest among geologists when Ferrari et al. (1989) presented Mount Calanna as evidence for the gravitational spreading of Etna's eastern flank due to the presence of several thrust faults. A later study by Ferlito and Nicotra (2010) contradicts this statement, where they didn't find any faulting but rather interpreted Mount Calanna as having a tensile regime of N-S extension. The unresolved question of the volcanic succession of Mount Calanna is another factor that makes this dyke interesting for researchers, given its importance in the evolution of Mount Etna (Romano and Guest, 1979; McGuire, 1982; Romano, 1982; Ferrari et al., 1989; Ferlito and Nicotra, 2010). Apart from the steep slopes and the dense vegetation that impedes access, the dykes are being covered by recent lava flows and ash falls. The study by Ferlito and Nicotra, 2010, reported the presence of more than 200 dykes on this small hill, with an intrusion intensity of up to 40%. However, the recent fieldwork carried out by us confirms that more than 90% of the dykes are under vegetation and covered by ash fall.

Table 6. 1. Short description of two representative geosites (dykes) from Mount Calanna with their field photos and sketches.

Name	Description	Field Photo
CD-1	One of the fresh dykes, sub-vertically emplaced, has a thickness of 3 m and is E-W oriented, easily accessible and visible. It is deselected by two sets of joints, sub-vertical joints oriented NW-SE and sub-horizontal joints oriented NE-SW. Magnetic fabric shows sub-vertical flow striking towards SW.	

CD-5	Altered, sub-horizontally emplaced dyke with a thickness of 1.6m. It has the local presence of pyroxene phenocryst and vesicles at the dyke centre. Two sets of joints (sub-vertical and sub-horizontal) dissected the dyke into small blocks. The dyke is quite visible, with less vegetation around. Hence it is comparatively more accessible. Magnetic fabric shows sub-horizontal flow striking NW-SE.	

We made an inventory of Mount Calanna dykes using the available data and assessed the potential of the geosite (dyke) using M-GAM. The list of two representative geosites with their main characteristics is given in Table 6.1, and the rest is compiled in Appendix Table 6.S 1. Following the standard procedure of M-GAM, we compiled the data from experts and tourists (*Im*) to produce the final ranking of the dykes of Mount Calanna to produce the M-GAM matrix (Table 6.2 and Figure 6.10). Owing to the fact that Mount Calanna is by no means a tourist place and there is no proper path to reach there, we collected the opinions of 15 people who have been to Mount Calanna before and calculated the Importance Factor (*Im*).

For the geosites in Mount Calanna, the highest-rated sub-indicators are *Representativeness* (0.9), *Environmental fitting of sites* (0.9), *Current condition* (0.9), and *Interpretative panels* (0.95) (Table 6.S 4). It is interesting to note that, apart from knowledge of geoscientific issues, all other sub-indicators of *Scientific/educational values* are deemed important for tourists. People visit Mount Calanna mainly for trekking, where they expect to be closer to nature and have the trekking experience. For this reason, the *Important road network* (0.25), *Restaurants* (0.20) and the *Additional functional values* (0.35) such as toilets and rest areas are not so important to them (Table 6.S 4).

As all the dykes have mostly the same characteristics, the results obtained show almost the same value for the *Main value* and the *Addition values* of all ten geosites. The geosites CD1 and CD2 show a slightly higher rating for the *Main value*, i.e. 3.1 and 3.2, respectively, compared to the rest of the geosites (Table 6.2). This is due to the high value of the two sub-indicators, *Representatives,* and *Knowledge of geoscientific issues*. The mean average of the

Additional value for all ten geosites has the same low value (2.16) as all the sub-indicators were rated low (Table 6.2). The geosites of Mount Calanna have been plotted on the M-GAM matrix (Figure 6.10) with means of the final value of the *Main* and *Additional values*. As expected, all ten geosites fall within the area of Z11 with a low final score for *Main* as well *Additional values.*

Table 6. 2 Final ranking of the Mount Calanna dykes by M-GAM

Geosites	CD1	CD2	CD3	CD4	CD5	CD6	CD7	CD8	CD9	CD10
Main value	3.14	3.20	2.53	2.98	2.91	2.75	2.75	2.69	2.75	2.69
Additional value	2.16	2.16	2.16	2.16	2.16	2.16	2.16	2.16	2.16	2.16
Field	Z_{11}	Z_{11}	Z_{11}	Z_{11}	Z_{11}	Z_{11}	Z_{11}	Z_{11}	Z_{11}	Z_{11}
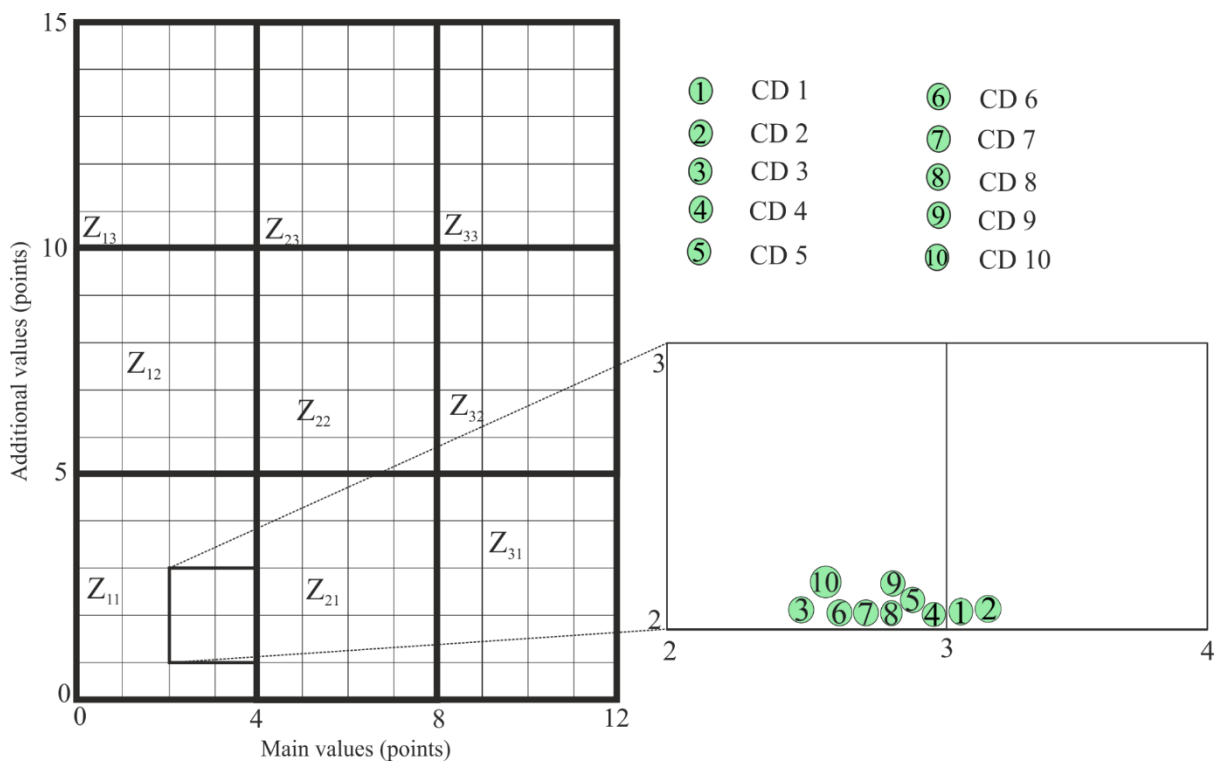
Figure 6. 10. Distribution of the geosites of Mount Calanna in the M-GAM matrix.

6.3.2.2 San Bartolo lava flow of Stromboli, Italy

Stromboli is one of the most active volcanic islands of the Aeolian archipelago, situated in the S-E of Italy (Figure 6.2). The beautifully exposed lava along the coastal line and the low-energy volcanic eruptions attract people worldwide. More than half of the total settlements are on a recent lava flow called San Bartolo, which has an age of ～2ka (Arrighi et al., 2004; Speranza

et al., 2008) and emplaced on the N-E of Stromboli. The lower part of the San Bartolo lava flow forms a delta and is characterized by the formation of several semi-arcuate structures, here called flows, at the flow front due to the interaction with the sea (Calvari et al., 2023). While San Bartolo is a site of interest to the scientific community because of its lava-sea interaction, it is also a well-liked tourist attraction because of its beautifully well-exposed beaches and surrounding landscape. The whole flow field of San Bartolo lava comprises 15 different flows, which fan out as a lobe formed by the interaction of lava with water. These flows are characterized by the presence of different lava components, mainly tube, inflated pāhoehoe, littoral, channel, and ramp components (Table 6.S 2). Here, we defined each component as an individual geosite in order to explore the geotourism potential and provide an improved management plan for geotourism. Two representative geosites with their corresponding descriptions and field photos are summarised in Table 6.3.

Table 6. 3. Short description of the proposed geosites of San Bartolo lava flow with the field photos and sketch

Name	Description	Field Photo
Inflated pāhoehoe	The classic example of an inflated pāhoehoe lava component at flow 12, which is at the SW end of the San Bartolo flow unit. The upper brittle surface crust, the massive core and, in between them, a small viscoelastic layer are clearly visible. The brittle crust was characterized by the vesiculated s-type pāhoehoe lava, while the central core has a massive, less vesiculated lava. At the surface, there are four inflated lobes, which are separated by the inflation cleft. As this geosite is at one of the main beaches in Stromboli, Spiaggia Lunga, it can be easily reachable and is well visible. Moreover, tourists mostly lounge on the spacious surface of the inflated pāhoehoe units. The process of inflation of the upper thin brittle layer is obtained from the vertical	

	magnetic foliation plane, whereas the horizontal lava flow of the lower part is obtained from the sub-horizontal magnetic foliation plane.	
Tube component	There are two tubes at Flow 1, which extends NE. The top of the tube got eroded by wave action, so the internal structure is visible and is quite preserved. The main tube has five accretionary layers and two arched-over layers. The central stream has rooted 'a'a clasts. This geosite is a good example to study the characteristic features and the formation of tube component. As the tube outcropped at the beach, it is easy to reach the geosite and is risk-free to visit and explore the site. The AMS results indicate a vertical foliation plane with flow towards south.	

In order to assess the geoheritage importance and geotourism potential of the beach at the flow front of the San Bartolo lava flow, we quantify the importance of the different components exposed there using M-GAM. The final M-GAM results with the aggregate of *Main* and *Additional values* for each geosite are given in Table 6.2 and 6.S 5. According to the tourist's evaluation of the importance of each sub-indicator (*Im*), *Scenic or aesthetic values* are of high importance compared to *Scientific and Protection values* (6.S 5). It may be that tourists' who visit a volcanic island for a beach holiday are mostly among the "general" geotourists (Božić and Tomić, 2015). Thus, they are more interested in the aesthetic value than in knowing more about the scientific importance of the geosite. In addition, tourists tend to pay little heed to

additional amenities like road networks, parking facilities, and gas stations, as they normally do not anticipate or concern themselves with such conveniences when visiting an island.

The sea entry of lava and the small beaches with caves formed by the erosion of the levee make the San Bartolo interesting to visitors from an aesthetic and bathing point of view. At the same time, the well-developed and preserved morphology of the lava and the different volcanic components due to lava-water interaction make it highly interesting to volcanologists (Calvari et al., 2023). Looking at the final M-GAM results, it is clear that there is no apparent difference in the total *Main* and *Additional values* between the individual geosites (Table 6.4). However, due to the lower representativeness and chaotic nature, littoral components have a slightly lower *Main value* (4.51). In terms of *Main values*, all the geosites show higher values due to the higher values for *Representativeness* and *Knowledge of geoscientific issues*.

From the M-GAM matrix shown in Figure 6.11, we can see that all five geosites are in the middle field (Z22) for both *Main values* and *additional values*. This clearly shows that it has the potential to attract both "general" and 'pure' geo tourists (Božić and Tomić, 2015). As all the sites are closely grouped, the inventory does not single out sites for the communication of AMS, these have to be chosen in relation to the best positioning for information.

Table 6. 4. Final ranking for the geosites from San Bartolo lava flow by M-GAM

Geosites	Tube	Inflate pāhoehoe	Littoral	Ramp	channel
Main Value	5.31	6.20	4.51	5.61	6.03
Additional value	6.23	6.64	6.29	6.13	6.44
Fields	Z22	Z22	Z22	Z11	Z22
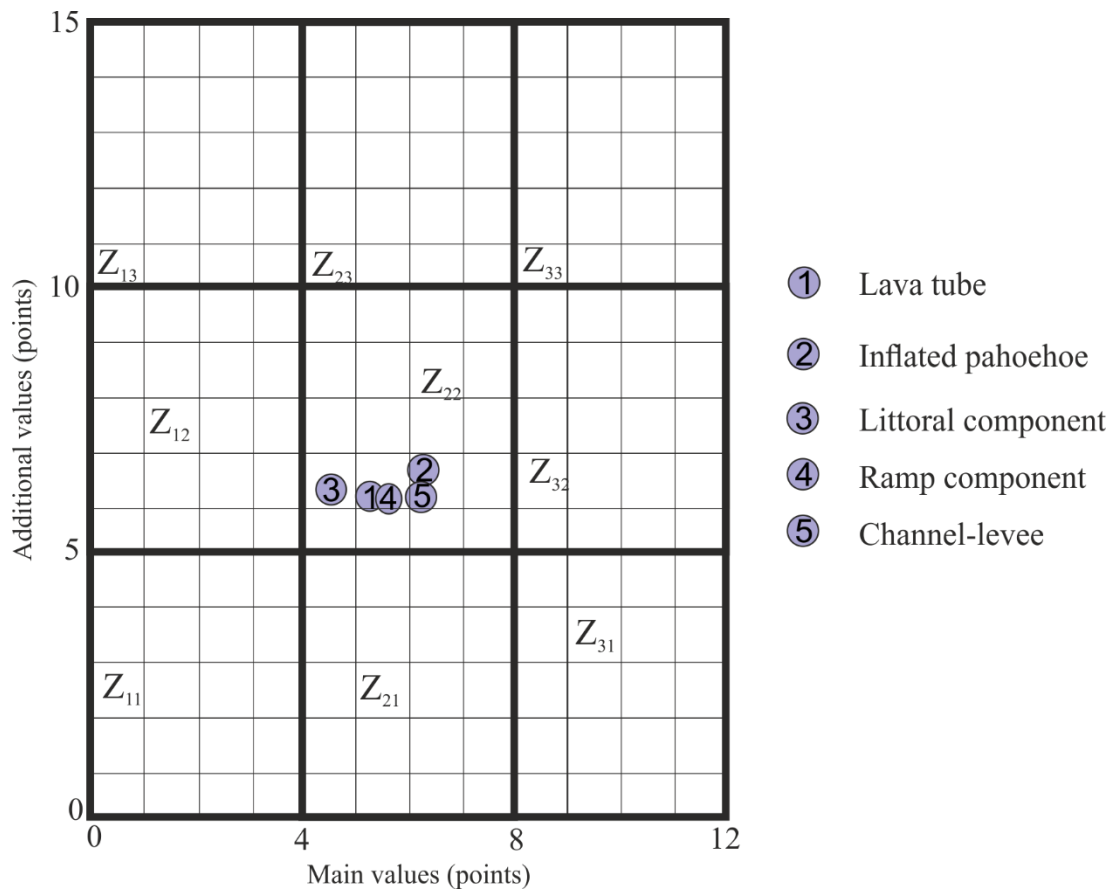
Figure 6. 11. Distribution of the geosites of San Bartolo lava flow in the M-GAM matrix.

 6.3.2.3 Thones le Vieux and Thones le Farges lava flow of Saint-Nectaire

The two lava flows of Thones le Vieux and Thones le Farges in Saint Nectaire are part of the Mont Dore-Sancy volcanic complex, which is geologically and geographically closely linked to the Massif Central, a vast mountainous and hilly area of central-southern France (Figure 6.3). The Mont Dore - Sancy complex is a composite volcanic edifice covering an area of ⁓500 km² for a volume of material produced of approximately 200 km³ (Brousse, 1971; Vincent, 1981).

The two main lava successions, a few kilometers apart, known as the Thones le Vieux and Farges series, are located in the eastern distal sectors of the Mont Dore volcanic complex. Besson (1978) dated these lavas to about 3.8 Ma from a stratigraphic comparison with lavas from the Puy de Bessoles. Lesage (2013) suggests a different of origin and flow for the Thones le Vieux and Farges series and emphasises that it is not possible to witness reliable correlations between the successions. Geochemical studies show a strong alteration in some units of the lava sequences, particularly those at the base, while the morphological and structural elements

derived from the soil analysis of the outcrops are not such as to assume any relationship between the two.

The complete succession of Thones le Vieux consists of seven units (BTn), with a total thickness of ~ 90 meters and a maximum elevation of 835 m a.s.l. The sequence constitutes an inverted relief, elongated in a WNW-ESE direction near the village of Thones le Vieux. Farges series consisting of five units (BFn). The outcrops are located southeast of the village of Farges, along the south-western escarpment of the Lacha plateau, on the road connecting the village of Farges with that of Thones le Vieux. The succession shows a thickness of about 90-100 m and culminates at about 876 m.a.s.l., 1200-1500 m from the series at Thones le Vieux.

Table 6. 5. Short description of the proposed geosite of Thones le Vieux and Farges lava sequences with the field photos.

Name	Description	Field Photo
BT4	The components are columnar of a thickness of 5 meters and at an elevation of 778 m.a.s.l, with the lavas being more vesicular than the previous ones. The columnar joints are strongly altered. The base of the wall has a centimetric layer of breccias mixed with small portions of terrigenous sediments, and the upper part of has rounded quartz fragments marking a sedimentary detrital level. The well-developed magnetic foliation plane shows a subvertical lava flow. A clear trail starting from the bottom of the lava unit takes you to BT4, as it is exposed at the top of the plateau. This geosite can be accessed by walking along the trail and is completely safe. In addition, the magnificent view of the entire Saint Nectar village makes this geosite more attractive to tourists.	
BF1	Highly altered outcrop at the base of the Farges series. This flow is lying above the granitic basement and Oligocene sediments, which are not visible because they are covered by vegetation and colluvium. The lavas present onion alteration structures at the base, followed by small columnar joints. Interestingly, at the base of the Farges series, we found a highly altered layer with hydrothermal alteration, which confirms the lower sequence of	

	BF1. AMS results gave a sub-horizontal lava flow direction with the flow striking along NW-SE.	

In our study, we evaluated eight different lava sequences, five from Thones le Vieux (BT1, BT2, BT4, BT5 and BT7) and three from Thones le Farges, (BF1, BF3 and BF4) of Saint-Nectaire, based on their outcropping. In order to obtain the opinion of visitors regarding the importance of each sub-indicator (*Im*), we conducted 15 surveys with groups of five people who discussed the site together (Table 6.S 6). According to them, the important sub-indicators are *representatives (0.89)*, *Level of interpretation (0.81)*, *Viewpoints (0.88), Surrounding landscape (0.86), and Accessibility (0.86).*

Visitors to the area are mostly local people who come for walks or short treks, and geology students, who formed a large part of each group surveyed - the others were non-geologist scientists. For them, therefore, the *Scenic or aesthetic value* is more important than *Protection*. Moreover, people who come to spend their leisure time do not pay much attention to the *Knowledge of Geoscientific issues* (0.38). It is also interesting that *Representativeness* and *Level of interpretation* have high values (> 0.80), which was not expected in this case, but probably correlated with the geological viewpoint of the public surveyed. For the visitors in Saint-Nectaire, the least interested sub-indicators are the *Annual number of organised visits* (0.12) and *Additional anthropogenic values* (0.15).

Among the described geosites in Saint Nectaire, BT1 (4.25) and BT4 (4.34) got the highest main values (Table 6.6 and Figure 6.12). This is because of the high value of *Representativeness* and *Viewpoints*. Whereas BT5 (3.09) and BF4 (3.08) have the lowest main values due to the absence of viewpoints and poor representativeness. Looking at the *Additional value*, BT1 has the highest value (3.14) owing to its highest value for *Accessibility* (0.86) as compared to the rest of the geosites (Table 6.6). It is interesting to note that, though BT4 has the highest main value, it is one of the geosites with the lower additional value. This is mainly due to the lower value for *Functional values,* especially *accessibility* (0.215).

Compared to the *Main value*, the *Additional value* shows more differences among each geosite, mainly because of their different *Representativeness*, *Level of interpretation* and *Aesthetic values*. This places the geosites in two different fields in the M-GAM matrix, with BT1 and BT3 falling in field Z21 and the remaining geosites in the Z11 field (Figure 6.12).

As the geosites have values that are grouped, so each one could serve as a site for AMS communication. However, a few stands slightly apart for main or for additional values. And these, BT1 and BT4 as well as BF1 would be the best candidates to develop.

Table 6. 6. Final ranking for the Thones le Vieux and Thones le Farges geosites using M-GAM

Geosites	BT1	BT2	BT4	BT5	BT7	BF1	BF3	BF4
Main Value	4.25	3.48	4.34	3.09	3.85	3.49	3.30	3.08
Additional Value	3.14	2.71	2.50	2.50	2.71	2.93	2.50	2.71
Field	Z21	Z11	Z21	Z11	Z11	Z11	Z11	Z11
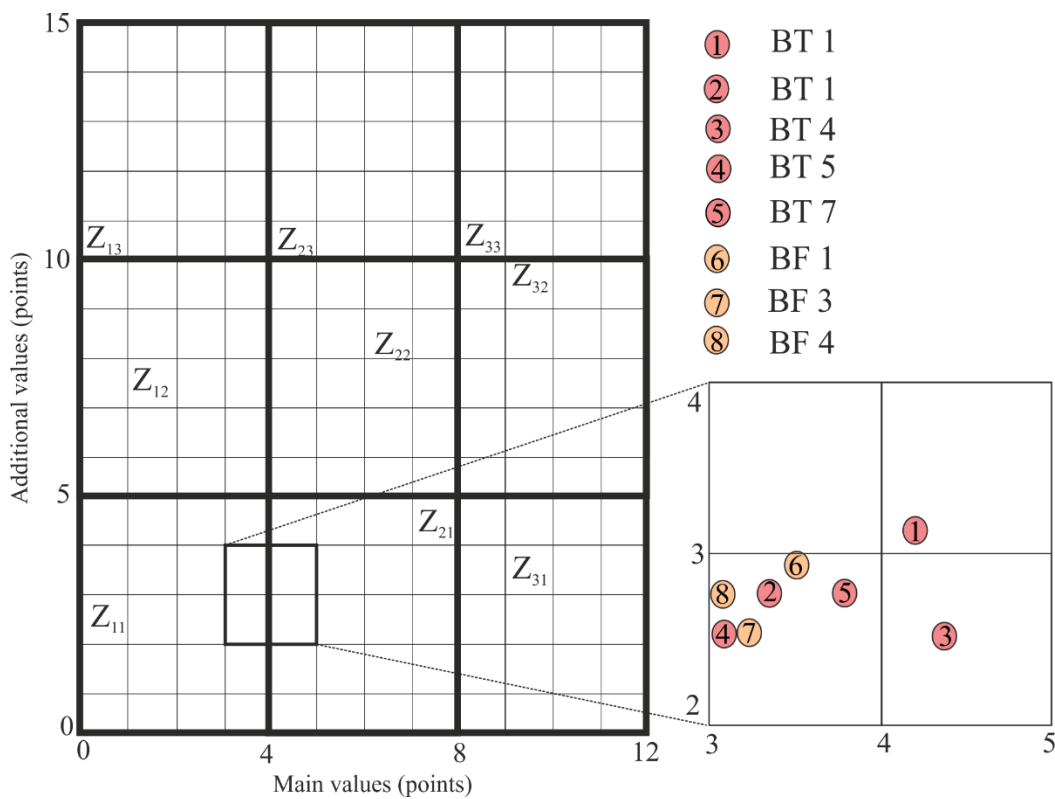
Figure 6. 12. Distribution of proposed geosites from the lava flow of Saint-Nectaire in M-GAM matrix.

6.4 Discussion

Considering first the inventory results, we discuss which sites and areas stood out for possible use in delivering the AMS message. And then suggest for each site what could be done. The practical application of this would be the logical next step to follow on from this study, and

could be done on these sites, and tested on others, possibly using also different scientific techniques that also are in need of more understanding. For example, age dating, petrological work, geochemistry, biological - geological interactions.

To ensure a fair assessment of the importance of each sub-indicator while mitigating potential biases introduced by tourist and other respondent preferences, we made a deliberate effort to encompass both "general" and "pure" geotourists. The obtained data on the importance value given by the tourists in three different geological sites show that the importance of each sub-indicator of M-GAM is totally geological site-specific. This also allowed us to classify the geotourists at these three geological sites according to Božić and Tomić (2015) classification. Visitors to Mount Calanna fall into the category of pure geotourists. The only people who visit the geosites of Mount Calanna are geologists or naive tourists (mainly adventurous trekkers) who visit for personal experience and education, mainly in the context of Mount Etna.

At the San Bartolo geosite, the main purpose of the visit is relaxation and recreation, i.e., general tourism. Incorporating scientific information presents an opportunity to appeal to both pure and general geotourists, thereby promoting geotourism.

Given that the majority of visitors to the geosites of Thones le Vieux and Thones le Farges comprise geologists conducting research, students, and local residents, the visitor demographic at these sites encompasses a combination of both "general" and "pure" geotourists. It is worth noting that, aside from the two categories mentioned above, visitors of San Nectaire include individuals from nearby villages who engage in leisurely Sunday walks. These individuals are the most frequent visitors to these geological sites.

The M-GAM matrix shows that the geosites from the three geological sites form three independent clusters (Figure 6.13). The San Bartolo geosites have medium *Main* and *Additional values*. Although the San Bartolo geosites have high *Scientific value* in terms of their representativeness and contributions to geological knowledge, there is a clear lack of enhancement in Additional values. However, the geosites could be strong contenders for geotourism potential due to their scientific and touristic interests. This is because the entire San Bartolo lava flow field offers compelling settings to study a'a lava interactions with the sea and shows the intricate dynamics of lava-water interactions. Additionally, along the San Bartolo coastline, prominent volcanic features, including ramps, lava tubes, and inflated lobes, are well-exposed, offering a valuable resource for volcanologists to learn and study. Additionally,

Stromboli Island is renowned for its tourism, particularly its beaches and volcanic trekking opportunities. Over 70% of the island's population and settlements are concentrated in the north-eastern part, in particular above the San Bartolo lava flow field. This highlights the considerable potential for geotourism and geoscience education at the San Bartolo geosites. The M-GAM suggests that by increasing the Additional values, increasing geotourism promotion (training guides, leaflets for tourist office/hotels) and tourism infrastructure (signage, and access path improvement) as well as introducing some interpretative support, with simple and attractive graphics, and QR codes for visitors to connect to information, the geotourism presence/experience can be improved. This would lead people towards the area, already armed with the idea that there is something of interest, and more able to see the rock as more than just a backdrop. Then they can be guided towards areas of geo-interest and lead towards the start of understanding the AMS.

The geosites at Mount Calanna were characterized by relatively low *Main* and *Additional values* (Figure 6.13), as expected by its remoteness, mainly due to the challenging access to the geosites, caused by poorly defined paths. In addition, Mount Calanna is mostly surrounded by recent lava flows and covered by dense vegetation and volcanic ash fall, obscuring our target geoheritage features. These constraints also prevent geologists from studying the emplacement dynamics of this small dyke swarm, which is nevertheless an important part of Etna's evolution. The M-GAM analysis shows that this area is not appropriate for communicating AMS, as it is hard to see how any of the values could be raised easily. The only way would be to have some remote/virtual information. But due to the isolation and the paucity of visitors, even this may not be viable.

The Thones le Vieux and Thones le Farges geosites exhibit a relatively low to medium *Main value* and low *Additional value* (Figure 6.13). Given this, there is potential to increase their *Main value* by enhancing their scientific and protection values. The remarkable viewpoints and the surrounding landscape already have a strong appeal, so by enhancing the scientific attributes we can not only foster a deeper appreciation among normal tourists but also attract geotourists to these sites. In essence, some of this work is underway, as there is ongoing research into the area, which will lead to a higher main value score as more scientific elements come to light.

The main reason for the relatively low rating of *Additional value* is the insufficient touristic infrastructure at these geosites. The absence of properly maintained trails, interpretive panels

and geotourism promotion initiatives significantly detracts from the overall visitor experience. These three factors are crucial for boosting the attractiveness of these geosites to current and prospective tourists. Addressing these issues would not only increase value, creating a more enriching and informative environment for all visitors.

It is worth considering with whom such work could be done. At present the locals (there is a small village nearby and some farms) do not engage in any tourism activity. There is one place for tourist accommodation in the small village of Thones, which has views over the area, and may have an interest in increasing its offer to visitors. Otherwise, other nearby sites, such as the Mysteres de Farges a few km away (https://www.st-nectaire.com/mysteres-de-farges/), that does tourist visits, and may support some extension. These are elements to work on in a future project, if Thones would be developed as a geotouristic site.
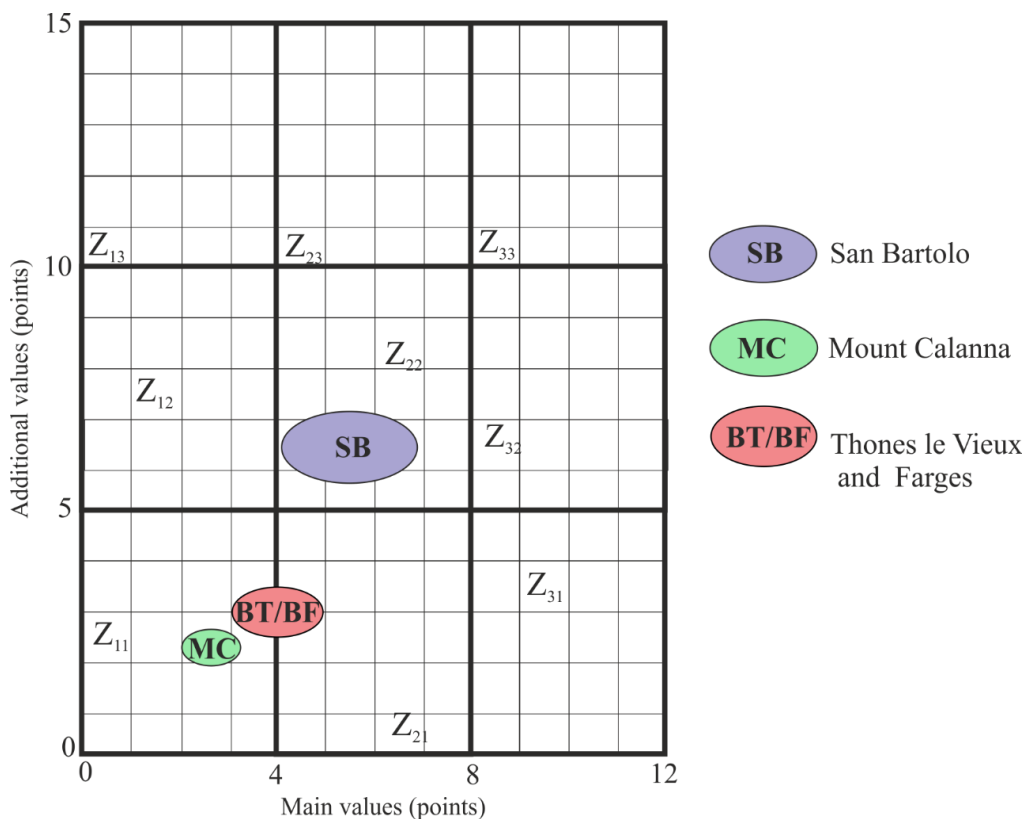
Figure 6. 13. Distribution of the averaged position of the defined geosites of Mount Calanna (MC), San Bartolo lava flow (SB) and Thones le Vieux and Thones le Farges lava flows (BT/BF). With more scientific knowledge the main values of each site could rise, although for Mount Calanna, its main values are already established and could be lower by the natural destruction of the site by Etna lava flows. Additional values for San Bartolo could be raised by some more tourist information provided to local information points, and this could also improved due to AMS communication. For the French sites a more comprehensive information and amenity package may be required, but there is plenty of possibility for this.

Recognising the significant geotourism potential associated with the San Bartolo lava flow on Stromboli, we took the strategic decision to use this site to integrate the AMS explanation with the geoheritage inventory. Our primary goals are to enhance the visitor experience and thus disseminate knowledge about the lava flow dynamics and emplacement processes, and finally give them an idea on AMS.

As a first step, for this article, we decided to create an informative interpretive panel near the coast of San Bartolo (this could also feature in a tourist leaflet). This displays features with compelling graphics, which efficiently provide the main geological insights from AMS analysis (Figure 6.14). The objective is to engage and educate visitors, enabling them to access and appreciate geological information more readily. By utilising visual representations, these insights become more accessible and engaging (Figure 6.14). They can then lead visitors to the three level AMS explanation. This can be placed on a website, accessible by the QR code, and could be delivered by local guides and tourist actors. They themselves can be trained to deliver this, in their own way.

Figure 6. 14. Cartoon illustration of the use of the AMS technique to find lava flow direction. This uses an anthropomorphised horse-shoe magnet 'Maggie magnet', and a cartoon lava, with bar magnets. This is the printed version of the simple first level experiment.

During our fieldwork at the San Bartolo lava flow, we observed a notable interest among tourists in gaining a deeper understanding of the lava flow process and our ongoing scientific endeavours. Visitors frequently approached us with curiosity, seeking information about our work. Thus, the introduction of interpretative panels (at least accessible via a QR code) will not only provide valuable insights to inquisitive tourists but also serve as a medium for them to enrich their experience and knowledge during their visit (Figure 6.15). Through our medium of AMS, we can convey the information needed for them in simple words.
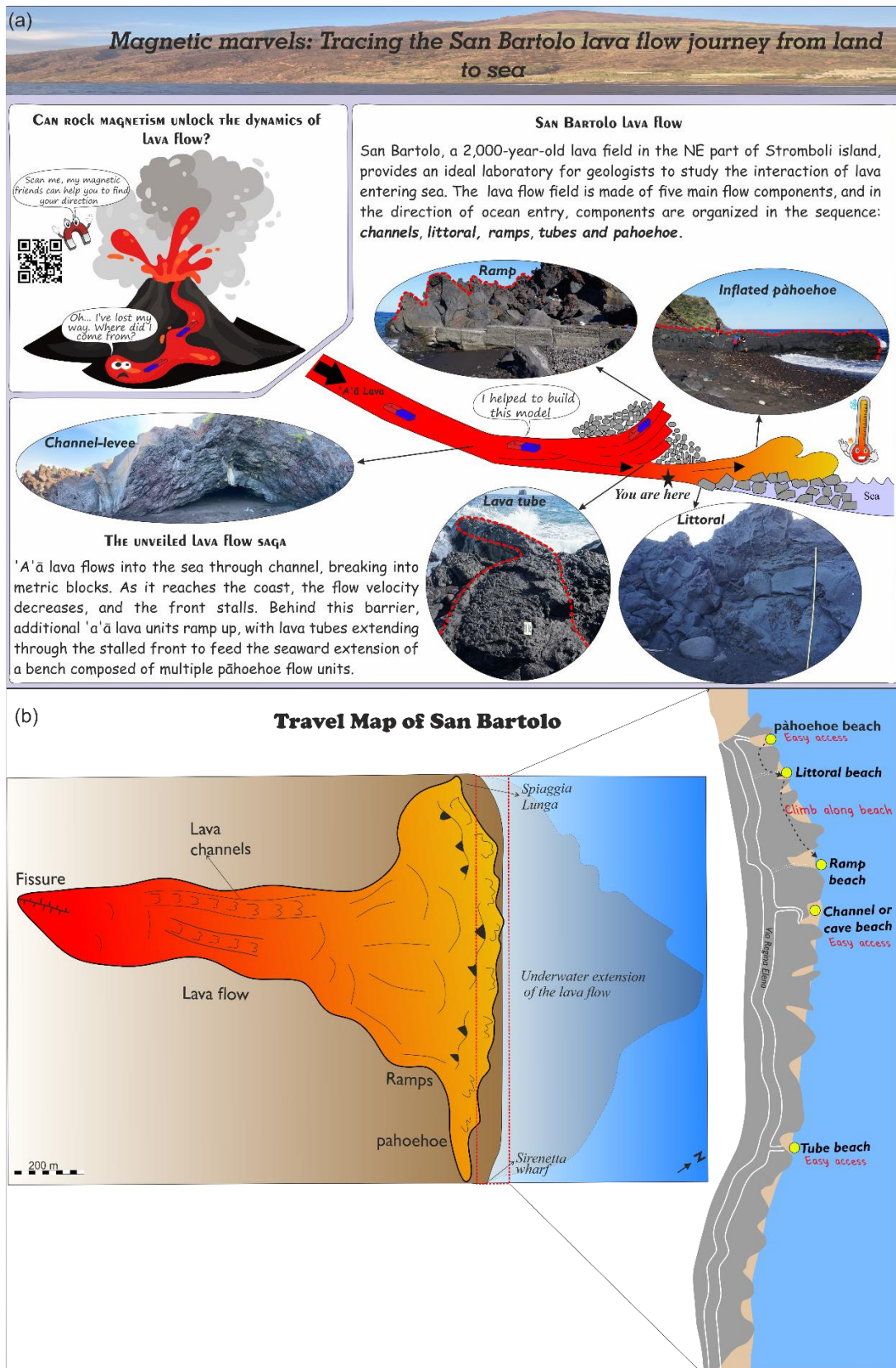
Figure 6. 15. a) Proposed model of the interpretative panel for the San Bartolo lava flow. This could be a general one, and for each site, only the image of that site could be employed. **b)** The map of San Bartolo, with basic tourist information on beach names and how to get to the beaches, can be included in information leaflets for local hotels and guides. This map gently draws the reader into the area to be presented with the basic information. This sets the scene for a more detailed, in-depth interaction if the visitor so wishes

Visitors interested in knowing more about the site can learn by scanning the QR code on the panel, where they will first access a user-friendly platform offering a three-level explanation of AMS and later find the model of emplacement we found through the AMS study (Figure 6.15). This method of presentation facilitates the promotion of geotourism and the dissemination of scientific knowledge to the general public by showcasing comparable geological discoveries from different geosites. It takes a simple explanation of AMS, embedded in accessible, tourist friendly material, to pique their natural curiosity and to draw them in. Alternatively, and in addition, the visitors may be informed and guided by local tourist actors, or even, if the scientist is there working, they now have a platform and a method to explain their work.

The methodology we have developed and used has shown that this approach could be effective in bridging the gap between the scientific and non-scientific parts of society. It not only allows you to use the public to see how the message is received but also to generate new projects with greater understanding between the scientist and the public. The system diagram in Figure 6.16, shows the full process that we have enacted and indicate a generalised method to undertake the exercise with other scientific information. We suggest that it could be used of any type of communication, such as panel design, websites, social media.

In our tests on 'naif' audiences, and other scientists, there has been a general acknowledgement that this approach has helped in understanding AMS. It remains to implement the technique in the field and test it with tourists and local actors around San Bartolo, which should be the next step.

The process described here (Figure 6.16) depends on putting the scientists within society, allowing them to interact in a more open way. Either part may initiate the initial dialogue, but it can happen only if there is close proximity and ease of interchange. At each step of the process, the researcher and their interlocutors improve their communication, and enhance their capacity or potential for understanding. The 'Consultation' space is where this occurs, and can lead to the joint definition of a Subject(s) for research and explanation. This, in turn, leads to explanations created both through scientific work and with continual interaction with through the Consultation. The choice of sites is a combination of the consultation (part of the participatory geoheritage inventory – M-GAM in this case) and the scientific work, and it is a loop between explanation, inventory, and assessment. The outcome can be both the popular descriptions and arcane scientific work, which now has a voice through the simplification

process and better communication. There is then a feedback to society, with the scientist included and further consultation.

The good circle of understanding can be joined at different stages, so while it would be most perfect to start with a consultation, the scientific work already done (often the case) can generate an explanation that can be improved by consultation. For another example, where a site exists with some reality (like tourist visitation or cultural significance), the process can be joined from this space, explanations and scientific material sought to start a consultation process.
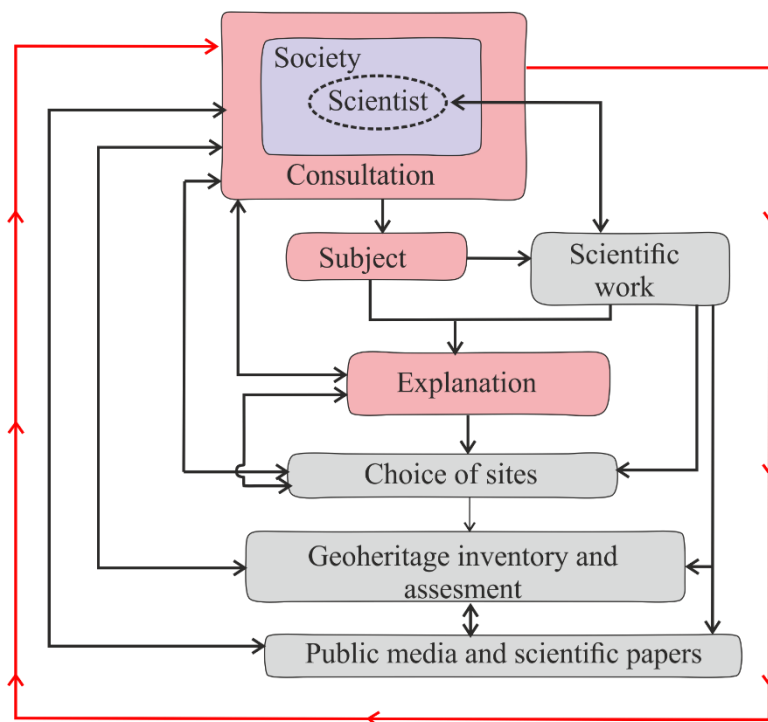
Figure 6. 16. Graphical system diagram showing the information and work-flow in the methodology we implemented. It shows how each component is related and how the whole process is circular, with the possibility to be joined at any stage

An important point to add is the use of the M-GAM method in assessing the geosites. While M-GAM is highly effective for experts, its complexity may be a challenge for the general public. To encourage wider public participation, a more accessible and open form of assessment is recommended. By simplifying the method to include simple questions and providing space for general comments, a wider audience can contribute their perspectives on the importance of these sites. This inclusive approach promotes a collaborative effort to understand and conserve geosites, ensuring that the insights of both experts and the general public are considered in the management and conservation of these valuable geological landmarks. This observation

106

underscores the significance of this study, emphasizing the need for inclusive approaches in science that can involve a wider range of public.

6.5 Conclusions

Scientific studies, along with their methods and findings, frequently present significant challenges for non-specialists, mainly because of their esoteric, arcane nature. This leads to a lack of societal value in science, lack of understanding between scientist and the community, or visitors. To change this poor situation, the primary challenge is thus to effectively communicate and clarify the scientific techniques utilised in research to the general public in a simple and understandable way.

We have chosen AMS (anisotropy of magnetic susceptibility) as an excellent test case of an inaccessible technique, far removed from normal experience. Initially, we explored how to make AMS understandable, starting by looking at how to communicate the technique in a clear and simple way, with a layering of increasing complexity.

To evaluate the efficacy of the AMS explanation, we opted to examine three distinct volcanic sites. In order to determine the most suitable candidate for potential applications, we decided it essential to conduct a geoheritage inventory for each site, employing the M-GAM method for this purpose. Our assessment involved a combination of our own understanding of the sites and solicited external viewpoints, wherever feasible.

Utilizing the M-GAM results, we focused on identifying suitable areas for ASM communication, and the best geological sites.

Consequently, geosites from Mount Calanna were excluded due to their limited potential for effective communication, as indicated by the low M-GAM values that could not be enhanced. In contrast, geosites from Saint-Nectaire showed promise, with the potential, and opportunity for both Main and Addition values to increase. Although it currently lacks sufficient visitation to be financially viable, there is optimism that as the scientific significance of the main values grows through ongoing research, local tourism stakeholders may become increasingly interested in its promotion.

The geosites of the San Bartolo lava flow of Stromboli Island emerged as the most promising, possessing the highest Mian and additional values and the greatest potential for geotourism

enhancement. M-GAM analysis revealed well-defined sites within this area, providing optimal and straightforward opportunities for effective communication.

With our focus set on San Bartolo, we coupled all the tangible geological features of outcrops with intangible elements (rock magnetic data) and built a narrative for popular comprehension of AMS, in the context of the local geology of lava flows.

The subsequent phase involves collaborating with tourism and other actors on Stromboli to spread the message, to install information panels and employ other media.

Following this implementation, we aim to assess the effectiveness of our method. This evaluation will likely involve soliciting feedback from tourists through a QR code questionnaire and conducting in-person surveys to gather opinions from both visitors and those involved in the tourism sector.

This method could be useful for researchers beginning a study, to allow them to initiate discourse with a wider public from the start, which could reinforce the scientific work open up to have more societal relevance and social impact. It could open the way for participatory science. Practically it could aid the development of geosites as geo-tourist attractions, enhancing economic benefit, respect for sites (that comes from knowledge), and thus better protection.

Finally, we suggest a two-pronged approach:

First, search for or create simple, clear, and understandable definitions of scientific methods and processes, using a stepped process.

Second, using a geoheritage inventory approach to structure the work, and provide the best strategy for subsequent outreach and interaction with visitors and local actors. This gives both the ease of communication and the rigorous structure within which to develop and communications strategy.

At all stages of this work, we have opted to involve 'naïve' public – non-scientific colleagues and others, a consulting them at every step, has allowed us to remain connected and to develop a general understanding of the AMS technique. Something so difficult to grasp has now the potential to become a concept all can share.

Chapter 7

SUMMARY

This thesis provides insights into the emplacement dynamics of the intrusive (dyke) and extrusive (lava flow) units of the volcanic system, together with a way of effectively communicating these scientific findings to the non-scientific community. Comprehensive rock magnetic techniques along with geochemical, textural, and field studies, have enabled to better constrain the flow dynamics and thereby build the emplacement model.

In the first case study (Chapter 4), we adopted an interdisciplinary approach to investigate the various forces that control the propagation and emplacement of dykes in a small dyke swarm of Monte Calanna (Figure 7.1). Given the small size of the dykes, the study enabled us to better constrain the magma flow dynamics across the dyke strike and provides an insight into the emplacement dynamics related to a small intrusive complex. The combined field observations and the magnetic fabrics suggest that Mount Calanna represents the upper part of a shallow plumbing system consisting of sub-vertically and sub-horizontally emplaced dykes, now exposed by erosion. The sub-vertical dykes migrated laterally from the central conduit to the surface, whereas the sub-horizontal dykes were fed by the deeper magma chamber. In addition, our study presents a new approach to infer magma flow direction in dykes using the AMS technique, and we substantiate the reliability of our approach using the SPO study. Finally, the dyke emplacement models proposed in our study apply to other small intrusive complexes to infer emplacement dynamics and cooling histories of dyke injection. The proposed modes are mainly based on the thermal stresses and physical forces acting during magma injection into the host rock and their subsequent changes during magma solidification. Magma movement during solidification could be extrapolated from the change in magnetic fabrics across the dyke width. It is important to emphasize that, as Mount Calanna is mostly surrounded by recent lava flow and covered by strong vegetation, our study may be one of the final investigations of the area.

In the second case study (Chapter 5), we explored the lava flow dynamics of San Bartolo lava flow and built a sea entry model of channel fed 'a'ā lava flow (Figure 7.1). Due to the exposure of the lava delta along a 1 km cliff section (Calvari et al. 2023), it provides an excellent location where entry dynamics, processes, and resulting structures can be described to study the sea entry of lava. To do this, we carried out a comprehensive field study along the coast plus

measurements of the magnetic fabric and palaeomagnetism to investigate the emplacement mechanisms of San Bartolo flow unit. We were able to define the five main lava flow components of a lava delta fed by 'a'ā formed by the sea entry of lava and the subsequent lava-water interaction. They are a) channel, b) littoral, c) ramps, d) tubes, and e) inflated pāhoehoe. The spatial distribution of these flow components enables to build the lava entry model into a water system. For San Bartolo, we have identified two potential models for the water entry of lava. The first model involves the channel fed 'a'ā stops before the coast and the second model describes the channel fed 'a'ā with a high effusion rate that crosses the coastline. In both cases, the flow dynamics is characterized by three main stages. Upon reaching the break-in slope, the channel-fed 'a'ā slows down and the flow front stalls. The subsequent lava pulses lead to the inflation and ramping up of the flow front. The continuous influx of lava results in the flow front failure and the formation of lava tubes to feed the pāhoehoe bench (Figure 7.1).

Finally (Chapter 6), the thesis presented a way to communicate these scientific observations to a wider audience and make them useful to the community at large via geoheritage. A significant and innovative outcome of this study is the novel approach of presenting a complex scientific technique (AMS) in a simplified way, making it accessible to people of all backgrounds and ages (Figure 7.1). The evaluation of each geosite of Mount Calanna (dyke), San Bartolo (lava flow components) and Thones le Vieux and Thones le Farges of Saint Nectaire (lava flows), using M-GAM, allowed us to select the site with geotourism potential and to integrate the explanation into the geosite inventory. We systematically connected the tangible geological features observed in the outcrops with intangible elements, such as rock magnetic data, constructing narratives designed for widespread comprehension. Other than conveying scientific results through extensive texts and complex numerical data, we embraced an approach of presenting the same findings in a simple cartoonist manner. This not only captures the attention of tourists but also ensures that the work is accessible to a broader audience. A future prospective of this work is to introduce an informative panel in the coast of San Bartolo after collaboration with Stromboli tourism and local administrative bodies. Additionally adding the panel image/information in the stromboli tourism brochure and the introduction of the simple AMS experiments to local guides would make tourists more interested and engaged.
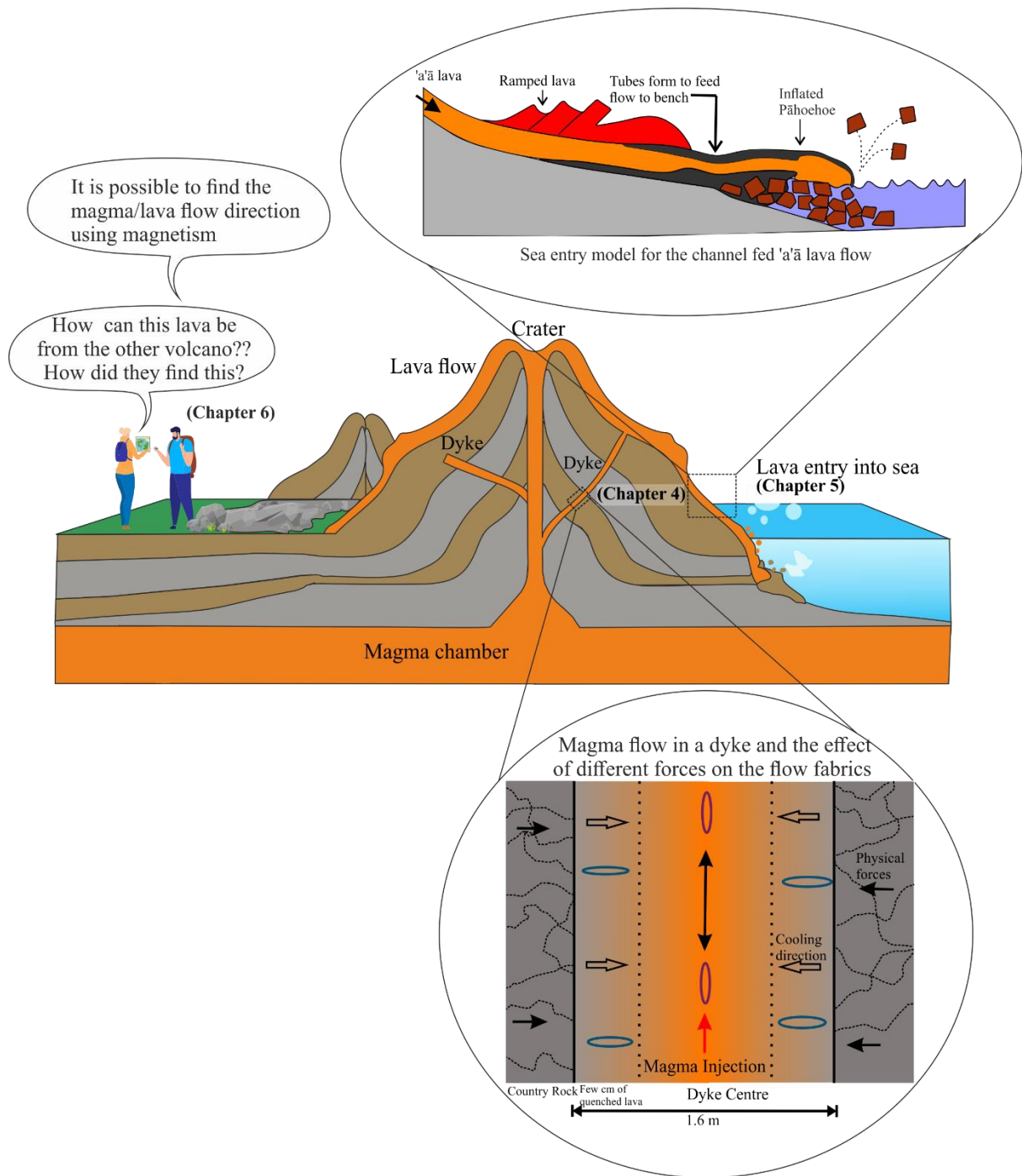
Figure 7. 1. Schematic diagram showing the summary of this thesis, highlighted with the key findings from each case study.

APPENDIX

Supplementary materials from Chapter 4

<u>Lowrie experiment results</u>
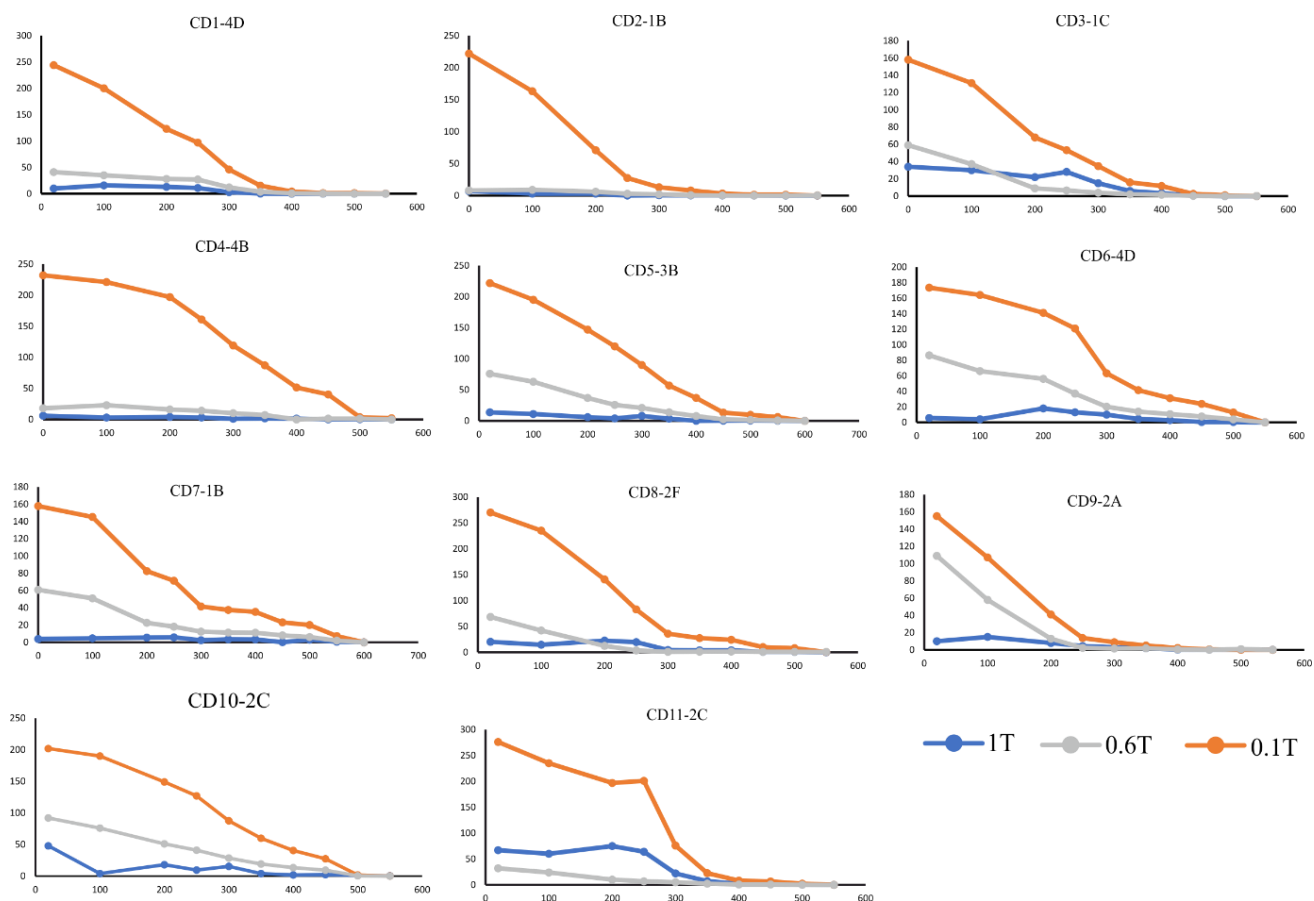
Figure 4.S 1. Representatives' thermal demagnetization of three-axial IRMs (Lowrie, 1990) for each dyke.

Unmix of coercivity spectra
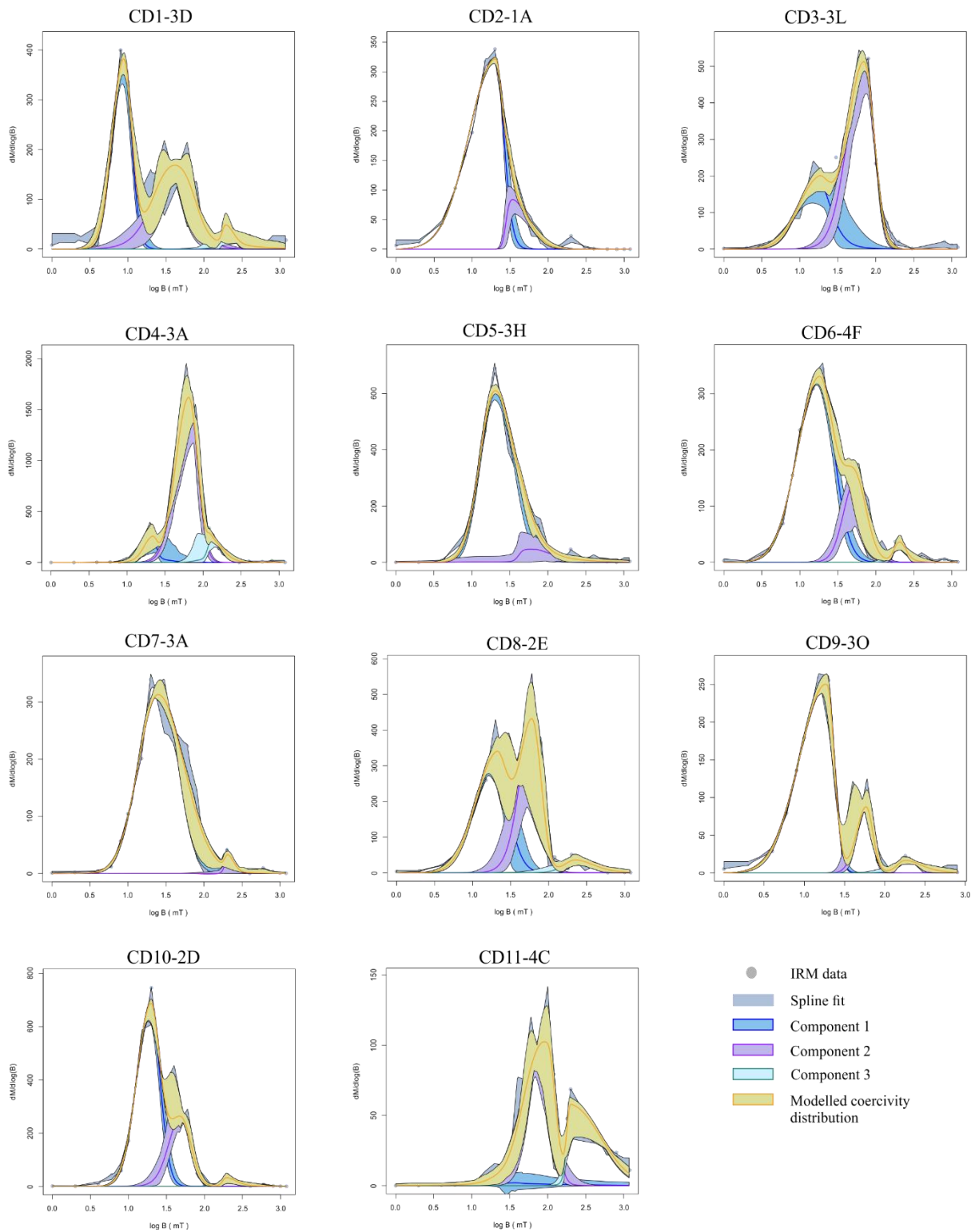
Figure 4.S 2. Representatives coercivity distribution and unmixing of IRM acquisition curves per each dyke (Maxbauer et al., 2016).

Distribution of dykes on Mount Calanna
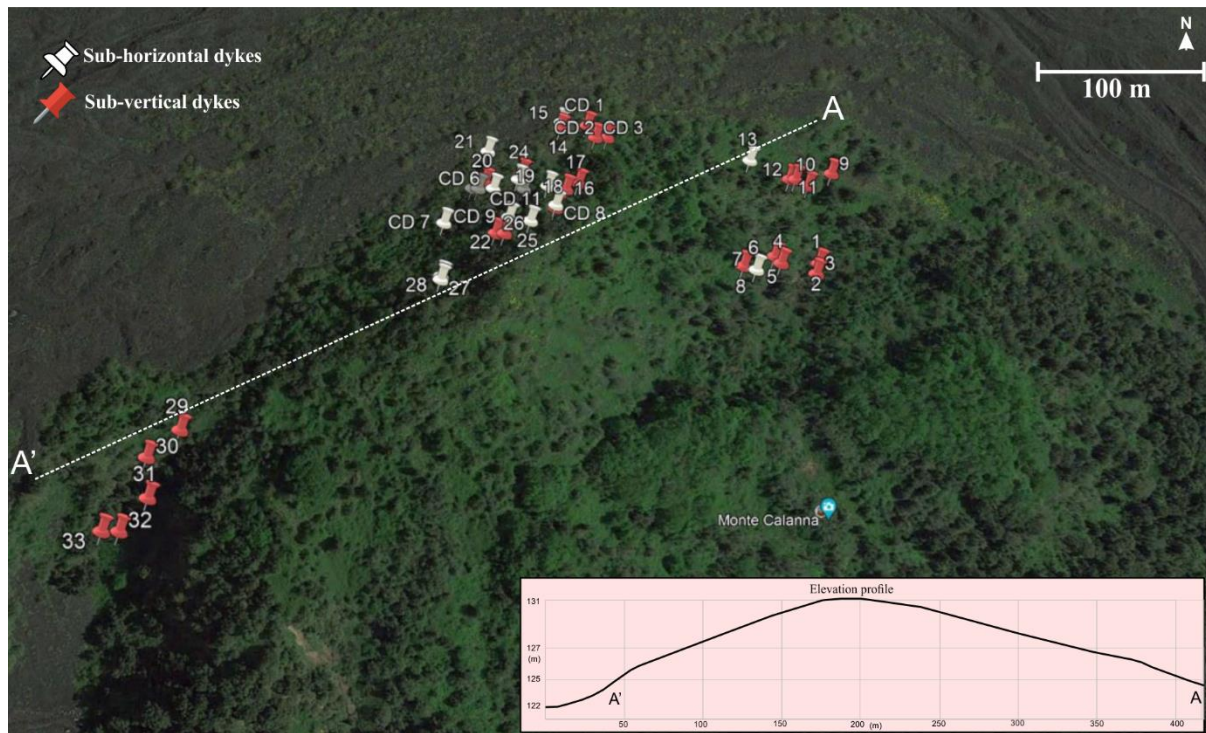
Figure 4.S 3. Google Earth image showing the location of all dykes on Mount Calanna (present study and old study - Ferlito and Nicotra, 2010). Nowadays, several of these dykes are not exposed and covered by the high vegetation and the ashfall of the more recent eruptions. The dykes have been grouped into sub-vertical (red) and sub-horizontal (white) dykes based on the structural data. The elevation profile along transects A-A' shown on the bottom right gives an idea of the topography of the northern part of Mount Calanna.

Table 4.S 1. Palaeomagnetic results of studied dykes from Mount Calanna dykes. N = number of samples analysed from each dyke; n = number of samples gave stable palaeomagnetic direction; Dm and Im = mean declination and inclination values respectively of the characteristic remanent magnetic (ChRM) directions; k = precision parameter; α_{95} = radius of the 95% confidence cone.

Dykes	n/N	ChRM			
		D_m (°)	I_m (°)	K	α_{95} (°)
CD 1	8/8	322	74	172	4.2
CD 2	8/13	357	70	69	6.7
CD 3	7/7	353	72	77	6.9
CD 4	10/11	321	57	29	9.1
CD 5	9/11	8	72	97	5.3
CD 6	6/10	22	33	74	7.8
CD 7	7/9	8	61	68	7.4
CD 8	7/7	353	56	123	5.5
CD 9	8/8	31	25	32	10
CD 10	8/11	10	66	68	6.8
CD 11	5/6	15	19	96	12.7

Vesicle distribution of the upper layer of inflated pāhoehoe flow unit
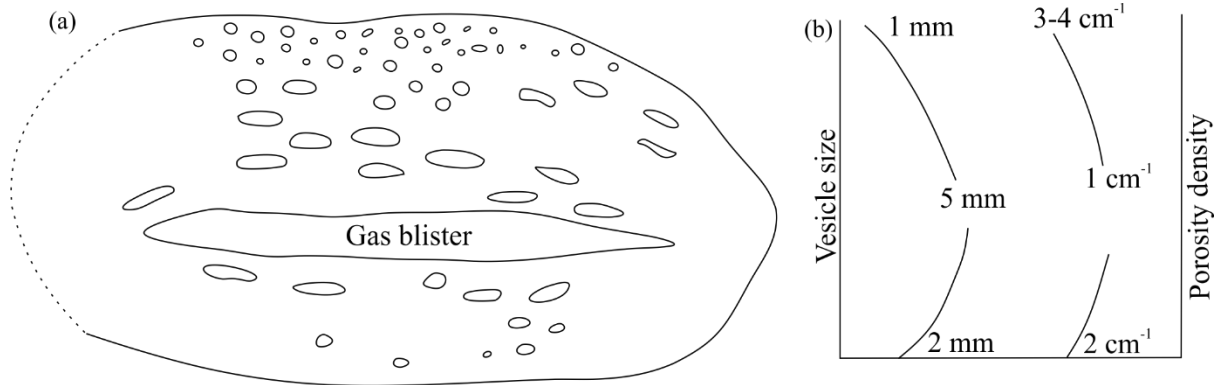
Figure 5.S 1. **a)** Cross section of S-type lobe at inflated pāhoehoe flow unit. **b)** Vesicle size and porosity density profile along a transverse section of the lobe.

Cross section of channel-levee component
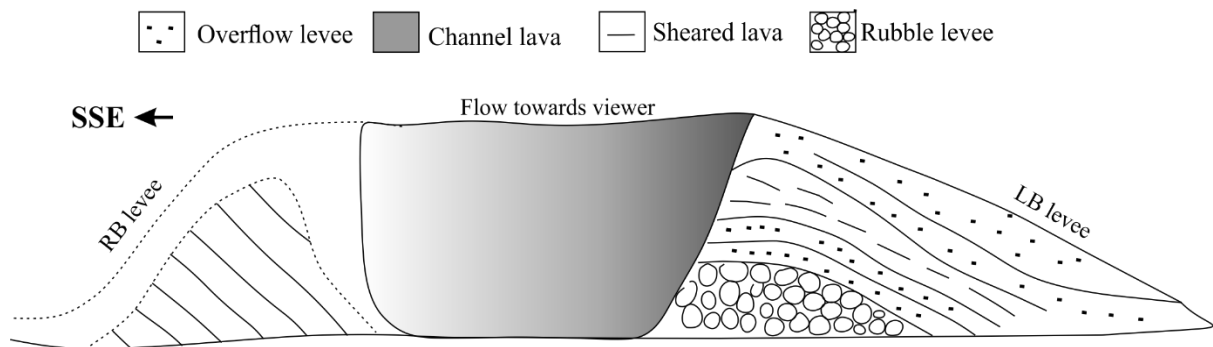
Figure 5.S 2. Schematic diagram showing the cross-section view of channel component observed at San Bartolo lava flow field. LB and RB levees are left bank and right bank levee respectively.

Ramp model
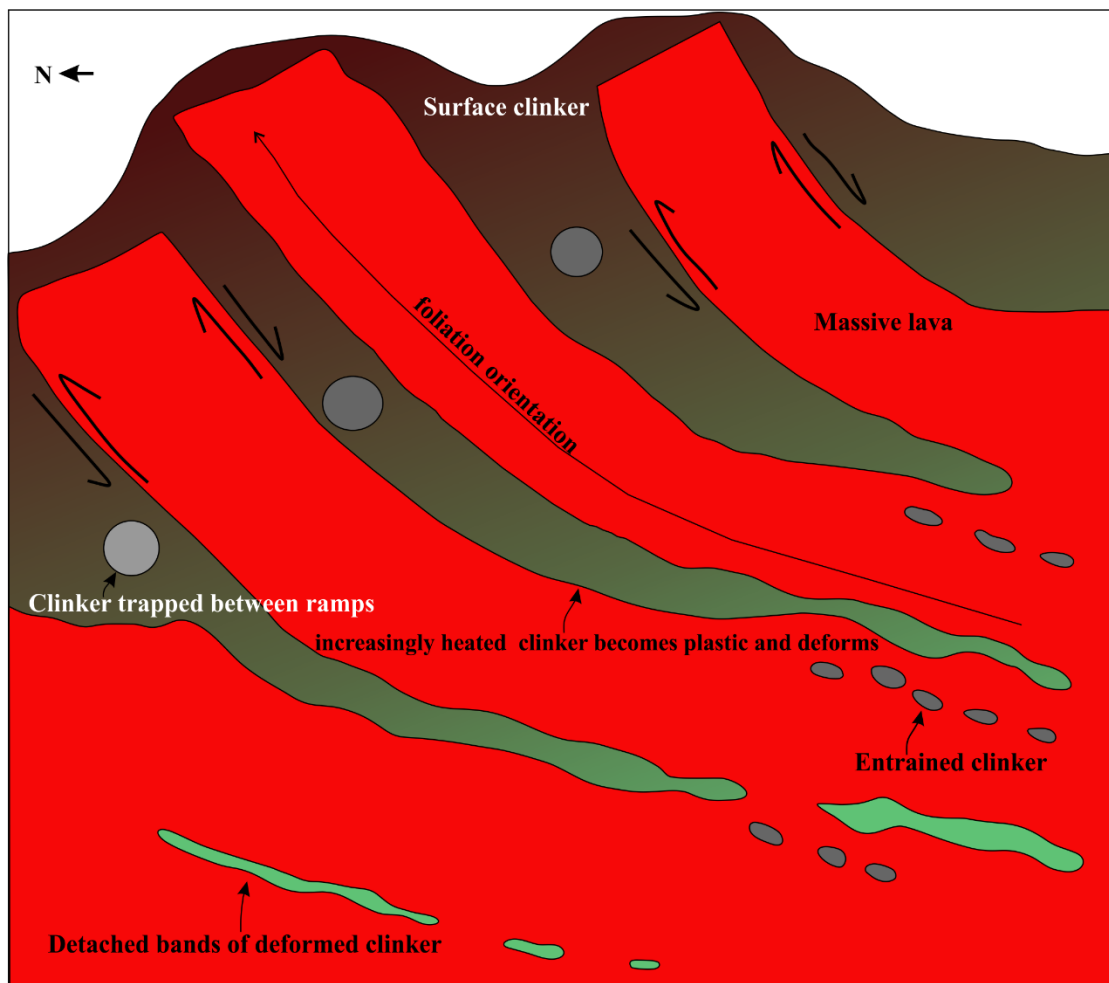
Figure 5.S 3. Diagram illustrating a section of the ramping of lava with clinker trapped between ramps.

Tube component model
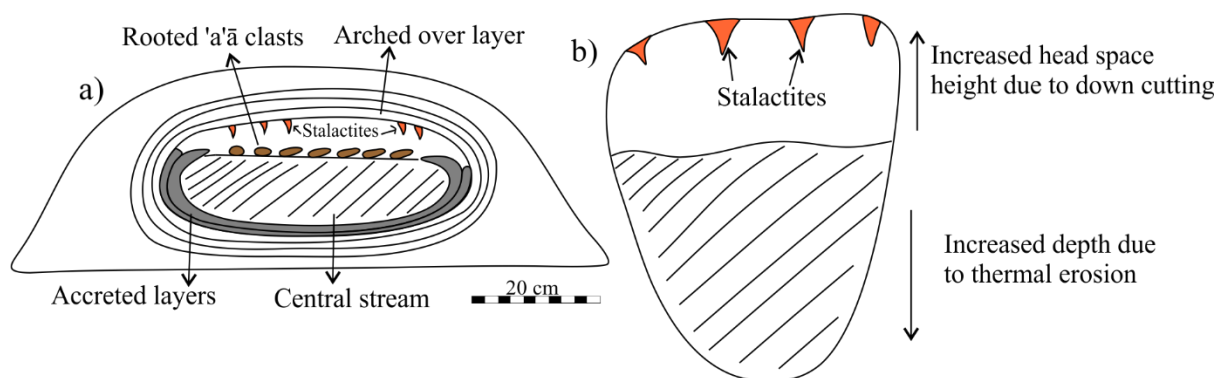
Figure 5.S 4. Diagram showing the cross-section view of the lava tube within Flow 1. **a)** Lava tube with a central stream with solid lava and void space, which are bounded by multiple layers. **b)** Increased head space and foot space by down-cutting and thermal erosion respectively.

Sketched of the development of Inflated pāhoehoe lava flow
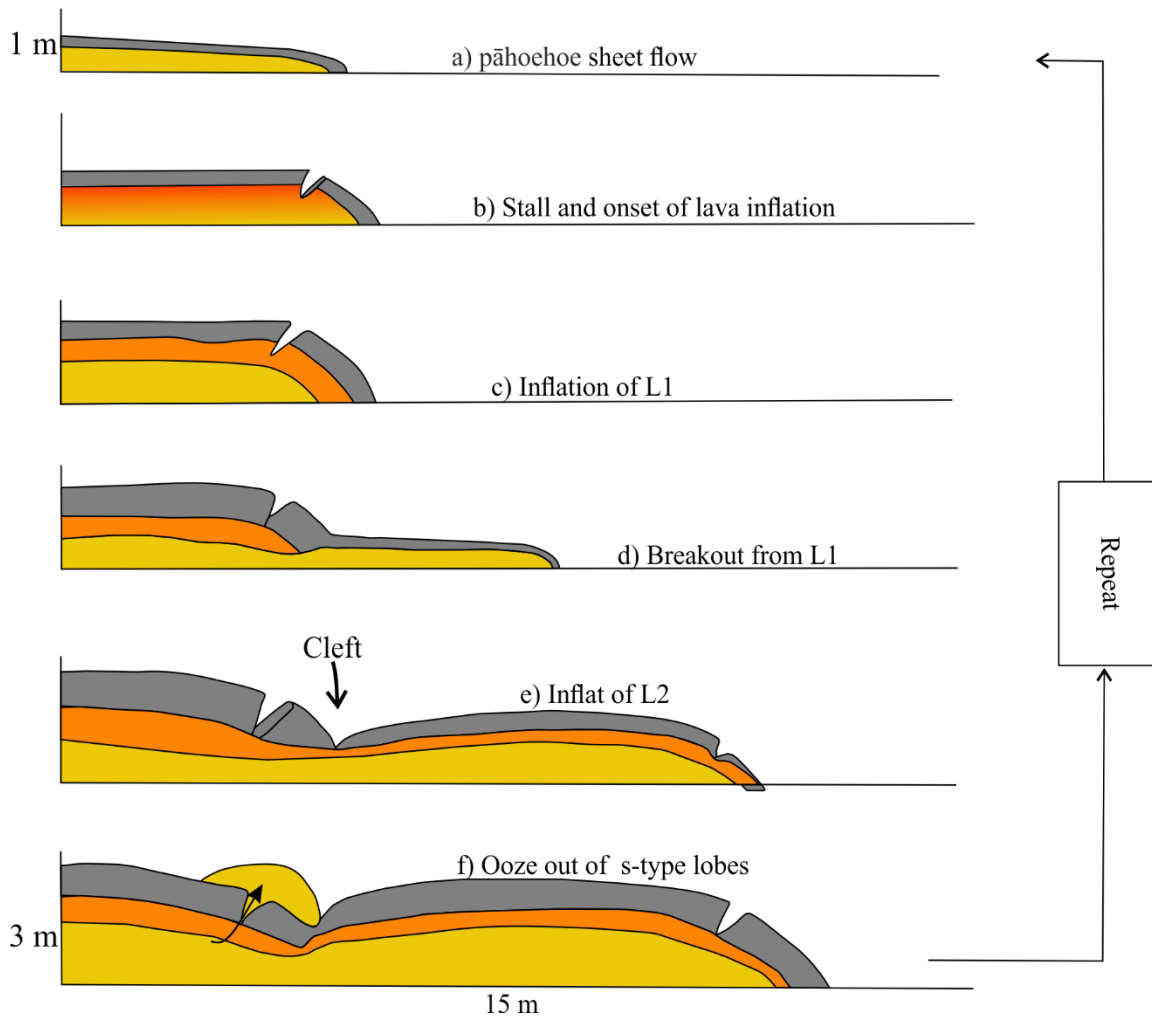
Figure 5.S 5. Cross-section sketch of Inflated pāhoehoe lava flow model with six different stages. **a)** Initial stage of pāhoehoe sheet flow. Chilled crust forms as soon as the lava emerges. **b)** Stalling and onset of lava inflation due to the continuous input of lava. **c)** As the lava flow continuous, the toe inflates and make 1st lobe 1(L1). **d)** The continuous influx of lava causes the breakout from L1. **e)** The breakout of L1 cause the formation of second lobe (L2). **f)** Further pressure in L1 cause the ooze out of s-type lobes.

Table 5.S 1. Mean AMS data of San Bartolo lava flow. n= Number of specimens considered; N= number of specimens measured; χ_m = mass susceptibility; L= magnetic lineation; F= magnetic foliation; P'= corrected degree of magnetic anisotropy; T= shape parameter; D = declination; I = Inclination; α_{95} = radius of the 95% confidence cone; K_1= maximum susceptibility axis; K_2= intermediate susceptibility axis; K_3 = minimum susceptibility axis

Flow	Facies	Sites	n/N	χ_m (x 10^{-3} m^3Kg^{-1})	st. dev.	L	F	P'	T	K_1 D	I	α_{95} conf. angles		K_2 D	I	α_{95} conf. angles		K_3 D	I	α_{95} conf. angles	
Flow 1	Tube	L1A-S1	9/11	3.77	0.56	1.000	1.003	1.004	0.534	331	59	38.5	10.2	89	16	38.8	8.4	187	26	8.7	8.6
		L1A-S2	12/15	2.03	0.12	1.001	1.001	1.002	0.109	181	23	27.3	9.6	294	43	33.6	14.8	71	39	26.7	8.5
		L1A-S3	5/5	7.04	0.83	1.003	1.008	1.012	0.493	37	68	7.1	3.1	271	14	13.2	2.7	176	17	13.2	6.4
		L1A-S4	11/14	1.62	0.39	1.001	1.002	1.003	-0.149	287	49	68.7	25.8	94	40	68.4	39	190	7	40.4	32.1
	Ramp	L1B	8/12	3.70	0.65	1.002	1.005	1.007	0.495	86	12	16.5	12.0	187	40	16.0	14.7	342	48	18.3	5.7
		L1C	7/9	8.05	1.80	1.000	1.007	1.008	0.298	92	71	76.2	7.6	312	15	76.2	10.0	219	12	12.0	5.4
Flow 2	Channel	L2A-S1	10/10	3.59	0.11	1.002	1.004	1.005	0.279	266	75	15.2	4.2	95	15	14.8	10.3	4	2	10.5	5.1
		L2A-S2	7/7	8.16	0.39	1.002	1.005	1.007	0.306	25	29	8.4	5.5	255	49	8.7	7.0	131	26	8.3	4.1
		L2A-S3	7/8	1.66	0.02	1.001	1.007	1.008	0.694	66	76	16.8	2.7	290	10	16.8	2.7	198	10	3.2	2.3
Flow 4	Ramp	L4A	8/10	5.20	1.21	1.001	1.005	1.007	0.266	154	40	57.0	11.0	253	10	56.6	8.6	354	48	13.3	9.2
		L4B	5/8	5.70	1.88	1.002	1.005	1.007	0.307	159	17	21.0	10.0	251	7	20.0	5.2	4	72	12.0	4.3
Flow 7	Ramp	L7A		6.84	3.16																
	Channel	L7B	28/28	6.14	1.69	1.002	1.010	1.013	0.532	131	33	33.5	16.4	7.7	40	33.0	14.7	246	32	18.4	14.5
		L7C	8/8	6.45	0.75	1.006	1.007	1.012	0.029	112	33	12.4	7.2	20	2	13.5	5.5	287	57	10.1	4.3
Flow 12	Inflated Phh	L12-S1 & S2	9/11	0.94	0.06	1.000	1.002	1.002	0.075	147	45	71.6	19.8	307	44	71.7	11.2	47	10		
		L12-S3 & S4	13/21	1.49	0.39	1.001	1.003	1.004	0.367	84	1	37.9	9.7	341	85	37.9	10.2	174	5	11.6	8.0
		L12-S5 & S6	16/23	1.03	0.48	1.001	1.004	1.005	0.397	11	19	26.5	12.3	280	4	26.7	16.2	179	70	17.4	11.4
		L12-S7	11/14	3.71	0.66	1.001	1.002	1.004	0.235	78	67	58.9	11.6	245	22	58.8	16.5	337	5	21.4	12.5
		L12-S8	8/10	3.04	0.56	1.002	1.002	1.004	0.103	196	13	18.7	6.7	306	57	14.4	12.6	98	30	14.2	12.6
		L12-S9	4/4	5.52	1.21	1.002	1.005	1.008	0.579	108	71	-	-	244	14	-	-	337	13	-	-
		L12-S10	10/11	3.77	1.92	1.000	1.006	1.009	0.670	73	41	59.4	11.2	248	49	59.4	18.0	341	3	19.8	6.8
		L12-11	9/13	2.83	0.66	1.002	1.002	1.004	0.316	298	18	24.0	15.7	30	8	37.0	21.8	143	70	36.1	16.1

Table 5.S 2. Palaeomagnetic results of San Bartolo lava flows. N = number of samples analysed from each dyke; n = number of samples gave stable palaeomagnetic direction; Dm and Im = mean declination and inclination values respectively of the characteristic remanent magnetic (ChRM) directions; k = precision parameter; α_{95} = radius of the 95% confidence cone.
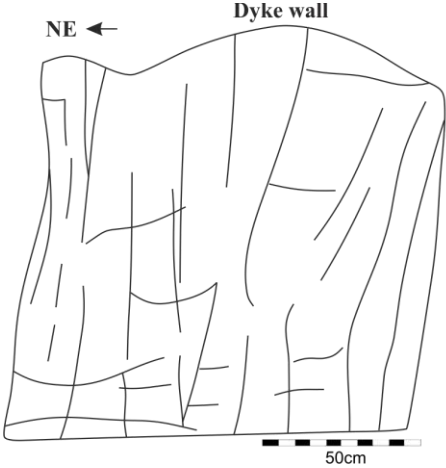
Flow	n/N	ChRM			
		D_m (°)	I_m (°)	k	α_{95} (°)
L1	13/17	359.4	59.2	54	5.7
L2	5/5	355.6	60.0	296	5.4
L4	8/8	10.6	69.8	63	7.1
L7	14/16	9.8	56.6	17	7.2
L12	10/14	356.9	56.7	43	7.5
Mean	50/60	2.5	61.9	37	3.4
San Bartolo flow (Speranza et al., 2008)	52/55	359.3	60.0	143	1.7
San Bartolo lava (Arrighi et al., 2004)	22/22	-4.2	53.4	386	1.5

Table 5.S 3. Physical properties of San Bartolo lava flow including porosity and connectivity. Øc = connected porosity, $Ø_T$ = Bulk Porosity, Øiso = Isolated porosity, DRI = dense rock equivalent.

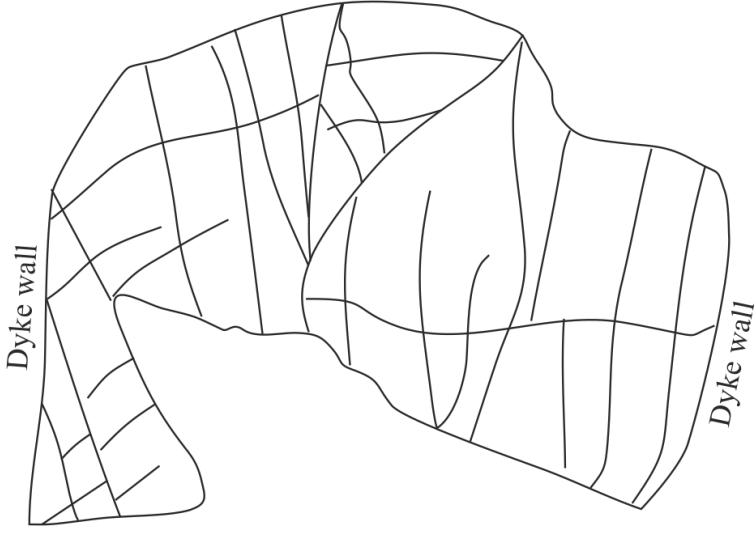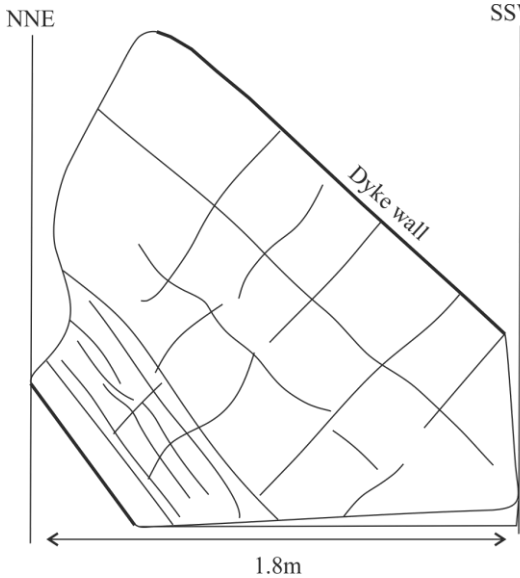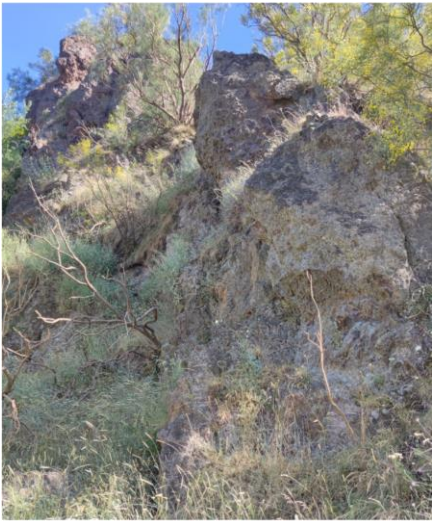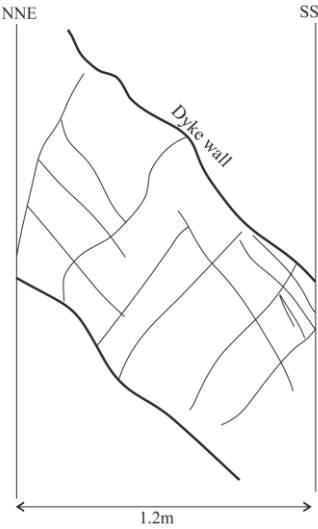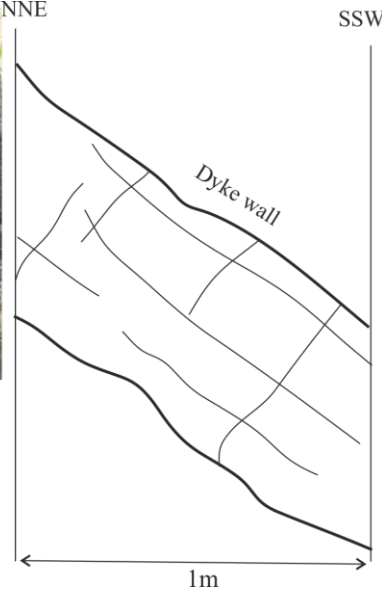| Samples	DRI	Sample mass (g)	He Pycn Volume He pycno (mm³)	Std Dev	cell size (mm³)	Geopycn Volume	Std Dev	Enveloppe density (gcm-³)	Std Dev	Porosity (%)	Øc	$Ø_T$	Øiso	Connectivity degree	Øiso
										Tube Component					
1-1G	2.9	20.75	7.15	0.001	35	9.85	0.008	2.11	0.002	27.38	0.27	0.27	-0.001	100.21	-0.21
1-1I	2.9	21.30	7.35	0.005	35	10.23	0.005	2.08	0.001	28.24	0.28	0.28	0.001	99.82	0.18
1-2I	2.9	19.87	6.86	0.005	35	9.28	0.026	2.14	0.006	26.13	0.26	0.26	0.001	99.79	0.21
1-2U	2.9	22.63	7.80	0.004	35	10.32	0.005	2.19	0.001	24.38	0.24	0.24	0.000	99.98	0.02
1-3AD	2.9	23.82	8.26	0.005	35	10.33	0.014	2.31	0.003	20.50	0.20	0.21	0.005	97.76	2.24
1-3AC	2.9	23.66	8.21	0.002	35	10.43	0.012	2.27	0.003	21.79	0.21	0.22	0.005	97.69	2.31
1-4CA	2.9	22.87	7.95	0.004	35	8.58	0.060	2.67	0.019	8.09	0.07	0.08	0.008	90.31	9.69
1-4CB	2.9	20.52	7.12	0.002	35	9.20	0.025	2.23	0.006	23.11	0.23	0.23	0.005	97.90	2.10
										Inflated phh					
12-1C	2.9	22.98	7.94	0.002	35	9.81	0.009	2.34	0.002	19.29	0.19	0.19	0.003	98.56	1.44
12-1D	2.9	21.32	7.40	0.001	35	9.19	0.008	2.32	0.002	20.05	0.20	0.20	0.005	97.39	2.61
12-2C	2.9	23.50	8.15	0.002	35	10.04	0.009	2.34	0.002	19.29	0.19	0.19	0.004	97.72	2.28
12-2E	2.9	24.54	8.51	0.001	35	10.53	0.018	2.33	0.004	19.62	0.19	0.20	0.004	97.82	2.18
12-3E	2.9	19.13	6.61	0.002	35	9.45	0.004	2.02	0.001	30.19	0.30	0.30	0.001	99.60	0.40
12-3F	2.9	19.30	6.67	0.001	35	9.56	0.013	2.02	0.003	30.42	0.30	0.30	0.002	99.44	0.56
12-4E	2.9	20.53	7.08	0.001	35	10.08	0.020	2.04	0.004	29.76	0.30	0.30	0.001	99.81	0.19
12-4A	2.9	18.38	6.33	0.002	35	9.03	0.006	2.03	0.001	29.85	0.30	0.30	0.000	100.16	-0.16
12-5E	2.9	19.69	6.81	0.001	35	9.08	0.024	2.17	0.006	25.22	0.25	0.25	0.002	99.16	0.84
12-5C	2.9	21.06	7.29	0.001	35	9.21	0.014	2.29	0.003	21.19	0.21	0.21	0.003	98.52	1.48
12-6C	2.9	22.49	7.79	0.002	35	10.55	0.006	2.13	0.001	26.53	0.26	0.27	0.003	98.81	1.19
12-6D	2.9	22.37	7.75	0.002	35	10.59	0.007	2.11	0.001	27.16	0.27	0.27	0.003	98.95	1.05
12-7H	2.9	19.67	6.78	0.001	35	9.91	0.019	1.94	0.004	33.14	0.32	0.33	0.015	95.38	4.62
12-7E	2.9	22.35	7.71	0.002	35	10.19	0.006	2.19	0.001	24.35	0.24	0.24	0.000	100.00	0.00
12-8F	2.9	21.05	7.26	0.001	35	9.89	0.007	2.13	0.001	26.59	0.27	0.27	0.000	100.09	-0.09
12-8I	2.9	21.28	7.33	0.002	35	9.42	0.007	2.26	0.002	22.08	0.22	0.22	-0.001	100.57	-0.57
12-9D	2.9	22.47	7.77	0.001	35	9.52	0.028	2.36	0.007	18.59	0.18	0.19	0.002	98.94	1.06
12-9A	2.9	22.80	7.88	0.002	35	9.70	0.018	2.35	0.004	18.92	0.19	0.19	0.002	99.05	0.95
12-10E	2.9	21.19	7.32	0.002	35	9.38	0.006	2.26	0.002	22.09	0.22	0.22	0.001	99.43	0.57
12-10A	2.9	20.75	7.20	0.001	35	8.97	0.016	2.31	0.002	20.20	0.20	0.20	0.005	97.44	2.56
12-14A	2.9	25.35	8.74	0.002	35	11.48	0.014	2.21	0.003	23.84	0.24	0.24	0.000	99.85	0.15
12-12A	2.9	24.33	8.35	0.002	35	11.39	0.016	2.14	0.003	26.33	0.27	0.26	-0.003	101.24	-1.24
										Ramp facies					
1B-6A	2.9	33.98	11.72	0.004	35	12.47	0.010	2.73	0.002	6.017	0.06	0.06	0.000	100.10	-0.10
1B-1A	2.9	32.80	11.27	0.002	35	12.92	0.018	2.54	0.004	12.462	0.13	0.12	-0.003	102.58	-2.58
1C-1A	2.9	30.51	10.54	0.002	35	11.44	0.005	2.66	0.001	8.269	0.08	0.08	0.004	95.08	4.92
1C-2A	2.9	26.94	9.33	0.006	35	10.61	0.007	2.54	0.002	12.421	0.12	0.12	0.004	97.03	2.97
4A-1A	2.9	25.89	8.97	0.001	35	10.18	0.012	2.54	0.003	12.269	0.12	0.12	0.004	96.33	3.67
4A-2A	2.9	21.22	7.38	0.001	35	9.64	0.021	2.20	0.005	24.059	0.23	0.24	0.006	97.52	2.48
4B-4A	2.9	28.76	9.95	0.001	35	11.40	0.015	2.52	0.003	13.024	0.13	0.13	0.003	97.60	2.40
4B-2A	2.9	28.21	9.75	0.000	35	11.24	0.014	2.21	0.004	23.766	0.13	0.24	0.105	55.77	44.23
7A-2A	2.9	32.53	11.21	0.001	35	11.92	0.009	2.73	0.002	5.921	0.06	0.06	-0.001	101.54	-1.54
7A-8B	2.9	28.63	9.94	0.001	35	11.14	0.013	2.57	0.003	11.390	0.11	0.11	0.006	94.80	5.20
										Channel Facies					
2-1A	2.9	26.32	9.05	0.004	35	10.56	0.005	2.49	0.001	14.021	0.14	0.14	-0.002	101.58	-1.58
2-1E	2.9	26.26	9.02	0.002	35	10.35	0.003	2.54	0.001	12.517	0.13	0.13	-0.003	102.32	-2.32
2-2C	2.9	27.69	9.59	0.002	35	10.97	0.009	2.52	0.002	12.997	0.13	0.13	0.004	96.75	3.25
2-2E	2.9	27.03	9.36	0.001	35	10.20	0.013	2.65	0.003	8.662	0.08	0.09	0.003	96.03	3.97
7B-4B	2.9	31.11	10.73	0.001	35	11.64	0.007	2.67	0.002	7.876	0.08	0.08	0.000	99.52	0.48
7B-14B	2.9	29.02	10.02	0.001	35	12.20	0.010	2.38	0.002	18.000	0.18	0.18	0.001	99.43	0.57
7C-1B	2.9	30.93	10.68	0.001	35	12.39	0.014	2.50	0.003	13.872	0.14	0.14	0.001	99.38	0.62
7C-3A	2.9	30.24	10.41	0.001	35	11.23	0.017	2.69	0.004	7.134	0.07	0.07	-0.001	102.00	-2.00
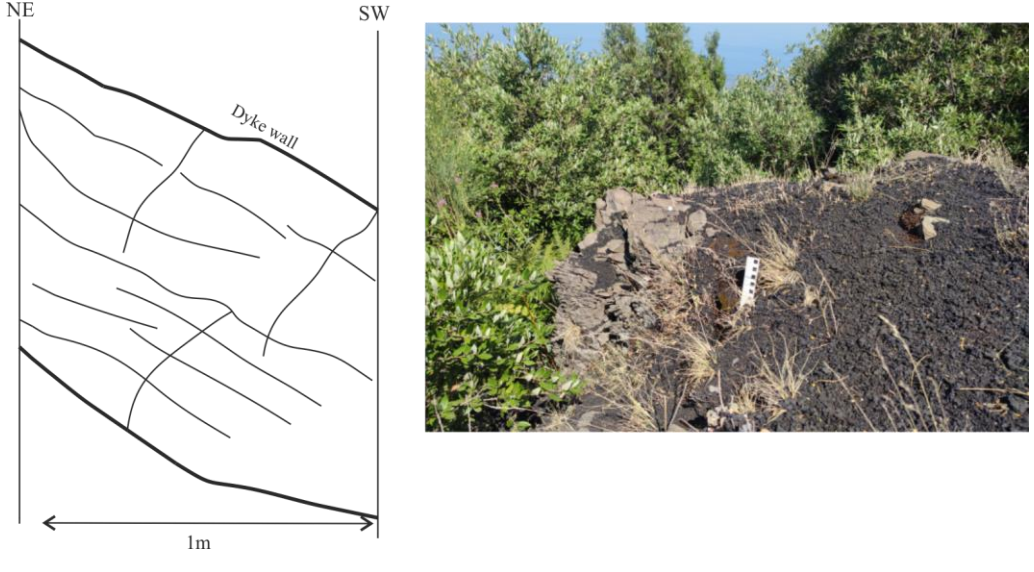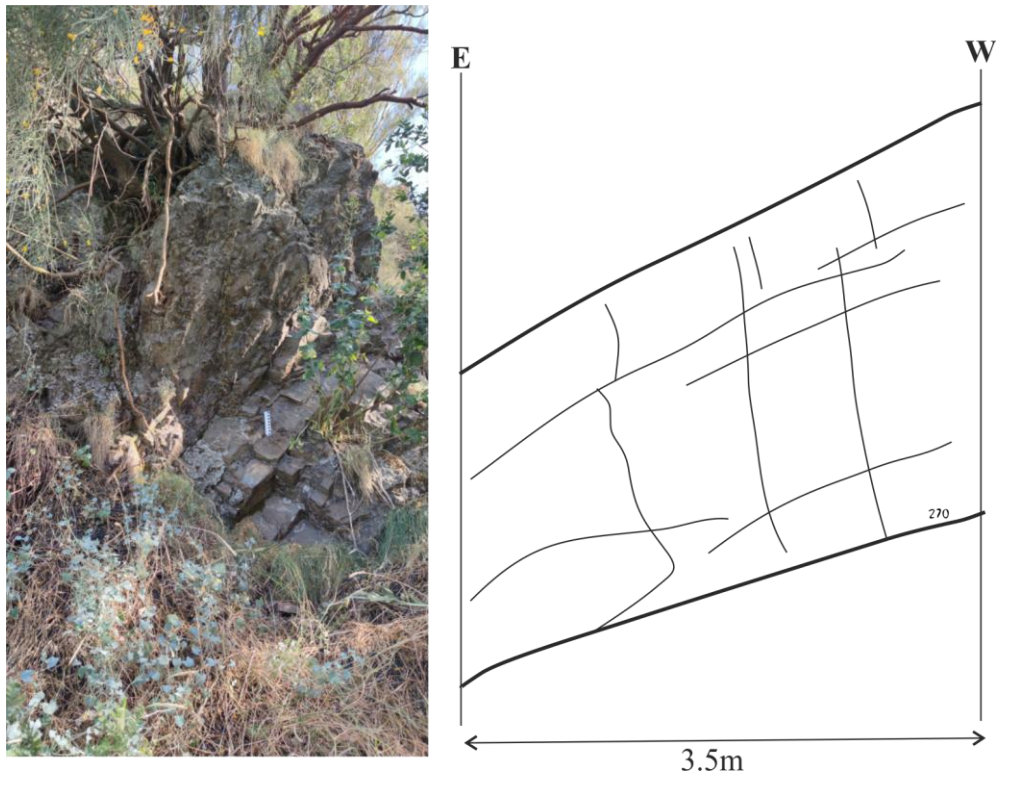
Table 6.S 1. Inventory of Mount Calanna

Geosites	Description with Figure
CD2	CD2 is a sub-vertical embankment with a thickness of 3 m and is oriented in an E-W direction. This is one of the fresh dykes, which can be easily identified. It is deselected by two sets of joints, sub-vertical joints oriented NW-SE and sub-horizontal joints oriented NE-SW. The sub-vertical joints have a spacing of 0.5-8cm on the left side and up to 15cm on the right and central part of the outcrop. Whereas the sub-horizontal joints have a spacing of 3-18 cm. In addition, irregular sub-horizontal fractures and a few randomly oriented phenocrysts are visible on the exposed part of the dykes. The magnetic fabrics give flow direction subparallel to the dyke wall
CD3	It is a highly weathered dyke which is surrounded by bushes and trees and is dissected by two sets of joints, i.e., sub-vertical and sub-horizontal joints. The sub-horizontal joints are homogeneously spaced from 5 to 15 cm, whereas sub-vertical joints don't show any kind of pattern. AMS results show a sub-horizontal magma flow with flow towards SW. This is not a safe geosite to access, as the dykes and the country rocks are highly unstable. Therefore, access to this geosite is not feasible.

CD4	It is a sub-horizontal dyke having a thickness of 1.8m. Reddish-brown alteration masked the original lithology of the dykes. It is characterized by visible phenocrysts and is dissected by both sub-vertical and sub-horizontal joints. The sub-horizontal joints are subparallel to the dyke wall and are more pervasive in the lower part of the outcrop, with spacing between 2 to 10 cm. While the rest are more spaced from 5 to 20 cm. The sub-vertical joints are equally spaced over the outcrop (spacing 10 to 50 cm). The dyke has the inclined flow towards NW. Most of the parts are covered by vegetation and are dangerous to reach.
CD6	It is a NW-SE trending sub-vertical dyke with visible contact with country rock. It has a thickness of 1.2 m and is dissected by both sub-vertical and sub-horizontal joints. The magma flow is inclined and strikes along NW-SE. It is visible without much vegetation.

CD7	It is the smallest dyke identified with a thickness of 1m and oriented E-W. It has highly pervasive fractures and joints. The original lithology was marked by brown-coloured alteration. It has inclined flow along NW-SE. It was mostly covered by the vegetation and ashfall of recent eruptions.
CD8	This dyke is highly fractured by sub-horizontal joints parallel to the dyke plane. The contact between the dyke and the country rock was not visible. It has a thickness of 1 m and has no visible sub-vertical joints. The magma flow is inclined and strikes along NE-SW. The upper part was mostly covered by ash from a recent eruption and by vegetation. Accessing the site was not as easy and dangerous as it was on the cliff.

CD9	It is a sub-horizontal dyke with a NE-SW orientation and a thickness of 3.5 m. The dyke is dissected by numerous sub-horizontal joints parallel to the dyke wall. Magnetic foliation strikes along NE-SW. The dyke is mostly covered by vegetation and lava flows. It is difficult to access.
CD10	It is an altered dyke with the local presence of phenocrysts and vesicles. It is dissected by two sets of joints, sub-vertical and sub-horizontal. It is difficult to access, and it is not easy to distinguish between dyke and country rock.
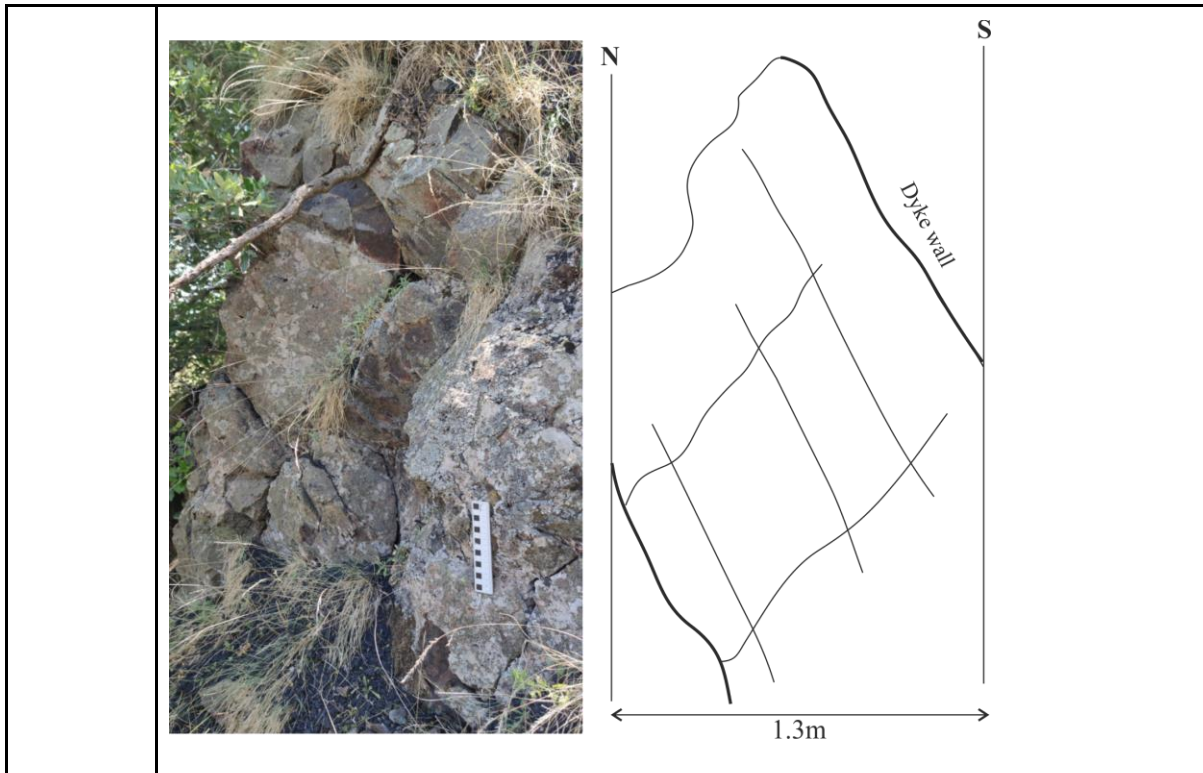
Table 6.S 2. Inventory of San Bartolo geosites

Geosites	Description with Figure
Littoral component	This is one of the most chaotic faces observed at the San Bartolo lava flow. This is well exposed at unit 11. This component is characterized by five different units formed by the interaction of lava with the sea when it is entrained into water. The top unit (A) is the vesicular a'a lava, which drapes the whole unit below. The next unit is characterized by the tilted plates of the shear zone with a thickness of 50cm. Below that are the tilted blocks of vesicular 'a'a lava. This is overlaid by pockets of 'a'a clinker, and the lower part contains balls of 'a'a clinker, which are wrapped by sheared vesicles.

	 a) 4.5 m b) 330N — Surface clinker — 3 m — Beach — Black sand with rounded pebbles of vesicular lava — 4.5 m
Ramp component	The ramp structure is outcropped all along the coast from Spiaggia Lunga in the NW to Sirenetta in the NE. Among them, the well-exposed ramp components are found at unit 4. Here, the ramp components are distinguished by parallel stacking of upward-thrust slabs of 'a'a lava flow. The ramp is formed when the fast-moving lava stalls and slows down after it encounters a break-in slope. Here, we observed five parallel ramps-oriented N-S, with ramp 1 being the well-exposed one. Here, the south end of the ramp, the horizontal tail, is characterized by massive foliated lava with bands of coarse vesicles. Other than that, you can find elongated clinker bands trapped in the foliated lava. At the south end of the ramp, the vertical ramped-up zone got bifurcated by entrained clinkers. In between the two ends, the outcrop is missing for ramp 1, which might be due to anthropogenic action or seawater interaction. This geosite is at one of the most visited beaches in Stromboli, Grotta d'Eeolo. The magnetic foliation on the ramp's northern section exhibits a moderate dip and follows an E-W striking, while the southern half displays a gentle E-W dipping foliation plane.

Channel component	Along the coast of San Bartolo lava flow, we observed two master channels at flows 7 and 2. The channel component observed at flow 7 is considered as the geosite due to their high representativeness and high level of interpretation. Here, the channel is characterized by a right bank rubble levee at the Grotta d'Eeolo and the cave at the centre due to the erosion of breccia. Sheared-aligned breccia and shear plates could be found on the roof of the cave. While the massive lava is distinguished by foliation and clinker entrainment, the levee has angular to subangular breccia clasts. As the cave is 2 m high, most of the tourists go inside and use it as a recreation place. The foliation plane and robust oblate ellipsoid indicate a flow direction towards the WSW. The lack of adequate safety and vulnerability information makes it attractive for people to walk inside the cave.

Table 6.S 3. Geoheritage inventory of geosites from Saint-Nectaire

a) Thones le Vieux lava flow (BTn)

Geosite	Description with Figure
BT1	The 12 m thick lava of BT1 is the base of the entire flow succession of Thones le Vieux at an altitude of 748 m.a.s.l. The upper part of the outcrop is deeply fractured and presents a small block structure. At the base, there is a brecciated and slightly vegetated level, followed by a rather altered metric level with characteristic 'onion skin' structures of several centimeters in diameter. The central part presents a columnar structure with clearly visible horizontally fractured prisms and a maximum height of 1-1.5 meters. At the base of the outcrop, moving slightly along the dirt road, there is a sandstone layer with rounded and heterogeneous pebbles, also of granite composition, approximately 1-2 meters thick. Further down is the granitic basement. The alteration at the base of the outcrop may be related to the presence of circulating water; in addition, the presence of sandy levels with

rounded pebbles somehow testifies to the presence of water or a fluvial system. The presence of such levels of presumably fluvial origin, which delimit the base of BT1 throughout the area, also confirms that this flow constitutes the first volcanic product. The AMS results show well-defined magnetic lineation with flow towards NE. Exposure to outcrops along the trail makes people (both scientific and non-scientific) identify easily. In addition, the different geological structures, such as the onion-skin weathering, columnar joints and colour variations along the outcrop due to weathering, making it an interesting site for tourists.

BT2	The contact between the two facies BT1 and BT2 was not visible topographically, as it was covered by vegetation. The outcrop is divided into two sections. The lower section is intensely deformed, with deformation planes bordering ramp structures, folded layers and segments that appear to give very dense foliation with kinematic indicators, such as shear zones. The lavas are organised in small ramps that tend to become vertical. The top of the outcrop, on the other hand, is characterized by a clearly visible horizontal laminar structure with spherical to oblate vesicles. In addition, the upper part of the outcrop is more vesicular. It is likely that the visible differences in the outcrop are due to a different rate of deformation, as if the upper part was at an earlier stage of deformation and in a more brittle condition, while the part below has undergone more intense deformation, almost at a ductile stage given the shear structures. AMS results show well-defined magnetic lineation with lava flow strikes along NE-SW. Although the site is quite visible from the closest road, accessibility to the site is quite difficult. Also, since the exposed part of the unit is on the sloppy part, it is a little bit dangerous to reach. Anyhow, the ramping and the vesiculated column give a special structure and visual effect to tourists.

| BT5 | This outcrop, as a whole, can be divided into six different parts. At the base, there is a poorly defined and barely visible brecciated level. Above is a level of fragmentarily rectangular blocks. At the top, lava is organised in columns which are at first poorly defined and then more regular and clearer. The lower columns are less developed and have an irregular dimension. Through a gradual transition, we can see the column that has a more continuous development is deformed and tilted 92° to the east. In the upper part of the outcrop, a chaotic and intensely fragmented portion is observed, with fractures perpendicular to the faces of the outcrop. It has a well-defined magnetic foliation with flow along NW-SE. At the top, the outcrop ends with a thin layer of breccias. |

BT7	This outcrop represents the last lava flow of the series at the summit of the relief (839 metres) and is characterized by a wall approximately 3.5 metres high. The outcrop presents a brecciated level at the base, while above it shows a very massive columnar structure, with very massive and only slightly deformed columns, in direct contact with the brecciated level below. The prisms are affected by a network of sub-horizontal fractures that increase towards the top of the outcrop. There are no brecciated levels at the end of the columnar structures. AMS results show lava flow along WNW-ESE.

b) Thones le Farges geosites

BF3	At the base of BF3 a thin layer of sediment, consisting of coarse pebbles, is visible, demonstrating the temporary blocking of the advanced flow and the deposition of a small sedimentary system. The outcrop is very altered and affected by intense fracturing, which compromises the study conditions. A columnar structure can be observed with prisms of metric height. AMS results show a well-defined magnetic foliation plane which strikes along NE-SW.
BF4	At the base of the flow, a thin layer of clay is observed with a fibrous, fossiliferous portion, which appears to resemble a wooden remnant. This clay level indicates the formation of a paleosol and a cessation in the deposition of lava flows. The facies are columnar of varying sizes. The shape of susceptibility ellipsoid is mostly oblate with NE-SW orienting foliation plane. At the top of BF3 is a level of stream sediment composed of quartz, feldspars and pyroxene and lithic fragments immersed in a fine matrix.

Table 6.S 4. Values given by experts and visitors for each sub-indicator for Mount Calanna in the M-GAM model

Main Indicators / Subindicators	Values given by experts (0.00-1.00)											Total									
I Scientific/Educational values (VSE)	GS1	GS2	GS3	GS4	GS5	GS6	GS7	GS8	GS9	GS10	Im	GS1	GS2	GS3	GS4	GS5	GS6	GS7	GS8	GS9	GS10
Rarity (SIMV1)	0.25	0.25	0.25	0.25	0.25	0.25	0.25	0.25	0.25	0.25	0.7	0.175	0.175	0.175	0.175	0.175	0.175	0.175	0.175	0.175	0.175
Representativeness (SIMV2)	0.5	0.75	0	0.5	0.25	0.25	0.25	0	0.25	0	0.9	0.45	0.675	0	0.45	0.225	0.225	0.225	0	0.225	0
Knowledge on geo-scientific issues (SIMV3)	0.75	0.75	0.75	0.75	0.75	0.75	0.75	0.75	0.75	0.75	0.45	0.3375	0.3375	0.3375	0.3375	0.3375	0.3375	0.3375	0.3375	0.3375	0.3375
Level of interpretation (SIMV4)	0.25	0.25	0.25	0.25	0.25	0.25	0.25	0.25	0.25	0.25	0.7	0.175	0.175	0.175	0.175	0.175	0.175	0.175	0.175	0.175	0.175
II Scenic/Aesthetic values (VSA)																					
Viewpoints (each must present a particular angle of view and be situated less than 1 km from the site) (SIMV5)	0	0	0	0	0	0	0	0	0	0	0.65	0.1625	0	0	0	0.1625	0	0	0.1625	0	0.1625
Surface (each considered in quantitative relation to other) (SIMV6)	0	0	0	0	0	0	0	0	0	0	0.35	0	0	0	0	0	0	0	0	0	0
Surrounding landscape and nature (SIMV7)	0.5	0.5	0.5	0.5	0.5	0.5	0.5	0.5	0.5	0.5	0.8	0.4	0.4	0.4	0.4	0.4	0.4	0.4	0.4	0.4	0.4
Environmental fitting of sites (SIMV8)	0.5	0.5	0.5	0.5	0.5	0.5	0.5	0.5	0.5	0.5	0.9	0.45	0.45	0.45	0.45	0.45	0.45	0.45	0.45	0.45	0.45
III Protection (VPr)																					
Current condition (SIMV9)	0.25	0.25	0.25	0.25	0.25	0.25	0.25	0.25	0.25	0.25	0.9	0.225	0.225	0.225	0.225	0.225	0.225	0.225	0.225	0.225	0.225
Protection level (SIMV10)	0	0	0	0	0	0	0	0	0	0	0.65	0	0	0	0	0	0	0	0	0	0
Vulnerability (SIMV11)	0.5	0.5	0.5	0.5	0.5	0.5	0.5	0.5	0.5	0.5	0.85	0.425	0.425	0.425	0.425	0.425	0.425	0.425	0.425	0.425	0.425
Suitable number of visitors (SIMV12)	0.25	0.25	0.25	0.25	0.25	0.25	0.25	0.25	0.25	0.25	1.35	0.3375	0.3375	0.3375	0.3375	0.3375	0.3375	0.3375	0.3375	0.3375	0.3375
I Functional values (VFn)																					
Accessibility (SIAV1)	0.25	0.25	0.25	0.25	0.25	0.25	0.25	0.25	0.25	0.25	0.45	0.1125	0.1125	0.1125	0.1125	0.1125	0.1125	0.1125	0.1125	0.1125	0.1125
Additional natural values (SIAV2)	1	1	1	1	1	1	1	1	1	1	0.6	0.6	0.6	0.6	0.6	0.6	0.6	0.6	0.6	0.6	0.6
Additional anthropogenic values (SIAV3)	0.25	0.25	0.25	0.25	0.25	0.25	0.25	0.25	0.25	0.25	0.35	0.0875	0.0875	0.0875	0.0875	0.0875	0.0875	0.0875	0.0875	0.0875	0.0875
Vicinity of emissive centres (SIAV4)	0.75	0.75	0.75	0.75	0.75	0.75	0.75	0.75	0.75	0.75	0.75	0.5625	0.5625	0.5625	0.5625	0.5625	0.5625	0.5625	0.5625	0.5625	0.5625
Vicinity of important road network (SIAV5)	0.5	0.5	0.5	0.5	0.5	0.5	0.5	0.5	0.5	0.5	0.25	0.125	0.125	0.125	0.125	0.125	0.125	0.125	0.125	0.125	0.125
Additional functional values (SIAV6)	0	0	0	0	0	0	0	0	0	0	0.35	0	0	0	0	0	0	0	0	0	0
II Touristic values (VTr)																					
Promotion (SIAV7)	0	0	0	0	0	0	0	0	0	0	0.6	0	0	0	0	0	0	0	0	0	0
Annual number of organised visits (SIAV8)	0	0	0	0	0	0	0	0	0	0	0.45	0	0	0	0	0	0	0	0	0	0
Vicinity of visitors centre (SIAV9)	0.5	0.5	0.5	0.5	0.5	0.5	0.5	0.5	0.5	0.5	0.4	0.2	0.2	0.2	0.2	0.2	0.2	0.2	0.2	0.2	0.2
Interpretative panels (characteristics of text and graphics, material quality, size, fitting to surroundings, etc.) (SIAV10)	0	0	0	0	0	0	0	0	0	0	0.95	0	0	0	0	0	0	0	0	0	0
Annual number of visitors (SIAV11)	0	0	0	0	0	0	0	0	0	0	0.45	0	0	0	0	0	0	0	0	0	0
Tourism infrastructure (pedestrian pathways, resting places, garbage cans, toilets, wellsprings etc.) (SIAV12)	0	0	0	0	0	0	0	0	0	0	0.35	0	0	0	0	0	0	0	0	0	0
Tour guide service (expertise level, knowledge of foreign language(s), interpretative skills, etc) (SIAV13)	0	0	0	0	0	0	0	0	0	0	0.9	0.225	0.225	0.225	0.225	0.225	0.225	0.225	0.225	0.225	0.225
Hostelry service (SIAV14)	0.75	0.75	0.75	0.75	0.75	0.75	0.75	0.75	0.75	0.75	0.2	0.15	0.15	0.15	0.15	0.15	0.15	0.15	0.15	0.15	0.15
Restaurant service (SIAV15)	0.5	0.5	0.5	0.5	0.5	0.5	0.5	0.5	0.5	0.5	0.2	0.1	0.1	0.1	0.1	0.1	0.1	0.1	0.1	0.1	0.1

Table 6.S 5. Values given by experts and visitors for each sub-indicator for San Bartolo

Main Indicators / Subindicators	Values given by experts (0.00-1.00)						Total				
I Scientific/Educational values (VSE)	GS1	GS2	GS3	GS4	GS5	Im	GS1	GS2	GS3	GS4	GS5
1.Rarity (SIMV1)	0.5	0.5	0.25	0.25	0.25	0.86	0.43	0.43	0.22	0.22	0.22
2.Representativeness (SIMV2)	1	1	0.75	1	1	0.82	0.82	0.82	0.62	0.82	0.82
3.Knowledge on geo-scientific issues (SIMV3)	1	1	1	1	1	0.59	0.59	0.59	0.59	0.59	0.59
4.Level of interpretation (SIMV4)	0.5	0.5	0.5	0.5	0.5	0.79	0.39	0.39	0.39	0.39	0.39
II Scenic/Aesthetic values (VSA)											
1.Viewpoints (each must present a particular angle of view) (SIMV5)	0.5	0.5	0.25	0.5	0.5	0.83	0.41	0.41	0.21	0.41	0.41
2.Surface (each considered in quantitative relation to other) (SIMV6)	0.25	0.75	0.25	0.25	0.75	0.82	0.21	0.62	0.21	0.21	0.62
3.Surrounding landscape and nature (SIMV7)	0.75	0.75	0.75	0.75	0.75	0.86	0.64	0.64	0.64	0.64	0.64
4.Environmental fitting of sites (SIMV8)	0.75	0.75	0.75	1	1	0.85	0.64	0.64	0.64	0.85	0.85
III Protection (VPr)											
1.Current condition (SIMV9)	0.5	0.75	0.25	0.5	0.5	0.69	0.35	0.52	0.17	0.35	0.35
2.Protection level (SIMV10)	0.5	0.5	0.5	0.5	0.5	0.69	0.34	0.34	0.34	0.34	0.34
3.Vulnerability (SIMV11)	0.5	0.5	0.5	0.5	0.5	0.66	0.33	0.33	0.33	0.33	0.33
4.Suitable number of visitors (SIMV12)	0.25	0.75	0.25	0.75	0.75	0.62	0.16	0.47	0.16	0.47	0.47
I Functional values (VFn)											
1. Accessibility (SIAV1)	0.25	0.5	0.25	0.25	0.25	0.71	0.20	0.40	0.20	0.20	0.20
2. Additional natural values (SIAV2)	1	1	1	1	1	0.80	0.61	0.61	0.61	0.61	0.61
3. Additional anthropogenic values (SIAV3)	0.25	0.25	0.25	0.25	0.25	0.61	0.13	0.13	0.13	0.13	0.13
4. Vicinity of emissive centres (SIAV4)	1	1	1	1	1	0.50	0.58	0.58	0.58	0.58	0.58
5. Vicinity of important road network (SIAV5)	0.25	0.25	0.25	0.25	0.25	0.58	0.14	0.14	0.14	0.14	0.14
6. Additional functional values (SIAV6)	0.5	0.5	0.5	0.5	0.5	0.55	0.28	0.34	0.34	0.34	0.34
II Touristic values (VTr)											
1. Promotion (SIAV7)	0.5	0.5	0.5	0.5	0.5	0.68	0.31	0.31	0.31	0.31	0.31
2. Annual number of organised visits (SIAV8)	0.25	0.25	0.25	0.25	0.25	0.61	0.14	0.14	0.14	0.14	0.14
3. Vicinity of visitors centre (SIAV9)	1	1	1	1	1	0.56	0.76	0.76	0.76	0.76	0.76
4. Interpretative panels(SIAV1 0)	0.5	0.75	0.5	0.5	0.75	0.76	0.31	0.46	0.31	0.31	0.46
5. Annual number of visitors (SIAV11)	0.75	0.75	0.75	0.75	0.75	0.61	0.58	0.58	0.58	0.58	0.58
6. Tourism infrastructure (SIAV12)	0.75	0.75	0.75	0.5	0.75	0.77	0.48	0.48	0.48	0.32	0.48
7. Tour guide service (SIAV13)	0.5	0.5	0.5	0.5	0.5	0.64	0.34	0.34	0.34	0.34	0.34
8. Hostelry service (SIAV14)	1	1	1	1	1	0.69	0.69	0.69	0.69	0.69	0.69
9. Restaurant service (SIAV15)	1	1	1	1	1	0.69	0.69	0.69	0.69	0.69	0.69

Table 6.S 6. Values given by experts and visitors for each sub-indicator for Saint-Nectaire

Main Indicators / Subindicators	Values given by experts (0.00-1.00)												Im	Total											
	Thones le Vieux							Thones le Farge						Thones le Vieux							Thones le Farge				
I Scientific/Educational values (VSE)	GS1	GS2	GS3	GS4	GS5	GS6	GS7	GS8	GS9	GS10	GS11	GS12		GS1	GS2	GS3	GS4	GS5	GS6	GS7	GS8	GS9	GS10	GS11	GS12
Rarity (SIMV1)	0.25	0.25	0.25	0.25	0.25	0.25	0.25	0.25	0.25	0.25	0.25	0.25	0.59	0.15	0.15	0.15	0.15	0.15	0.15	0.15	0.15	0.15	0.15	0.15	0.15
Representativeness (SIMV2)	0.5	0.5	0.5	0.25	0	0	0.25	0	0	0.25	0.25	0	0.74	0.37	0.37	0.37	0.19	0.00	0.00	0.19	0.00	0.00	0.19	0.19	0.00
Knowledge on geo-scientific issues (SIMV3)	0.25	0.25	0.25	0.25	0.25	0.25	0.25	0.25	0.25	0.25	0.25	0.25	0.38	0.10	0.10	0.10	0.10	0.10	0.10	0.10	0.10	0.10	0.10	0.10	0.10
Level of interpretation (SIMV4)	0.25	0.25	0.25	0.25	0.25	0.25	0.25	0.25	0.25	0.25	0.25	0.25	0.5	0.13	0.13	0.13	0.13	0.13	0.13	0.13	0.13	0.13	0.13	0.13	0.13
II Scenic/Aesthetic values (VSA)																									
Viewpoints (each must present a particular angle of view and) (SIMV5)	0.5	0.25	0.5	0.75	0	0	0.75	0.25	0	0	0.25	0.75	0.83	0.42	0.21	0.42	0.62	0.00	0.00	0.62	0.21	0.00	0.00	0.21	0.62
Surface (each considered in quantitative relation to other) (SIMV6)	0.5	0.5	0.25	0.75	0.5	0.75	0.25	0.25	0.25	0.25	0.25	0.5	0.75	0.38	0.38	0.19	0.56	0.38	0.56	0.19	0.19	0.19	0.19	0.19	0.38
Surrounding landscape and nature (SIMV7)	0.75	0.75	0.75	0.75	0.75	0.75	1	1	1	1	1	1	0.74	0.56	0.56	0.56	0.56	0.56	0.56	0.74	0.74	0.74	0.74	0.74	0.74
Environmental fitting of sites (SIMV8)	0.5	0.75	0.5	0.5	0.5	0.5	0.5	0.5	0.5	0.5	0.5	0.5	0.75	0.38	0.56	0.38	0.38	0.38	0.38	0.38	0.38	0.38	0.38	0.38	0.38
III Protection (VPr)																									
Current condition (SIMV9)	0.5	0.5	0.5	0.5	0.5	0.5	0.5	0.25	0.25	0.25	0.25	0.25	0.48	0.24	0.24	0.24	0.24	0.24	0.24	0.24	0.12	0.12	0.12	0.12	0.12
Protection level (SIMV10)	0	0	0	0	0	0	0	0	0	0	0		0.38	0.00	0.00	0.00	0.00	0.00	0.00	0.00	0.00	0.00	0.00	0.00	0.00
Vulnerability (SIMV11)	0.5	0.5	0.5	0.5	0.5	0.5	0.5	0.5	0.5	0.5	0.5	0.5	0.64	0.32	0.32	0.32	0.32	0.32	0.32	0.32	0.32	0.32	0.32	0.32	0.32
Suitable number of visitors (SIMV12)	0.5	0.25	0.25	0.25	0.25	0.5	0.5	0.5	0.25	0.5	0.5	0.75	0.5	0.25	0.13	0.13	0.13	0.13	0.25	0.25	0.25	0.13	0.25	0.25	0.38
I Functional values (VFn)																									
Accessibility (SIAV1)	0.75	0.5	0.25	0.5	0.5	0.5	0.5	0.5	0.5	0.25	0.5	0.75	0.86	0.65	0.43	0.22	0.43	0.43	0.43	0.43	0.43	0.43	0.22	0.43	0.65
Additional natural values (SIAV2)	0.75	0.75	0.75	0.75	0.75	0.75	0.75	0.75	0.75	0.75	0.75	0.75	0.63	0.47	0.47	0.47	0.47	0.47	0.47	0.47	0.47	0.47	0.47	0.47	0.47
Additional anthropogenic values (SIAV3)	0.75	0.75	0.75	0.75	0.75	0.75	0.75	0.75	0.75	0.75	0.75	0.75	0.15	0.11	0.11	0.11	0.11	0.11	0.11	0.11	0.11	0.11	0.11	0.11	0.11
Vicinity of emissive centres (SIAV4)	0	0	0	0	0	0	0	0	0	0	0	0	0.25	0.00	0.00	0.00	0.00	0.00	0.00	0.00	0.00	0.00	0.00	0.00	0.00
Vicinity of important road network (SIAV5)	0.5	0.5	0.5	0.5	0.5	0.5	0.5	0.5	0.5	0.5	0.5	0.5	0.54	0.27	0.27	0.27	0.27	0.27	0.27	0.27	0.27	0.27	0.27	0.27	0.27
Additional functional values (SIAV6)	0.25	0.25	0.25	0.25	0.25	0.25	0.25	0.25	0.25	0.25	0.25	0.25	0.42	0.11	0.11	0.11	0.11	0.11	0.11	0.11	0.11	0.11	0.11	0.11	0.11
II Touristic values (VTr)																									
Promotion (SIAV7)	0.25	0.25	0.25	0.25	0.25	0.25	0.25	0.25	0.25	0.25	0.25	0.25	0.26	0.07	0.07	0.07	0.07	0.07	0.07	0.07	0.07	0.07	0.07	0.07	0.07
Annual number of organised visits (SIAV8)	0	0	0	0	0	0	0	0	0	0	0	0	0.12	0.00	0.00	0.00	0.00	0.00	0.00	0.00	0.00	0.00	0.00	0.00	0.00
Vicinity of visitors centre (SIAV9)	0.25	0.25	0.25	0.25	0.25	0.25	0.25	0.25	0.25	0.25	0.25	0.25	0.37	0.09	0.09	0.09	0.09	0.09	0.09	0.09	0.09	0.09	0.09	0.09	0.09
Interpretative panels (characteristics of text and graphics, fitting to surroundings, etc.) (SIAV10)	0.25	0.25	0.25	0.25	0.25	0.25	0.25	0.25	0.25	0.25	0.25	0.25	0.68	0.17	0.17	0.17	0.17	0.17	0.17	0.17	0.17	0.17	0.17	0.17	0.17
Annual number of visitors (SIAV11)	0.25	0.25	0.25	0.25	0.25	0.25	0.25	0.25	0.25	0.25	0.25	0.25	0.21	0.05	0.05	0.05	0.05	0.05	0.05	0.05	0.05	0.05	0.05	0.05	0.05
Tourism infrastructure (pedestrian pathways, resting places, toilets, wellsprings etc.) (SIAV12)	0.5	0.5	0.5	0.5	0.5	0.5	0.5	0.5	0.5	0.5	0.5	0.5	0.32	0.16	0.16	0.16	0.16	0.16	0.16	0.16	0.16	0.16	0.16	0.16	0.16
Tour guide service (expertise level, knowledge of foreign language(s) (SIAV13)	0.25	0.25	0.25	0.25	0.25	0.25	0.25	0.25	0.25	0.25	0.25	0.25	0.27	0.07	0.07	0.07	0.07	0.07	0.07	0.07	0.07	0.07	0.07	0.07	0.07
Hostelry service (SIAV14)	1	1	1	1	1	1	1	1	1	1	1	1	0.1	0.10	0.10	0.10	0.10	0.10	0.10	0.10	0.10	0.10	0.10	0.10	0.10
Restaurant service (SIAV15)	0.75	0.75	0.75	0.75	0.75	0.75	0.75	0.75	0.75	0.75	0.75	0.75	0.45	0.34	0.34	0.34	0.34	0.34	0.34	0.34	0.34	0.34	0.34	0.34	0.34

REFERENCES

Acocella, V., & Neri, M. (2009). Dike propagation in volcanic edifices: Overview and possible developments. *Tectonophysics*, *471*(1–2), 67–77. https://doi.org/10.1016/j.tecto.2008.10.002

Acocella, V., Neri, M., & Scarlato, P. (2006a). Understanding shallow magma emplacement at volcanoes: Orthogonal feeder dikes during the 2002–2003 Stromboli (Italy) eruption. *Geophysical Research Letters*, *33*(17), L17310. https://doi.org/10.1029/2006GL026862

Acocella, V., Porreca, M., Neri, M., Mattei, M., & Funiciello, R. (2006b). Fissure eruptions at Mount Vesuvius (Italy): Insights on the shallow propagation of dikes at volcanoes. *Geology*, *34*(8), 673. https://doi.org/10.1130/G22552.1

Allan M, Dowling RK, Sanders D (2015) The motivations for visiting geosites: the case of Crystal Cave, Western Australia. GeoJournal of Tourism and Geosites 16:141–152

Allred, K. (1998). Lava tube remelt by radiant heat and burning gasses. International Journal of Speleology, 27(1), 13.

Aloisi, M., Bonaccorso, A., Cannavò, F., Gambino, S., Mattia, M., Puglisi, G., & Boschi, E. (2009). A new dyke intrusion style for the Mount Etna May 2008 eruption modelled through continuous tilt and GPS data. *Terra Nova*, *21*(4), 316–321. https://doi.org/10.1111/j.1365-3121.2009.00889.x

Alonso, I., Santana-Sarmiento, F. J., Andrés-Araujo, F., Casamayor, M., Montoya-Montes, I., Brenes, A., Herrera, R., & Sánchez-García, M. J. (2023). Morphosedimentary characteristics and formation mechanisms of new beaches generated after the Tajogaite volcano eruption of 2021 (La Palma, Spain). *Marine Geology*, *462*, 107099. https://doi.org/10.1016/j.margeo.2023.107099

Anderson, E. M. (1937). IX.—The Dynamics of the Formation of Cone-sheets, Ring-dykes, and Caldron-subsidences. *Proceedings of the Royal Society of Edinburgh*, *56*, 128–157. https://doi.org/10.1017/S0370164600014954

Andersson, M., Almqvist, B. S. G., Burchardt, S., Troll, V. R., Malehmir, A., Snowball, I., & Kübler, L. (2016). Magma transport in sheet intrusions of the Alnö carbonatite complex, central Sweden. *Scientific Reports*, *6*(1), 27635. https://doi.org/10.1038/srep27635

Archanjo, C. J., & Launeau, P. (2004). Magma flow inferred from preferred orientations of plagioclase of the Rio Ceará-Mirim dyke swarm (NE Brazil) and its AMS significance. *Geological Society, London, Special Publications*, *238*(1), 285–298. https://doi.org/10.1144/GSL.SP.2004.238.01.17

Arrighi, S., Rosi, M., Tanguy, J., & Courtillot, V. (2004). Recent eruptive history of Stromboli (Aeolian Islands, Italy) determined from high-accuracy archeomagnetic dating. *Geophysical Research Letters*, *31*(19), 2004GL020627. https://doi.org/10.1029/2004GL020627

Atarita, F. R., Bijaksana, S., Ndari, N. R. D. W., Pratama, A., Taqwantara, R. F., Fajar, S. J., & Latief, F. D. E. (2019). Anisotropy of Magnetic Susceptibility and Preferred Pore Orientation in Lava Flow from the Ijen Volcanic Complex, East Java, Indonesia. *Geosciences*, *9*(7), 304. https://doi.org/10.3390/geosciences9070304

Aubourg, C., Tshoso, G., Le Gall, B., Bertrand, H., Tiercelin, J.-J., Kampunzu, A. B., Dyment, J., & Modisi, M. (2008). Magma flow revealed by magnetic fabric in the Okavango giant dyke swarm, Karoo igneous province, northern Botswana. *Journal of Volcanology and Geothermal Research*, *170*(3–4), 247–261. https://doi.org/10.1016/j.jvolgeores.2007.10.013

Aubry, L., Roperch, P., De Urreiztieta, M., Rossello, E., & Chauvin, A. (1996). Paleomagnetic study along the southeastern edge of the Altiplano - Puna Plateau: Neogene tectonic rotations. *Journal of Geophysical Research: Solid Earth*, *101*(B8), 17883–17899. https://doi.org/10.1029/96JB00807

Azzaro, R., Bonforte, A., Branca, S., & Guglielmino, F. (2013). Geometry and kinematics of the fault systems controlling the unstable flank of Etna volcano (Sicily). *Journal of Volcanology and Geothermal Research*, *251*, 5–15. https://doi.org/10.1016/j.jvolgeores.2012.10.001

Bakker, R. R., Fazio, M., Benson, P. M., Hess, K., & Dingwell, D. B. (2016). The propagation and seismicity of dyke injection, new experimental evidence. *Geophysical Research Letters*, *43*(5), 1876–1883. https://doi.org/10.1002/2015GL066852

Balsley, J. R., & Buddington, A. F. (1960). Magnetic susceptibility anisotropy and fabric of some Adirondack granites and orthogneisses. American Journal of Science, 258(6), e20.

Bascou, J., Camps, P., & Marie Dautria, J. (2005). Magnetic versus crystallographic fabrics in a basaltic lava flow. *Journal of Volcanology and Geothermal Research*, *145*(1–2), 119–135. https://doi.org/10.1016/j.jvolgeores.2005.01.007

Besson, J. C. (1978). Les formations volcaniques du versant oriental du massif du Mont-Dore (Massif Central français):(Feuille 1/25 000 Veyre-Montonn° 5-6) (Doctoral dissertation).

Bhatt, S., Rana, V., & Mamtani, M. A. (2017). Deciphering relative timing of fabric development in granitoids with similar absolute ages based on AMS study (Dharwar Craton, South India). *Journal of Structural Geology*, *94*, 32–46. https://doi.org/10.1016/j.jsg.2016.11.002

Bityukova, L., Scholger, R., & Birke, M. (1999). Magnetic susceptibility as indicator of environmental pollution of soils in Tallinn. *Physics and Chemistry of the Earth, Part A: Solid Earth and Geodesy*, *24*(9), 829–835. https://doi.org/10.1016/S1464-1895(99)00122-2

Boiron, T., Bascou, J., Camps, P., Ferré, E. C., Maurice, C., Guy, B., Gerbe, M.-C., & Launeau, P. (2013). Internal structure of basalt flows: Insights from magnetic and crystallographic fabrics of the La Palisse volcanics, French Massif Central. *Geophysical Journal International*, *193*(2), 585–602. https://doi.org/10.1093/gji/ggs115

Borradaile, G. J., & Jackson, M. (2004). Anisotropy of magnetic susceptibility (AMS): Magnetic petrofabrics of deformed rocks. *Geological Society, London, Special Publications*, *238*(1), 299–360. https://doi.org/10.1144/GSL.SP.2004.238.01.18

Bosman, A., Casalbore, D., Romagnoli, C., & Chiocci, F. L. (2014). Formation of an 'a'ā lava delta: Insights from time-lapse multibeam bathymetry and direct observations during the Stromboli 2007 eruption. *Bulletin of Volcanology*, *76*(7), 838. https://doi.org/10.1007/s00445-014-0838-2

Bouchez, J. L. (1997). Granite is Never Isotropic: An Introduction to AMS Studies of Granitic Rocks. In J. L. Bouchez, D. H. W. Hutton, & W. E. Stephens (Eds.), *Granite: From Segregation of Melt to Emplacement Fabrics* (Vol. 8, pp. 95–112). Springer Netherlands. https://doi.org/10.1007/978-94-017-1717-5_6

Božić, S., & Tomić, N. (2015). Canyons and gorges as potential geotourism destinations inSerbia: Comparative analysis from two perspectives – generalgeotourists' and pure geotourists'. *Open Geosciences*, *7*(1), 20150040. https://doi.org/10.1515/geo-2015-0040

Branca, S., Coltelli, M., De Beni, E., & Wijbrans, J. (2008). Geological evolution of Mount Etna volcano (Italy) from earliest products until the first central volcanism (between 500 and 100 ka ago) inferred from geochronological and stratigraphic data. *International Journal of Earth Sciences*, *97*(1), 135–152. https://doi.org/10.1007/s00531-006-0152-0

Branca, S., Coltelli, M., & Groppelli, G. (2004). Geological evolution of Etna volcano. In A. Bonaccorso, S. Calvari, M. Coltelli, C. Del Negro, & S. Falsaperla (Eds.), *Geophysical Monograph Series* (Vol. 143, pp. 49–63). American Geophysical Union. https://doi.org/10.1029/143GM04

Branca, S., De Guidi, G., Lanzafame, G., & Monaco, C. (2014). Holocene vertical deformation along the coastal sector of Mt. Etna volcano (eastern Sicily, Italy): Implications on the time–space constrains of the volcano lateral sliding. *Journal of Geodynamics*, *82*, 194–203. https://doi.org/10.1016/j.jog.2014.07.006

Branca, Stefano. (2011). Geological map of Etna volcano, 1:50,000 scale. *Italian Journal of Geosciences*, *Vol. 130, n. 3*, 265–291. https://doi.org/10.3301/IJG.2011.15

Brousse, R. (1971). Magmatologie du volcanisme néogène et quaternaire du Massif Central. In *Symposium Jean Jung, Plein Air Service, Clermont-Fd* (pp. 377-478).

Burchardt, S., Galland, O., & Németh, K. (2016). Studying volcanic plumbing systems–multidisciplinary approaches to a multifaceted problem. Updates in volcanology-from volcano modelling to volcano geology, 23-53.

Bussey, D. B. J., Guest, J. E., & Sørensen, S. -A. (1997). On the role of thermal conductivity on thermal erosion by lava. *Journal of Geophysical Research: Planets*, *102*(E5), 10905–10908. https://doi.org/10.1029/97JE00415

Cagnoli, B., & Tarling, D. H. (1997). The reliability of anisotropy of magnetic susceptibility (AMS) data as flow direction indicators in friable base surge and ignimbrite deposits: Italian examples. *Journal of Volcanology and Geothermal Research*, *75*(3–4), 309–320. https://doi.org/10.1016/S0377-0273(96)00038-8

Callot, J. P., & Guichet, X. (2003a). Rock texture and magnetic lineation in dykes: A simple analytical model. *Tectonophysics*, *366*(3–4), 207–222. https://doi.org/10.1016/S0040-1951(03)00096-9

Calvari, S., Branca, S., Corsaro, R. A., De Beni, E., Miraglia, L., Norini, G., Wijbrans, J., & Boschi, E. (2011). Reconstruction of the eruptive activity on the NE sector of Stromboli volcano: Timing of flank eruptions since 15 ka. *Bulletin of Volcanology*, *73*(1), 101–112. https://doi.org/10.1007/s00445-010-0412-5

Calvari, S., Marotta, E., Vicari, A., Famiglietti, N. A., Ganci, G., Miraglia, L., Avino, R., Avvisati, G., Belviso, P., Bilotta, G., Cappello, A., D'Ambrosio, C., Moschillo, R., De Luca, G., Memmolo, A., Messina, L., Minichiello, F., & Peluso, R. (2023). *The San Bartolo Lava Flow Field Along the Northeast Flank of Stromboli Volcano: A Preliminary Study for Field Survey*. https://doi.org/10.5281/ZENODO.7760868

Calvari, S., & Pinkerton, H. (1999). Lava tube morphology on Etna and evidence for lava flow emplacement mechanisms. *Journal of Volcanology and Geothermal Research*, *90*(3–4), 263–280. https://doi.org/10.1016/S0377-0273(99)00024-4

Cañón-Tapia, E. (1996). Single-grain versus distribution anisotropy: A simple three-dimensional model. *Physics of the Earth and Planetary Interiors*, *94*(1–2), 149–158. https://doi.org/10.1016/0031-9201(95)03072-7

Cañón-Tapia, E. (2004). Anisotropy of magnetic susceptibility of lava flows and dykes: A historical account. *Geological Society, London, Special Publications*, *238*(1), 205–225. https://doi.org/10.1144/GSL.SP.2004.238.01.14

Cañón-Tapia, E., & Chávez-Álvarez, J. (2004). Theoretical aspects of particle movement in flowing magma: Implications for the anisotropy of magnetic susceptibility of dykes. *Geological Society, London, Special Publications*, *238*(1), 227–249. https://doi.org/10.1144/GSL.SP.2004.238.01.15

Cañón-Tapia, E., & Coe, R. (2002). Rock magnetic evidence of inflation of a flood basalt lava flow. *Bulletin of Volcanology*, *64*(5), 289–302. https://doi.org/10.1007/s00445-002-0203-8

Cañón-Tapia, E., & Pinkerton, H. (2000). The anisotropy of magnetic susceptibility of lava flows: An experimental approach. *Journal of Volcanology and Geothermal Research*, *98*(1–4), 219–233. https://doi.org/10.1016/S0377-0273(99)00155-9

Cañón-Tapia, E., Walker, G. P. L., & Herrero-Bervera, E. (1995). Magnetic fabric and flow direction in basaltic Pahoehoe lava of Xitle volcano, Mexico. *Journal of Volcanology and Geothermal Research*, *65*(3–4), 249–263. https://doi.org/10.1016/0377-0273(94)00110-3

Cañón-Tapia, E., Walker, G. P. L., & Herrero-Bervera, E. (1996). The internal structure of lava flows—insights from AMS measurements I: Near-vent a'a. *Journal of Volcanology and Geothermal Research*, *70*(1–2), 21–36. https://doi.org/10.1016/0377-0273(95)00050-X

Cañón-Tapia, E., Walker, G. P. L., & Herrero-Bervera, E. (1997). The internal structure of lava flows—insights from AMS measurements II: Hawaiian pahoehoe, toothpaste lava and 'a'ā. *Journal of Volcanology and Geothermal Research*, *76*(1–2), 19–46. https://doi.org/10.1016/S0377-0273(96)00073-X

Cardona, C., Gil-Cruz, F., Franco-Marín, L., San Martín, J., Valderrama, O., Lazo, J., Cartes, C., Morales, S., Hernández, E., Quijada, J., Pinto, C., Vidal, M., Bravo, C., Pedreros, G., Contreras, M., Figueroa, M., Córdova, L., Mardones, C., Alarcón, A., … Bucarey, C. (2021). Volcanic activity accompanying the emplacement of dacitic lava domes and effusion of lava flows at Nevados de Chillán Volcanic Complex – Chilean Andes (2012 to 2020). *Journal of Volcanology and Geothermal Research*, *420*, 107409. https://doi.org/10.1016/j.jvolgeores.2021.107409

Cashman, K. V., & Kauahikaua, J. P. (1997). Reevaluation of vesicle distributions in basaltic lava flows. *Geology*, *25*(5), 419. https://doi.org/10.1130/0091-7613(1997)025<0419:ROVDIB>2.3.CO;2

Chadima, M., Cajz, V., & Týcová, P. (2009). On the interpretation of normal and inverse magnetic fabric in dikes: Examples from the Eger Graben, NW Bohemian Massif. *Tectonophysics*, *466*(1–2), 47–63. https://doi.org/10.1016/j.tecto.2008.09.005

Chadima, M., Hrouda, F., 2006. Remasoft 3.0 a user-friendly paleomagnetic data browser and analyzer. Travaux Géophysiques, 27, p.20.

Chadima, M., & Jelínek, V. (2008). Anisoft 4.2.—Anisotropy data browser. *Contributions to Geophysics and Geodesy*, *38*(Special Issue), 38-41.

Chouet, B., Hamisevicz, N., & McGetchin, T. R. (1974). Photoballistics of volcanic jet activity at Stromboli, Italy. *Journal of Geophysical Research*, *79*(32), 4961–4976. https://doi.org/10.1029/JB079i032p04961

Colombier, M., Wadsworth, F. B., Gurioli, L., Scheu, B., Kueppers, U., Di Muro, A., & Dingwell, D. B. (2017). The evolution of pore connectivity in volcanic rocks. *Earth and Planetary Science Letters*, *462*, 99–109. https://doi.org/10.1016/j.epsl.2017.01.011

Correa-Gomes, L. C., Souza Filho, C. R., Martins, C. J. F. N., & Oliveira, E. P. (2001). Development of symmetrical and asymmetrical fabrics in sheet-like igneous bodies: The role of magma flow and wall-rock displacements in theoretical and natural cases. *Journal of Structural Geology*, *23*(9), 1415–1428. https://doi.org/10.1016/S0191-8141(01)00007-4

Coward, M. P. (1980). The analysis of flow profiles in a basaltic dyke using strained vesicles. *Journal of the Geological Society*, *137*(5), 605–615. https://doi.org/10.1144/gsjgs.137.5.0605

Cristofolini, R., Corsaro, R. A., & Ferlito, C. (1991). Variazioni petrochimiche nella successione etnea: un riesame in base a nuovi dati da campioni di superficie e da sondaggi. Acta Vulcanol, 1(2).

Cruden, A. R., & Weinberg, R. F. (2018). Mechanisms of Magma Transport and Storage in the Lower and Middle Crust—Magma Segregation, Ascent and Emplacement. In *Volcanic and Igneous Plumbing Systems* (pp. 13–53). Elsevier. https://doi.org/10.1016/B978-0-12-809749-6.00002-9

Daniels, K. A., & Menand, T. (2015). An experimental investigation of dyke injection under regional extensional stress. *Journal of Geophysical Research: Solid Earth*, *120*(3), 2014–2035. https://doi.org/10.1002/2014JB011627

Das, A., & Mallik, J. (2020). Applicability of AMS technique as a flow fabric indicator in dykes: Insight from Nandurbar–Dhule Deccan dyke swarm. *International Journal of Earth Sciences*, *109*(3), 933–944. https://doi.org/10.1007/s00531-020-01841-9

Das, A., Mallik, J., Bandyopadhyay, K., & Alam, R. (2019). A review of anisotropy of magnetic susceptibility analysis of Indian dykes: Implications for magma emplacement. *Iranian Journal of Earth Sciences*, *11*(1). https://doi.org/10.30495/ijes.2019.544593

Das, A., Mallik, J., & Banerjee, S. (2021). Characterization of the magma flow direction in the Nandurbar-Dhule Deccan dyke swarm inferred from magnetic fabric analysis. *Physics of the Earth and Planetary Interiors*, *319*, 106782. https://doi.org/10.1016/j.pepi.2021.106782

Datta, S., Banerjee, S., Samal, A. K., & Srivastava, R. K. (2023). Aspect ratio analysis of distinct Paleoproterozoic mafic dyke swarms and related fracture systems in the Eastern Dharwar Craton, India: Implications for emplacement mechanism and depth of origin. *Physics of the Earth and Planetary Interiors*, *336*, 106998. https://doi.org/10.1016/j.pepi.2023.106998

De Beni, E., Wijbrans, J. R., Branca, S., Coltelli, M., & Groppelli, G. (2005). New results of 40Ar/39Ar dating constrain the timing of transition from fissure-type to central volcanism at Mount Etna (Italy). *Terra Nova*, *17*(3), 292–298. https://doi.org/10.1111/j.1365-3121.2005.00614.x

De Beni, Emanuela. (2011). 40Ar/39Ar isotopic dating of Etna volcanic succession. *Italian Journal of Geosciences*, *Vol. 130, n. 3*, 292–305. https://doi.org/10.3301/IJG.2011.14

Decker, R. W. (1987). Dynamics of Hawaiian volcanoes: an overview. US Geol. Surv. Prof. Pap, 1350, 997-1018.

DeFrates, J., Malone, D. H., & Craddock, J. P. (2006). Anisotropy of magnetic susceptibility (AMS) analysis of basalt dikes at Cathedral Cliffs, WY: Implications for Heart Mountain faulting. *Journal of Structural Geology*, *28*(1), 9–18. https://doi.org/10.1016/j.jsg.2005.09.002

Delcamp, A., Petronis, M. S., & Troll, V. R. (2014). Discerning magmatic flow patterns in shallow-level basaltic dykes from the NE rift zone of Tenerife, Spain, using the Anisotropy of Magnetic Susceptibility (AMS) technique. *Geological Society, London, Special Publications*, *396*(1), 87–106. https://doi.org/10.1144/SP396.2

Di Traglia, F., Nolesini, T., Solari, L., Ciampalini, A., Frodella, W., Steri, D., Allotta, B., Rindi, A., Marini, L., Monni, N., Galardi, E., & Casagli, N. (2018). Lava delta deformation as a proxy for submarine slope instability. *Earth and Planetary Science Letters*, *488*, 46–58. https://doi.org/10.1016/j.epsl.2018.01.038

Dietterich, H. R., Poland, M. P., Schmidt, D. A., Cashman, K. V., Sherrod, D. R., & Espinosa, A. T. (2012). Tracking lava flow emplacement on the east rift zone of Kīlauea, Hawai'i, with synthetic aperture radar coherence. *Geochemistry Geophysics Geosystems*, *13*, Q05001. https://doi.org/10.1029/2011GC004016

Dowling, R. K. (2011). Geotourism's global growth. Geoheritage, 3(1), 1-13.

Dragoni, M., Lanza, R., & Tallarico, A. (1997). Magnetic anisotropy produced by magma flow: Theoretical model and experimental data from Ferrar dolerite sills (Antarctica). *Geophysical Journal International*, *128*(1), 230–240. https://doi.org/10.1111/j.1365-246X.1997.tb04083.x

Duermeijer, C. E., Van Vugt, N., Langereis, C. G., Meulenkamp, J. E., & Zachariasse, W. J. (1998). A major late Tortonian rotation phase in the Crotone basin using AMS as tectonic tilt correction and timing of the opening of the Tyrrhenian basin. *Tectonophysics*, *287*(1–4), 233–249. https://doi.org/10.1016/S0040-1951(98)80071-1

Dundas, C. M., Keszthelyi, L., Lev, E., Rumpf, M. E., Hamilton, C. W., Höskuldsson, Á., & Thordarson, T. (2020). Lava–water interaction and hydrothermal activity within the 2014–2015 Holuhraun Lava Flow Field, Iceland. *Journal of Volcanology and Geothermal Research*, *408*, 107100. https://doi.org/10.1016/j.jvolgeores.2020.107100

Ellwood, B. B. (1980). Application of the anisotropy of magnetic susceptibility method as an indicator of bottom-water flow direction. *Marine Geology*, *34*(3–4), M83–M90. https://doi.org/10.1016/0025-3227(80)90066-3

Ellwood, B. B. (1978). Flow and emplacement direction determined for selected basaltic bodies using magnetic susceptibility anisotropy measurements. *Earth and Planetary Science Letters*, *41*(3), 254–264. https://doi.org/10.1016/0012-821X(78)90182-6

Eriksson, P. I., Riishuus, M. S., & Elming, S.-Å. (2015). Magma flow and palaeo-stress deduced from magnetic fabric analysis of the Álftafjörður dyke swarm: Implications for shallow crustal magma transport in Icelandic volcanic systems. *Geological Society, London, Special Publications*, *396*(1), 107–132. https://doi.org/10.1144/SP396.6

Ernst, R. E., & Baragar, W. R. A. (1992). Evidence from magnetic fabric for the flow pattern of magma in the Mackenzie giant radiating dyke swarm. *Nature*, *356*(6369), 511–513. https://doi.org/10.1038/356511a0

Fagents, S., & Greeley, R. (2001). Factors influencing lava-substrate heat transfer and implications for thermomechanical erosion. *Bulletin of Volcanology*, *62*(8), 519–532. https://doi.org/10.1007/s004450000113

Fanjat, G., Camps, P., Shcherbakov, V., Barou, F., Sougrati, M. T., & Perrin, M. (2012). Magnetic interactions at the origin of abnormal magnetic fabrics in lava flows: A case study from Kerguelen flood basalts: Magnetic interactions at the origin of abnormal AMS. *Geophysical Journal International*, *189*(2), 815–832. https://doi.org/10.1111/j.1365-246X.2012.05421.x

Ferlito, C., & Nicotra, E. (2010). The dyke swarm of Mount Calanna (Etna, Italy): An example of the uppermost portion of a volcanic plumbing system. *Bulletin of Volcanology*, *72*(10), 1191–1207. https://doi.org/10.1007/s00445-010-0398-z

Ferrari, L., Calvari, S., Coltelli, M., Innocenti, F., Pasquarè, G., Pompilio, M., Vezzoli, L& Villa, I. (1989). Nuovi dati geologici e strutturali sulla Valle di Calanna, Etna: implicazioni per l'evoluzione del vulcanismo etneo. *Boll. GNV*, *2*, 849-860.

Fisher, R. (1953). Dispersion on a Sphere. *Proceedings of the Royal Society A: Mathematical, Physical and Engineering Sciences*, *217*(1130), 295–305. https://doi.org/10.1098/rspa.1953.0064

Francalanci, L., Braschi, E., Di Salvo, S., Lucchi, F., & Petrone, C. M. (2014). When magmas do not interact: Paired Roman-age activity revealed by tephra studies at Stromboli volcano. *Bulletin of Volcanology*, *76*(12), 884. https://doi.org/10.1007/s00445-014-0884-9

Francalanci, L., Lucchi, F., Keller, J., De Astis, G., & Tranne, C. A. (2013). Chapter 13 Eruptive, volcano-tectonic and magmatic history of the Stromboli volcano (north-eastern Aeolian archipelago). *Geological Society, London, Memoirs*, *37*(1), 397–471. https://doi.org/10.1144/M37.13

Francalanci, L., Manetti, P., & Peccerillo, A. (1989). Volcanological and magmatological evolution of Stromboli volcano (Aeolian Islands): The roles of fractional crystallization, magma mixing, crustal contamination and source heterogeneity. *Bulletin of Volcanology*, *51*(5), 355–378. https://doi.org/10.1007/BF01056897

Francis, P. (1993). Volcanoes. A planetary perspective. In *Volcanoes. A planetary perspective*. https://ui.adsabs.harvard.edu/abs/1993vpp..book.....F

Franco, D. R., & Hinnov, L. A. (2013). Anisotropy of magnetic susceptibility and sedimentary cycle data from Permo-Carboniferous rhythmites (Paraná Basin, Brazil): A multiple proxy record of astronomical and millennial scale palaeoclimate change in a glacial setting. *Geological Society, London, Special Publications*, *373*(1), 355–374. https://doi.org/10.1144/SP373.11

Fuller, M. D. (1963). Magnetic anisotropy and paleomagnetism. *Journal of Geophysical Research*, *68*(1), 293–309. https://doi.org/10.1029/JZ068i001p00293

Geoffroy, L., Aubourg, C., Callot, J.-P., & Barrat, J.-A. (2007). Mechanisms of crustal growth in large igneous provinces: The north Atlantic province as a case study. In *Special Paper 430: Plates, Plumes and Planetary Processes* (Vol. 430, pp. 747–774). Geological Society of America. https://doi.org/10.1130/2007.2430(34)

Geoffroy, L., Callot, J. P., Aubourg, C., & Moreira, M. (2002). Magnetic and plagioclase linear fabric discrepancy in dykes: A new way to define the flow vector using magnetic foliation. *Terra Nova*, *14*(3), 183–190. https://doi.org/10.1046/j.1365-3121.2002.00412.x

Geshi, N. (2008). Vertical and lateral propagation of radial dikes inferred from the flow-direction analysis of the radial dike swarm in Komochi Volcano, Central Japan. *Journal of Volcanology and Geothermal Research*, *173*(1–2), 122–134. https://doi.org/10.1016/j.jvolgeores.2008.01.001

Gillot, P. Y., Kieffer, G., & Romano, R. (1994). The evolution of Mount Etna in the light of potassium-argon dating. Acta Vulcanol, 5, 81-87.

Giordano, G., Porreca, M., Musacchio, P., & Mattei, M. (2008). The Holocene Secche di Lazzaro phreatomagmatic succession (Stromboli, Italy): Evidence of pyroclastic density current origin deduced by facies analysis and AMS flow directions. *Bulletin of Volcanology*, *70*(10), 1221–1236. https://doi.org/10.1007/s00445-008-0198-x

Graham, J. W. (1954). Magnetic susceptibility, an unexploited element of petrofabric. Geological Society of American Bulletin, 65, 1257-1258.

Greeley, R., & Baer, R. (1971). Hambone, California and its magnificent lava tubes-Preliminary report. In Geol. Soc. Am. Abstr. Programs (Vol. 3, p. 128).

Gudmundsson, A. (1990). Emplacement of dikes, sills and crustal magma chambers at divergent plate boundaries. *Tectonophysics*, *176*(3–4), 257–275. https://doi.org/10.1016/0040-1951(90)90073-H

Guimarães, L. F., Raposo, M. I. B., Janasi, V. A., Cañón-Tapia, E., & Polo, L. A. (2018). An AMS study of different silicic units from the southern Paraná-Etendeka Magmatic Province in Brazil: Implications for the identification of flow directions and local sources. *Journal of Volcanology and Geothermal Research*, *355*, 304–318. https://doi.org/10.1016/j.jvolgeores.2017.11.014

Gvirtzman, Z., & Nur, A. (1999). The formation of Mount Etna as the consequence of slab rollback. *Nature*, *401*(6755), 782–785. https://doi.org/10.1038/44555

Hachimi, H. E., Youbi, N., Madeira, J., Bensalah, M. K., Martins, L., Mata, J., Medina, F., Bertrand, H., Marzoli, A., Munhá, J., Bellieni, G., Mahmoudi, A., Abbou, M. B., & Assafar, H. (2011). Morphology, internal architecture and emplacement mechanisms of lava flows from the Central Atlantic Magmatic Province (CAMP) of Argana Basin (Morocco). *Geological Society, London, Special Publications*, *357*(1), 167–193. https://doi.org/10.1144/SP357.9

Hargraves, R. B., Johnson, D., & Chan, C. Y. (1991). Distribution anisotropy: The cause of AMS in igneous rocks? *Geophysical Research Letters*, *18*(12), 2193–2196. https://doi.org/10.1029/91GL01777

Harris, A. J. L., & Rowland, S. K. (2015). Lava Flows and Rheology. In *The Encyclopedia of Volcanoes* (pp. 321–342). Elsevier. https://doi.org/10.1016/B978-0-12-385938-9.00017-1

Hastie, W. W., Aubourg, C., & Watkeys, M. K. (2011a). When an 'inverse' fabric is not inverse: An integrated AMS-SPO study in MORB-like dykes: Inverse fabric: an integrated study. *Terra Nova*, *23*(1), 49–55. https://doi.org/10.1111/j.1365-3121.2010.00983.x

Hastie, W. W., Watkeys, M. K., & Aubourg, C. (2011b). Significance of magnetic and petrofabric in Karoo-feeder dykes, northern Lebombo. *Tectonophysics*, *513*(1–4), 96–111. https://doi.org/10.1016/j.tecto.2011.10.008

Hastie, W. W., Watkeys, M. K., & Aubourg, C. (2014). Magma flow in dyke swarms of the Karoo LIP: Implications for the mantle plume hypothesis. *Gondwana Research*, *25*(2), 736–755. https://doi.org/10.1016/j.gr.2013.08.010

Henry, B., Plenier, G., & Camps, P. (2003). Post-emplacement tilting of lava flows inferred from magnetic fabric study: The example of Oligocene lavas in the Jeanne d'Arc Peninsula (Kerguelen Islands). *Journal of Volcanology and Geothermal Research*, *127*(1–2), 153–164. https://doi.org/10.1016/S0377-0273(03)00198-7

Herrero-Bervera, E., Cañon-Tapia, E., Walker, G. P. L., & Tanaka, H. (2002). Magnetic fabrics study and inferred flow directions of lavas of the Old Pali Road, O'ahu, Hawaii. *Journal of Volcanology and Geothermal Research*, *118*(1–2), 161–171. https://doi.org/10.1016/S0377-0273(02)00255-X

Hext, G. R. (1963). The estimation of second-order tensors, with related tests and designs. *Biometrika*, *50*(3–4), 353–373. https://doi.org/10.1093/biomet/50.3-4.353

Hirt, A. M., & Almqvist, B. S. G. (2011). Unraveling magnetic fabrics. *International Journal of Earth Sciences*, *101*(3), 613–624. https://doi.org/10.1007/s00531-011-0664-0

Hon, K., Kauahikaua, J., Denlinger, R., & Mackay, K. (1994). Emplacement and inflation of pahoehoe sheet flows: Observations and measurements of active lava flows on Kilauea Volcano, Hawaii. *Geological Society of America Bulletin*, *106*(3), 351–370. https://doi.org/10.1130/0016-7606(1994)106<0351:EAIOPS>2.3.CO;2

Houghton, B. F., & Wilson, C. J. N. (1989). A vesicularity index for pyroclastic deposits. *Bulletin of Volcanology*, *51*(6), 451–462. https://doi.org/10.1007/BF01078811

Hrouda, F. (1982). Magnetic anisotropy of rocks and its application in geology and geophysics. *Geophysical Surveys*, *5*(1), 37–82. https://doi.org/10.1007/BF01450244

Hrouda, F. (1993). Theoretical models of magnetic anisotropy to strain relationship revisited. *Physics of the Earth and Planetary Interiors*, *77*(3–4), 237–249. https://doi.org/10.1016/0031-9201(93)90101-E

Hrouda, F., Chlupáčová, M., Schulmann, K., Šmíd, J., & Závada, P. (2005). On the effect of lava viscosity on the magnetic fabric intensity in alkaline volcanic rocks. *Studia Geophysica et Geodaetica*, *49*(2), 191–212. https://doi.org/10.1007/s11200-005-0005-5

Hrouda, F., Faryad, S., Kubínová, Š., Verner, K., & Chlupáčová, M. (2019). Simultaneous Free Flow and Forcefully Driven Movement of Magma in Lamprophyre Dykes as Indicated by Magnetic Anisotropy: Case Study from the Central Bohemian Dyke Swarm, Czech Republic. *Geosciences*, *9*(3), 104. https://doi.org/10.3390/geosciences9030104

Hughes, J. W. (1990). Changing styles of effusive eruption on Mount Etna since AD 1600. *Magma transport and storage*, 385-406.

Hulme, G. (1974). The Interpretation of Lava Flow Morphology. *Geophysical Journal International*, *39*(2), 361–383. https://doi.org/10.1111/j.1365-246X.1974.tb05460.x

Jelínek, V. (1977). The statistical theory of measuring anisotropy of magnetic susceptibility of rocks and its application (Vol. 29, pp. 1-87). Brno, Czech Republic: Geofyzika.

Jelínek, V. (1978). Statistical processing of anisotropy of magnetic susceptibility measured on groups of specimens. *Studia Geophysica et Geodaetica*, *22*(1), 50–62. https://doi.org/10.1007/BF01613632

Jelinek, V. (1981). Characterization of the magnetic fabric of rocks. *Tectonophysics*, *79*(3–4), T63–T67. https://doi.org/10.1016/0040-1951(81)90110-4

Jenks, M. D., Bonnichsen, B., & Chamberlain, V. E. (1989). Subaqueous basalt eruptions into Pliocene Lake Idaho, Snake River Plain, Idaho. Guidebook to the geology of northern and western Idaho and surrounding area: Idaho Geological Survey Bulletin, 28, 17-34.

Jonić, V. (2018). Comparative analysis of Devil's town and Bryce canyon geosites by applying the modified geosite assessment model (M-GAM). *Zbornik Radova Departmana Za Geografiju, Turizam i Hotelijerstvo*, *47–2*, 113–125. https://doi.org/10.5937/ZbDght1802113J

Jurado-Chichay, Z., Rowland, S. K., & Walker, G. P. L. (1996). The formation of circular littoral cones from tube-fed p?hoehoe: Mauna Loa, Hawai'i. *Bulletin of Volcanology*, *57*(7), 471–482. https://doi.org/10.1007/BF00304433

Keating, G. N., Valentine, G. A., Krier, D. J., & Perry, F. V. (2008). Shallow plumbing systems for small-volume basaltic volcanoes. *Bulletin of Volcanology*, *70*(5), 563–582. https://doi.org/10.1007/s00445-007-0154-1

Kent, D. V., & Lowrie, W. (1975). On the magnetic susceptibility anisotropy of deep-sea sediment. *Earth and Planetary Science Letters*, *28*(1), 1–12. https://doi.org/10.1016/0012-821X(75)90067-9

Kerr, R. C. (2001). Thermal erosion by laminar lava flows. *Journal of Geophysical Research: Solid Earth*, *106*(B11), 26453–26465. https://doi.org/10.1029/2001JB000227

Kerr, R. C. (2009). Thermal erosion of felsic ground by the laminar flow of a basaltic lava, with application to the Cave Basalt, Mount St. Helens, Washington. *Journal of Geophysical Research: Solid Earth*, *114*(B9), 2009JB006430. https://doi.org/10.1029/2009JB006430

Khalifa, K. (2013). The Role of Explanation in Understanding. *The British Journal for the Philosophy of Science*, *64*(1), 161–187. https://doi.org/10.1093/bjps/axr057

Khan, M. A. (1962). The anisotropy of magnetic susceptibility of some igneous and metamorphic rocks. *Journal of Geophysical Research*, *67*(7), 2873–2885. https://doi.org/10.1029/JZ067i007p02873

Kilburn, C. R. (2000). Lava flows and flow fields. Encyclopedia of volcanoes, 291-305.

Kirschvink, J. L. (1980). The least-squares line and plane and the analysis of palaeomagnetic data. *Geophysical Journal International*, *62*(3), 699–718. https://doi.org/10.1111/j.1365-246X.1980.tb02601.x

Kiyosugi, K., Connor, C. B., Wetmore, P. H., Ferwerda, B. P., Germa, A. M., Connor, L. J., & Hintz, A. R. (2012). Relationship between dike and volcanic conduit distribution in a highly eroded monogenetic volcanic field: San Rafael, Utah, USA. *Geology*, *40*(8), 695–698. https://doi.org/10.1130/G33074.1

Klerkx, J. (1970). La caldera de la Valle del Bove: Sa signification dans l'évolution de l'Etna (Sicile). *Bulletin Volcanologique*, *34*(3), 726–737. https://doi.org/10.1007/BF02596701

Knight, M. D., & Walker, G. P. L. (1988). Magma flow directions in dikes of the Koolau Complex, Oahu, determined from magnetic fabric studies. *Journal of Geophysical Research: Solid Earth*, *93*(B5), 4301–4319. https://doi.org/10.1029/JB093iB05p04301

Kolofikova, O. (1976). Geological interpretation of magnetic properties of basalts an example of the Chribsky Les lava flow of the Velky Roudny volcano (Nizky Jesenik, Cas). Mineral. Geol., 21, 387-396.

Köpping, J., Cruden, A. R., Magee, C., McCarthy, W., Geissman, J., & Holm, D. (2023). Magnetic fabrics reveal three-dimensional flow processes within elongate magma fingers at the margin of the Shonkin Sag laccolith (MT, USA). *Journal of Structural Geology*, *169*, 104829. https://doi.org/10.1016/j.jsg.2023.104829

Kauahikaua J, Denlinger R, Foster J, & Keszthelyi L (1993). Lava delta instability: Is it mass-wasting or is it triggered by lava flowing through tubes. Eos, Transactions, 74, 616.

Laiolo, M., & Cigolini, C. (2006). Mafic and ultramafic xenoliths in San Bartolo lava field: New insights on the ascent and storage of Stromboli magmas. *Bulletin of Volcanology*, *68*(7–8), 653–670. https://doi.org/10.1007/s00445-005-0040-7

Lambeck, K., Antonioli, F., Purcell, A., & Silenzi, S. (2004). Sea-level change along the Italian coast for the past 10,000yr. *Quaternary Science Reviews*, *23*(14–15), 1567–1598. https://doi.org/10.1016/j.quascirev.2004.02.009

Le Maitre, R. W., Streckeisen, A., Zanettin, B., Le Bas, M. J., Bonin, B., & Bateman, P. (Eds.). (2002). *Igneous Rocks: A Classification and Glossary of Terms* (2nd ed.). Cambridge University Press. https://doi.org/10.1017/CBO9780511535581

Lefort, J.-P., Aïfa, T., Jelenska, M., Kadzialko-Hofmokl, M., & Max, M. D. (2001). Paleomagnetic and AMS evidence for a Variscan ductile clockwise rotation of the île de Groix blueschists (South Brittany, France): Consequence on the Late Hercynian structural pattern of westernmost Europe. *Tectonophysics*, *337*(3–4), 223–235. https://doi.org/10.1016/S0040-1951(01)00118-4

Lesage, L., (2013). Étude morphologique, pétrologique et géochimique des coulées de laves de Thônes le Vieux et de Farges. Thesis, Université Blaise Pascal, Clermont-Ferrand.

Lister, J. R., & Kerr, R. C. (1991). Fluid-mechanical models of crack propagation and their application to magma transport in dykes. *Journal of Geophysical Research*, *96*(B6), 10049. https://doi.org/10.1029/91JB00600

Lipman PW, & Banks NG (1987). A'a flow dynamics, 1984 Mauna Loa eruption. US Geol. Surv. Prof. Pap, 1350, 1527-1567.

Lo Giudice, E., PATANÈ, G., Rasà, R., & ROMANO, R. (1982). The structural framework of Mount Etna. Memorie della Società Geologica Italiana, 23, 125-158.

Loock, S., Diot, H., Van Wyk De Vries, B., Launeau, P., Merle, O., Vadeboin, F., & Petronis, M. S. (2008). Lava flow internal structure found from AMS and textural data: An example in methodology from the Chaîne des Puys, France. *Journal of Volcanology and Geothermal Research*, *177*(4), 1092–1104. https://doi.org/10.1016/j.jvolgeores.2008.08.017

Lowrie, W. (1990). Identification of ferromagnetic minerals in a rock by coercivity and unblocking temperature properties. *Geophysical Research Letters*, *17*(2), 159–162. https://doi.org/10.1029/GL017i002p00159

Lubnina, N. V., Stepanova, A. V., Ernst, R. E., Nilsson, M., & Söderlund, U. (2016). New U–Pb baddeleyite age, and AMS and paleomagnetic data for dolerites in the Lake Onega region belonging to the 1.98–1.95 Ga regional Pechenga–Onega Large Igneous Province. *GFF*, *138*(1), 54–78. https://doi.org/10.1080/11035897.2015.1129549

Lyra, D. S., Savian, J. F., Bitencourt, M. D. F., Trindade, R. I. F., & Tomé, C. R. (2018). AMS fabrics and emplacement model of Butiá Granite, an Ediacaran syntectonic peraluminous granite from southernmost Brazil. *Journal of South American Earth Sciences*, *87*, 25–41. https://doi.org/10.1016/j.jsames.2017.12.006

Macdonald, G. A. (1972). Composite Lava Flows on Haleakala Volcano, Hawaii. *Geological Society of America Bulletin*, *83*(10), 2971. https://doi.org/10.1130/0016-7606(1972)83[2971:CLFOHV]2.0.CO;2

Maeno, F., Nakada, S., & Kaneko, T. (2016). Morphological evolution of a new volcanic islet sustained by compound lava flows. *Geology*, *44*(4), 259–262. https://doi.org/10.1130/G37461.1

Maeno, F., & Taniguchi, H. (2006). Silicic lava dome growth in the 1934–1935 Showa Iwo-jima eruption, Kikai caldera, south of Kyushu, Japan. *Bulletin of Volcanology*, *68*(7–8), 673–688. https://doi.org/10.1007/s00445-005-0042-5

Matasova, G., Petrovský, E., Jordanova, N., Zykina, V., & Kapička, A. (2001). Magnetic study of Late Pleistocene loess/palaeosol sections from Siberia: Palaeoenvironmental implications. *Geophysical Journal International*, *147*(2), 367–380. https://doi.org/10.1046/j.0956-540x.2001.01544.x

Mattox, T. N., & Mangan, M. T. (1997). Littoral hydrovolcanic explosions: A case study of lava–seawater interaction at Kilauea Volcano. *Journal of Volcanology and Geothermal Research*, *75*(1–2), 1–17. https://doi.org/10.1016/S0377-0273(96)00048-0

Maxbauer, D. P., Feinberg, J. M., & Fox, D. L. (2016). MAX UnMix: A web application for unmixing magnetic coercivity distributions. *Computers & Geosciences*, *95*, 140–145. https://doi.org/10.1016/j.cageo.2016.07.009

McDonough, W. F., & Sun, S. -s. (1995). The composition of the Earth. *Chemical Geology*, *120*(3–4), 223–253. https://doi.org/10.1016/0009-2541(94)00140-4

McGuire, W. J. (1982). Evolution of the etna volcano: Information from the southern wall of the Valle Del Bove Caldera. *Journal of Volcanology and Geothermal Research*, *13*(3–4), 241–271. https://doi.org/10.1016/0377-0273(82)90053-1

McGuire, W. J., & Pullen, A. D. (1989). Location and orientation of eruptive fissures and feederdykes at Mount Etna; influence of gravitational and regional tectonic stress regimes. *Journal of Volcanology and Geothermal Research*, *38*(3–4), 325–344. https://doi.org/10.1016/0377-0273(89)90046-2

Mertanen, S., & Karell, F. R. E. D. R. I. K. (2011). Rock magnetic investigations constraining relative timing for gold deposits in Finland. *Bulletin of the Geological Society of Finland*, *83*(2), 75-94.

Minakov, A., Yarushina, V., Faleide, J. I., Krupnova, N., Sakoulina, T., Dergunov, N., & Glebovsky, V. (2018). Dyke emplacement and crustal structure within a continental large igneous province, northern Barents Sea. *Geological Society, London, Special Publications*, *460*(1), 371–395. https://doi.org/10.1144/SP460.4

Monaco, C., Catalano, S., Cocina, O., De Guidi, G., Ferlito, C., Gresta, S., Musumeci, C., & Tortorici, L. (2005). Tectonic control on the eruptive dynamics at Mt. Etna Volcano (Sicily) during the 2001 and 2002–2003 eruptions. *Journal of Volcanology and Geothermal Research*, *144*(1–4), 211–233. https://doi.org/10.1016/j.jvolgeores.2004.11.024

Monaco, C., Tapponnier, P., Tortorici, L., & Gillot, P. Y. (1997). Late Quaternary slip rates on the Acireale-Piedimonte normal faults and tectonic origin of Mt. Etna (Sicily). *Earth and Planetary Science Letters*, *147*(1–4), 125–139. https://doi.org/10.1016/S0012-821X(97)00005-8

Monaco, Carmelo, De Guidi, Giorgio, & Ferlito, Carmelo. (2010). The Morphotectonic map of Mt. Etna. *Italian Journal of Geosciences*, *3*, 408–428. https://doi.org/10.3301/IJG.2010.11

Moore, J. G., Phillips, R. L., Grigg, R. W., Peterson, D. W., & Swanson, D. A. (1973). Flow of Lava into the Sea, 1969–1971, Kilauea Volcano, Hawaii. *Geological Society of America Bulletin*, *84*(2), 537. https://doi.org/10.1130/0016-7606(1973)84<537:FOLITS>2.0.CO;2

Moreira, M., Geoffroy, L., & Pozzi, J.-P. (1999). Ecoulement magmatique dans les dykes du point chaud des Açores: Étude préliminaire par anisotropie de susceptibilité magnétique (ASM) dans l'île de San Jorge. *Comptes Rendus de l'Académie des Sciences - Series IIA - Earth and Planetary Science*, *329*(1), 15–22. https://doi.org/10.1016/S1251-8050(99)80222-5

Moskowitz, B. M. (1981). Methods for estimating Curie temperatures of titanomaghemites from experimentalJs-T data. *Earth and Planetary Science Letters*, *53*(1), 84–88. https://doi.org/10.1016/0012-821X(81)90028-5

Mueller, W. U., Garde, A. A., & Stendal, H. (2000). Shallow-water, eruption-fed, mafic pyroclastic deposits along a Paleoproterozoic coastline: Kangerluluk volcano-sedimentary sequence, southeast Greenland. *Precambrian Research*, *101*(2–4), 163–192. https://doi.org/10.1016/S0301-9268(99)00087-X

Mulas, M., Cioni, R., Andronico, D., & Mundula, F. (2016). The explosive activity of the 1669 Monti Rossi eruption at Mt. Etna (Italy). *Journal of Volcanology and Geothermal Research*, *328*, 115–133. https://doi.org/10.1016/j.jvolgeores.2016.10.012

Nagaraju, E., & Parashuramulu, V. (2019). AMS studies on a 450 km long 2216 Ma dyke from Dharwar craton, India: Implications to magma flow. *Geoscience Frontiers*, *10*(5), 1931–1939. https://doi.org/10.1016/j.gsf.2018.12.003

Nagata, T. (1961). Rock magnetism, Maruzen, Tokyo. Nnange, J. Mining, Poudjom Djomani, 350.

Németh, K., & Martin, U. (2007). Shallow sill and dyke complex in western Hungary as a possible feeding system of phreatomagmatic volcanoes in "soft-rock" environment. *Journal of Volcanology and Geothermal Research*, *159*(1–3), 138–152. https://doi.org/10.1016/j.jvolgeores.2006.06.014

Nicotra, E., Ferlito, C., Viccaro, M., & Cristofolini, R. (2011). Volcanic geology and petrology of the Val Calanna succession (Mt. Etna, Southern Italy): Discovery of a new eruptive center. *Periodico Di Mineralogia*, *80*(2), 287–307. https://doi.org/10.2451/2011PM0021

Nicotra, E., & Viccaro, M. (2012). Unusual magma storage conditions at Mt. Etna (Southern Italy) as evidenced by plagioclase megacryst-bearing lavas: Implications for the plumbing system geometry and summit caldera collapse. *Bulletin of Volcanology*, *74*(4), 795–815. https://doi.org/10.1007/s00445-011-0566-9

Nicotra, E., Viccaro, M., Ferlito, C., & Cristofolini, R. (2010). Influx of volatiles into shallow reservoirs at Mt. Etna volcano (Italy) responsible for halogen-rich magmas. *European Journal of Mineralogy*, *22*(1), 121–138. https://doi.org/10.1127/0935-1221/2010/0022-1991

Obata, S., & Umino, S. (1999). Morphology of AD 864 Aokigahara lava flow exposed on the coast of Motosuko Lake, Fuji Volcano. Kazan, 44(4), 201-216.

Ohashi, M., Ichihara, M., & Toramaru, A. (2018). Bubble deformation in magma under transient flow conditions. *Journal of Volcanology and Geothermal Research*, *364*, 59–75. https://doi.org/10.1016/j.jvolgeores.2018.09.005

Otmane, K., Errami, E., Olivier, P., Berger, J., Triantafyllou, A., & Ennih, N. (2018). Magnetic fabric and flow direction in the Ediacaran Imider dyke swarms (Eastern Anti-Atlas, Morocco), inferred from the Anisotropy of Magnetic Susceptibility (AMS). *Journal of African Earth Sciences*, *139*, 55–72. https://doi.org/10.1016/j.jafrearsci.2017.11.030

Pan, X., Shen, Z., Roberts, A. P., Heslop, D., & Shi, L. (2014). Syntectonic emplacement of Late Cretaceous mafic dyke swarms in coastal southeastern China: Insights from magnetic fabrics, rock magnetism and field evidence. *Tectonophysics*, *637*, 328–340. https://doi.org/10.1016/j.tecto.2014.10.018

Park, J. K., Tanczyk, E. I., & Desbarats, A. (1988). Magnetic Fabric and Its Significance in the 1400 Ma Mealy Diabase Dykes of Labrador, Canada. *Journal of Geophysical Research: Solid Earth*, *93*(B11), 13689–13704. https://doi.org/10.1029/JB093iB11p13689

Passey, S. R., & Bell, B. R. (2007). Morphologies and emplacement mechanisms of the lava flows of the Faroe Islands Basalt Group, Faroe Islands, NE Atlantic Ocean. *Bulletin of Volcanology*, *70*(2), 139–156. https://doi.org/10.1007/s00445-007-0125-6

Patrick, M. R., Harris, A. J. L., Ripepe, M., Dehn, J., Rothery, D. A., & Calvari, S. (2007). Strombolian explosive styles and source conditions: Insights from thermal (FLIR) video. *Bulletin of Volcanology*, *69*(7), 769–784. https://doi.org/10.1007/s00445-006-0107-0

Peltier, A., Ferrazzini, V., Staudacher, T., & Bachèlery, P. (2005). Imaging the dynamics of dyke propagation prior to the 2000-2003 flank eruptions at Piton de La Fournaise, Reunion Island: DYKE PROPAGATION AT PITON DE LA FOURNAISE. *Geophysical Research Letters*, *32*(22), n/a-n/a. https://doi.org/10.1029/2005GL023720

Peterson, D. W., Holcomb, R. T., Tilling, R. I., & Christiansen, R. L. (1994). Development of lava tubes in the light of observations at Mauna Ulu, Kilauea Volcano, Hawaii. *Bulletin of Volcanology*, *56*(5), 343–360. https://doi.org/10.1007/BF00326461

Petronis, M. S., Delcamp, A., & Van Wyk De Vries, B. (2013). Magma emplacement into the Lemptégy scoria cone (Chaîne Des Puys, France) explored with structural, anisotropy of magnetic susceptibility, and Paleomagnetic data. *Bulletin of Volcanology*, *75*(10), 753. https://doi.org/10.1007/s00445-013-0753-y

Philpotts, A. R., & Dickson, L. D. (2000). The formation of plagioclase chains during convective transfer in basaltic magma. *Nature*, *406*(6791), 59–61. https://doi.org/10.1038/35017542

Philpotts, A. R., & Philpotts, D. E. (2007). Upward and downward flow in a camptonite dike as recorded by deformed vesicles and the anisotropy of magnetic susceptibility (AMS). *Journal of Volcanology and Geothermal Research*, *161*(1–2), 81–94. https://doi.org/10.1016/j.jvolgeores.2006.11.006

Poland, M. P., & Orr, T. R. (2014). Identifying hazards associated with lava deltas. *Bulletin of Volcanology*, *76*(12), 880. https://doi.org/10.1007/s00445-014-0880-0

Potter, D. K., & Stephenson, A. (1988). Single-domain particles in rocks and magnetic fabric analysis. *Geophysical Research Letters*, *15*(10), 1097–1100. https://doi.org/10.1029/GL015i010p01097

Raposo, M. I. B., & Ernesto, M. (1995). Anisotropy of magnetic susceptibility in the Ponta Grossa dyke swarm (Brazil) and its relationship with magma flow direction. *Physics of the Earth and Planetary Interiors*, *87*(3–4), 183–196. https://doi.org/10.1016/0031-9201(94)02970-M

Rasband, W. S. (2012). ImageJ: Image processing and analysis in Java. *Astrophysics Source Code Library*, ascl:1206.013.

Ray, R., Sheth, H. C., & Mallik, J. (2007). Structure and emplacement of the Nandurbar–Dhule mafic dyke swarm, Deccan Traps, and the tectonomagmatic evolution of flood basalts. *Bulletin of Volcanology*, *69*(5), 537–551. https://doi.org/10.1007/s00445-006-0089-y

Rochette, P. (1987). Magnetic susceptibility of the rock matrix related to magnetic fabric studies. *Journal of Structural Geology*, *9*(8), 1015–1020. https://doi.org/10.1016/0191-8141(87)90009-5

Rochette, P. (1988). Inverse magnetic fabric in carbonate-bearing rocks. *Earth and Planetary Science Letters*, *90*(2), 229–237. https://doi.org/10.1016/0012-821X(88)90103-3

Rochette, P., Aubourg, C., & Perrin, M. (1999). Is this magnetic fabric normal? A review and case studies in volcanic formations. *Tectonophysics*, *307*(1–2), 219–234. https://doi.org/10.1016/S0040-1951(99)00127-4

Rochette, P., Jackson, M., & Aubourg, C. (1992). Rock magnetism and the interpretation of anisotropy of magnetic susceptibility. *Reviews of Geophysics*, *30*(3), 209. https://doi.org/10.1029/92RG00733

Rochette, P., Jenatton, L., Dupuy, C., Boudier, F., & Reuber, I. (1991). Diabase Dikes Emplacement in the Oman Ophiolite: A Magnetic Fabric Study with Reference to Geochemistry. In Tj. Peters, A. Nicolas, & R. G. Coleman (Eds.), *Ophiolite Genesis and Evolution of the Oceanic Lithosphere* (Vol. 5, pp. 55–82). Springer Netherlands. https://doi.org/10.1007/978-94-011-3358-6_5

Romagnoli, C. (2013). Chapter 3 Characteristics and morphological evolution of the Aeolian volcanoes from the study of submarine portions. *Geological Society, London, Memoirs*, *37*(1), 13–26. https://doi.org/10.1144/M37.3

Romano, R. O. M. O. L. O. (1982). Succession of the volcanic activity in the Etnean area. *Memorie della Società Geologica Italiana*, *23*, 27-48.

Romano, R., & STURIALE, C. (1975). Geologia della Tavoletta Monte Etna Sud (F262-III SO). *Bollettino della Società geologica italiana*, *94*(5), 1109-1148.

Roni, E., Westerman, D. S., Dini, A., Stevenson, C., & Rocchi, S. (2014). Feeding and growth of a dyke–laccolith system (Elba Island, Italy) from AMS and mineral fabric data. *Journal of the Geological Society*, *171*(3), 413–424. https://doi.org/10.1144/jgs2013-019

Rosi, M., Bertagnini, A., & Landi, P. (2000). Onset of the persistent activity at Stromboli Volcano (Italy). *Bulletin of Volcanology*, *62*(4–5), 294–300. https://doi.org/10.1007/s004450000098

Sahagian, D. (1985). Bubble Migration and Coalescence during the Solidification of Basaltic Lava Flows. *The Journal of Geology*, *93*(2), 205–211. https://doi.org/10.1086/628942

Sangode, S. J., Sharma, R., Mahajan, R., Basavaiah, N., Srivastava, P., Gudadhe, S. S., Meshram, D. C., & Venkateshwarulu, M. (2017). Anisotropy of magnetic susceptibility and rock magnetic applications in the Deccan volcanic province based on some case studies. *Journal of the Geological Society of India*, *89*(6), 631–642. https://doi.org/10.1007/s12594-017-0672-1

Sangode, S. J., Tembhurne, S., Mahajan, R., Deenadayalan, K., Meshram, D. C., Dongre, A. N., Bhagat, A. R., & Satyanarayana, K. V. V. (2022). Magnetic fabrics and magnetic mineralogical variations in Lava Channel: An example from the Deccan Volcanic Province, India. *Journal of Earth System Science*, *131*(1), 24. https://doi.org/10.1007/s12040-021-01769-x

Sawłowicz, Z. (2020). A short review of pyroducts (lava tubes). *Annales Societatis Geologorum Poloniae*. https://doi.org/10.14241/asgp.2020.34

Schmiedel, T., Burchardt, S., Mattsson, T., Guldstrand, F., Galland, O., Palma, J., & Skogby, H. (2021). Emplacement and Segment Geometry of Large, High-Viscosity Magmatic Sheets. *Minerals*, *11*(10), 1113. https://doi.org/10.3390/min11101113

Schneider, J.-L., & Fisher, R. V. (1998). Transport and emplacement mechanisms of large volcanic debris avalanches: Evidence from the northwest sector of Cantal Volcano (France). *Journal of Volcanology and Geothermal Research*, *83*(1–2), 141–165. https://doi.org/10.1016/S0377-0273(98)00016-X

Shaar, R., & Feinberg, J. M. (2013). Rock magnetic properties of dendrites: Insights from MFM imaging and implications for paleomagnetic studies. *Geochemistry, Geophysics, Geosystems*, *14*(2), 407–421. https://doi.org/10.1002/ggge.20053

Shelley, D. (1985). Determining paleo-flow directions from groundmass fabrics in the Lyttelton radial dykes, New Zealand. *Journal of Volcanology and Geothermal Research*, *25*(1–2), 69–79. https://doi.org/10.1016/0377-0273(85)90005-8

Silva, P. F., Marques, F. O., Machek, M., Henry, B., Hirt, A. M., Roxerová, Z., Madureira, P., & Vratislav, S. (2014). Evidence for non-coaxiality of ferrimagnetic and paramagnetic fabrics, developed during magma flow and cooling in a thick mafic dyke. *Tectonophysics*, *629*, 155–164. https://doi.org/10.1016/j.tecto.2014.04.017

Skilling, I. P. (2002). Basaltic pahoehoe lava-fed deltas: Large-scale characteristics, clast generation, emplacement processes and environmental discrimination. *Geological Society, London, Special Publications*, *202*(1), 91–113. https://doi.org/10.1144/GSL.SP.2002.202.01.06

Sparks, R. S. J., Pinkerton, H., & Hulme, G. (1976). Classification and formation of lava levees on Mount Etna, Sicily. *Geology*, *4*(5), 269. https://doi.org/10.1130/0091-7613(1976)4<269:CAFOLL>2.0.CO;2

Speranza, F., Pompilio, M., D'Ajello Caracciolo, F., & Sagnotti, L. (2008). Holocene eruptive history of the Stromboli volcano: Constraints from paleomagnetic dating. *Journal of Geophysical Research: Solid Earth*, *113*(B9), 2007JB005139. https://doi.org/10.1029/2007JB005139

Stacey, F. D., Joplin, G., & Lindsay, J. (1960). Magnetic anisotropy and fabric of some foliated rocks from S.E. Australia. *Geofisica Pura e Applicata*, *47*(1), 30–40. https://doi.org/10.1007/BF01992481

Stevenson, C. T. E., O'Driscoll, B., Holohan, E. P., Couchman, R., Reavy, R. J., & Andrews, G. D. M. (2008). The structure, fabrics and AMS of the Slieve Gullion ring-complex, Northern Ireland: Testing the ring-dyke emplacement model. *Geological Society, London, Special Publications*, *302*(1), 159–184. https://doi.org/10.1144/SP302.12

Stevenson, J. A., Mitchell, N. C., Mochrie, F., Cassidy, M., & Pinkerton, H. (2012). Lava penetrating water: The different behaviours of pāhoehoe and ʻaʻā at the Nesjahraun, Þingvellir, Iceland. *Bulletin of Volcanology*, *74*(1), 33–46. https://doi.org/10.1007/s00445-011-0480-1

Suzuki, D. A., & Takagi, H. (2018). Evaluation of Geosite for Sustainable Planning and Management in Geotourism. *Geoheritage*, *10*(1), 123–135. https://doi.org/10.1007/s12371-017-0225-4

Symons, D. T. A. (1975). Age and flow direction from magnetic measurements on the historic Aiyansh flow, British Columbia. *Journal of Geophysical Research*, *80*(17), 2622–2626. https://doi.org/10.1029/JB080i017p02622

Taisne, B., Brenguier, F., Shapiro, N. M., & Ferrazzini, V. (2011). Imaging the dynamics of magma propagation using radiated seismic intensity: DYNAMICS OF DIKE PROPAGATION. *Geophysical Research Letters*, *38*(4), n/a-n/a. https://doi.org/10.1029/2010GL046068

Tarling D, & Hrouda F (Eds.). (1993). Magnetic anisotropy of rocks. Springer Science & Business Media.

Tanguy, J.-C., Condomines, M., & Kieffer, G. (1997). Evolution of the Mount Etna magma: Constraints on the present feeding system and eruptive mechanism. *Journal of Volcanology and Geothermal Research*, *75*(3–4), 221–250. https://doi.org/10.1016/S0377-0273(96)00065-0

Thivet, S., Gurioli, L., & Di Muro, A. (2020). Basaltic dyke eruptions at Piton de La Fournaise: Characterization of the eruptive products with implications for reservoir conditions, conduit processes and eruptive dynamics. *Contributions to Mineralogy and Petrology*, *175*(3), 26. https://doi.org/10.1007/s00410-020-1664-5

Tibaldi, A. (2015). Structure of volcano plumbing systems: A review of multi-parametric effects. *Journal of Volcanology and Geothermal Research*, *298*, 85–135. https://doi.org/10.1016/j.jvolgeores.2015.03.023

Tomić, N., & Božić, S. (2014). A modified geosite assessment model (M-GAM) and its application on the Lazar Canyon area (Serbia). *International journal of environmental research*, *8*(4), 1041-1052.

Tribble, G. W. (1991). Underwater observations of active lava flows from Kilauea volcano, Hawaii. *Geology*, *19*(6), 633. https://doi.org/10.1130/0091-7613(1991)019<0633:UOOALF>2.3.CO;2

Trippanera, D., Porreca, M., Urbani, S., Kissel, C., Winkler, A., Sagnotti, L., Nazzareni, S., & Acocella, V. (2020). Interpreting Inverse Magnetic Fabric in Miocene Dikes From Eastern Iceland. *Journal of Geophysical Research: Solid Earth*, *125*(11), e2020JB020306. https://doi.org/10.1029/2020JB020306

Tucker, D. S., & Scott, K. M. (2009). Structures and facies associated with the flow of subaerial basaltic lava into a deep freshwater lake: The Sulphur Creek lava flow, North Cascades, Washington. *Journal of Volcanology and Geothermal Research*, *185*(4), 311–322. https://doi.org/10.1016/j.jvolgeores.2008.11.028

Varga, R. J., Gee, J. S., Staudigel, H., & Tauxe, L. (1998). Dike surface lineations as magma flow indicators within the sheeted dike complex of the Troodos Ophiolite, Cyprus. *Journal of Geophysical Research: Solid Earth*, *103*(B3), 5241–5256. https://doi.org/10.1029/97JB02717

Vincent, P. M. (1980). Volcanisme et chambres magmatiques: l'exemple des Monts Dore.

Walker, G. P. L. (1991). Structure, and origin by injection of lava under surface crust, of tumuli, ?lava rises?, ?lava-rise pits?, and ?lava-inflation clefts? In Hawaii. *Bulletin of Volcanology*, *53*(7), 546–558. https://doi.org/10.1007/BF00298155

Wassmer, P., Schneider, J.-L., Fonfrège, A.-V., Lavigne, F., Paris, R., & Gomez, C. (2010). Use of anisotropy of magnetic susceptibility (AMS) in the study of tsunami deposits: Application to the 2004 deposits on the eastern coast of Banda Aceh, North Sumatra, Indonesia. *Marine Geology*, *275*(1–4), 255–272. https://doi.org/10.1016/j.margeo.2010.06.007

Weaver, R., Roberts, A. P., & Barker, A. J. (2002). A late diagenetic (syn-folding) magnetization carried by pyrrhotite: Implications for paleomagnetic studies from magnetic iron sulphide-bearing sediments. *Earth and Planetary Science Letters*, *200*(3–4), 371–386. https://doi.org/10.1016/S0012-821X(02)00652-0

Wei, W., Chen, Y., Faure, M., Shi, Y. H., Martelet, G., Hou, Q. L., Lin, W., Le Breton, N., & Wang, Q. C. (2014). A multidisciplinary study on the emplacement mechanism of the Qingyang–Jiuhua Massif in Southeast China and its tectonic bearings. Part I: Structural geology, AMS and paleomagnetism. *Journal of Asian Earth Sciences*, *86*, 76–93. https://doi.org/10.1016/j.jseaes.2013.06.003

Wiegand, M., Trumbull, R. B., Kontny, A., & Greiling, R. O. (2017). An AMS study of magma transport and emplacement mechanisms in mafic dykes from the Etendeka Province, Namibia. *Tectonophysics*, *716*, 149–167. https://doi.org/10.1016/j.tecto.2016.08.016

Wing-Fatt, L., & Stacey, F. D. (1966). Magnetic anisotropy of laboratory materials in which magma flow is simulated. *Pure and Applied Geophysics PAGEOPH*, *64*(1), 78–80. https://doi.org/10.1007/BF00875533

Woo, J. Y. L., & Kilburn, C. R. J. (2010). Intrusion and deformation at Campi Flegrei, southern Italy: Sills, dikes, and regional extension. *Journal of Geophysical Research*, *115*(B12), B12210. https://doi.org/10.1029/2009JB006913

Wood, C. (1981). Exploration and geology of some lava tube caves on the Hawaiian volcanoes. Trans. British Cave Res. Assoc, 8, 111-129.

Yu, X., Huang, B., Guan, S., Fu, S., Cheng, F., Cheng, X., Zhang, T., & Guo, Z. (2014). Anisotropy of magnetic susceptibility of Eocene and Miocene sediments in the Qaidam Basin, Northwest China: Implication for Cenozoic tectonic transition and depocenter migration. *Geochemistry, Geophysics, Geosystems*, *15*(6), 2095–2108. https://doi.org/10.1002/2014GC005231

Zananiri, I., Dimitriadis, S., Kondopoulou, D., & Kilias, A. (2004). MAGNETIC FABRICS OF THE TERTIARY VRONDOU PLUTONIC COMPLEX, NORTHERN GREECE. *Bulletin of the Geological Society of Greece*, *36*(3), 1316. https://doi.org/10.12681/bgsg.16475

Zhu, R., Shi, C., & Liu, Q. (2003). Anisotropy of magnetic susceptibility of Hannuoba basalt, northern China: Constraints on the vent position of the lava sequences. *Geophysical Research Letters*, *30*(2), 2002GL016215. https://doi.org/10.1029/2002GL016215

Zhu, Z., Zhang, S., Tang, C., Li, H., Xie, S., Ji, J., & Xiao, G. (2012). Magnetic fabric of stalagmites and its formation mechanism. *Geochemistry, Geophysics, Geosystems*, *13*(6), 2011GC003869. https://doi.org/10.1029/2011GC003869